ALEXANDER L. KOLLHOFF

OBSERVATIONS OF SOLAR ENERGETIC PARTICLES WITH THE ELECTRON PROTON TELESCOPE ON SOLAR ORBITER

OBSERVATIONS OF SOLAR ENERGETIC PARTICLES WITH THE ELECTRON PROTON TELESCOPE ON SOLAR ORBITER

ALEXANDER L. KOLLHOFF

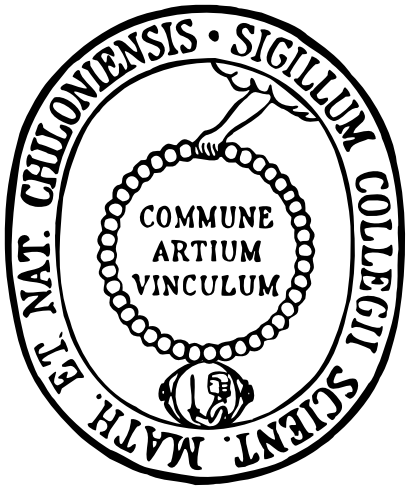

DISSERTATION
zur Erlangung des Doktorgrades
der Mathematisch-Naturwissenschaftlichen Fakultät
der Christian-Albrechts-Universität zu Kiel

4. März 2025

Alexander L. Kollhoff: *Observations of Solar Energetic Particles with the Electron Proton Telescope on Solar Orbiter*, 4. März 2025

ERSTER GUTACHTER (SUPERVISOR):
Prof. Dr. Robert F. Wimmer-Schweingruber

ZWEITER GUTACHTER:
Prof. Dr. Wolfgang J. Duschl

TAG DER MÜNDLICHEN PRÜFUNG:
28. Mai 2025

ZUM DRUCK GENEHMIGT:
28. Mai 2025

ZUSAMMENFASSUNG

Die Erforschung von solaren Eruptionen und der dabei frei werdenden ionisierenden Teilchenstrahlung, den sogenannten solaren energiereichen Teilchen (engl. solar energetic particles, SEPs), ist eines der Kerngebiete der Extraterrestrischen Physik. Mit dem Electron Proton Telescope (EPT) wurde an der Christian-Albrechts-Universität zu Kiel ein Instrument entwickelt, das als Teil der Solar-Orbiter-Mission seit 2020 ionisierende Teilchenstrahlung im interplanetaren Raum misst. Die Messungen des EPT sollen dabei helfen zu verstehen, wie SEPs an der Sonne beschleunigt werden und wie sie sich durch den interplanetaren Raum ausbreiten. Für die korrekte Interpretation der Messdaten müssen jedoch eine Reihe instrumenteller Effekte berücksichtigt werden.

Im Rahmen dieser Arbeit werden anhand von Monte-Carlo-Simulationen Ansprechfunktionen des EPT gegenüber energiereichen Teilchen bestimmt. Diese Ansprechfunktionen ermöglichen es, die Messungen des EPT besser zu interpretieren und fehlerhafte Identifikationen von Teilchenarten oder Teilchenenergien zu vermeiden. Anhand von Beispielen wird gezeigt, wie Teilchen mit Energien weit oberhalb des beabsichtigten Messbereiches Hintergrundsignale im Instrument erzeugen und wie hochenergetische Elektronen vermeintliche Ionensignale herbeiführen können. Die hier bestimmten Ansprechfunktionen werden zudem verwendet, um die öffentlich verfügbaren Daten des EPT aufzubereiten, die von einer breiten wissenschaftlichen Community genutzt werden.

Darüber hinaus beschäftigt sich diese Arbeit mit der Frage, wie sich Beobachtungen von Teilchenereignissen erklären lassen, bei denen große Teile der inneren Heliosphäre mit SEPs gefüllt werden. In einer entsprechenden Fallstudie (Kollhoff u. a., 2021) werden In-situ-Messungen von SEPs und Remote-Sensing-Beobachtungen der solaren Eruption von vier unterschiedlichen Raumsonden ausgewertet. Als Ergebnis der Auswertung werden zwei mögliche Szenarien diskutiert, welche die enorme räumliche Ausbreitung der energiereichen Teilchen erklären könnten.

Abschließend widmet sich diese Arbeit der Frage, welchen Einfluss der interplanetare Teilchentransport auf Beobachtungen von Teilchenereignissen hat. Hierfür werden Beobachtungen desselben Teilchenereignisses bei unterschiedlichen solaren Abständen verglichen (Kollhoff u. a., 2023). Das Ergebnis deutet darauf hin, dass sich charakteristische Größen von Ereignissen, wie beispielsweise der maximale Teilchenfluss, je nach Ereignis variabel mit solarem Abstand ändern. Als mögliche Erklärung für starke Unterschiede zwischen einzelnen Ereignissen werden Probleme in den Methoden zur Bestimmung der charakteristischen Größen, instrumentelle Unterschiede und der unbekannte Zustand des interplanetaren Mediums diskutiert.

ABSTRACT

The research on solar eruptions and the associated particle radiation, so-called solar energetic particles (SEPs), is an essential part of extraterrestrial physics. With the Electron Proton Telescope (EPT), the Christian-Albrechts-Universität zu Kiel has developed an instrument that measures the ionising particle radiation in interplanetary space since 2020 as part of the Solar Orbiter mission. The measurements of EPT should help to understand how SEPs are accelerated at the Sun and how they propagate through interplanetary space. However, for a correct interpretation of the measurements, several instrumental effects need to be considered.
As part of this work, the response functions of EPT for energetic particles were determined from Monte Carlo simulations. These response functions allow for a better interpretation of the measurements and help to prevent incorrect identifications of particle species and particle energies. In two examples, the response functions are used to show how particles with energies well above the intended measuring range can create background signals in the instrument and how highly energetic electrons can create supposed ion signals. The response functions obtained here are now the basis for the production of the public EPT data, which is used by a broad scientific community.
Moreover, this work investigates how observations of particle events can be explained in which large parts of the inner heliosphere are filled with energetic particles. In a case study of a corresponding event (Kollhoff et al., 2021), in situ SEP observations and remote sensing observations of the solar eruption from four different spacecraft are analysed. As a result of the analysis, two possible scenarios are discussed that could explain the large spatial spread of the energetic particles.
Finally, the work addresses the question of how interplanetary transport effects influence observations of SEP events. For this purpose, observations of the same event at different solar distances are compared (Kollhoff et al., 2023). The results indicate that characteristic event parameters, such as the maximum particle flux, change differently with solar distances in different events. As a possible explanation for large variations between individual events, the study discusses limitations of the chosen parameters, instrumental differences and the unknown condition in the interplanetary medium.

LIST OF PUBLICATIONS

During the preparation of this thesis, I collaborated on several peer-reviewed publications. Two of these publications are included in chapters 6 and 7. The other publications are beyond the focus of this thesis and are therefore only listed here.

Allen, R. C. et al. (Dec. 2021). "Energetic ions in the Venusian system: Insights from the first Solar Orbiter flyby." In: *A&A* 656, A7. DOI: 10.1051/0004-6361/202140803.

Brüdern, M. et al. (July 2022). "A new method to determine solar energetic particle anisotropies and their associated uncertainties demonstrated for STEREO/SEPT." In: *A&A* 663, A89. DOI: 10.1051/0004-6361/202142761.

Bučík, R. et al. (Dec. 2021). "The long period of ^{3}He-rich solar energetic particles measured by Solar Orbiter 2020 November 17-23." In: *A&A* 656, L11. DOI: 10.1051/0004-6361/202141009.

Dresing, N. et al. (Feb. 2020). "Statistical Results for Solar Energetic Electron Spectra Observed over 12 yr with STEREO/SEPT." In: *ApJ* 889.2, 143. DOI: 10.3847/1538-4357/ab64e5.

Fleth, S. et al. (Aug. 2023). "Anisotropies of solar energetic electrons in the MeV range measured with Solar Orbiter/EPD/HET." In: *A&A* 676, A58. DOI: 10.1051/0004-6361/202345909.

Freiherr von Forstner, J. L. et al. (Dec. 2021). "Radial evolution of the April 2020 stealth coronal mass ejection between 0.8 and 1 AU. Comparison of Forbush decreases at Solar Orbiter and near the Earth." In: *A&A* 656, A1. DOI: 10.1051/0004-6361/202039848.

Gómez-Herrero, R. et al. (2021). "First near-relativistic solar electron events observed by EPD onboard Solar Orbiter." In: *A&A* 656, p. L3. DOI: 10.1051/0004-6361/202039883.

Klein, K.-L. et al. (Oct. 2024). "Non-thermal electrons in an eruptive solar event: Magnetic structure, confinement, and escape into the heliosphere." In: *A&A* 690, A382. DOI: 10.1051/0004-6361/202450456.

Kollhoff, A. et al. (2021). "The first widespread solar energetic particle event observed by Solar Orbiter on 2020 November 29." In: *A&A* 656, A20. DOI: 10.1051/0004-6361/202140937.

Kollhoff, A. et al. (2023). "Multi-spacecraft observations of near-relativistic electron events at different radial distances." In: *A&A* 675, A155. DOI: 10.1051/0004-6361/202345955.

Lario, D. et al. (July 2022). "Influence of Large-scale Interplanetary Structures on the Propagation of Solar Energetic Particles: The

Multispacecraft Event on 2021 October 9." In: *ApJ* 934.1, 55. DOI: 10.3847/1538-4357/ac6efd.

Mason, G. M. et al. (Dec. 2021). "Solar energetic particle heavy ion properties in the widespread event of 2020 November 29." In: *A&A* 656, L12. DOI: 10.1051/0004-6361/202141310.

Strauss, R. D. et al. (July 2020). "On the Shape of SEP Electron Spectra: The Role of Interplanetary Transport." In: *ApJ* 897.1, 24. DOI: 10.3847/1538-4357/ab91b0.

Wimmer-Schweingruber, R. F. et al. (2021). "First year of energetic particle measurements in the inner heliosphere with Solar Orbiter's Energetic Particle Detector." In: *A&A* 656, A22. DOI: 10.1051/0004-6361/202140940.

Wimmer-Schweingruber, R. F. et al. (Oct. 2023). "Unusually long path length for a nearly scatter-free solar particle event observed by Solar Orbiter at 0.43 au." In: *A&A* 678, A98. DOI: 10.1051/0004-6361/202346319.

Yang, L. et al. (May 2023). "Acceleration of suprathermal protons near an interplanetary shock." In: *A&A* 673, A73. DOI: 10.1051/0004-6361/202245681.

Yang, L. et al. (June 2024). "Dynamic acceleration of energetic protons by an interplanetary collisionless shock." In: *A&A* 686, A132. DOI: 10.1051/0004-6361/202348723.

CONTENTS

ACRONYMS

ADC analogue-to-digital converter
CAU Christian-Albrechts-Universität zu Kiel
EPT Electron Proton Telescope
PIPS passivated implanted planar silicon
SEPT Solar Electron and Proton Telescope
SSD solid state detector
HET High Energy Telescope
EPD Energetic Particle Detector
STEREO Solar TErrestrial RElations Observatory
PTB Physikalisch-Technische Bundesanstalt
HIMAC Heavy Ion Medical Accelerator in Chiba
DPS Data Product Scheduler
FOV field of view
DP data product
DPI data product item
DNL differential nonlinearity
GCR galactic cosmic rays
ACR anomalous cosmic rays
ESA European Space Agency
NASA National Aeronautics and Space Administration
SEP solar energetic particle
STEP SupraThermal Electron Proton
SIS Suprathermal Ion Spectrograph
MAG Solar Orbiter Magnetometer
PHA pulse height analysis
CERN European Organization for Nuclear Research
HCI heliocentric inertial
LHC Large Hadron Collider
XRS Solar X-Ray Sensor
AIA Atmospheric Imaging Assembly
SDO Solar Dynamics Observatory
ORFEES Observations Radiospectrographiques pour FEDOME et l'Etude des Eruptions Solaires

GBM Gamma-ray Burst Monitor

NRH Nançay Radioheliograph

SXR soft X-ray

HXR hard X-ray

EUV extreme ultraviolet

CME coronal mass ejection

MHD magnetohydrodynamic

IMF interplanetary magnetic field

LASCO Large Angle Spectroscopic Coronagraph

SOHO Solar and Heliospheric Observatory

SWA Solar Wind Analyser

AMS Alpha Magnetic Spectrometer

ESP energetic storm particle

CIR corotating interaction region

STIX Spectrometer/Telescope for Imaging X-rays

RPW Solar Orbiter Radio and Plasma Waves instrument

EPHIN Electron Proton Helium Instrument

LIS local interstellar spectrum

3DP Three-Dimensional Plasma and Energetic Particle Investigation

HMI Helioseismic and Magnetic Imager

Part I

INTRODUCTION

1 MOTIVATION AND GOALS

Alongside the continuous emission of electromagnetic radiation and solar plasma, the Sun occasionally produces massive eruptions of electromagnetic radiation, energetic particles, plasma and magnetic structures. These eruptions can change the interplanetary environment so drastically that they pose a threat to modern technology and human life in space. Some of the most violent eruptions are solar flares and coronal mass ejections.

Solar flares are eruptions of electromagnetic radiation that frequently occur on the Sun. In a solar flare, energy stored in the solar magnetic field is abruptly released and particles of the solar plasma are accelerated. These accelerated particles interact with the solar atmosphere and surface, thereby emitting characteristic electromagnetic radiation. In some cases, a portion of the accelerated particles is released into interplanetary space, where they can be observed in the form of so-called SEP events. SEP events are strong increases in the flux of energetic particles, often by orders of magnitude, which can last for hours or days. The energetic particles in these events act as ionising radiation and pose a potential danger to astronauts and modern space technology (see e.g. Parsons et al., 2000 or Stephens et al., 2005 for worst-case dose estimates for SEP events).

Coronal mass ejections (CMEs) are large eruptions of coronal plasma and magnetic structures which are ejected from the Sun into the interplanetary space. They often occur together with solar flares, but the connection between the two phenomena is still under debate today. CME structures that collide with Earth are able to disturb the geomagnetic field, causing geomagnetic storms. The resulting changes in the geomagnetic field can lead to the induction of currents in electric grids on Earth, which can cause large-scale blackouts. A fairly recent example of such dramatic events was the geomagnetic storm on 29 to 31 October 2003, which left 50.000 Swedish grid customers without electricity for an hour (Pulkkinen et al., 2005). Some CMEs drive strong magnetohydrodynamic shock waves at which energetic particles can be accelerated to energies of several GeV. Such CMEs are considered as the strongest sources of SEPs.

The dangers emanating from the Sun for modern technology and human life in space are a major motivation for solar science and studies on solar eruptions. Predicting eruptions and estimating the particle radiation that they may produce is one of the key objectives in this field. However, forecasting such events requires a profound knowledge of all physical processes involved in these phenomena.

In 2020, the European Space Agency (ESA) launched the Solar Orbiter mission with the aim of investigating how the Sun creates and controls

the Heliosphere. In doing so, the mission also helps to acquire the fundamental knowledge needed to forecast solar eruptions and SEP events. With four specially developed sensors the mission observes the elemental composition and the directional flux of energetic particles in the inner heliosphere. These observations can be used to characterise SEP events, to estimate potential hazards and to develop physical models describing the acceleration and propagation of SEPs.
One of the four sensors is the Electron Proton Telescope (EPT). EPT was developed and built at the Christian-Albrechts-Universität zu Kiel (CAU) and is designed to measure the flux of near-relativistic electrons and ions in the inner heliosphere. However, instrumental effects influence the reliability of the research. As with any complex experiment, EPT has a number of instrumental effects that must be carefully considered before its measurements can be used to answer scientific questions. This thesis focuses on the correct interpretation of EPT measurements in order to further our knowledge about SEP events. It aims to answer the following three questions:

1. How exactly does EPT respond to directional and energy-dependent fluxes of energetic particles in space? The purpose of this question is to improve the general understanding of EPT measurements, which is essential for interpreting the observations. To answer this question, instrument response functions for various particle species are determined from Monte Carlo simulations.
2. What instrumental effects must be considered when analysing EPT measurements? This question addresses specific instrumental effects, which, without a proper description, could lead to wrong interpretations of the observations. Using the simulated response functions determined in this work, several instrumental effects are identified and their influence on the EPT science data is quantified.
3. How can measurements from EPT be combined with observations made by other spacecraft to study the sources of SEPs and the SEP propagation in interplanetary space? This question focuses on the scientific interpretation of the EPT data with the goal to better understand the physical processes behind SEP events. In two corresponding publications multi-spacecraft observations of SEP events are presented and analysed with regard to possible sources and transport conditions.

The thesis is structured into three parts. Part 1 provides a summary of the theoretical background to the physics of the Sun, solar eruptions and SEP events as well as a detailed description of EPT. Part 2 is dedicated to the simulation of instrument response functions and the analysis of instrumental effects. Part 3 presents multi-spacecraft observations of SEP events and discusses possible sources and transport conditions.

2 SCIENTIFIC BACKGROUND

As part of the Solar Orbiter mission, EPT was designed to study how energetic particles are accelerated at the Sun, how they are released from their source into interplanetary space and how they distribute in space and time. These three fundamental questions regarding SEPs have been studied for several decades now, but many aspects are still not fully understood.
This chapter briefly summarises the theoretical background regarding SEPs and other populations of energetic particles in the heliosphere in Sect. 2.2. An overview of the Solar Orbiter mission is given in Sect. 2.3, together with a description of how it aims to answer open questions regarding SEPs. But first, the following section gives a basic description of the structure of the Sun, its extended atmosphere, its varying activity and of different solar eruptions. Thereby, Sect. 2.1 introduces some of the essential terminology and provides the fundamental background needed to understand the nature of SEPs.

2.1 THE SUN

The Sun is an active star in the centre of our solar system, one astronomical unit ($1\,\mathrm{AU} = 1.49 \cdot 10^8\,\mathrm{km}$) away from Earth. It illuminates the solar system and constantly floods it with a stream of a thin plasma, called the solar wind. The appearance of the Sun and its activity are subject to periodic changes. Within a 22-year cycle, the Sun's magnetic field reverses its polarity, changing the structure of the solar atmosphere and the frequency of eruptive phenomena. Energetic particles, accelerated during solar eruptions, are guided by the extended magnetic field of the Sun. The solar magnetic field is dragged outward by the solar wind to distances beyond 100 AU and is winded on Archimedean spirals due to the solar rotation. The Sun is therefore not only a gigantic source of energetic particles, but it also defines the conditions in interplanetary space that determine how these particles propagate within it.

2.1.1 *Structure of the Sun*

The structure of the Sun is most commonly described using a shell model with six distinct layers (see e.g. Kallenrode, 2004; Goossens, 2003). The internal structure consists of a core, a radiation zone and a convection zone, while the atmosphere is divided into photosphere, chromosphere and corona. Figure 2.1 illustrates this basic shell model.

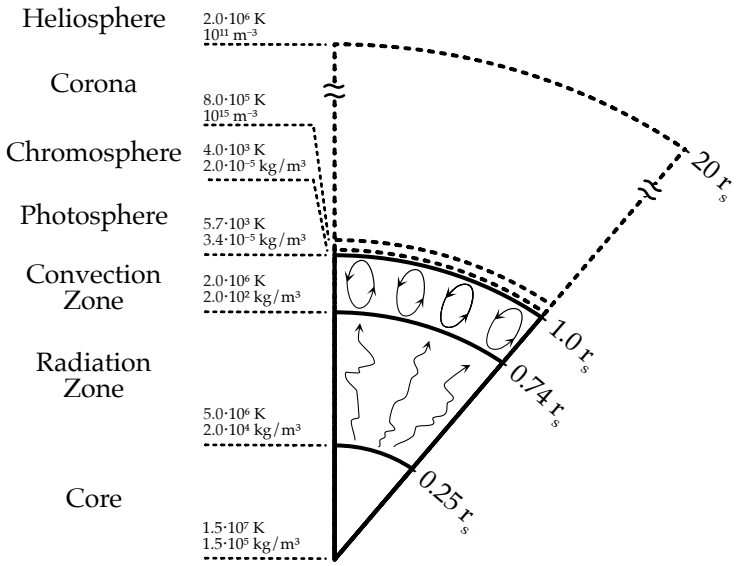

Figure 2.1: Illustration of the Sun's structure with typical estimates for the temperatures and densities at the inner boundaries of the different layers. Temperature and density estimates taken from Kallenrode (2004) and Goossens (2003).

The core on the Sun is the region where nuclear fusion takes place. It extends to around $0.25\,r_s$ ($1\,r_s = 6.96 \cdot 10^5$ km, the solar radius) and has a temperature of about $1.5 \cdot 10^7$ K. The fusion process in the Sun is described by the so-called proton-proton chain, in which hydrogen nuclei merge into helium (Bethe, 1939), thereby releasing energy mainly in the form of electromagnetic radiation, positrons and neutrinos. While neutrinos interact only weakly with matter and will leave the Sun practically unhindered, photons are strongly scattered on their path towards the solar surface. The mean free path of photons in the inner Sun is on the order of a few centimetres and although they travel with the speed of light, they need 170.000 years on average to diffuse through the second layer above the core, the so-called radiation zone (Mitalas et al., 1992).

The radiation zone ranges from about $0.25\,r_s$ to $0.74\,r_s$ and is defined as the region where energy is transported primarily by radiative diffusion and thermal conduction. At $\sim 0.74\,r_s$, the radiation zone transitions into the convection zone.

In the convection zone, plasma is continuously moving and the energy is primarily transported via convection. The interface between the radiation and convection zones also marks a change in the rotational dynamic of the Sun. While the core and the radiation zone rotate like rigid bodies, the convection zone rotates differentially like a fluid. The interface at which large changes in the rotation occur is called tachocline. The different rotation speeds in the tachocline produce

shearing forces which are thought to be fundamental for the solar dynamo and the generation of the solar magnetic field (more details given in Sect. 2.1.3).

At 1.0 r_s, the radiation zone transitions into the 'surface' of the Sun, the photosphere. The photosphere is the region in which the visible light is emitted. It has a temperature of about 5700 K and is a few hundred kilometres thick. A variety of visible structures can be recognised on it: On spacial scales of about $10^3 - 10^4$ km (Rast, 2003) granulation can be observed, which is caused by the underlying convection. An even more prominent feature on the photosphere are sunspots, which are dark areas with typical sizes of $10^7 - 10^8$ km^2 (Bogdan et al., 1988)[1]. They occur in regions where strong magnetic fields locally restrict the heat transport from the inner parts of the Sun to the surface. Sunspots often form the foot points of complex magnetic structures, such as coronal loops, which can extend far into the Sun's atmosphere.

The photosphere transitions into the chromosphere, where the temperature increases to 10^4 K, while the density decreases to about 10^{-4} times the photospheric density. Electromagnetic emission in the chromosphere is dominated by line emissions of various ions, giving this layer its name. The most prominent line is the $H\alpha$-line at 653 nm, emitted by hydrogen that has been thermally excited in the chromosphere. $H\alpha$ observations are frequently used to visualise solar structures such as magnetic loops, which are not recognisable in white-light images because of the overexposure of the photospheric emission. The same observations are also used to track the so-called Moreton waves (Moreton, 1960). Moreton waves are rapidly propagating (1000 km/s) disturbances in the chromosphere triggered by solar flares. A physical explanation for Moreton waves is given in Uchida (1968). More details on the general physics of the chromosphere and a comprehensive description of various chromospheric observations can be found in Carlsson et al. (2019).

Above the chromosphere, at a height of around 2000 km, an interface region separates the chromosphere from the much hotter solar corona. This region with a thickness of a few hundred kilometres is called the transition region. In this transition region, the temperature rises from 10^4 K to $8 \cdot 10^5$ K, atmospheric ions become strongly ionised and the magnetohydrodynamic conditions change drastically. A classical description of the transition region is given by Gabriel (1976).

The upper solar corona has a temperature of about $2 \cdot 10^6$ K and a plasma density of about 10^{11} m^{-3}. The enormous temperatures in the corona, which are hundreds of times higher than the temperatures in the photosphere and chromosphere, raise the question of how exactly the corona is heated. This coronal heating problem has not yet been conclusively solved, but current theories primarily consider wave heat-

1 The size of particular large sunspots (10^8 km^2) can be similar to the surface of the Earth ($5.1 \cdot 10^8$ km^2)

ing and small-scale magnetic reconnection as key processes. In wave heating theory it is assumed that magnetoacoustic and Alfvén waves carry energy through the lower atmosphere into the corona, where they dissipate into heat. The original description of this theory was introduced by Alfvén (1947). Small-scale magnetic reconnections, which occur in microflares, nanoflares and the recently discovered picoflares (Berghmans, D. et al., 2021), are also considered to contribute to the heating of the corona. More details on the coronal heating problem can be found in Aschwanden (2005) and van Ballegooijen et al. (2011).
A variety of solar phenomena can be observed in the corona. Band-pass filters in the extreme ultraviolet (EUV) range, for example at 17.1 nm, are used to observe hot coronal loops and solar flares. So-called EUV waves (Neupert, 1989), which propagate similarly to Moreton waves, can also be observed in the corona. EUV waves are recognisable as propagating emission fronts that spread outward from an active region. They often occur together with CMEs, but neither the connection between EUV waves and CMEs is fully understood, nor the relationship between Moreton and EUV waves. For further details on the three phenomena and their possible connection, see for example Wang et al. (2020) and references therein. The corona has no sharp outer boundary but transitions smoothly into the solar wind.

2.1.2 *The solar wind and the IMF*

The solar wind is the continuous outflow of coronal plasma from the Sun into the heliosphere. The idea of such a continuous flow was initially suggested by Ludwig Biermann in 1951 (Biermann, 1951). He proposed that solar particle radiation is responsible for the varying curvatures observed in comet tails. In 1956, Eugene Parker took up Biermann's idea and presented the fundamental concept that the solar corona is in a state of steady expansion, in which coronal plasma constantly overcomes the gravitational force of the Sun (Parker, 1958). At that time, Parker's theory was highly controversial, but only one year later, the Soviet spacecraft Luna 1 was able to observe the solar wind in space and in 1962 the US spacecraft Mariner 2 confirmed the observations, providing strong evidence of the solar wind (Obridko et al., 2017).
Today, the solar wind can be characterised fairly well with measurements from a number of solar wind experiments on various spacecraft. It primarily consists of ionised protons and alpha particles (He/H varies between 2 to 4.5%; Aellig et al., 2001) but also contains heavier ions. Kinetic energies of solar wind particles range from about 0.5 to 10 keV. The solar wind is usually described by its velocity distribution function, which describes the particle number density at a time in a three-dimensional velocity space. The velocity distribution function generally features a bulk that resembles a Maxwellian distribution.

The number density in the solar wind (0-th order moment of the 3D velocity distribution function) is on the order of a few particles per cubic centimetre. The bulk proton speed (1-st order moment) usually ranges from 250 to 800 km/s, but it can occasionally exceed speeds of 1000 km/s (Lopez, 1987). Proton temperature (2-nd order moment) ranges from approximately $5 \cdot 10^4$ K to $2 \cdot 10^5$ K (Lopez, 1987).
Often the solar wind is categorised empirically as fast and slow solar wind, where the slow solar wind has a bulk speed of around 400 km/s, a temperature of 10^6 K and a composition similar to that of the corona. Contrary, the fast solar wind has a bulk speed of around 750 km/s, a lower temperature and a composition similar to that of the photosphere. The origin and the acceleration of fast and slow solar wind is still under debate (for a review on the sources of fast and slow solar wind see, e.g., Feldman et al., 2005). While the properties of the solar wind are influenced by the solar cycle, they also vary on long-term scales between different cycles (McComas et al., 2008).
The domain of the solar wind extends well beyond solar distances of 100 AU. In 2010, Voyager 1 was the first spacecraft that reached the outer boundary of the solar wind. At a distance of 113.5 AU the spacecraft observed a flow of solar plasma with no radial velocity (Krimigis et al., 2011). Two years later, the spacecraft passed the so-called heliopause (Gurnett et al., 2013), which is defined as the boundary between the heliosphere and the interstellar medium.
Within the heliosphere the solar wind is shaping the interplanetary magnetic field (IMF). The plasma beta $\beta = p_{\text{thermal}}/p_{\text{magnetic}}$, which describes the ratio of thermal pressure to magnetic pressure, is commonly used to differentiate between domains where the magnetic field follows the solar wind and domains where the magnetic field constrains the motion of the plasma. At solar distances below $\sim 2\,r_s$ (Gary, 2001), a high magnetic pressure is present in the solar atmosphere and thus $\beta << 1$. In these regions, magnetic structures such as coronal loops can build up. Beyond $2\,r_s$, the plasma pressure exceeds the magnetic pressure ($\beta > 1$) and the solar magnetic field is 'frozen in'[2] the solar wind, which drags it radially outwards.
The boundary between the two β-regions, where the magnetic field is approximately radial, is called the source surface of the IMF (Schatten et al., 1969). Beyond the source surface the field follows the stream lines of the solar plasma. Due to the Sun's rotation, it winds on Archimedean spirals. In an ideal model, the curvature of the IMF can be determined simply from the solar rotation speed (period of ~ 27 days per sidereal rotation at the equator) and the solar wind speed. Figure 2.2 illustrates the IMF according to the described model. In reference to the first theoretical description of this IMF shape (Parker,

2 Due to the high conductivity all electric fields vanish in the reference frame of the solar wind and the term 'frozen in' refers to a magnetic field that obeys the equation $\vec{E} - \vec{v}/c \times \vec{B} = 0$, where $\vec{v}$ is the velocity of the solar wind, $\vec{B}$ is the magnetic field and $\vec{E}$ is the electric field vector in the reference frame of an observer.

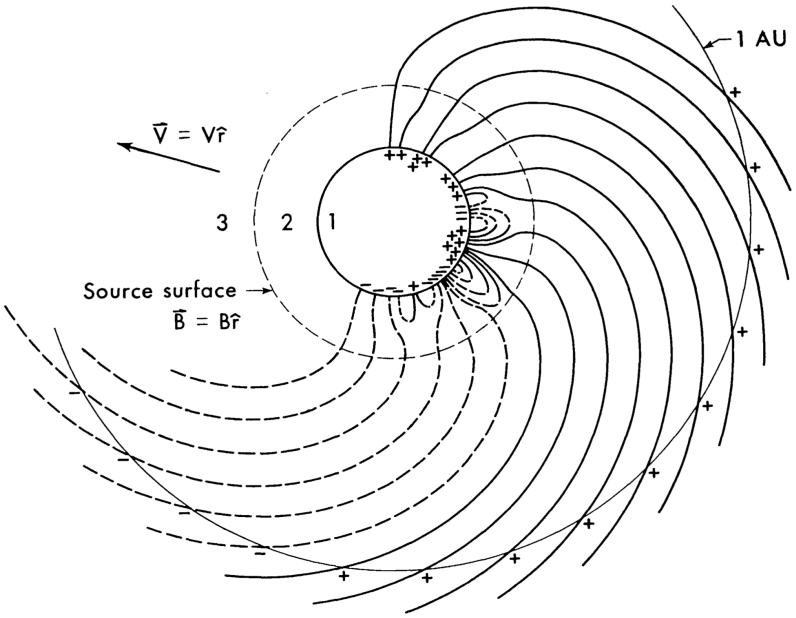

Figure 2.2: Illustration of the solar magnetic field in the source surface model. The inner region (1) illustrates the polarity of the photospheric magnetic field. Region 2 shows magnetic structures such as coronal loops. Region 3 shows the IMF behind the source surface winded on an Archimedean spiral. Figure taken from (Schatten et al., 1969).

1958) the ideal IMF field is also called Parker field or Parker spiral. The typical strength of the IMF decreases from $|B| \simeq 10^{-4}\,\mathrm{T}$ at the photosphere (outside of sunspots) to much smaller values of $\sim 10^{-8}\,\mathrm{T}$ at 1 AU (Kallenrode, 2004). However, the observed field strength is subject to strong variations. In fact, the IMF is often disturbed and can differ significantly from an ideal Archimedean spiral. Variations in the solar magnetic field strength and its polarity that occur on the photosphere and in the lower corona can be propagated into the IMF. Changes in solar wind speed and interplanetary structures such as CMEs can further change the topology and strength of the IMF. Nevertheless, by combining in situ measurements of the IMF and the solar wind with observations of the photospheric magnetic field (observed through the Zeeman effect), it is feasible to derive realistic approximations for the actual IMF (corresponding models are presented e.g. in Schatten et al., 1969; Pomoell et al., 2018).

2.1.3 *The solar cycle*

The solar magnetic field changes its polarity within a 22-year cycle, the so-called *Hale's cycle*, featuring one polarity reversal every 11 years. During each polarity reversal the appearance of the Sun and its activity changes dramatically. In a nearly periodic way the number of visible sunspots and the frequency of solar eruptions change in an 11-year

cycle. The 11-year variation is called the solar cycle or *Schwabe cycle*, in honour of Heinrich Schwabe, who was the first to properly identify periodic changes in the size and number of visible sunspots in 1843 (Schwabe, 1844).

During periods with a low sunspot number, referred to as solar minima, sunspots primarily emerge at high solar latitudes and in small groups. As the solar cycle progresses, the number of visible sunspots increases and they move towards the equator until the sunspot number peaks at the so-called solar maximum. The latitudinal distribution of sunspots over the solar cycle is described by an empirical law, the *Spörer's law* (Carrington, 1858; Spörer, 1880).

The magnetic field within sunspots features a characteristic polarity pattern: While the leading sunspot of a group, i.e. the one closest to the equator, usually has the same polarity as the hemisphere on which it emerged, the following sunspot shows the opposite polarity. Every 11 years the polarity of leading sunspots will reverse together with the large-scale magnetic field of the two hemispheres. This polarity pattern in sunspots is empirically described by *Hale's polarity law* (Hale et al., 1925).

Figure 2.3 illustrates the solar cycle based on the number of observed sunspots and their distribution in terms of latitude. The lower panel of the figure illustrates *Spörer's law* and is often referred to as the *Butterfly Diagram* (Maunder, 1922a). By convention, the solar cycles are numbered starting with *solar cycle 1* in 1755. The current *solar cycle 25* started in December 2019 (SILSO World Data Center, 2024) with a solar minimum.

The solar cycle is driven by the solar dynamo. A classical description of the solar dynamo can be found in Parker (1955). Today, various elaborate magnetohydrodynamic (MHD) models of the solar dynamo exist, which attempt to reproduce the cycle and provide explanations for the observations related to it. Some models are able to reproduce the 11-year activity cycle, the 22-year polarity cycle, the equator-ward drift of sunspot groups and a characteristic tilt of sunspot groups, which is described by the so-called *Joy's law* (Hale et al., 1919). However, not all observations can be well modelled yet. For example, the occurrence of prolonged sunspot minima, such as the *Maunder* minimum between 1645 and 1715 (Maunder, 1922b) and asymmetries in the occurrence of sunspots in the northern and southern hemispheres are often ignored in existing models. Nonetheless, dynamo models have improved considerably in the last few decades (a recent review on the existing solar dynamo models can be found in Charbonneau, 2020).

In its simplest form, the dynamo process and the resulting solar cycle may be described as follows: The magnetic field is generated primarily in the tachocline and in the convection zone by the differential rotation of conducting fluids, which generates a dipole field. Over the progressing cycle, the poloidal field gets wound up by the non-uniform

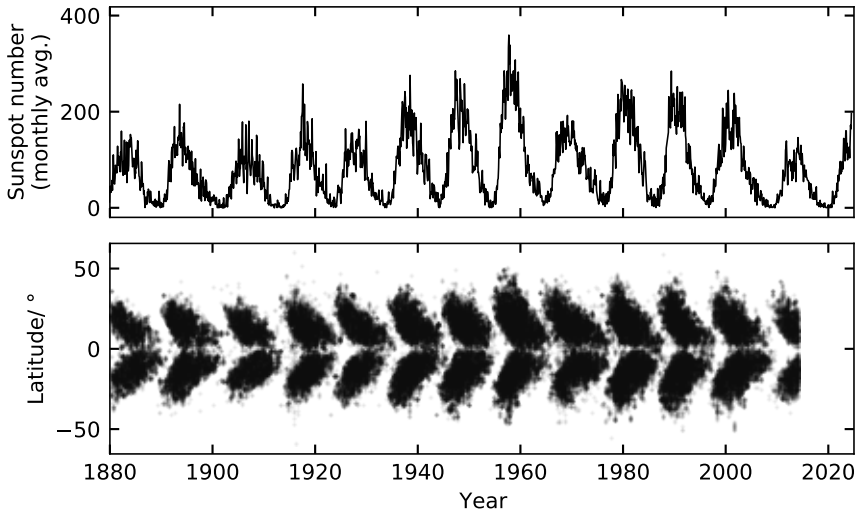

Figure 2.3: Variation of the monthly mean total sunspot number (upper panel) and their heliolatitudinal distribution (lower panel) over the last 14 solar cycles. Created with sunpot data from *WDC-SILSO, Royal Observatory of Belgium, Brussels* (upper panel) and the *Royal Observatory, Greenwich - USAF NOAA* (lower panel).

rotation and a toroidal component evolves. Within this process, tubes with a concentrated magnetic field, so-called flux tubes, emerge and magnetic buoyancy drives them up through the photosphere, creating the sunspots. Some flux tubes will extend far into the solar atmosphere, where they become observable in the form of coronal loops or prominences. Flux tubes and their associated groups of sunspots are often referred to as active regions. The latitudes at which active regions and sunspots primarily emerge are determined by the field strength of the underlying magnetic field and the differential rotation. The emergence of new sunspots reduces the local magnetic pressure and subsequently emerging sunspots appear at lower latitudes. Near the equator, sunspots on the different hemispheres approach each other and magnetic reconnection of their differently polarised fields is likely to occur. The complete reversal of the poloidal field is not well understood but could be caused by either reconnection of the poloidal field and the magnetic field in the following sunspots (which have an opposite polarity to the hemisphere), or by the occurrence of strong toroidal currents that induce a reverted poloidal field (Kallenrode, 2004).

Figure 2.4 shows a composition of images of the Sun at different wavelengths, where sunspots, active regions and coronal loops can be recognised.

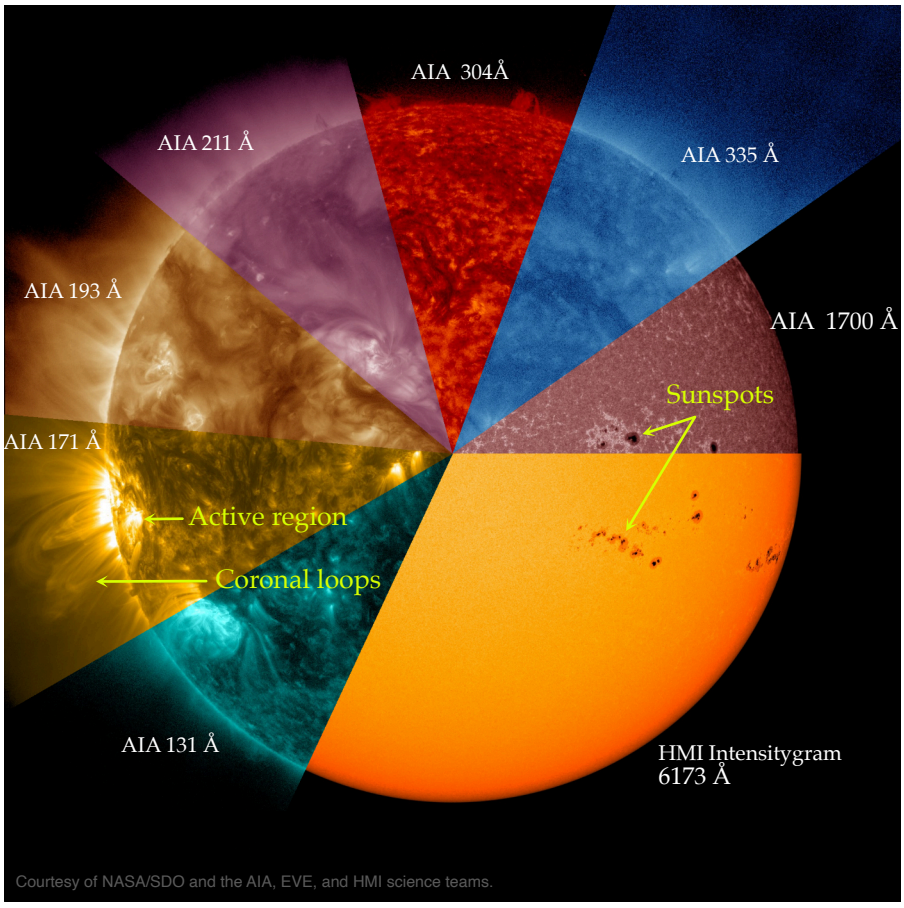

Figure 2.4: Image of the Sun composed from multiple images take from the Atmospheric Imaging Assembly (AIA) and the Helioseismic and Magnetic Imager (HMI) at different wavelengths on 1 August 2024. Two sunspot groups, an active region and coronal loops are marked by arrows.

2.1.4 *Solar eruptions*

Solar eruptions are powerful explosions on the Sun that can release electromagnetic radiation, coronal plasma, magnetic structures and energetic particles. The Sun's most prominent eruptive phenomena are solar flares and CMEs. Their frequency varies within the 11-year solar cycle – during a solar minimum both may occur only once a week while during a solar maximum several CMEs and flares can occur in a single day (Webb et al., 1994).

2.1.4.1 *Solar flares*

Solar flares are prompt increases in electromagnetic radiation emitted from the solar atmosphere that have a limited temporal ($10^3 - 10^4$ s) and spatial (up to 10^5 km) extent (Shibata et al., 2011). They usually occur in active regions with complex magnetic fields where field lines with opposing polarity converge (see e.g. Toriumi et al., 2019

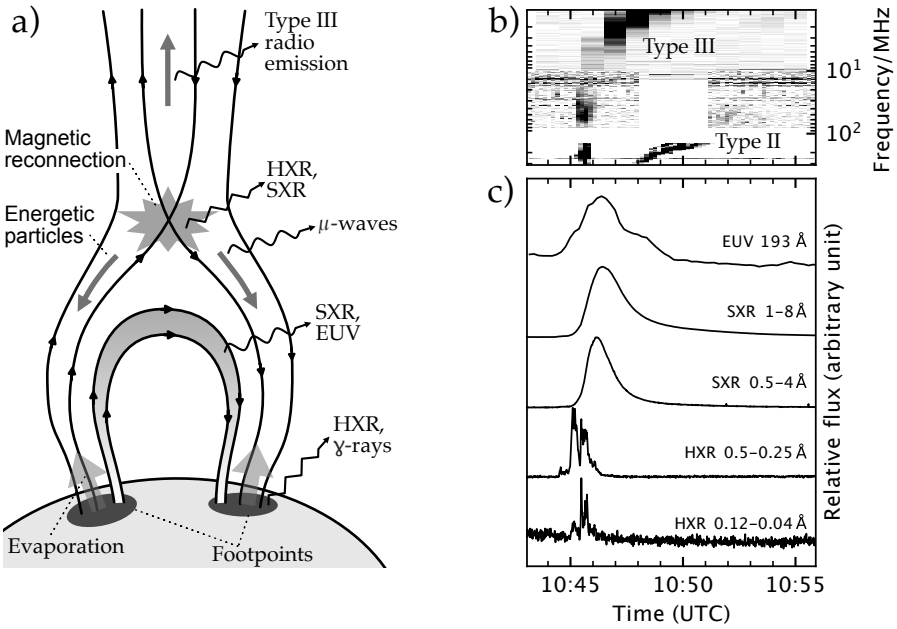

Figure 2.5: a) Sketch of a standard flare model (further description in Sect. 2.1.4.1). b) Radio spectrogram showing type-III and type-II radio emission shortly after the observation of a flare at 10:44 UT on 29 May 2020 c) Normalised light curves of hard X-rays (HXRs), soft X-ray (SXR) and EUV light observed during the flare. Created with radio data from ORFEES, NRH and Wind/WAVES (Bougeret et al., 1995). Light curve data from GBM (HXRs), XRS (SXRs) and AIA (EUV).

for details on flare production). During the process of magnetic reconnection (Parker, 1957) magnetic energy is abruptly released and ultimately converted into thermal and kinetic energy (Shibata et al., 2011). Particles accelerated within flares produce a broad spectrum of electromagnetic radiation via different emission processes ranging from thermal emission to bremsstrahlung.

Early observations of solar flares date back to 1859 when R. C. Carrington reported on the observation of a local brightening in white light on the solar surface that lasted several minutes (Carrington, 1859). With modern instruments flare emission can be studied at various wavelengths: Observatories such as the Observations Radiospectrographiques pour FEDOME et l'Etude des Eruptions Solaires (ORFEES; Hamini, A. et al., 2021) or the Nançay Radioheliograph (NRH; Kerdraon et al., 1997) are able to detect the radio emission from solar flares. Atmospheric imagers such as the Atmospheric Imaging Assembly (AIA; Lemen et al., 2012) on the Solar Dynamics Observatory (SDO) are able to observe the EUV emission. X-ray detectors such as the Solar X-Ray Sensor (XRS; Hanser et al., 1996) on the GOES satellites or the Gamma-ray Burst Monitor (GBM; Meegan et al., 2009) on the Fermi Observatory can observe the soft and hard X-ray emission from solar flares.

Figure 2.5 shows the electromagnetic emission observed by the instruments mentioned above during a typical solar flare. The figure also illustrates a basic model of a flare, which shows where the emission of different wavelengths originates (similar models were described e.g. in Yokoyama et al., 1998; Lysenko et al., 2019).
In the presented model, magnetic reconnection takes place within a magnetic loop structure at an so-called X-point, where magnetic field lines of opposing polarity converge. In proximity to the X-point, electrons and some ions are accelerated up to relativistic speeds. The exact acceleration process is not well known, but it likely involves acceleration due to direct electric fields, turbulences and shocks (see e.g. Scholer, 1988). Close to the top of the loop structure, the accelerated electrons interact with the thermal plasma, whereby HXRs and SXRs are emitted by bremsstrahlung. Electrons with $E > 100\,\mathrm{keV}$ can further produce microwaves through synchrotron radiation. Some of the nonthermal particles channel along the magnetic field towards the footpoints. Once they hit the denser plasma of the chromosphere, electrons produce hard X-rays via thick-target bremsstrahlung and in some cases ions produce γ-rays via nuclear interactions. Eventually, the nonthermal particles will heat and evaporate the plasma at the magnetic footpoints. The heated plasma ($\sim 10^7\,\mathrm{K}$; Antonucci et al., 1984) then raises in the loop and slowly emits SXRs and light in the EUV to visible range via thermal emission. The observed time-integrated light curves of hard X-rays and microwaves usually resemble the light curves of soft X-rays. This correlation is known as the Neupert effect (Dennis et al., 1992; Neupert, 1968).
In some flares, a fraction of the accelerated particles escape as SEPs on open field lines into the corona and interplanetary space. The escaping electrons can produce so-called type-III radio bursts. Type-III radio bursts are produced by beamed, outward-propagating electrons that excite Langmuir waves in a narrow band at the local electron plasma frequency (proportional to the square root of the local electron density) by so-called bump-on-tail instabilities. The Langmuir waves subsequently convert into electromagnetic waves through nonlinear plasma processes (for details see Thejappa et al., 2012; Buttighoffer, 1998 and references therein). As the emitted frequency depends on the local electron density, which decreases exponentially with solar distance, the emitted frequency decreases rapidly over time while the electron beam propagates outwards. An example of a type-III radio burst with its characteristic fast frequency drift is shown in panel b) in Fig. 2.5.
Although type-III radio bursts provide direct evidence of the release of energetic electrons from a flare into interplanetary space, it is not well understood how particles manage to escape from a flare into the interplanetary space. It seems possible that magnetic reconnection establishes a connection between open field lines with the closed mag-

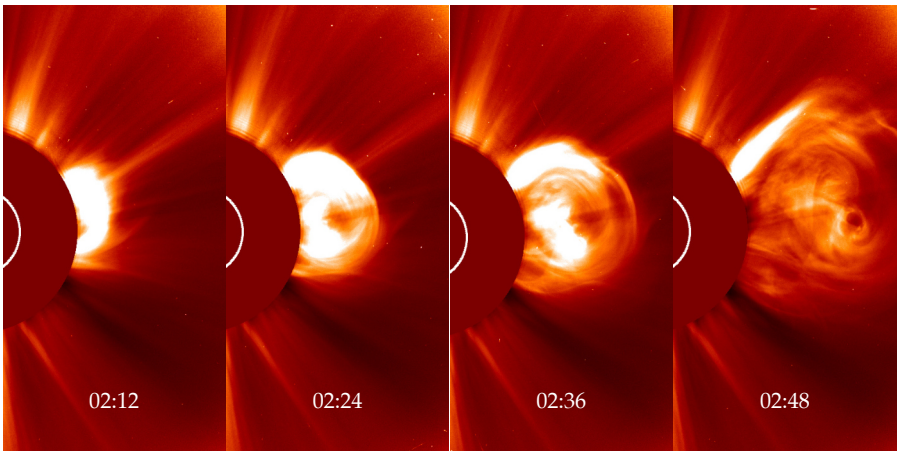

Figure 2.6: Coronagraph images of a CME observed by SOHO/LASCO COR2 on 9 September 2024. Composed with data produced by the SOHO/LASCO consortium.

netic structures of the flare. An example of MHD simulations that try to explain the acceleration and release of energetic particles is presented in Masson et al. (2012). In order to validate and further optimise such simulations, detailed observations of the different flare emissions are required. Providing such observations is one objective of Solar Orbiter.

2.1.4.2 *Coronal mass ejections*

CMEs are large solar eruptions during which billions of tons of magnetised plasma are ejected from the Sun into interplanetary space. Nowadays, CMEs are frequently observed using white-light coronagraphs such as the Large Angle Spectroscopic Coronagraph (LASCO; Brueckner et al., 1995) on the Solar and Heliospheric Observatory (SOHO) spacecraft. They can also be identified in situ by observing the plasma disturbances they cause in interplanetary space. An example of a CME observed by LASCO is shown in Fig. 2.6.
The average mass ejected in a CME is on the order of $3.5 \cdot 10^{11}$ kg and has an average kinetic energy of $2.9 \cdot 10^{22}$ J (Gopalswamy et al., 2009)[3]. The average speed at which CMEs are moving away from the Sun is about 475 km/s but some CMEs exceed speeds of more than 2000 km/s (Gopalswamy et al., 2009). CMEs that exceed the local sound and Alfvèn speed can drive MHD shocks. As the Alfvèn speed in the lower corona is high compared to the average CME speed, most CMEs will not form strong shocks below a solar distance of a few solar radii. At a distance of ~ 1 AU about one third of the CMEs show signatures of MHD shocks (Gosling, 1993).
Figure 2.7 shows an example of typical magnetic field and plasma

3 For comparison: The average kinetic energy of a CME, $2.9 \cdot 10^{22}$ J, exceeds hundred thousand times the energy released by the Tsar bomb explosion, which is the largest man-made explosion ever with an approximate yield of $2.1 \cdot 10^{17}$ J.

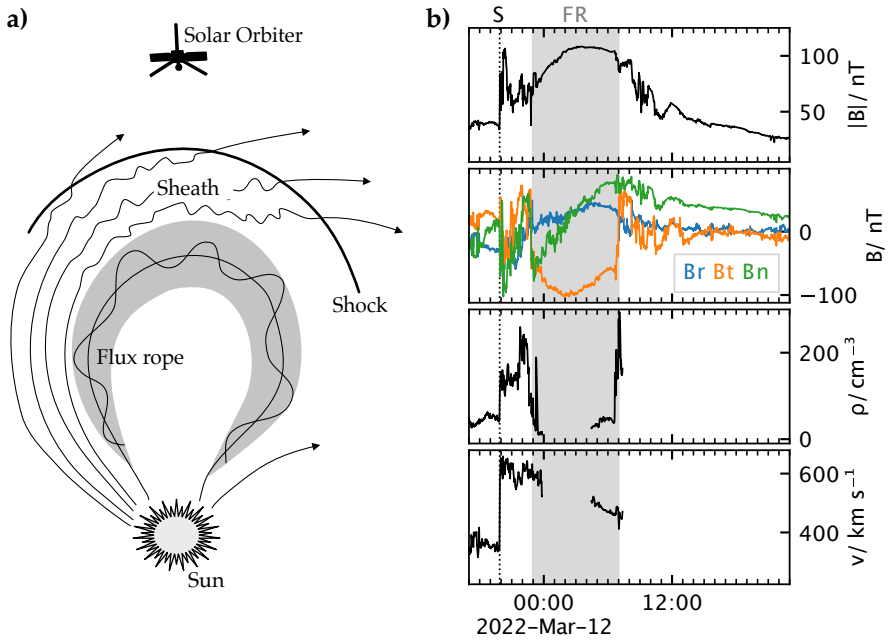

Figure 2.7: Illustration of a simple CME model (a) where a flux rope (FR), which is ejected into interplanetary space, drives an interplanetary shock (S). Time profiles of key magnetic field and plasma parameters in (b) show typical signatures of a CME observed in situ. From top to bottom the profiles show the magnetic field strength, the magnetic field components (radial, tangential and normal), the plasma density and the solar wind proton bulk speed.

observations made by the Solar Orbiter Magnetometer (MAG; Horbury et al., 2020) and the Solar Wind Analyser (SWA; Owen et al., 2020) on Solar Orbiter during the passage of a CME. The observations are shown together with a basic CME model. The time profiles in Fig. 2.7 show a typical signature of a CME-driven interplanetary shock (S) that causes an abrupt increase in the magnetic field strength, the plasma density and the solar wind speed as it passes the observer. The shock is followed by a turbulent sheath region, in which the magnetic field changes chaotically. After the sheath region the spacecraft enters the actual CME plasma, confined in a flux rope (FR) structure. In the flux rope, a slow rotation of the magnetic field is observed, during which the field components B_r, B_t and B_n change smoothly (see Zurbuchen et al., 2006 for a detailed description of in situ CME signatures).
CMEs usually occur in regions with closed magnetic structures where the fields feature large shears. It is generally assumed that magnetic reconnection below some kind of twisted magnetic structure releases energy that abruptly accelerates an overlaying magnetic structure. Acceleration occurs mainly in the lower corona on time scales of several minutes to a few hours (Zhang et al., 2006). As the plasma inside the magnetic structure scatters light from the photosphere via Thomson scattering, it becomes visible in white-light coronagraphs. The ejected

magnetic structures often have loop-like appearances, but there are also observations of other morphologies which likely correspond to different pre-eruptive field configurations.
As the magnetic structure propagates through the local plasma, it causes disturbances. Super-Alfvènic CMEs that drive shock waves can accelerate ions to high energies (up to $\sim 1\,\mathrm{GeV/nuc}$; Zank et al., 2000), which can be observed as SEPs in the interplanetary space. Such CMEs can also accelerate electrons. Although electron enhancements are generally small, they do produce noticeable electromagnetic signatures in the form of Type-II radio bursts. Type-II radio bursts are enhancements in the MHz to kHz radio emission with a slow frequency drift (for details on Type-II burst see e.g. Gopalswamy et al., 2019). CMEs are also frequently associated with other forms of solar activity such as prominence eruptions (more than 70% of CMEs) and/or solar flares (40% of CMEs; Munro et al., 1979) and they also show a correlation with EUV-waves (see Biesecker et al., 2002 for a discussion on the correlation between CMEs and EUV-waves).
To date, there is no generally accepted theory that links or distinguishes the physical processes behind the different phenomena. However, in recent decades, much progress has been made in understanding the physical processes involved in the initiation, formation and propagation of CMEs and several elaborate MHD models are able to reasonably reproduce CME observations (a noteworthy example is the *EUHFORIA* model, Pomoell et al., 2018).

2.2 ENERGETIC PARTICLES IN THE HELIOSPHERE

In the interplanetary space, energetic particles with supra-thermal energies from a few keV up to 10^{20} eV (Hillas, 1984) can be observed. The particles originate from a variety of sources, ranging from solar flares, CMEs, high-speed solar wind streams and planetary magnetospheres to galactic accelerators such as supernova remnants. Populations from the different sources can be distinguished by in situ observations of their energy spectra, abundances, spatial and angular distributions and their temporal variation. The same quantities are also used to study the physical processes involved in the acceleration and the transport from the source to the observer.

2.2.1 *Solar energetic particles*

Solar energetic particles (SEPs) are a population of particles with typical energies in a range from a few keV up to a few 100 MeV which are accelerated close to the Sun in association with eruptive phenomena such as solar flares and CMEs. In interplanetary space, SEPs can be observed most strikingly in the form of SEP events, where the flux of solar energetic particles temporarily increases, often by orders of

magnitude. SEP events are highly versatile: They are often electron- or proton-rich, but also contain heavier ions with a varying elemental composition (Reames, 1988). Typically, the duration of such events ranges from a few minutes to several days. Particle fluxes increase either promptly, within minutes, or gradually over hours before they decrease again (Reames, 1995). The flux decrease is usually slow compared to the increase and can last for several days (Daibog et al., 2003). Observed fluxes can either be isotropic with an equal flux from all directions or directional. In most events, the energy distribution of the SEPs resembles a power law, where the energy-dependent particle flux $J(E)$ shows a proportionality of $J(E) \propto E^{\gamma}$, with the spectral index γ varying strongly between events. The spectral indices observed in near-relativistic electron events, for example, range from -1 to -7, (Dresing et al., 2020).

Until the 1990s, it was widely assumed that solar flares are the fundamental cause of SEP events and that transport effects cause the strong variation in the in situ observed event characteristics (Reames, 2013). This historic picture emerged from a close association between solar flares and SEP events (see e.g. Lin, 1970). In 1993, J. T. Gosling reviewed the growing observational evidence that large SEP events are rather caused by CMEs and CME-driven shocks than solar flares and, moreover, that solar flares do not play a fundamental roll in producing CMEs (Gosling, 1993). By the end of the 1990s there was a broad consensus that solar flares *and* CMEs are two distinct sources of SEPs (Cane et al., 1988; Reames, 1995) which produce different types of SEP events (Reames, 1995; Cane et al., 1986; Reames, 1988).

Following Reames (1995), SEPs are accelerated by fundamentally different mechanisms in solar flares or at CME-driven shock waves. In flares, particles are accelerated up to relativistic speeds within seconds or minutes by direct electric field, which are related to magnetic reconnection and by resonant stochastic acceleration. At CME-driven coronal and interplanetary shocks, particles experience stochastic Fermi acceleration (Jones et al., 1991), in which they repeatedly interact with the CME-driven magnetic field, gaining small amounts of energy with each interaction. The different acceleration mechanisms produce two classes of events, which are called impulsive and gradual SEP events: Impulsive or He^3-rich SEP events are produced by solar flares. He^3-rich events are typically electron-rich but they are primarily characterised by a high abundance of He^3. The He^3/He^4-ratio in these events occasionally reaches values 1000 times higher than the corresponding ratio found in the coronal plasma. Reames (1995) suggests that the He^3 enhancement results from resonant stochastic acceleration that occurs in solar flares. Energetic electrons with unstable velocity distributions produce so-called hydrogen electromagnetic ion cyclotron waves (Temerin et al., 1992). These waves only efficiently accelerate He^3 as it is the only species with a gyrofrequency in the resonant absorption

Table 2.1: Properties of SEP events in the paradigm of two event classes (values taken from (Desai et al., 2016)).

Property	Impulsive (He^3-rich)	Gradual
Electron/proton	$\sim 10^2 - 10^4$	$\sim 50 - 100$
$^3He/^4He$	~ 1	$4 \cdot 10^{-4}$
Fe/O	~ 1	~ 0.1
H/He	~ 10	~ 100
Duration	$< 1 - 20$ h	$< 1 - 3$ days
Longitudinal spread	$< 30°$	$> 100° - 200°$
Seed particles	Heated Corona	Ambient Corona
Radio emission	Type-III	Type-II
X-ray duration	~ 10 min $- 1$ h	> 1 h
Events/year	~ 1000	~ 10

range (Reames, 1995). The result is a selective acceleration of this rare isotope. Enhancements of heavier ions and unusual high ratios of $(Z > 50)/O$ are also observed in He^3-rich events and may result from interactions of these ions with other wave modes. In addition to their composition, He^3-rich events are characterised by a short duration (hours) and are often accompanied by type-III radio bursts. Compared to gradual events, He^3-rich events show rather small spacial extents, i.e. they usually show a longitudinal[4] spread $<30°$.

Gradual SEP events are produced by CMEs. The particles are accelerated over longer durations in the shock waves and turbulences created by the moving CME (see Zhang et al., 2013 for a review on stochastic acceleration of energetic particles). In gradual events, the shock waves 'democratically' sample and accelerate particles from the coronal plasma. Thus, the observed compositions in gradual events are similar to the composition of the coronal plasma. Compared to He^3 events, gradual events usually show slower but longer-lasting flux increases (on the order of days). They are often accompanied by type-II radio emission. Due to the wide extent of the source, particles can fill large parts of the inner heliosphere and SEPs occasionally spread over more than 180° in longitude.

Table 2.1 compares the typical characteristics of He^3-rich and gradual SEP events (see also Reames, 1990b; Reames, 1990a; Reames, 2013 for more details on the acceleration mechanisms and event classes).

The paradigm of two classes of SEP events certainly offers a compelling explanation for many SEP observations, however there are events that do not fit into this differentiation. The so-called mixed events, for ex-

4 The spacial extent of SEP events is usually described in terms of a longitudinal spread. The latitudinal spread of events is rarely observed as most SEP observing spacecraft are located at similar latitudes close to the ecliptic plane.

ample, show characteristics of gradual and He^3-rich events at the same time (see e.g. Kocharov et al., 2002; Mason et al., 1999, and further discussion below). Furthermore, most event properties are determined not only by the acceleration mechanism(s) but also by the prevailing conditions in the corona and interplanetary space. For instance, seed populations of supra-thermal particles that are available to CMEs for acceleration may vary.

In addition to the acceleration process, interplanetary transport also influences the properties of SEP events. From an idealised view one could assume that SEPs are first accelerated near the Sun and subsequently injected into interplanetary space, where they find themselves in an ideal IMF. In the IMF the SEPs are forced into a gyromotion due to the Lorentz force. Assuming that the SEPs do not interact with other particles and do not affect the magnetic field, they will propagate in a helical motion around a guiding field line of the IMF.

With respect to the guiding magnetic field line the particle motion can then be described by $v_\parallel$, the velocity parallel to the magnetic field, and $v_\perp$, the velocity perpendicular to the magnetic field. The relation of $v_\parallel$ and $v_\perp$ defines the so-called pitch-angle α by $\cos\alpha = v_\perp / v_\parallel$.

As the SEPs propagate along the magnetic field away from the Sun, the magnetic field changes slowly and the motion of the SEPs will adapt to the changes according to adiabatic invariants of plasma physics (see e.g Kallenrode, 2004): According to the first adiabatic invariant, the magnetic moment is preserved with $\gamma m_0 v_\perp / 2B = \text{const.}$, where γ is the Lorentz factor, m_0 is the rest mass of the particle and B is the magnetic field strength. This implies that the particle motion becomes increasingly aligned with the magnetic field and that the pitch-angles decrease while the magnetic field strength decreases, a process referred to as pitch-angle focusing. The focusing is particularly strong near the Sun, where the magnetic field strength decreases rapidly.

Moreover, if SEPs with different velocities are injected simultaneously into the IMF they will exhibit velocity dispersion, where faster particles run ahead slower ones. Assuming that SEPs neither loose nor gain energy during propagation and that all particles travel the same path, the first arrival time at a remote observer should be reciprocal to the velocity of the particles.

According to such an ideal propagation scenario, one would expect observing SEPs at e.g. 1 AU as a highly focused particle population with clear signatures of velocity dispersion. Although there are such observations, many SEP events observed at ~ 1 AU show rather isotropic fluxes, equal from all directions, without clear signatures of velocity dispersion. These observations suggest a particle transport dominated by diffusion. In a diffusive particle transport scenario, SEPs interact with irregularities in the magnetic field (Parker, 1965). As a result of each interaction the particle's pitch-angles can change – known as pitch-angle scattering – or the particles can move to neighbouring field

lines – known as perpendicular diffusion. A theoretical description of the diffusive transport is given by the so-called focused transport equation (Ruffolo, 1995), that describes not only pitch-angle focusing, pitch-angle scattering and perpendicular diffusion but also incorporates solar wind convection and adiabatic deceleration (for a review of current transport models see also Dröge, 2005).
Nowadays, by combining models of the acceleration process and the interplanetary transport, it is possible to convincingly reproduce observations of individual SEP events (see Ding et al., 2022 for an example). Yet, there is no single model that is able to reproduce all SEP observations and there often is a lack of measurements to properly constrain the existing models. The Solar Orbiter mission intends to provide the necessary measurements and seeks to answer three fundamental questions regarding SEPs:

HOW AND WHERE ARE SEPS ACCELERATED AT THE SUN? Although solar flares and CMEs are considered as sources of SEPs, the relationship between observations of these sources and in situ measurements of the SEPs are often questionable. Typical source characteristics such as the hard X-ray flux in flares and the speeds of CMEs correlate poorly with the in situ observed SEP fluxes. For instance, SEP fluxes sometimes differ by several orders of magnitude for similar CME speeds (see e.g. Kahler, 2001; Richardson et al., 2015). Explanations for the strong variation must be found and further parameters that influence the production of SEPs need to be identified. The shock geometry, for example, is one such parameter that is nowadays often considered (see Kahler, 2001 for a discussion on possible parameters).
The timing between remote sensing observations of the sources and in situ measurements of the particles is also not fully understood. In a case study Kollhoff et al. (2021) (publication included in Sect. 6) presented observations of an event where in situ observed onset times of electrons and protons are apparently inconsistent with the timing of the remotely observed source, i.e. the time when the coronal shock wave intersects with the magnetic footpoints of the observers. The observations raise the question whether the observed shock wave actually represents the source of both particle species.
In a statistical study Richardson et al. (2014) analysed a wider sample of large SEP events. The authors recognise systematic differences in the timing of electrons and protons that pose a problem for a scenario of a single moving source, such as a coronal shock, that accelerates and releases electrons and protons simultaneously. They note that the observed delays are rather suggestive of some type of diffusion process near the Sun that transports the different species with different speeds to the magnetic footpoints of the observer (see also Posner et al., 2024).
By providing remote sensing observations of the sources and simul-

taneous in situ measurements of the SEPs, Solar Orbiter will help to decipher the acceleration of SEPs.

HOW ARE ENERGETIC PARTICLES RELEASED FROM THEIR SOURCES AND DISTRIBUTED IN SPACE AND TIME? Since it is practically impossible to disentangle acceleration, injection and transport processes on the basis of in situ SEP observations, often multiple explanations for the same observations arise.
For example, Masson et al. (2012) presented a 3D-MHD model, in which energetic particles are injected into field lines with moving photospheric footpoints and could thus explain a wide longitudinal spread of impulsive SEP events without perpendicular diffusion. In contrast, Wibberenz et al. (2006) considered diffusive coronal transport to be responsible for a wide longitudinal spread of particles in events with relativistic electrons. The role of coronal transport in SEP events is still under debate.
The interplanetary transport is also not fully understood. Here, it is particularly important to better understand the influence of interplanetary structures, which can have a major impact on the propagation of SEP events (for examples see Lario et al., 2008 and Ding et al., 2022).
In combination with measurements from other spacecraft, Solar Orbiter can observe the transport of SEPs in the inner heliosphere and can thus provide new observational boundaries for many transport models. The orbit of the spacecraft in particular allows observations at varying solar distances to be compared. An example in which observations of near-relativistic electrons at different radial distances are compared will be presented in chapter 7.

WHAT ARE THE SEED POPULATIONS FOR ENERGETIC PARTICLES? There are observations of so-called mixed or hybrid events, in which large flares and fast CMEs coincide (for an example see Kocharov et al., 2002; Mason et al., 1999). Mixed events can for example show increased He^3/He^4-ratios but otherwise typical characteristics of a gradual event. These events raise the questions of how and to what extent solar flares might be able to produce seed populations of lower energetic particles which are further accelerated by CMEs. In addition, there are numerous studies showing that multiple CMEs in close succession can lead to particularly strong SEP events (see e.g. Kallenrode et al., 2001; Bieber et al., 2002). These observations indicate that CMEs can provide seed populations for subsequent CMEs. The exact interplay between multiple CMEs is however not well understood.
With the remote sensing and in situ observations of CMEs and the observations of SEPs, Solar Orbiter aims to provide the necessary observations to identify possible seed populations for SEPs.

2.2.2 *Galactic cosmic rays*

Galactic cosmic rays (GCR) are energetic particles that originate from outside the heliosphere. The particles are likely accelerated in association with supernovae and supernova remnants (Aharonian et al., 2004). They can reach extreme energies with individual particles exceeding kinetic energies of 10^{20} eV (Hillas, 1984). The GCR consist primarily of protons (87 %) and alpha particles (helium nuclei; 12 %) but also have a small component of heavier nuclei ($\sim$ 1 %) and electrons (Simpson, 1983). Relative abundances in GCR are similar to the abundances of elements in our solar system, with the exception of some rare elements such as Li, Be, and B that have significantly higher abundances in the GCR. The higher abundances of these elements have been recognised as the result of nuclear spallation, in which GCR interact with the interstellar gas and heavier GCR elements such as C, N and O are broken, for example, into Li, Be, or B (Wiedenbeck et al., 2007). Relative abundances observed in the GCR can be used to identify potential sources and to constrain interstellar transport models (examples can be found in Meneguzzi et al., 1971; Binns et al., 2022).
The GCR flux observed in the inner heliosphere is almost isotropic and shows a slow temporal variation. Below a few 100 MeV, the GCR flux is strongly modulated by the Sun, following the 11-year cycle. Changes in the interplanetary magnetic field that occur during each cycle influence the interplanetary propagation of GCR. The highest GCR fluxes are usually observed during a solar minimum. The modulation of the GCR is commonly quantified using the so-called *modulation parameter* Φ. Under some limitations, Φ can be used to describe the average energy loss of a cosmic ray between the interstellar space and the inner heliosphere (a detailed description is given in Moraal, 2013; Gleeson et al., 1968).
Figure 2.8 illustrates how the GCR flux at 1 AU changes over the solar cycle. On the left, time profiles show that the modulation parameter Φ follows the total number of sunspots and thus the solar cycle. On the right, energy spectra show 27-days averaged Alpha Magnetic Spectrometer (AMS) proton fluxes and illustrate how different levels of modulation change the flux of GCR protons below several hundred MeV.
Due to their high energy, GCR can significantly affect SEP measurements: Highly energetic GCR particles can fully penetrate instruments and in some SEP detectors they can produce signals that are indistinguishable from the signals produced by SEPs (see Wraase et al., 2018 for one example). In this way, GCR particles can create background signals in instruments that are supposed to observe SEPs. In Sect. 5.2, the GCR background in EPT will be discussed in more detail.

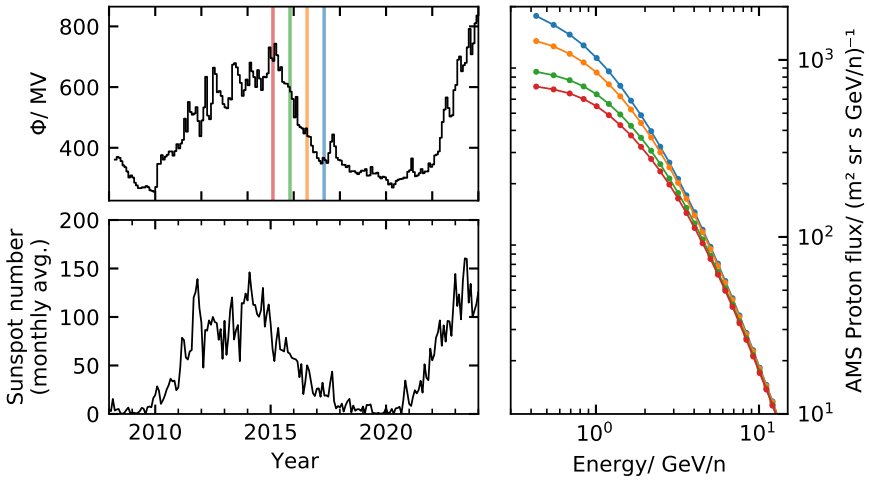

Figure 2.8: Illustration of the GCR modulation. The modulation parameter (upper left panel; from Usoskin et al., 2011) follows the total sunspot number (lower left panel; data from *WDC-SILSO, Royal Observatory of Belgium, Brussels*). The GCR proton flux observed by AMS (Aguilar et al., 2021) (right panel) increases between the four different time periods (coloured intervals in the upper left panel) as the level of modulation decreases.

2.2.3 *Anomalous cosmic rays*

Anomalous cosmic rays (ACR) are a population of particles that is recognised as an anomalous increase in the observed fluxes of H, He3, N, O and Ar in the heliosphere. It is widely assumed that ACR originate from neutral particles of the interstellar medium that enter the heliosphere, where they get singly ionised near the Sun. After ionisation, the particles interact with the interplanetary magnetic field in the solar wind and convect outward until they reach the heliospheric termination shock, the point where the solar wind is slowed down to subsonic speed. Close to the termination shock, the particles are strongly accelerated, reaching energies of about $\sim 50\,\mathrm{MeV}$ (Cummings et al., 1990). The exact acceleration process is not well understood, but measurements made by the two Voyager spacecraft have provided remarkable in situ observations of ACR around the termination shock (see e.g. Decker et al., 2005). The observations also led to new models of the ACR acceleration including the stochastic acceleration via reconnection processes (see e.g. Zhao et al., 2019).

2.2.4 *Other particle populations*

In addition to SEPs, GCR and ACR, several other populations of particles exist in the interplanetary space. A longer description of all populations would go beyond the scope of this thesis, but for the sake of completeness they should be mentioned briefly:

Energetic storm particles (ESPs) with energies up to several hundred keV are causing high ion flux increases observed around interplanetary shocks. They are the result of continuous particle acceleration and trapping in CMEs (see e.g. Gosling et al., 1981).
Corotating interaction region (CIR) accelerated particles are ions with energies up to $\sim 10\,\mathrm{MeV}$ which are accelerated at the interaction region between fast solar wind streams and the slow solar wind (see e.g. Barnes et al., 1976).
Jovian electrons are a population of energetic electrons with energies up to several MeV which are accelerated in the vicinity of Jupiter. Depending on the distance and/or the magnetic connection to the planet, Jovian electrons can be the primary source of MeV electrons (see e.g. (Teegarden et al., 1974) for details).

2.3 THE SOLAR ORBITER MISSION

Solar Orbiter is an ESA mission with a strong contribution from the National Aeronautics and Space Administration (NASA) that was developed by an international team over a time frame of nearly four decades. The spacecraft was finally launched on 10 February 2020 from Cape Canaveral. As an overarching science objective, Solar Orbiter is dedicated to the question of how our Sun and the heliosphere interact. To answer this question, the Solar Orbiter is equipped with ten scientific instruments and was sent on an unique orbit around the Sun. Six of the ten instruments are so-called remote sensing instruments, which take images of the Sun from a distance. Four instruments are in situ instruments, which are intended to observe phenomena directly at the spacecraft's location. The combination of remote sensing and in situ observations offers a unique synergy that allows solar phenomena to be observed on the surface of the Sun and to subsequently monitor their impact in interplanetary space. A complete list of all scientific instruments of the mission is given in Müller et al. (2020). Detailed descriptions of all ten instruments are part of A&A's Special Issue *The Solar Orbiter mission* (Forveille, T. et al., 2020).
In the case of SEP events, almost all instruments on Solar Orbiter can contribute to their understanding. One example of this is the combination of the Spectrometer/Telescope for Imaging X-rays (STIX; Krucker et al., 2020), the Solar Orbiter Radio and Plasma Waves instrument (RPW; Maksimovic et al., 2020) and the Energetic Particle Detector (EPD; Rodríguez-Pacheco et al., 2020). By combining the observations of these three instruments it is possible to observe and link the acceleration or particles at the Sun, their injection into interplanetary space and their transport in the inner heliosphere. In this example, STIX is used to observe the X-ray emission of a solar flare in which particles are accelerated. RPW can observe the injection of the accelerated particles into interplanetary space in the form of type-III radio bursts. EPD

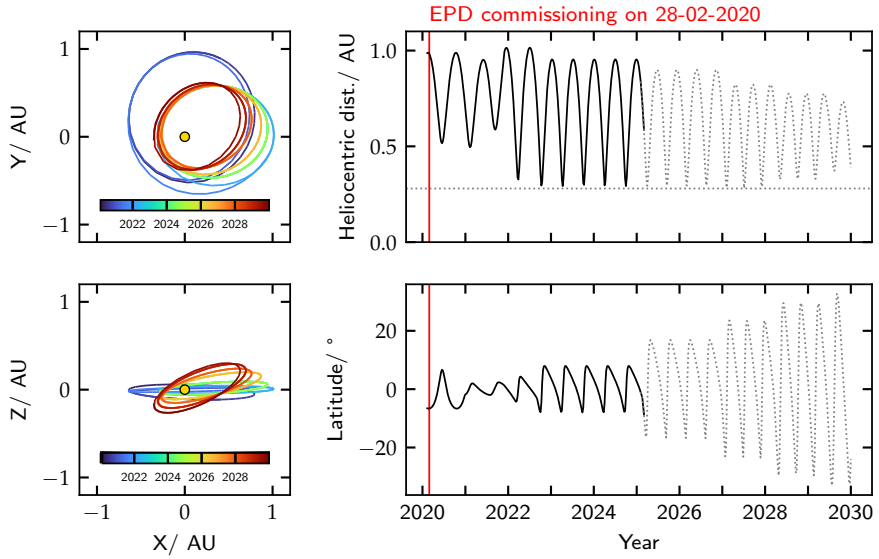

Figure 2.9: Completed and upcoming orbit of Solar Orbiter (on April 2024). Left panels show the spacecraft coordinates in the heliocentric inertial (HCI) system. Panels on the right show the corresponding heliocentric distance and the latitude with the dotted line being the upcoming orbit. The vertical red lines indicate the commissioning of EPD shortly after the launch of the spacecraft.

can finally detect their arrival at the spacecraft and measure properties such as the timing or the anisotropy of the particle flux. By combining these observations the entire process of the event can be studied. See Gómez-Herrero et al. (2021) for an example where measurements of RPW and EPD have been combined.

The high-quality observations generated by the synergy of the individual instruments are all the more promising when considering the mission's unique orbit that brings it both close to the Sun and out of the ecliptic plane. To reach this unique orbit, Solar Orbiter has performed a series of gravity assist manoeuvres around Venus and Earth. At perihelion, Solar Orbiter reaches a minimal solar distance of just 0.28 AU. This close, the remote sensing instruments can produce images of the Sun with an unprecedented resolution, while the in situ instruments are able to, for example, observe some of the smallest SEP events, which would be impossible to detect at a distance of 1.0 AU due to the spatial diffusion of the particles. With its observations close to the Sun, Solar Orbiter continues the efforts of the Helios missions (1974), which have reached a distance of 0.3 AU, and will provide new data from modern instruments.

Another remarkable aspect of Solar Orbiter's orbit is that it will move out of the solar ecliptic over the mission phase and the extended mission. Solar Orbiter is expected to reach a heliolatitude of 33° by 2029 and will thus provide the first remote sensing and in situ observations ever made from the poles of the Sun from such close proximity.

Therefore, the mission not only follows in the footsteps of Ulysses, a mission that observed the poles of the Sun between 1990 and 2009, but it will also enter completely new territory. An illustration of the completed and future orbit is shown in Fig. 2.9.
The scientific objectives of Solar Orbiter can be summarised in four top-level science questions (from Müller et al., 2012):

1. What drives the solar wind and where does the coronal magnetic field originate?
2. How do solar transients drive heliospheric variability?
3. How do solar eruptions produce energetic particle radiation that fills the heliosphere?
4. How does the solar dynamo work and drive connections between the Sun and the heliosphere?

These top level questions can be further broken down into a number of more specific sub-questions. Sect. 2.2.1 has already presented three sub-questions regarding the energetic particle radiation. To answer any of these scientific questions, the measurements by the various instruments must be reliable and the data must be interpreted correctly. Therefore, a fundamental instrumental question should be answered prior to all scientific questions: What instrumental effects impact the measurements and how should they be taken into account when analysing the data? This additional question can be an extensive one and must be answered individually for each instrument and sensor. Part of this work is dedicated to help answering this instrumental question for the EPT sensor of EPD.

3

INSTRUMENTAL BACKGROUND

The EPD instrument of Solar Obiter has four distinct sensors, which all observe energetic particles in different energy ranges with individual resolutions. The measurements of the individual sensors are complementary and allow to observe energetic particles in a wide energy range. This chapter first gives a short description of the four different EPD sensors in Sect. 3.1. As the focus of this work is primarily on EPT, Sect. 3.2 will provide more details on this specific sensor. The section includes an explanation of the complete signal processing chain in EPT and a description of the scientific data generation. While some details may be irrelevant for the rest of this work, the full description given here should be useful to readers who intend to work with unprocessed EPT data. Lastly, Sect. 3.3 describes the formal relationship between count rates observed by EPT and the prevailing directional and energy-dependent particle flux following Sullivan (1971) and describes how directional and energy-dependent detector response functions can be obtained from Monte Carlo simulations.

3.1 THE ENERGETIC PARTICLE DETECTOR (EPD)

The Energetic Particle Detector (EPD) is an instrument suite with four distinct sensors on Solar Orbiter (see Fig. 3.1). The four sensors measure energetic particles with kinetic energies from a few keV to several hundred MeV with a high time and energy resolution while providing directional and compositional information. The individual EPD sensors use different measuring techniques and cover different

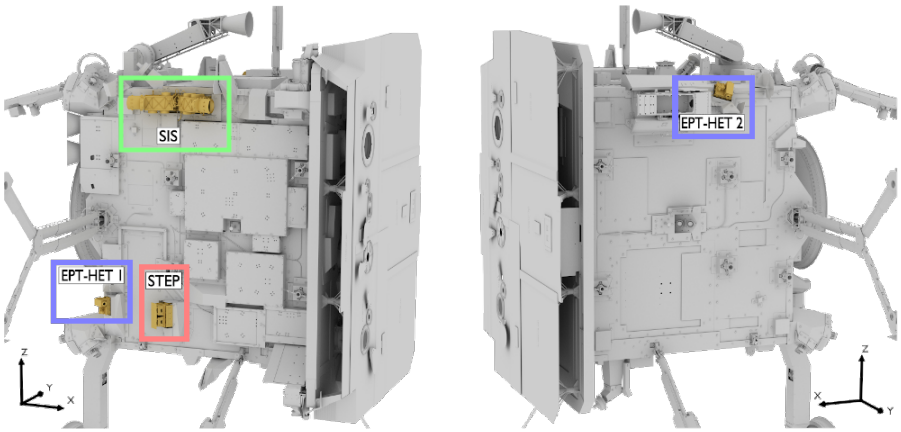

Figure 3.1: Location of the four different EPD sensors on the Solar Orbiter spacecraft. Figure adapted from Rodríguez-Pacheco et al. (2020).

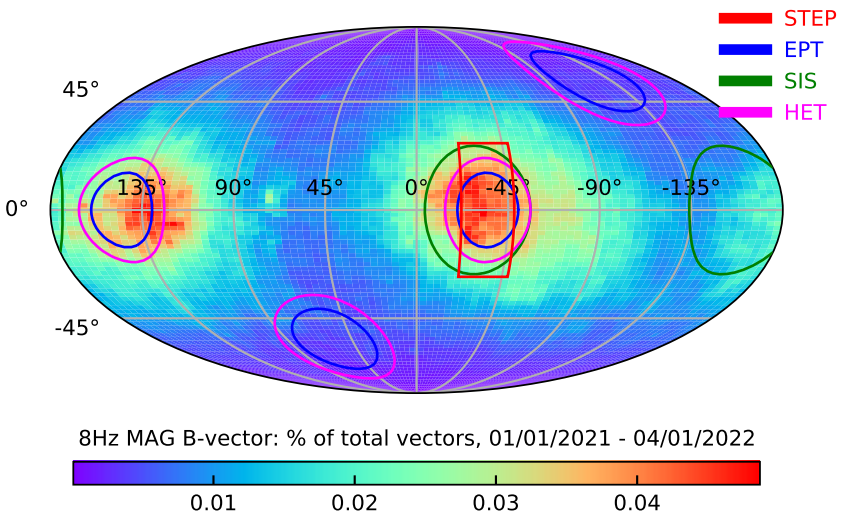

Figure 3.2: FOVs of all EPD sensors in spacecraft coordinates shown in a Mollweide-projection. 0° polar and 0° azimuth correspond to the sunward pointing X-axis of Solar Orbiter. The underlying histogram shows the distribution of magnetic field vectors obtained from 8 Hz Solar Orbiter MAG data.

energy ranges. They also provide different resolutions in time, energy, direction and composition.

The SupraThermal Electron Proton (STEP) sensor measures electrons and ions with energies from a few keV up to about 100 keV with a time resolution of up to 1 s. STEP provides directional information from 15 slightly different field of views (FOVs) that all look in a sunward direction while Solar Orbiter maintains its regular flight orientation. The coordinate axes in the bottom right and left in Fig. 3.1 show the spacecraft coordinate system. In the regular flight orientation, the X-axis is pointing towards the Sun.

The Electron Proton Telescope (EPT) primarily measures electrons in the energy range 40 – 400 keV and protons from 50 keV – 6 MeV with 1 s time resolution. EPT consists of two identical instrument units, named HET-EPT-1 (HE1) and HET-EPT-2 (HE2). Each of the two EPT units shares a common electronics box with one of two units of the High Energy Telescope (HET). The HE1 unit is mounted on the -Y-deck of Solar Orbiter and has two FOVs pointing in a sunward and anti-sunward direction. The HE2 unit is mounted on the +Y-deck and has two FOVs pointing out of the ecliptic in a northward and southward direction. A detailed description of the EPT sensor is given in Sect. 3.2.

The High Energy Telescope (HET) measures electrons in the range of 400 keV – 30 MeV and ions from several MeV/nuc up to several hundred MeV/nuc. HET consists of two identical instrument units mounted together with EPT units on a common electronic box. HET has four FOVs that point in the same direction as the EPT FOVs, but they

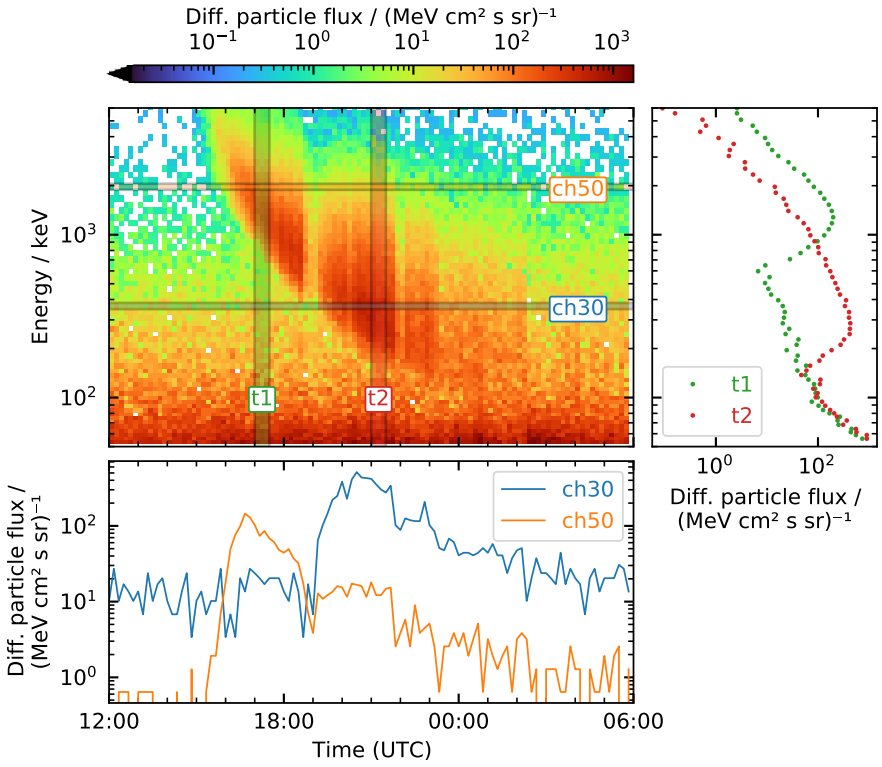

Figure 3.3: An example of EPT measurement data. The dynamic spectrum (upper left panel) shows the complete 3D dataset measured by EPT's sunward looking ion detector on 12 December 2024. The time profiles (bottom panel) show the differential particle fluxes observed in two specific energy channels: ch30 (350-380 keV) and ch50 (1.9-2 MeV). The two energy spectra t1 and t2 (right panel) show 1-hour time averaged fluxes observed during the two periods indicated in the dynamic spectrum.

feature a slightly larger opening angle. HET can distinguish different ion species and can thus provide compositional information.

The Suprathermal Ion Spectrograph (SIS) measures ions with energies between a few hundred keV/nuc and several MeV/nuc at a maximum time resolution of 3 s. The sensor provides a detailed resolution of the ion composition. SIS has two FOVs that point sunward and anti-sunward. The sunward FOV looks in a similar direction as the EPT and HET sunward FOVs, while the anti-sunward FOV has a slightly different orientation compared to the anti-sunward FOVs of HET and EPT.

Figure 3.2 shows the different FOVs of all four EPD sensors in the spacecraft coordinate system in a Mollweide-projection (Snyder, 1987; Cartesian coordinates of the spacecraft system are shown in Fig. 3.1). The underlying colour-coded histogram shows the orientation of the magnetic field vectors observed by MAG between 2021 and 2022. The figure shows that the sunward and anti-sunward FOVs of EPT and HET are preferentially looking along the IMF.

The most relevant measurements of the four EPD sensors are the time-

and energy-dependent particle fluxes observed in the different FOVs. Figure 3.3 shows an example of typical EPD observations during an SEP event. The figure includes the three most common visualisation formats: The so-called dynamic spectrum (upper left panel) shows time versus energy and colour-coded differential particle fluxes. This kind of visualisation allows an easy identification of energy- and time-dependent processes such as velocity dispersion. The time series (bottom panel) shows the temporal change of the particle flux in a given energy range (channel). Such time series are commonly used for the identification of event onsets and flux maxima. The energy spectra (right panel) show the differential flux in all energy channels averaged over a certain time period. Such energy spectra are used e.g. to identify spectral features such as spectral slopes and break points where the spectral slope changes.

3.2 THE ELECTRON PROTON TELESCOPE (EPT)

EPT is a direct heritage of the Solar Electron and Proton Telescope (SEPT Müller-Mellin et al., 2008) onboard the Solar TErrestrial RElations Observatory (STEREO) mission and uses the same measuring principle and a similar instrument design. However, EPT features multiple design improvements and some adjustments compared to SEPT that were necessary for the unique mission requirements of Solar Orbiter. Figure 3.4 shows one of the two HET-EPT units. The following section will first describe the general measuring principle of EPT and the instrument design, followed by Sect. 3.2.2 that describes the complete signal processing chain of the instrument.

3.2.1 *Measuring principle and instrument design*

EPT uses the so-called magnet/foil-technique to separate and measure energetic electrons and ions. In different apertures, the instrument uses magnetic fields to deflect electrons and plastic foils to stop ions. This allows electrons and ions to be separated to a certain degree. After separation, the kinetic energy of the particles is observed by measuring their ionisation losses in silicon-based solid state detectors (SSDs). Figure 3.5 shows a cross section of one EPT unit including the most relevant components of the instrument.
Each EPT unit has two double-ended telescopes in an anti-parallel setup. The telescopes create 30°-wide opening angles on each end for a stack of two 300 μm thick SSDs that is housed in the centre of each telescope. The two SSDs in each detector stack are mounted back-to-back with a small gap of 0.4 mm between them. One detector of each stack is coated with a 5 μm thick polyimide foil on its outward facing side. The polyimide foil will stop almost all ions $<$400 keV/nuc, while electrons above 30 keV can penetrate it without losing significant

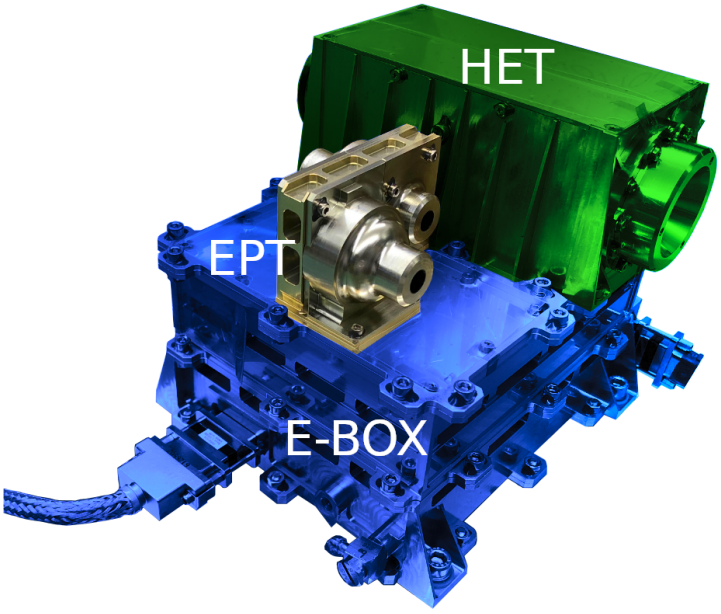

Figure 3.4: Picture of one HET-EPT unit. EPT is highlighted in silver, HET is shaded green and the electronic box (E-BOX) is shaded blue.

amounts of their energy in it. This detector (from here on referred to as foil detector) should thus primarily detect electrons. The second detector of each stack has no such foil and is facing a magnetic field produced by a permanent magnet with a strength of $\sim 0.4\,\mathrm{T}$. The field will deflect most electrons below several hundred keV entering through the aperture on the magnet-side, whereas the trajectories of ions above several tens of keV are barely altered by the magnetic field due to their heavier mass. The detector (from here on referred to as magnet detector) should thus primarily detect ions. Electrons that overcome the magnetic field and ions that penetrate the foil can produce unwanted contamination in the detectors that generally needs to be considered.

The main science data of EPT originate from particles that stop within the first detector they hit. To identify whether a particle stops in a detector, the signals in the two SSDs are compared. If only one detector detects a signal, it is assumed that the particle stopped in it. Such stopping particles usually lose most of their total kinetic energy in the detector and their original energy can be reconstructed by measuring the energy deposition in the SSD. EPT also provides measurements of penetrating particles, which lose a part of their total kinetic energy in both detectors of one stack. The original kinetic energy of these penetrating particles may be estimated from the ratio and the sum of the deposited energy in both detectors.

The SSDs in EPT are passivated implanted planar silicon (PIPS) detectors manufactured by *Canberra Semiconductor NV*. All detectors are segmented into an inner and an outer segment with diameters of 6 mm and 12 mm, respectively. The different segments are read out

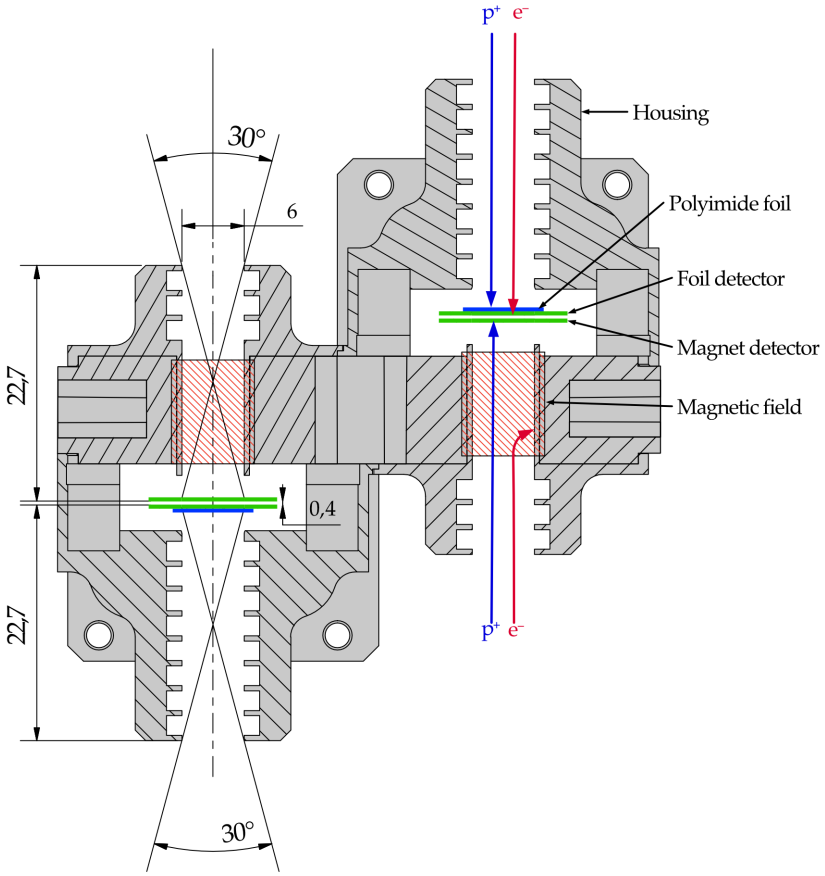

Figure 3.5: Schematic cross section of EPT. Arrows in the double-ended telescope on the right illustrate possible electron (red) and proton (blue) trajectories.

separately and can be used in the signal processing to define individual trigger conditions (more details are given in Sect. 3.2.2). Figure 3.6 shows a top view (a) of the detector layout and cross sections of the magnet (b) and foil (c) detectors. The top view shows the hexagonal detector carrier with bonding pads at its corners used to connect the individual detector segments. Technically, each detector has four segments: A centre segment, a narrow crosstalk guard ring, an anticoincidence segment and an outer guard ring. The centre segment represents the 6 mm inner detector segment. The narrow crosstalk guard ring and the anticoincidence segment are read out together and serve as one 12 mm wide outer segment. The outer guard ring is not read out.

The cross sections in Fig. 3.6 show the different layers of the detectors: The sensitive silicon, in which the energy deposition is measured, has a depletion depth of $300 \pm 15\,\mu$m. On the inward facing junction sides several non-sensitive layers form a total dead layer of $\sim 1.5\,\mu$m. On the outward facing ohmic side, the magnet detector has a total dead layer of ~ 220 nm thickness. The foil detector has a $5\,\mu$m poly-

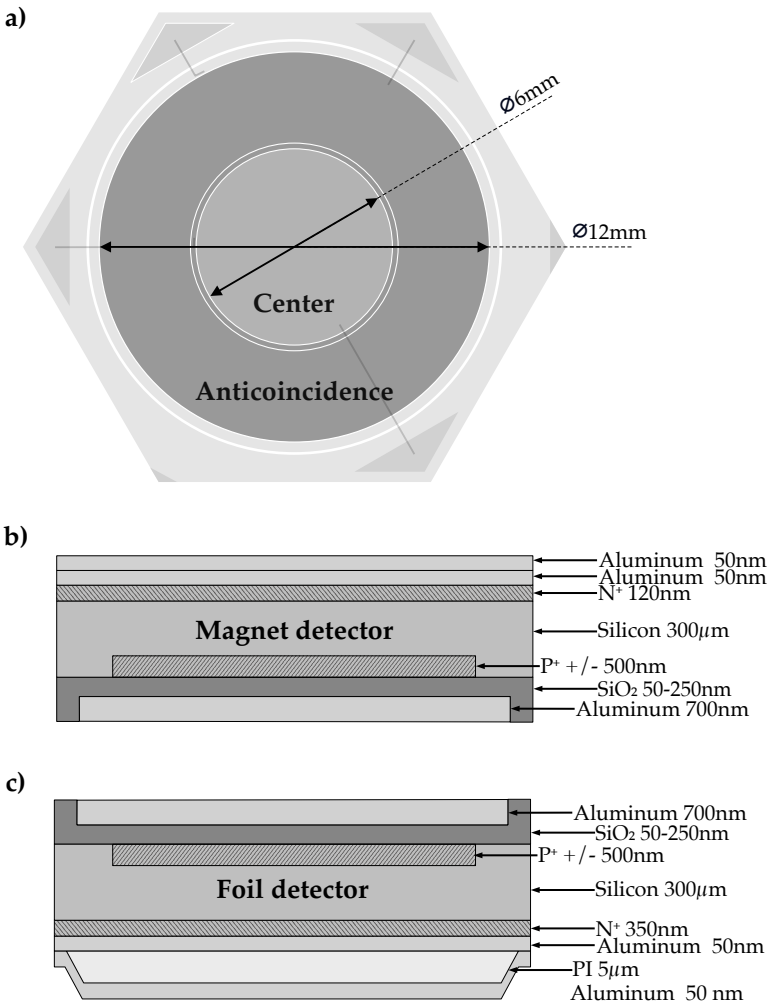

Figure 3.6: Sketch of the EPT SSDs. The top view (a) shows the hexagonal detector with the different segments. The cross section of the magnet detector (b) and foil detector (c) show the different layers in the detector. Sketch is not to scale. Layer thicknesses taken from (Grunau, 2013).

imide (PI) layer on the ohmic side, positioned between two 50 nm thick aluminium layers, which adds to a total dead layer of $\sim 5.5\,\mu$m. The dead layers must be taken into account when determining the original kinetic energy of particles from the deposited energy in the detectors. Especially at the lower end of the measuring range of EPT (i.e. <100 keV), particles can lose a significant fraction of their total energy in the dead layers.
Following this short summary of the instrumental setup, the next section will explain the signals which particles create in the detectors and how these signals are processed into the scientific measurement data of EPT.

3.2.2 *Signal processing and data pipeline*

The EPT signal processing can be divided into four steps: The generation and the processing of the analogue signal, the detection of event signals by the level-1/2 trigger, the classification and storage of events by the level-3 trigger and the generation of data products by a data product scheduler. The individual steps can be described as follows:

THE ANALOGUE SIGNAL The PIPS detectors of EPT are reverse biased with +70 V and fully depleted in this state. Ionising particles that pass through the depletion zone of the detector can ionise the silicon and thus produce free charge carriers in the form of electron-hole pairs. As a rule of thumb, an ionising particle will create one electron-hole pair per 3.6 eV (Pehl et al., 1968) of ionisation loss in silicon. Due to the electric field in the detector, the electrons and holes will drift through the detector. The currents of these individually drifting charges will compose one charge pulse with a typical duration of a few nanoseconds. The height of the pulse is proportional to the total ionisation loss of a particle in the detector. In EPT, the charge will be fed to a feedback capacitor of a charge-sensitive pulse amplifier, which preamplifies the signal. This signal is fed to a second current-feedback operational amplifier with pole-zero correction, which further shapes and amplifies the pulse. Next, the shaped pulse is passed through a low-pass RC filter, before it is digitised by an 8-bit analogue-to-digital converter (ADC) at 1 megasample per second (1 Msps). Analogue signals from all detector segments are continuously digitised and the last 16 digitised values of each segment are stored in a ring buffer.

THE LEVEL-1/2 TRIGGER For each detector segment, the level-1/2 trigger of EPT calculates a digital measurement of the pulse height, the so-called A-value. A-values are calculated every microsecond by a linear combination $A = \sum a_i s_i$, where s_i are the 16 last ADC values stored in the ring buffer and a_i represent a set of 16 fixed coefficients. The linear combination serves as a digital filter for well-shaped pulses and also increases the resolution of the pulse height compared to the use of a single ADC value. The predefined in-flight filter coefficients are

$$a_i = [0, 0, 0, -3, -3, -3, -3, 1, 1, 2, 2, 3, 2, 1, 0, 0]. \tag{3.1}$$

Figure 3.7 illustrates the signal processing chain from a charge pulse to an A-value.
Analogous to the A-values, the level-1/2 trigger also calculates so-called B-values. B-values are calculated every microsecond by $B = \sum b_i s_i$ with a second set of predefined filter coefficients

$$b_i = [0, 0, 0, 0, 0, 0, 0, -2, -3, -1, 0, 2, 2, 1, 1, 0]. \tag{3.2}$$

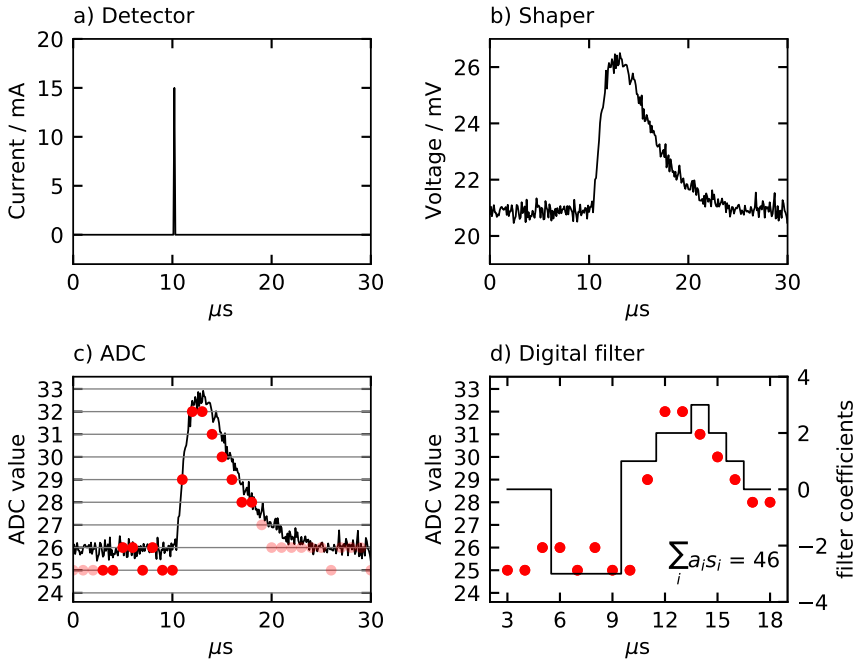

Figure 3.7: Illustration of the EPT signal processing chain. In the detector (a) a charge pulse is observed at $t = 10\,\mu s$. The amplifier and shaper (b) shapes a voltage pulse from the signal. The ADC (c) digitises the shaped pulse with 1 Msps. The red dots mark the ADC samples obtained for the pulse. At an arbitrary time, here $t = 18\,\mu s$, the 16 ADC samples highlighted by a solid red colour in (c) are stored in the ring buffer. The digital filter (d) uses these samples to calculate a linear combination with 16 filter coefficients. The result of the linear combination is the final measured pulse height. In this example the measured pulse height is $A = 46$.

These B-values are not further considered by the onboard logic, but can be used on ground to analyse the phase of a shaped pulse with respect to the timing of the ADC.

Further, the level-1/2 trigger compares the A-values to a set of level-1 thresholds and sets individual trigger-bits for each segment that exceeds its threshold. In the latest flight configuration (internal version number v10 at the time of writing), the level-1 thresholds of EPT are set to an A-value equivalent of 25 keV for the centre segments and 1 MeV for the outer segments.

Besides A- and B-values, the trigger also determines the so-called pulse age T. It is determined at each microsecond for each segment and indicates whether a local maximum was present in the history of the observed A-values and how 'old' the maximum is. The pulse age is also used to configure temporal coincidence windows during which signals in several segments are attributed to the same particle/event. A pulse age T_i at a microsecond i is determined from the A-value A_i seen at i, the previous pulse age T_{i-1} and a reference A-value A_m observed T_{i-1} microseconds ago. The reference A-value memorises

possible previous local maximum and allows a comparison with the current A-value. The pulse age T_i is defined as

$$T_i = \begin{cases} 1 & \text{when } A_i > A_m \\ T_{i-1} + 1 & \text{when } A_i < A_m \text{ and } 0 < T_{i-1} < 6 \\ 0 & \text{otherwise.} \end{cases} \tag{3.3}$$

The level-1/2 trigger considers three different pulse age limits (*min/trig/-max* = 2/4/6). If the pulse age of a segment reaches the limit *min* (2), the segment has observed a local maximum in the A-values 2 μs ago and the trigger will memorises the maximum. If the maximum exceeds the level-1 threshold, the trigger waits another 2 μs until the pulse age reaches the limit *trig* (4), before it triggers a level-2 event. Any maxima observed in other segments of the detector stack during the 2 μs between *min* and *trig* will also be memorised and attributed to the same level-2 event. After a pulse age reached the limit *max* (6) it will be reset to zero. All EPT level-2 events will be further analysed by the level-3 trigger.[1]

THE LEVEL-3 TRIGGER The level-3 trigger further analyses the signals and classifies level-2 events either as stopping, penetrating or invalid events based on the signals in the individual detector segments. According to this classification the energy deposition of the events is counted in different so-called l3 histograms. In addition, A-values, B-values and pulse ages are recorded for a sample of events in so-called pulse height analysis (PHA)-words. The PHA-words are stored in three separate buffers, one for each event class. The event classification works as follows:
First, the level-3 trigger calibrates A-values measured in the different detector segments to energy values. This A-value-to-keV calibration is unique for each detector segment and has a temperature dependency. The level-3 trigger uses calibration factors for discrete temperature values, which can be adjusted to the instrument temperature from ground via commanding. A list of calibration factors for the different temperature settings and detectors can be found in Appendix E in Tab. E.1. After calibration, the energy values in the individual detector segments can be compared to each other and to certain energy thresholds.
The level-3 trigger then defines two significance thresholds: An absolute threshold of 30 keV and a relative threshold of 1% of the energy observed in the centre segment with the highest signal. Signals below the absolute threshold are considered to be within the noise level of

1 The level-1/2 trigger logic was reconfigured during the in-flight configuration update (v9.2) on 4 December 2021 in order to fix an issue where electronic cross talk generated artificial events. More details on the configuration change are included in the Appendix B.

the detector. Signals below the relative threshold are considered to be within the expected signal crosstalk in the detector or in the electronics. If a signal is below either of the two thresholds, it is considered non-significant.
Events with significant signals in any outer segment are classified as invalid events. Events where only one centre segment saw a significant signal are classified as stopping events and events where the two centre segments of one detector stack saw significant signals are classified as penetrating events.[2]
After the classification, a PHA-word of the events is sent to one of three PHA buffers. The PHA-word includes the complete event information with all A-, B-values and pulse ages of all segments of the detector stack that was triggered. Each PHA-word also includes a counter, which counts the microseconds that have elapsed since the last level-2 trigger. PHA-words from invalid, penetrating and stopping events are stored in three corresponding PHA buffers with the numbers 0, 1 and 2, respectively. The buffers have a size of 1 kB and will record PHA-words until their full capacity is reached (about 42 events fit into each buffer). If a buffer is full, no further PHA-words are recorded, but the total number of events sent to each buffer is counted. The buffers are transmitted and emptied at a fixed cadence of 300 s.
In addition, all stopping and penetrating events are counted in different l3-histograms, which are stored in the so-called l3 memory. It contains six distinct EPT histograms as well as several histograms for HET. Four 256 bin histograms, with one histogram reserved for each centre detector, are used for counting stopping events. These histograms count the energy depositions of individual particles in a logarithmic binning, which is 16 bins per energy doubling (bin $= \log_2(E/2\,\mathrm{keV}) \cdot 16$), starting at 2 keV.
Penetrating events are recorded in two 2D-histograms with 64x128 bins with one histogram per telescope. These two histograms count the ratio of the energy deposition E_m/E_f in 64 logarithmic bins from 1/16 to 16, with 8 bins per ratio doubling ($\mathrm{bin}_x = \log_2(E_m/E_f) \cdot 8$) together with the total deposited energy $E_m + E_f$ in a logarithmic binning with 16 bins per energy doubling ($\mathrm{bin}_y = \log_2((E_m + E_f)/1\,\mathrm{MeV}) \cdot 16$).
Figure 3.8 illustrates the l3 memory and the different histograms. Panel (a) shows the part of the memory that contains the 6 EPT histograms (memory address range 0x4000 − 0xa000). While the four stopping event histograms are stored in the address range 0x4000 − 0x4400, the two histograms for penetrating events are stored in the range 0x6000 − 0xa000. Panel (b) shows the 256 bins and their corresponding energy edges of one of the four stopping event histograms (the same

2 With configuration patches v9.2, v9.3 and v10 (last change on 14 June 2024), the level-3 trigger will now further classify all events in which any segment saw a significant negative signal as invalid. Negative values can occur with incorrectly reconstructed pulse height and all corresponding events are now classified as invalid events. More details about the different configuration changes are included in Appendix B.

counts are shown in panel (a) at addresses 0x4000 – 0x4100). Panel (c) shows the 64x128 bins and their corresponding total energy and energy ratio edges of one of the two penetrating event histograms (with the same counts shown in panel (a) at addresses 0x6000 – 0x*a*000). The l3 histograms are read out and reset every second by the Data Product Scheduler (DPS).

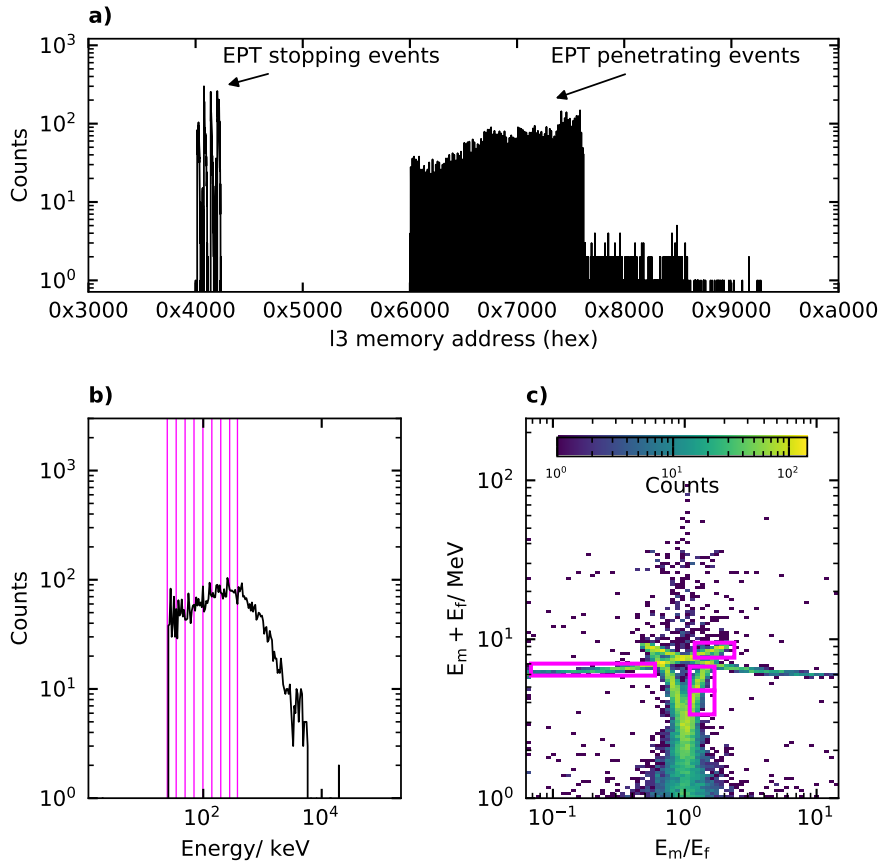

Figure 3.8: Illustration of the data product generation in EPT, with (a) showing the l3 memory, (b) showing an l3 histogram for stopping particles and (c) showing a 2D l3 histogram for penetrating particles. The magenta edges in (b) and (c) illustrate DPI. See main text for further explanation.

THE DATA-PRODUCT-SCHEDULER The DPS creates the final scientific data of EPT. It sums counts from certain l3 histogram bins over various time periods. The combinations of l3 bins are called data product items (DPIs). The DPIs are the final energy channels of EPT. Multiple DPIs can be combined to a data product (DP). Counts in the individual DPIs can be converted to count rates by dividing them by the accumulation time of the DP. These resulting count rates are referred to as level-1 science data.

As an example: The LL_EPT_e_s data product of EPT (internal naming of data products is described in the next section) has 8 DPIs in which

stopping events are recorded. Each DPI combines 4 consecutive l3 histogram bins. Counts in these bins are accumulated for 5 seconds, after which the data product is transmitted and the DPS starts again, resetting the counts to zero. The magenta lines in Fig. 3.8 panel (b) mark the 8 DPIs of LL_EPT_e_s. As another example, the magenta boxes in panel (c) show the DPIs of the NO_EPTP_p_s data product that counts penetrating events.

3.2.3 *EPT Data Products*

In addition to some housekeeping and PHA data which is primarily used to monitor the instrument's health status, EPT generates a variety of science data products. The nominal science data products are the largest and are transmitted sporadically, depending on the available telemetry budgets assigned to EPT. So-called low-latency data products contain scientific data with a reduced resolution, which are transmitted more frequently and in a more timely manner.
Data products are given internal names that identify whether a data product is a nominal (NO) or a low-latency (LL) product, whether it counts EPT stopping events (EPT) or EPT penetrating events (EPTP), whether it counts events in the magnet (mag or p) or foil detector (foil or e) and whether it counts events in the sunward (s), anti-sunward (a), northward (n) or southward (d) looking detector. As an example, the NO_EPT_mag_s data product is a nominal data product that counts stopping events in the magnet detector that is sunward looking.
All data products can be changed by updating the flight configuration. This includes the cadence of the individual data products and also the pattern according to which bins of the l3 histogram are combined in each data product item. During the commissioning and cruise phase of Solar Orbiter the in-flight configuration of EPT has been changed several times and the original definition of the different data products given in Rodríguez-Pacheco et al. (2020) is outdated. A complete list of the data products generated with the latest EPT in-flight configuration (internal configuration version v10) can be found in Appendix A in Tab. A.1.

3.3 DETECTOR RESPONSE FUNCTIONS

The count rates measured by EPT are an integration of the directional and energy-dependent particle flux over some detector area, field of view (solid angle) and energy range. In order to determine the relevant physical quantity, i.e. the flux of particles, the measured count rates must be translated back into this quantity. A formal description of the relationship between the observed count rate in a detector and the prevailing directional and energy-dependent particle flux was given by Sullivan (1971). Following Sullivan, the count rate observed in a detector in a given measuring period can be described as

$$C = \int_S d\vec{\sigma} \cdot \hat{r} \int_\Omega d\omega \int_0^\infty dE \times \sum_\alpha \epsilon_\alpha(E, \vec{\sigma}, \omega) J_\alpha(E, \omega) \tag{3.4}$$

where

C	count rate
S	total surface area of the detector
$d\vec{\sigma}$	element of the surface area
$\hat{r}$	unit vector in direction ω
$d\vec{\sigma} \cdot \hat{r}$	effective element of area looking into ω.
Ω	solid angle
ω	direction (θ, ϕ)
$d\omega$	solid angle element - also expressed as $d\omega = \sin(\theta) d\theta d\phi$ where ϕ is the azimuth and θ the polar angle
E	particle energy
ϵ_α	detection efficiency for species α
J_α	differential particle flux of the species α

The count rates observed by EPT are most likely well described by Eq. 3.4 but it should be noted that the equation already implies multiple simplifying assumptions, such as a spatial independence of ϵ_α and J_α as well as a temporal independence during the measuring period.
The equation can be further broken down by defining a directional energy response function $A_\alpha(E, \omega)$ of the detector, where

$$A_\alpha(E, \omega) = \int_S d\vec{\sigma} \hat{r} \times \epsilon_\alpha(E, \vec{\sigma}, \omega). \tag{3.5}$$

The directional energy response function $A_\alpha(E, \omega)$ has the unit cm^2 and describes the effective detector area that is exposed to a flux of particles α with energy E from direction ω. With $A_\alpha(E, \omega)$, Eq. 3.4 can be written as

$$C = \int_\Omega d\omega \int_0^\infty dE \times \sum_\alpha A_\alpha(E, \omega) J_\alpha(E, \omega). \tag{3.6}$$

In the special case of an isotropic flux, where the flux from all directions is equal, and thus $J_\alpha(E)$ is independent of ω, the equation can be simplified further to

$$C = \int_0^\infty dE \times \sum_\alpha R_\alpha(E) J_\alpha(E), \tag{3.7}$$

where $R_\alpha(E)$ is the so-called energy response function. It can be calculated by integrating $A_\alpha(E, \omega)$ over Ω:

$$R_\alpha(E) = \int_\Omega d\omega \times A_\alpha(E, \omega), \tag{3.8}$$

and has the unit $\mathrm{cm}^2\mathrm{sr}$. The energy response function of an ideal detector is a box function with a constant value in a certain energy range and a response of 0 outside this range. In this ideal case, where the response of the detector depends solely on its geometry, the term geometry factor G is used instead of energy response.
For an ideal detector, the geometry factor and the directional response function may be calculated analytically from the geometry of the detector. For a cylindrical detector telescope with circular symmetry, where the directional response function does not depend on ϕ and $A(\omega) = A(\theta)$, a solution is given in Sullivan (1971). In this case, the ideal directional response is given by

$$A(\theta) = \begin{cases} \pi R_s^2 \cos\theta & \theta_c \geq \theta \geq 0 \\ \cos\theta \left[\frac{1}{2} R_1^2 (2\psi_1 - \sin 2\psi_1) + \frac{1}{2} R_2^2 (2\psi_2 - \sin 2\psi_2)\right] & \theta_m \geq \theta \geq \theta_c \\ 0 & \theta \geq \theta_m, \end{cases} \tag{3.9}$$

where

$R_1, R_2 =$ radii of two parallel circular surfaces with distance l that limit the incidence of the particles and thus define a telescope,
$R_s =$ smaller radius of (R_1, R_2),
$\theta_c = \tan^{-1} \frac{|R_1 - R_2|}{l}$,
$\theta_m = \tan^{-1} \frac{R_1 + R_2}{l}$ and
$\psi_1 = \cos^{-1} \left[\frac{R_1^2 + l^2 \tan^2\theta - R_2^2}{2 l R_1 \tan\theta}\right]$,
$\psi_2 = \cos^{-1} \left[\frac{R_2^2 + l^2 \tan^2\theta - R_1^2}{2 l R_2 \tan\theta}\right]$.

Figure 3.9 shows the results of Eq. 3.9 for an ideal directional response with the EPT geometry. In the case of an isotropic flux, the ideal directional response (Eq. 3.9) can be integrated over the full 4π solid angle giving an analytic solution for the geometry factor that is

$$G = \frac{1}{2}\pi^2 \left[R_1^2 + R_2^2 + l^2 - ((R_1^2 + R_2^2 + l^2)^2 - 4R_1^2 R_2^2)^{\frac{1}{2}}\right]. \tag{3.10}$$

For EPT, the geometry factor for stopping particles is 1.54 mm^{2}sr following Eq. 3.10 and using the measurements shown in Fig. 3.9 while taking into account a 0.3 mm detector thickness.

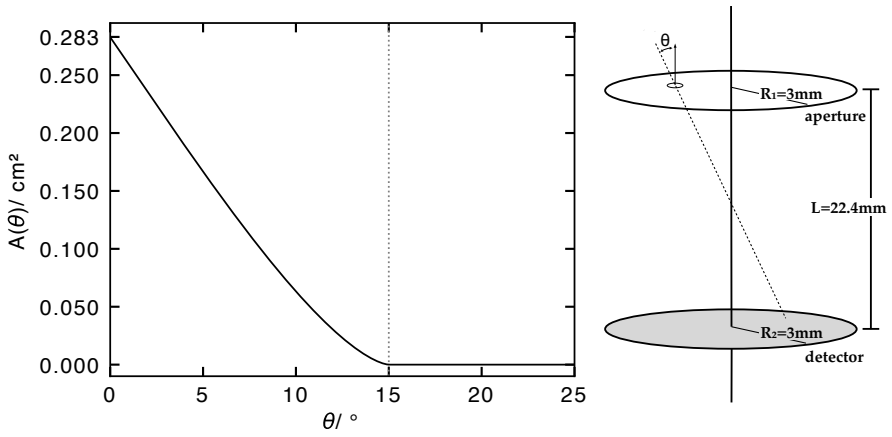

Figure 3.9: Ideal directional response function for a circular symmetric detector with an EPT-like geometry. Relevant dimensions of EPT are shown in the sketch on the right.

In order to derive directional fluxes from measured count rates, the directional energy response functions $A(\omega, E)$ must be determined and an $J(E, \omega)$ must be found that solves Eq. 3.6. For the special case of an isotropic flux, it is sufficient to determine the energy response functions $R(E)$ and to find $J(E)$ that solve Eq. 3.7.
The following section will describe how the response functions can be determined from Monte Carlo simulations. Section 3.3.2 describes various methods for finding optimal solutions to equations 3.6 and 3.7.

3.3.1 *Monte Carlo simulations of response functions*

For real detectors with complex geometries it is practically impossible to derive analytical descriptions of the directional energy response functions. In such cases, the response functions can be obtained from Monte Carlo simulations. A corresponding simulation for EPT can be performed in the following way:
First, a model of the instrument is created with a realistic geometry and material composition. This model is placed in a simulation environment together with a particle source that emits a large number of particles, creating a well-defined fluence of particles. Then, the interaction of the individual particles with the instrument matter is simulated and the energy losses in the sensitive detector layers are recorded. Finally, the instrument response is calculated from the ratio of the simulated particle fluence and the number of events registered in the detector. In detail:

The simulation creates a well-defined fluence $F_{\text{sim}}(\omega, E)$ by emitting $N_{\text{sim}}(\omega, E)$ particles with energy E into direction ω, starting from random positions on a plane source surface with an effective area $A_{\text{sim}}(\omega)$ looking along ω. The simulated fluence is then

$$F_{\text{sim}}(\omega, E) = \frac{N_{\text{sim}}(\omega, E)}{A_{\text{sim}}(\omega)}. \tag{3.11}$$

The individual particles are propagated through the geometry and their interaction with the instrument is simulated utilising some suitable physics models. Energy losses due to ionisation processes from particles that hit the sensitive volumes of the detectors are tracked and the resulting total deposited energy, together with the particle's initial energy, direction and position, is recorded for each detector. By applying EPT's trigger logic, the energy deposits are used to decide whether a particle would generate a valid trigger signal in EPT and to determine the energy channels of EPT in which the particle should be counted in. At the end of the simulation, the total number of detected particles N_{det} is determined for each channel. From this number, the directional response $A(\omega, E)$ can be calculated for particles with energy E from direction ω:

$$A(\omega, E) = \frac{N_{\text{det}}}{F_{\text{sim}}(\omega, E)} = \frac{N_{\text{det}}}{N_{\text{sim}}(\omega, E)} \cdot A_{\text{sim}}(\omega) \tag{3.12}$$

Complete response functions $A(\omega, E)$ for all directions and for a certain energy range can be derived from a single simulation run by simulating an isotropic fluence with a particular energy distribution. An isotropic fluence can be simulated by randomly sampling the start position of the particles on a source surface, while their initial direction is sampled according to Lambert's cosine law (see e.g. Zhao et al., 2013 for a more detailed description). In order to create an isotropic flux anywhere around the instrument, the instrument must be enclosed by the source, for example by using a spherical source surface around the instrument. For a spherical source and an isotropic flux, the effective area of the source $A_{\text{sim}}(\omega)$ is equal for all directions with $A_{\text{sim}}(\omega) = A_{\text{sim}} = \pi r^2$, where r is the radius of the sphere.
To further resolve the energy dependency, the initial energy E of the particles is randomly sampled. For the EPT simulations, E is sampled from a power-law probability distribution such that $N_{\text{sim}}(\omega, E) \propto E^{-1}$. This particular power-law distribution provides uniform statistics for a logarithmic binning of the energy that is used to discretise $A(\omega, E)$. From the isotropic simulation with a power-law energy distribution a discrete directional response function A_{etp} can be calculated with

$$A_{\text{etp}} = \frac{N_{\text{det}}}{N_{\text{sim,etp}}} \cdot A_{\text{sim}} \ , \tag{3.13}$$

where the indices $(\mathrm{e}, \mathrm{t}, \mathrm{p}) \in \{1...i\} \times \{1...j\} \times \{1...k\} \subseteq \mathbb{N}^3$ are the notations for i energy bins, j azimuth bins and k polar bins used to

discretise $A(\omega, E)$. $N_{\text{sim,etp}}$ is the number of simulated particles within the energy bin e, azimuth bin t and polar bin p and A_{etp} is the mean direction response for particles in this bin.
The discrete energy response function R_e for isotropic fluxes can be calculated either from an integration of the directional response function over the 4π solid angle or directly from the simulation output with

$$R_e = \frac{N_{\text{det}}}{F_{\text{sim}}} = \frac{N_{\text{det}}}{N_{\text{sim},e}} \cdot G_{\text{sim}} \,, \tag{3.14}$$

where G_{sim} is the geometry factor of the simulated particle source. It can be calculated by an integration of $\cos(\theta)$ over the solid angle and over the source surface with

$$G_{\text{sim}} = \int_S ds \int_\Omega \cos\theta d\omega. \tag{3.15}$$

Statistical uncertainties of the simulation are given by

$$\Delta A_{\text{etp}} = \frac{\sqrt{N_{\text{det}}}}{N_{\text{sim,etp}}} \cdot A_{\text{sim}} \tag{3.16}$$

and

$$\Delta R_e = \frac{\sqrt{N_{\text{det}}}}{N_{\text{sim},e}} \cdot G_{\text{sim}}. \tag{3.17}$$

The response functions of several energy channels can be combined into so-called response matrices. For n energy channels, the resulting directional energy response matrix $\mathbf{A} \in \mathbb{R}^{n\times i\times j\times k}$ is four-dimensional. The respective energy response matrix $\mathbf{R} \in \mathbb{R}^{n\times i}$ is two-dimensional.

3.3.2 *Inversion of EPT measurements*

The count rates $\mathbf{c} \in \mathbb{R}^n$ observed in a data product of EPT with n energy channels may be described as

$$\mathbf{c} = \mathbf{R}\mathbf{j}, \tag{3.18}$$

where $\mathbf{R} \in \mathbb{R}^{n\times e}$ is a response matrix that describes the energy response functions of n energy channels, discretised in e energy bins, and $\mathbf{j} \in \mathbb{R}^e$ is the average isotropic particle flux in the e energy bins. To determine $\mathbf{j}$, which is the quantity of interest, from the measured count rate $\mathbf{c}$, an inversion of Eq. 3.18 must be found. For the sake of simplicity only isotropic fluxes are considered here, but in principle Eq. 3.18 could also be rewritten for anisotropic cases, using a directional particle flux and a directional response matrix.
Even under the assumption of an isotropic flux, the inversion of the problem is not trivial. In fact, the problem is an ill-posed one – the n

energy channels provide a limited resolution, the count rates suffer from measurement uncertainties and the instrument response $\mathbf{R}$ is only known to a certain degree. However, there are various methods that aim to find an optimal solution for the problem by introducing some additional constraints for J. Examples that utilise such methods can be found, for example, in Wraase et al. (2018) or Böhm et al. (2007). Böhm et al. (2007) use multiple different approaches, including an iterated Tikhonov regularisation method (Tikhonov et al., 1977) to solve a similar problem for the Electron Proton Helium Instrument (EPHIN) onboard SOHO. The iterated Tikhonov regularisation is based on the traditional Tikhonov regularisation, in which a regularisation term is introduced in order to improve the condition of the problem without substantially increasing the bias. The traditional Tikhonov regularisation minimises

$$||\mathbf{Rj} - \mathbf{c}||^2 + ||\mathbf{\Gamma j}||^2 = \min, \tag{3.19}$$

where $\mathbf{\Gamma}$ is the so-called Tikhonov matrix. The Tikhonov matrix allows to favour certain solutions. For example, if a multiple of the identity is used ($\mathbf{\Gamma} = \alpha\mathbf{I}$), solutions with a smaller norm of $\mathbf{j}$ will be preferred. Alternatively, smooth solutions of $\mathbf{j}$ can be favoured, e.g. by using a difference operator. A detailed description of the application of the regularisation method for EPHIN is given in Böhm et al. (2007). A more general description of the Tikhonov regularisation and its iterative version can be found in Tikhonov et al. (1977), Hansen (1992) and Neumaier (1998).
Wraase et al. (2018) solve a similar problem for SEPT onboard STEREO by assuming a specific spectral shape for the differential particle flux. With a given shape, $\mathbf{j}$ could be described by a few free parameters, which were derived from the measured count rates via a χ^2 minimisation of

$$||\mathbf{Rj} - \mathbf{c}||^2 = \min. \tag{3.20}$$

The method provides reasonable results for $\mathbf{j}$ in the presented examples, but a major disadvantage is the strong bias of the solution due to the initially assumed spectral shape.
Another more rudimentary approach for the inversion is the assumption of energy-independent geometry factors. For this method, it is assumed that the response functions of individual energy channels can be approximated by geometry factors although the actual responses are not ideal box functions. For each energy channel an attempt is made to find energy limits E^{low} and E^{high} for which it can be assumed that the response between these limits is approximately constant and that the response outside these limits can be neglected. The count rate in any channel is then given by

$$c = g \cdot j \cdot (E^{\text{high}} - E^{\text{low}}), \tag{3.21}$$

where g is the average response between E^{low} and E^{high} of the channel and j is the average differential flux in the energy range between E^{low} and E^{high}.

Equation 3.21 allows for a direct conversion between c and j, but for real detectors there are often no energy limits and geometry factors that would adequately describe the actual response. However, this method is a practical tool for getting a first estimate of particle fluxes from the observed count rates and therefore it is frequently used. A slightly modified version of this method is used to calibrate the EPT science data (level2 data), which will be further described in Sect. 5.1. For all inversion methods it is essential that the response function of the detector is sufficiently well determined. The following chapter is dedicated to Monte Carlo simulations of EPT response functions.

Part II

INSTRUMENT RESPONSE

4

MONTE CARLO SIMULATIONS OF EPT RESPONSE FUNCTIONS

For the inversion of EPT measurements into meaningful physical units, i.e. differential particle fluxes in $(\mathrm{cm}^2\,\mathrm{sr}\,\mathrm{s}\,\mathrm{MeV})^{-1}$, the exact instrument response needs to be known. The formal relation between the measured count rate, the ambient particle flux and the detector response is summarised in Sect. 3.3.

For an ideal detector, the directional response function and the geometry factor can be calculated analytically (Eqs. 3.9 and 3.10 in Sect. 3.3), but the results are usually a poor description of the actual response of a real detector. Research facilities with particle accelerators such as Physikalisch-Technische Bundesanstalt (PTB) offer the possibility of directly measuring the detector response under certain conditions, but it is practically impossible to replicate the complete directional and energy-dependent particle environment that is present in space. Therefore, measurements at accelerators are often combined with Monte Carlo simulations of the instrument response in order to derive directional and energy-dependent response functions for various particle species.

In the case of EPT, accelerator measurements were performed at the PTB with protons in the energy range $[0.1 - 6]\,\mathrm{MeV}$ and at the Heavy Ion Medical Accelerator in Chiba (HIMAC) with various ion species at energies $>100\,\mathrm{MeV/nuc}$. In addition to these measurements, results of Monte Carlo simulations of the response were published by Rodríguez-Pacheco et al. (2020).

In this chapter, the existing simulation results are reviewed, optimised and extended. In particular, the EPT instrument model used in previous simulations is optimised, the angular range and energy range of previous simulations are extended and the influence of the spacecraft on the instrument response is investigated.

Section 4.1 briefly reviews the existing EPT response functions and points out some limitations of these functions. In Sect. 4.2 new Monte Carlo simulations are described, featuring improved geometries and simulation setups. The simulation results are presented in Sect. 4.3 for different EPT data products. This section gives a detailed description of the energy response functions and the directional energy response functions of different EPT data products. Section 4.4 briefly summarises the comprehensive description of the results and discusses their implications.

4.1 REVIEW OF PREVIOUSLY PUBLISHED RESPONSE FUNCTIONS

The energy response functions of EPT were determined before the launch of Solar Orbiter. The results of simulations and calibration measurements at the PTB have been summarised and published in Rodríguez-Pacheco et al. (2020). Figure 4.1 shows the simulated energy response functions for stopping particles. They can be described as follows:

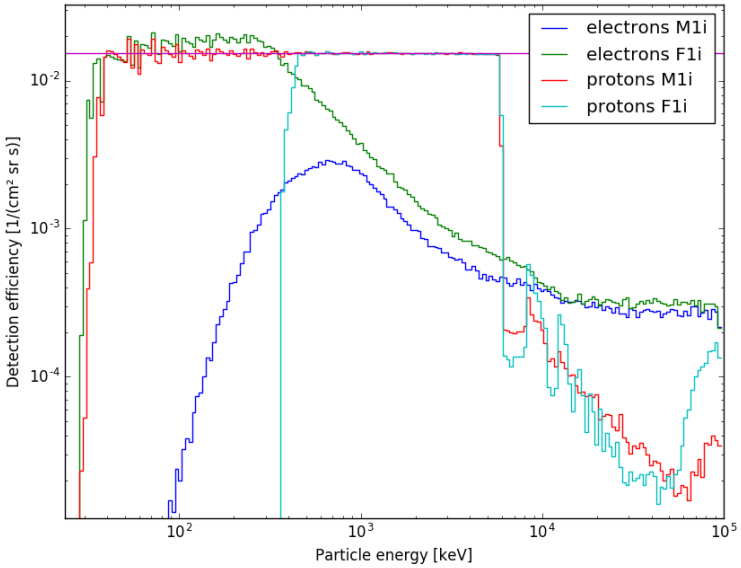

Figure 4.1: EPT response functions for stopping particles.[1] The four curves show the response for protons stopping in the magnet detectors (red), electrons stopping in the magnet detector (blue), protons stopping in the foil detector (cyan) and electrons stopping in the foil detectors (green). The horizontal line (magenta) shows the ideal geometry factor of EPT. Figure taken from Rodríguez-Pacheco et al. (2020).

In the magnet detector, stopping protons have an almost constant response of about 1.5 mm^2sr in the energy range $[0.04 - 6]$ MeV. Above 6 MeV, the response decreases rapidly to values below 0.04 mm^2sr as protons start to penetrate the detector. In the magnet detector, stopping electrons have a significantly lower response than protons. It increases from 90 keV to $\sim$700 keV, where a maximum response of only 0.3 mm^2sr is reached. Above 700 keV, the electron response drops again as the probability decreases for electrons to stop in the detector. In the foil detector, stopping protons have an almost constant response of $\sim$1.5 mm^2sr in the energy range $[0.35 - 6]$ MeV. Below $\sim$350 keV, the foil stops all protons. Above 6 MeV, the response decreases rapidly and remains below 0.07 mm^2sr as protons start to penetrate the detector. In the foil detector, stopping electrons show an almost constant

response somewhere between 1.5 mm^2sr and 2 mm^2sr in the energy range $[40 - 350]$ keV. Above 350 keV, the response decreases slowly.
In essence, the results presented in Fig. 4.1 suggest that the overall detector response for stopping particles is small for energies above the intended measuring ranges ($[0.05 - 6]$ MeV for protons and $[40 - 400]$ keV for electrons) and that the electron response in the magnet detector is considerably smaller than the proton's response in this detector.
However, the presented response functions suffer from at least two problems. One problem is the limited energy range of 100 MeV that was considered for protons. EPT is exposed to particle fluxes with much higher energies. GCR protons, for example, usually exhibit a peak flux at energies above 200 MeV. The response to these highly energetic particles has not been considered properly.
The second problem lies in the setup of the simulations: The simulation used a small particle source positioned directly in front of EPT's telescopes. With this setup, particles were only simulated within the instrument's aperture. In space, however, the instrument is usually exposed to fluxes from almost all directions. Particles that penetrate the instrument housing instead of passing through the aperture could possibly generate valid signals in EPT. The response for such particles was not considered either and should be investigated.

4.2 EPT GEANT4 SIMULATIONS

In order to reproduce and extend existing instrument response functions, Monte Carlo simulations of the detector response are carried out utilising the Geant4 (**Ge**ometry **an**d **T**racking) toolkit version 10.5 (Geant4 Collaboration, 2024). Geant4 was developed at the European Organization for Nuclear Research (CERN) to accurately simulate the passage of particles through matter. The toolkit is widely used in different research fields including space science, where the interaction of space radiation with instruments and astronauts is simulated (see e.g. Böhm et al., 2007; Wraase et al., 2018; Khaksarighiri et al., 2020). Geant4 is also used in high energy physics, where e.g. observations of the ATLAS experiment at the Large Hadron Collider (LHC) are simulated (Costanzo et al., 2006) or in nuclear medicine, where medical imaging processes are simulated, e.g. for tomography and radiotherapy (Jan et al., 2004).
Here, Geant4 is used to simulate the directional energy-dependent response functions for EPT while taking into account the influence of surrounding masses, like the Solar Orbiter spacecraft, on the detector response. In simple terms, a Geant4 based simulation can be broken

1 Note that the unit of the 'Detection efficiency' (equivalent to response in this work) should be cm^2 sr instead of $1/(cm^2\,sr\,s)$.

down into two components: The geometry and the tracking.
The geometry describes the experiment, including all relevant components and their material composition. Here, the geometry describes EPT including all its detectors, the magnet system and its housing. Later, the EPT geometry is extended by additional geometries that represent HET, an electronic box underneath the instrument and the spacecraft.
The tracking describes the propagation of the particles and their interaction with matter. First, all particle species and physics processes considered in the simulation are defined in a so-called Physics List. Geant4 provides a number of predefined Physics Lists called Reference Physics Lists which are validated, tested and benchmarked by the Geant4 developers (Geant4 Collaboration, 2024). Next, so-called primary particles are released from a virtual particle source. The particle source defines the spatial, angular and energy distribution of the primary particles that are simulated. The individual particles are propagated in steps through the geometry, creating trajectories in space. Along the trajectories, processes such as energy loss, scattering and the production of secondary particles are simulated. The trajectories of secondary particles can be further simulated. All trajectories end either if the particles are stopped or if they leave the simulation geometry. Finally, the simulation records all hits between particles and certain sensitive volumes of the geometry. The energy loss of particles in these sensitive volumes can be written into an output file, together with information about the primary particles.
For the purpose here, the eight SSD segments of EPT are defined as sensitive volumes and the energy deposition by ionisation is recorded. Together with the initial position and direction of the primary particles, this information is written into a simulation output file. From the output, detector response functions are calculated.
In all simulations, the QGSP_BERT_HP_LIV Reference Physics List (Geant4 Docs, 2023b; Geant4 Docs, 2023a) is used. This list makes use of the *Quark gluon string model* to simulate elastic, inelastic, and capture processes of high energy hadrons with nuclei, of the *Bertini cascade model* to simulate nuclear reactions of hadrons and gamma rays in the energy range 0 to 10 GeV, of the *High precision neutron model* to simulate neutron scattering up to 20 MeV and of the *Livermore model* to simulate electromagnetic physics (details on the different physics models can be found in Apostolakis et al., 2009; Ivanchenko et al., 2019, and references therein).
In addition, the default energy limits for the generation of secondary particles are adjusted. These values, called *production cuts* within Geant4, have been lowered so that all secondary particles that could possibly generate valid signals in one of the EPT detectors are created and tracked in the simulation.

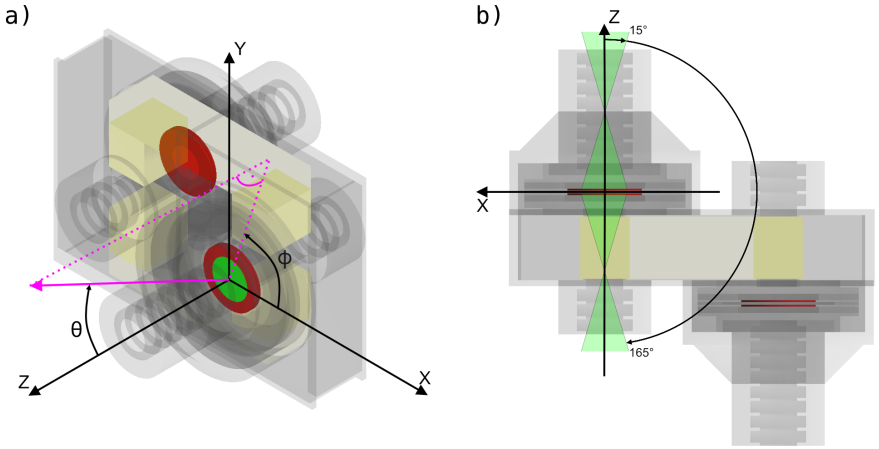

Figure 4.2: Illustration of the *EPT geometry* and the simulation coordinate system. Further explanations given in Sect. 4.2.1.

4.2.1 *Geant4 geometries*

To simulate the response of EPT to various particle species in a wide energy range, three distinct geometries are defined. The first one is the *EPT geometry*, which represents the EPT sensor itself. Two more geometries include additional masses surrounding the sensor. All geometries are simplified representations of the actual assemblies, where only essential components are considered and approximated by simplified geometric shapes. Furthermore, the material composition of the individual components is also approximated. The level of detail used in the different geometries resembles a compromise between accuracy and complexity. In principle, it is possible to create geometries with a higher level of detail, but additional volumes and materials cost more runtime and the expected improvement of the accuracy of the results is small. The three geometries can be described as follows:

THE EPT GEOMETRY This geometry is a simple model of EPT that includes the most relevant components of the instrument. Figure 4.2 shows the geometry and its internal components. The 3D view (a) and the top view (b) show the housing and other aluminium parts (grey transparent), the neodymium magnets (dark yellow), the cobalt-iron alloy yoke of the magnet (light yellow), the sensitive silicon detector area (red) and the polyimide foil on top of the foil detector (green). The figure also illustrates the coordinates used in all simulations: θ is the angle between a given vector and the Z-axis and ϕ is the angle between the X-axis and a projection of the given vector onto the XY-plane. In the top view (b), also the foil-side FOV ($0° < \theta < 15°$) and the magnet-side FOV ($165° < \theta < 180°$) are shown. The model was adapted from the original simulations presented by Rodríguez-Pacheco et al. (2020), but the detectors were reconfigured according to the detector layout shown in Fig. 3.6. A reconfiguration was necessary

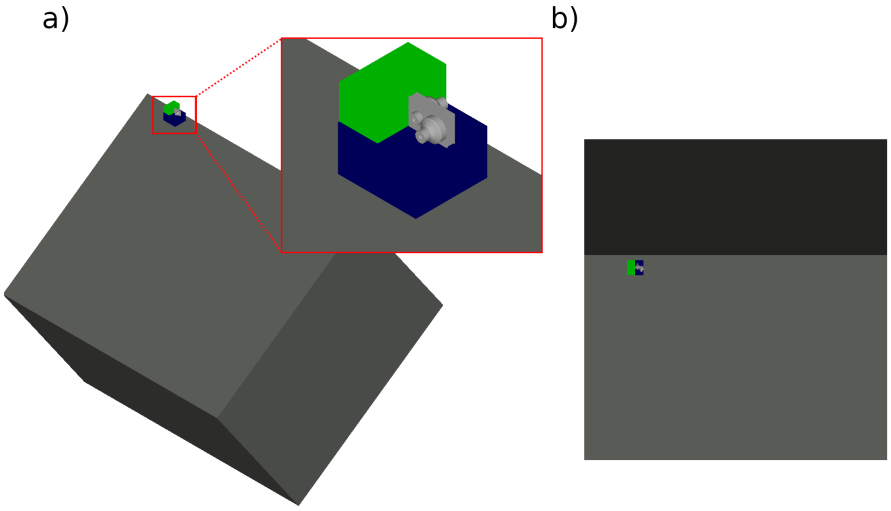

Figure 4.3: Illustration of the *EPT+Boxes geometry*. The 3D view (a) and the top view (b) show the EPT geometry (light grey), the HET box (green), the EBox (blue) and the spacecraft box (dark grey). The inset in panel (a) shows a zoom on EPT.

because some non-sensitive layers were missing in the original simulations.

THE EPT+BOXES GEOMETRY This geometry is a combination of the *EPT geometry* with three additional box-shaped geometries that represent the most relevant masses around the instrument. The spacecraft is approximated by a 2.2x1.8x1.5 m^3 wide box with a weight of 1700 kg. The material composition of the spacecraft was approximated to be 12% hydrazine (N, H compound), 44% aluminium alloy (Al, Zn, Mg, Cu) and 44% of a composition that represents printed circuit boards (mainly Cu, AL, Pb and Ni) (the same approximation of the Solar Orbiter spacecraft was used in Forstner, 2020). Approximations of HET and the electronic box (EBox) were constructed by extracting the total mass and outer measurements from the instrument CAD files. The HET box weighs 0.377 kg and measures 5.3x5.9x10.6 cm^3. The EBox weighs 0.29 kg and measures 12.0x6.9x11.0 cm^3. For both boxes the same material as for the spacecraft was assumed. They were placed relative to the *EPT geometry* so that their position corresponds to the arrangement of the HE1 unit on the spacecraft. The *EPT+Boxes geometry* is illustrated in Fig. 4.3. This geometry is not used directly to simulate response functions but its only purpose here is to create the third geometry.

THE EPT+SHELL GEOMETRY This geometry is an extension of the *EPT geometry* surrounded by a segmented spherical shell. This shell model is intended to represent the masses of the spacecraft, HET and EBox in a similar way as the *EPT+Boxes geometry*, but with much

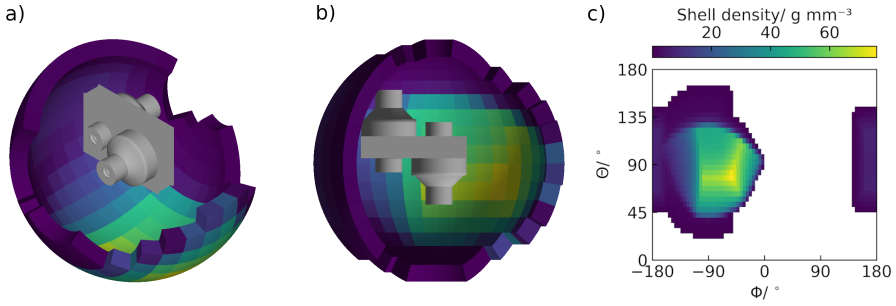

Figure 4.4: Illustration of the *EPT+Shell geometry*. (a) shows a 3D-view of the geometry, (b) shows a top view on the geometry and (c) shows a density map of the individual shell elements.

smaller external dimensions. Due to the smaller dimensions, the geometry can be placed in a smaller particle source, which allows simulating a higher fluence with fewer particles. As a result, better statistics can be achieved in a lower runtime compared to a simulation with the *EPT+Boxes geometry*. The *EPT+Shell geometry* is shown in Fig. 4.4. A similar application of a shell model was used to simulate the detector response of STEREO/SEPT (Wraase et al., 2018).

The shell model is constructed from the *EPT+Boxes geometry* in the following way: In the *EPT+Boxes geometry* a test source is placed at the centre of the detector stack in one EPT telescope. From this source, non-interacting test particles are shot radially outwards into all directions. The directions and path lengths through the spacecraft, EBox and HET box are recorded for all test particles. The output is used to sort the particles by their direction into $5° \times 5°$ wide solid angle bins. For each bin, the averaged path length of the gathered particles through the HET box, EBox and spacecraft box is determined. Figure 4.5 illustrates the simulation and shows three exemplary tracks with different lengths through the three geometries (panel a) as well as the obtained path lengths through the HET box, the EBox and the spacecraft box in all directions (panel b). The average path length through each geometry in each solid angle bin is used to define shell elements with specific densities.

The final shell has an inner radius of 6 cm, a thickness of 1 cm and the density ρ_i of each shell element i is determined from

$$\rho_i = \frac{\rho_{\mathrm{HET}} \cdot L_{\mathrm{HET},i} + \rho_{\mathrm{Ebox}} \cdot L_{\mathrm{Ebox},i} + \rho_{\mathrm{S/C}} \cdot L_{\mathrm{SC},i}}{1\,\mathrm{cm}} \tag{4.1}$$

where ρ_{HET}, ρ_{Ebox}, ρ_{SC} are the densities of the HET box, Ebox and spacecraft box and $L_{\mathrm{HET},i}$, $L_{\mathrm{Ebox},i}$, $L_{\mathrm{S/C},i}$ are the average path lengths through the HET box, EBox and spacecraft box of all particles in a solid angle bin i.

The resulting shell model (Fig. 4.4) is a strongly simplified description of the masses surrounding the EPT sensor. For an observer at the centre of the shell, the model allocates the total mass in such a way that

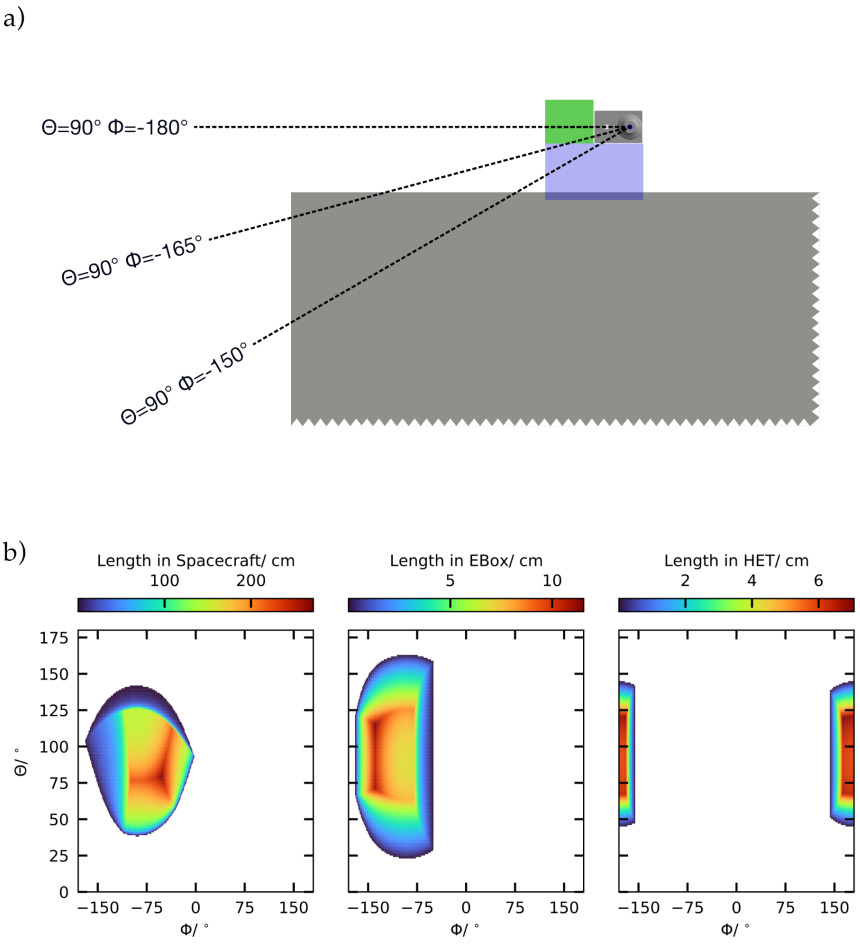

Figure 4.5: Illustration of the construction of the spacecraft shell model. (a) shows an example of five test particles with different path lengths through the box geometries. (b) shows the average path length of test particles through the spacecraft, EBox and the HET box.

a correct fraction of the total mass is contained in each solid angle, which is identical to the mass that would be found in each solid angle bin if the box geometries were present. In the *EPT+Shell geometry*, the sphere is centred around one detector stack of the *EPT geometry* and the shell radius (6 cm) was chosen to be large relative to the detector dimensions ($r = 3$ mm for the centre segments). For these dimensions, it can be assumed that the detector stack at the centre of the shell sees a realistic mass distribution over the solid angle. Hence, the shell should reasonably reproduce the shielding and the production of secondary particles within HET, the EBox and the spacecraft.

It should be noted that the model does not take into account the actual material composition and density of the numerous spacecraft components surrounding EPT. This could result in inaccuracies if, for instance, gamma rays were generated in specific components of high density on the actual spacecraft. Furthermore, processes such as scat-

tering at the spacecraft's surfaces cannot be simulated with the model as it does not reflect the actual surfaces in any way.

4.2.2 *Geant4 simulation runs*

The *EPT geometry* and the *EPT+Shell geometry* are used in three different simulation setups in order to simulate the response functions for electrons, protons, helium and oxygen. Figure 4.6 illustrates the three simulation setups which can be described as follows:

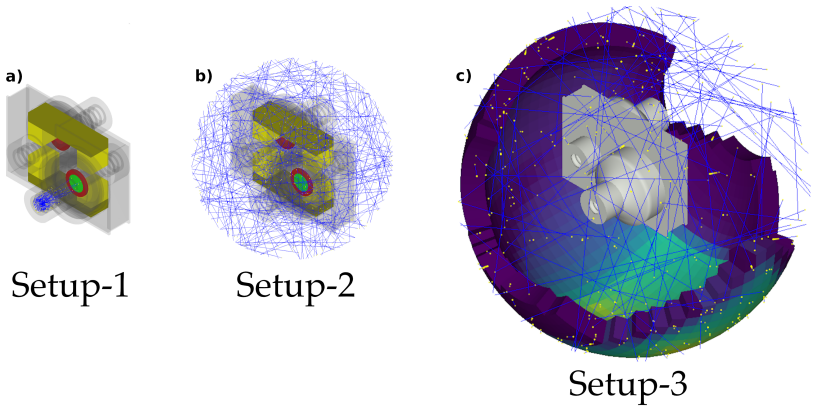

Figure 4.6: Illustration of the three simulation setups with exemplary particle trajectories in blue. Setup-1 (a) uses the *EPT geometry* with a circular source in front of the aperture. Setup-2 (b) uses a spherical source around EPT. Setup-3 (c) uses a spherical source around the *EPT+Shell geometry*.

SETUP-1 The first setup uses the *EPT geometry* and a circular particle source placed directly in front of the telescope openings. It emits particles isotropically within a limited angular range that is slightly larger than the opening angle of the EPT telescopes. This setup provides good statistics, as most simulated particles will hit the detectors. However, it is insufficient to describe the potential response for particles that originate from outside the nominal FOV. This setup is used to reproduce former published response functions with good statistics. Sequentially, the source is placed in front of the magnet detector and then in front of the foil in order to simulate the response of both detectors individually. Separate simulations for electrons, protons, helium and oxygen are performed. The source has a radius of 3 mm and particles are emitted isotropically within an angular range of 45° with respect to the surface normal of the source. The resulting geometry factor of the source, given by Eq. 3.15, is 0.44 cm^2sr. With this setup $5 \cdot 10^8$ particles in the energy range 20 keV to 100 MeV are simulated per particle species and per detector.

SETUP-2 For the second setup, the *EPT geometry* and a spherical source is used. The source, placed around the instrument, emits particles isotropically from a full 4π solid angle. This setup is used to simulate the response for particles from all directions and in particular to identify the possible contribution of particles that could penetrate the housing of the instrument. Subsequent simulations of electrons, protons, helium and oxygen are performed in an increased energy range from 20 keV to 20 GeV. The source sphere has a radius of 4 cm and with particles isotropically emitted into the sphere the geometry factor of this source is 631.66 cm^2sr. Due to the larger geometry factor of the source, more particles have to be simulated to achieve similar statistics as with the first setup. Here, $2 \cdot 10^9$ particles are simulated per particle species.

SETUP-3 The third setup uses the *EPT+Shell geometry* with a spherical source, which is placed around the geometry and emits particles isotropically from a full 4π solid angle. This setup is used to simulate the response for particles coming from all directions while considering possible shielding effects of HET, the electronic box and the spacecraft. It can also approximate the response due to secondary particles generated in the matter surrounding EPT. The source sphere has a radius of 7.1 cm and with particles isotropically emitted into the sphere the geometry factor of this source is 1990.11 cm^2sr. This setup has the largest source and the overall runtime is longer compared to the other simulation setups because a large number of interactions between particles and the shell model will be simulated. Due to the longer runtime it is not feasible to further increase the number of simulated particles here. Again, $2 \cdot 10^9$ particles in the energy range 20 keV to 20 GeV are simulated per particle species with this setup.

4.3 SIMULATION RESULTS

From the simulation outputs the energy response functions and the directional energy response functions (see Sect. 3.3) are determined for all nominal science data products of EPT. As part of this work, the results for data products NO_EPT_mag and NO_EPT_foil (see Sect. 3.2.3) are provided. These two data products count all stopping events in the magnet and foil detectors of EPT and they present the scientifically most relevant data products. In addition, results are provided for the NO_EPTP_p (ecliptic) data product. This data product intends to count events of penetrating protons in HE1 (the unit with FOVs in the ecliptic plane) with similar energy depositions in the two detectors of one detector stack. Here, this data products serves as one representative example for the various different EPT data products that count penetrating events.
The resulting energy response functions and the directional energy response functions are presented and described in Sect. 4.3.1 and Sect. 4.3.2, respectively.

4.3.1 *Energy response functions*

The energy response functions and their statistical uncertainties are calculated from Eq. 3.14 and Eq. 3.17, respectively. A logarithmic binning with 20 bins per energy decade is used to resolve the particle energy. The energy response functions $R_\alpha(E)$ of the different energy channels (DPI) of each data product are combined into one energy response matrix here. Thus, the final simulation result is one energy response matrix $\mathbf{R}_\alpha$ per particle species α and per data product. In addition to the response matrix, a total response function is calculated for each data product and particle species by summing the response functions of all energy channels (DPI).

Energy response functions of NO_EPT_mag

The energy response matrices and total energy response functions of the NO_EPT_mag data product for electrons, protons, helium and oxygen, calculated from simulations with setup-1, setup-2 and setup-3, are shown in Fig. 4.7. In the figure, the responses for different particle species are shown in different colours. The upper panels show response matrices where the opacity of each colour indicates the level of the response. As a reference, the colour bar shows the opacity of the colour black. The lower panels show the total energy response functions and their statistical uncertainties. The figures intend to illustrate the response of one data product to different particle species. To enhance the visualisation of absolute response values, an additional set of figures is provided in Appendix C. The figures in the appendix

present the same response matrices with separate panels for each particle species and a colourcoding that makes the absolute values more easily identifiable. The result can be described as follows:

RESULTS FROM SETUP-1 In setup-1, only particles within the instrument aperture are considered. The resulting response matrices and total response functions are comparable to the previously reported results of Rodríguez-Pacheco et al. (2020). The total response functions for protons and electrons in Fig. 4.7 (a) show the same response as the corresponding functions in Fig. 4.1 with only one minor deviation: For protons, the total response function obtained here increases at slightly higher energies, as can be seen by comparing the blue line in the lower panel of Fig. 4.7 (a) with the red line in Fig. 4.1. This difference results from previously missing dead layers that were added to the *EPT geometry* in this work. Here, these additional dead layers effectively stop all protons below $\sim 40\,\mathrm{keV}$, whereas the results of Rodríguez-Pacheco et al. (2020) show a clear response to protons even below 30 keV.

RESULTS FROM SETUP-2 Setup-2 simulates particles from a full 4π solid angle. The resulting response matrices and total response functions differ significantly from those obtained with setup-1: Here, the simulated response for particles with energies above the intended measuring range is significantly higher. In particular, the total response for electrons above $\sim 450\,\mathrm{keV}$ (red line, lower panel in Fig. 4.7 (b)) shows a continuous increase with increasing energy and the total response for ions shows significant increases above $\sim 20\,\mathrm{MeV/nuc}$. For electrons above $\sim 1\,\mathrm{MeV}$ and protons above $\sim 20\,\mathrm{MeV}$, the total response even exceeds the ideal geometry factors of $0.0154\,\mathrm{cm^2 sr}$ (dotted horizontal lines in the lower panels of Fig. 4.7).
The additional response seen in simulations with setup-2 results from particles that scatter within the telescopes, particles that penetrate the instrument housing and particles that produce secondary particles in the housing. The contribution of these particles was not fully simulated with setup-1.
Electrons with energies above $\sim 100\,\mathrm{keV}$ can scatter multiple times in the telescopes. Due to the changes in direction from scattering, these electrons are able to pass the magnetic field and generate valid stopping events in the magnet detector. This way, even electrons that originate outside the nominal FOV can reach the detector. Furthermore, electrons with energies above several hundred keV have the potential to penetrate the aluminium structure of the telescope or other parts of the instrument housing and can thus generate valid event signals on various additional trajectories. In most cases, penetrating and scattered electrons will lose a significant part of their initial kinetic energy before hitting the detector. Therefore, the initial kinetic energy of these electrons is poorly correlated with the energy ultimately de-

posited in the detector. As a result, the lower energy channels (DPI) of NO_EPT_mag all show a similar response to electrons with the same energy (compare, e.g., the response of the different energy channels for 1 MeV electrons in Fig. 4.7). Energy channels (DPI) above channel 50 show no response to electrons because the probability of depositing the necessary energies of more than 2 MeV in the detector becomes increasingly small for electrons.

Ions that penetrate the housing can create signals of valid stopping events in three different ways: They can either penetrate the housing and stop in the detector, they can penetrate both the housing and the detector or they can generate secondary particles within the housing, which then generate valid signals in the detector.

Ions above ~ 10 MeV/nuc can penetrate the housing and subsequently stop in the detector. In the response matrices, such particles cause a noticeable response of the upper energy channels (DPI) above channel 40 to ions in the energy range $[10 - 100]$ MeV/nuc. In the total response functions, they create a noticeable peak at ~ 20 MeV/nuc. Ions that penetrate the housing can hit the detectors under an oblique angle and thus, they can exhibit larger path lengths ($>300\,\mu$m) through the detectors. As a result, penetrating protons, such as those propagating diagonally along the long edge of the sensitive volume, can deposit more than 10 MeV, potentially generating valid signals in the highest energy channels (DPI) of NO_EPT_mag. From the simulation with setup-1 one would assume that the energy channels above channel 64 have no response to protons and only count heavier ions. Considering the results with setup-2, this is apparently not the case.

Ions with even higher energies can penetrate both the housing and the detector. These particles create another noticeable feature in the response matrices, where the deposited energy shows a decrease with increasing initial ion energy. For example, in the proton response matrix (best recognisable in Fig. C.2 in Appendix C), the energy channels (DPI) around channel 60 show a response to ~ 100 MeV protons that penetrate the detector. With increasing energy, the response shifts towards lower energy channels, until channel 45 that shows an enhanced response to ~ 20 GeV protons. The response results from particles entering or leaving the detector stack through the 0.4 mm gap between the magnet and foil detectors. By passing through this gap, these particles avoid the anti-coincidence that the other detector segments normally provide.

Ions above ~ 30 MeV/nuc can further produce secondary particles, which in turn can generate signals of valid stopping events. Such secondary particles are responsible for the large response in the lower energy channels (DPI) below channel 50 for ions above ~ 30 MeV/nuc. Secondary particles that contribute to valid events are primarily electrons and gamma rays. With increasing energy of the initial ions, their number and energy increase, too. The energies deposited by secondary

particles correlate poorly with the original ion energy. Heavier ions tend to produce more secondary particles that generate valid signals. As a result, at the same energy per nucleon above 30 MeV/nuc, there is a higher response for helium and oxygen compared to protons.

RESULTS FROM SETUP-3 Setup-3 adds the spacecraft shell model to the 4π simulations. The resulting response matrices and total response functions appear overall similar to the results from setup-2. However, there are some differences: The spacecraft effectively shields ions below $\sim$400 MeV/nuc as well as electrons and slightly reduces the response for these particles. Above $\sim$400 MeV/nuc the ion response increases more drastically, as a large number of secondary particles is created in the spacecraft model by such highly energetic ions. A direct comparison between the total energy response functions obtained with the three different simulation setups is included in Appendix C, Fig. C.10. Note, that the differences in the logarithmic scale may appear small, but the response for 10 GeV protons, for example, is more than three times higher in the simulation with a spacecraft model..

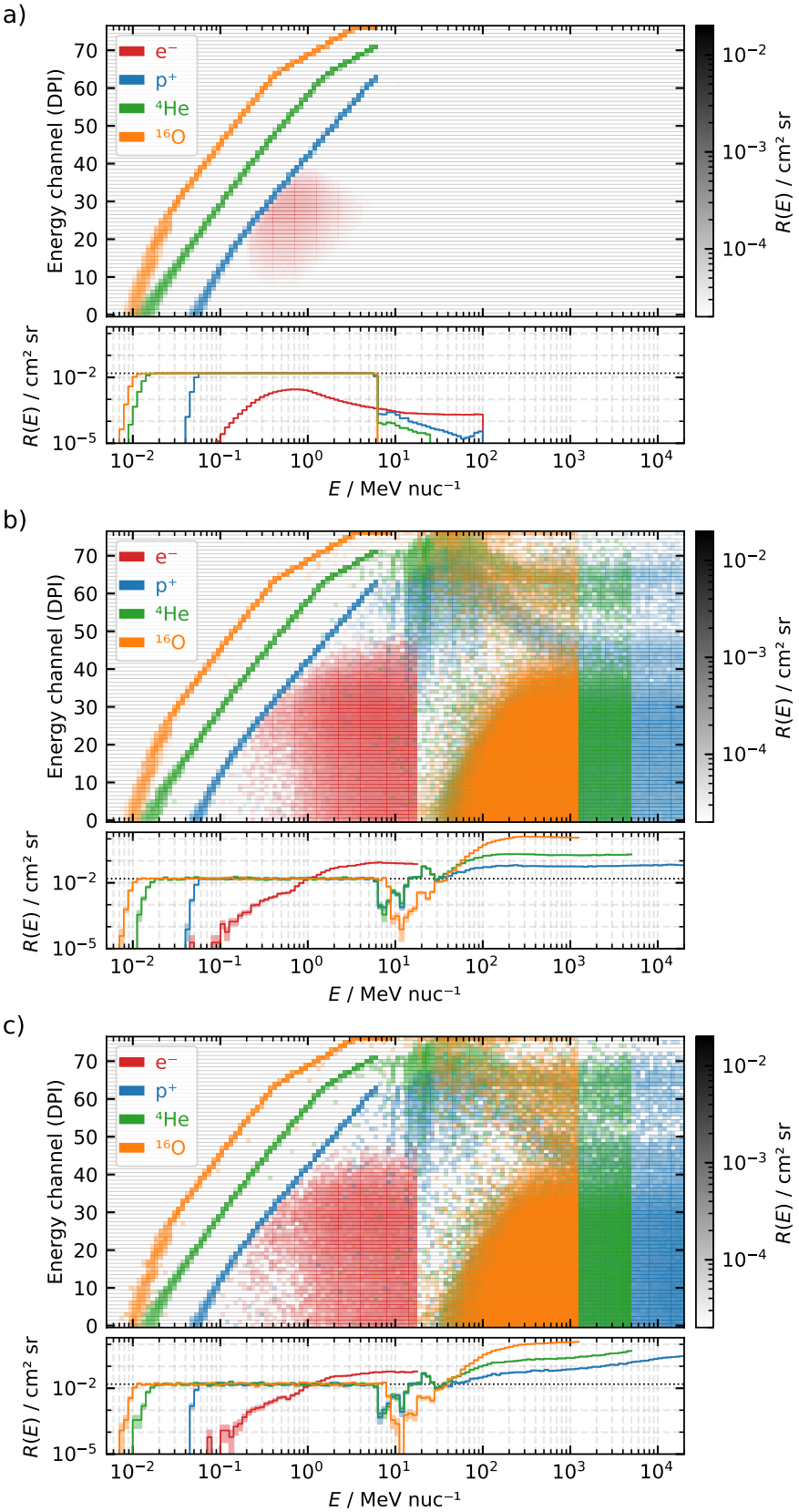

Figure 4.7: Energy response functions of the **NO_EPT_mag** data product simulated with **setup-1** (a), **setup-2** (b) and **setup-3** (c).

Energy response functions of NO_EPT_foil

In Fig. 4.8 the energy response matrices and total energy response functions of the NO_EPT_foil data product for electrons, protons, helium and oxygen, calculated from simulations with setup-1, setup-2 and setup-3, are shown. The results can be described as follows:

RESULTS FROM SETUP-1 Simulations with setup-1 produce response matrices and total response functions that are comparable to the results previously reported by Rodríguez-Pacheco et al. (2020).

RESULTS FROM SETUP-2 Simulations with setup-2 produce response matrices and total response functions that show a higher response to particles with energies above the intended measuring range, similar to the results presented for the NO_EPT_mag data product. Again, the additional response in simulations with setup-2 results from penetrating particles and secondary particles produced in the housing. Compared to the magnet detector and the response functions of the NO_EPT_mag data product, there are only some minor differences in the response of NO_EPT_foil to particles with energies above the intended measuring range. They mainly result from the different housings around the two detectors and the relative location of the magnet system. In general, simulations with setup-2 suggest a similar response of NO_EPT_foil and NO_EPT_mag to particles with energies above the intended measuring range.

RESULTS FROM SETUP-3 Simulations with setup-3 produce response matrices and total response functions that are overall similar to the results from setup-2. However, the spacecraft shields some electrons and ions with energies below $\sim 400\,\mathrm{MeV/nuc}$ and increases the response for ions with energies greater than $\sim 400\,\mathrm{MeV/nuc}$. A direct comparison between the total energy response functions obtained with the three different simulation setups is included in Appendix C, Fig. C.11.

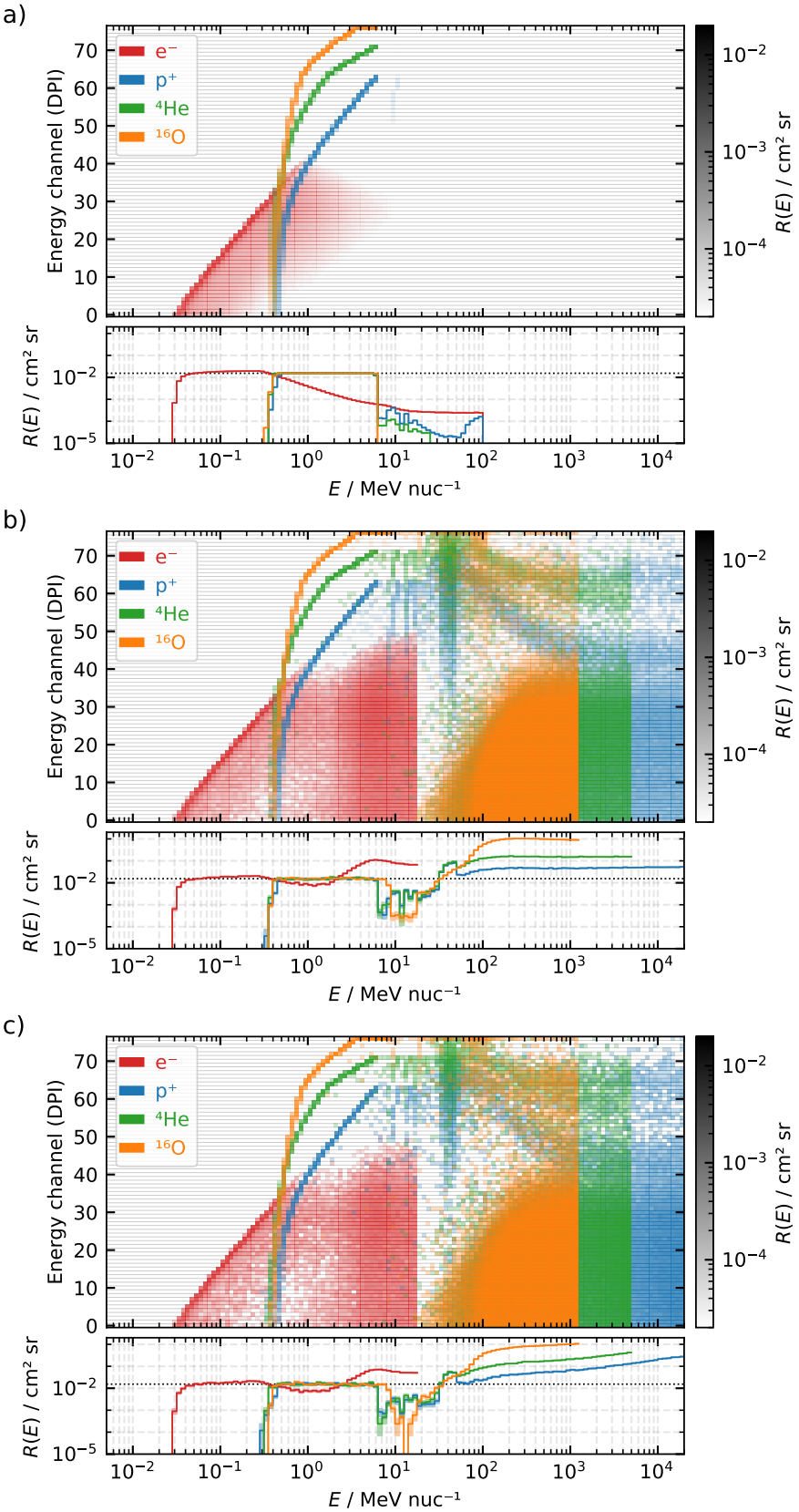

Figure 4.8: Energy response functions of the **NO_EPT_foil** data product simulated with **setup-1** (a), **setup-2** (b) and **setup-3** (c).

Energy response functions of NO_EPTP_p (ecliptic)

In Fig. 4.9 the energy response matrices and total energy response functions of the NO_EPTP_p (ecliptic) penetrating data product for electrons, protons, helium and oxygen, calculated from simulations with setup-1, setup-2 and setup-3, are shown. Note, that in the actual instrument, all penetrating data products sum events observed in the two double-ended telescopes. The response functions here show the response of only one telescope to achieve better comparability of the different simulation setups. Assuming that both telescopes have the same response, the response of the actual data products is higher by a factor of 2. The result can be described as follows:

RESULTS FROM SETUP-1 Simulations with setup-1 produce response matrices and total response functions that resemble an almost ideal detector response. The data product has four energy channels (DPI) that respond almost exclusively to protons and the response functions overlap only slightly in energy.

RESULTS FROM SETUP-2 Simulations with setup-2 produce fundamentally different response matrices and total response functions compared to setup-1. All four energy channels (DPI) show an extended response to protons in a wider energy range (about 20 MeV to 20 GeV). The additional proton response, compared to the response functions obtained with setup-1, results from protons with energies high enough to penetrate the telescopes or other structures of the instrument housing. Moreover, all energy channels show some response to helium and oxygen at energies greater than $\sim$30 MeV/nuc. These heavier ions were not simulated in setup-1, as the maximum simulated energy for all ions was 100 MeV. At energies well above $\sim$30 MeV/nuc, heavier ions can also create secondary particles, which in turn can generate valid signals in the data product.

RESULTS FROM SETUP-3 Simulations with setup-3 again produce overall similar results as simulations with setup-2. However, the spacecraft effectively shields ions below energies of $\sim$200 MeV/nuc and slightly increases the response to particles with energies above this limit. A direct comparison between the total energy response functions obtained with the three different simulation setups is included in Appendix C, Fig. C.12.

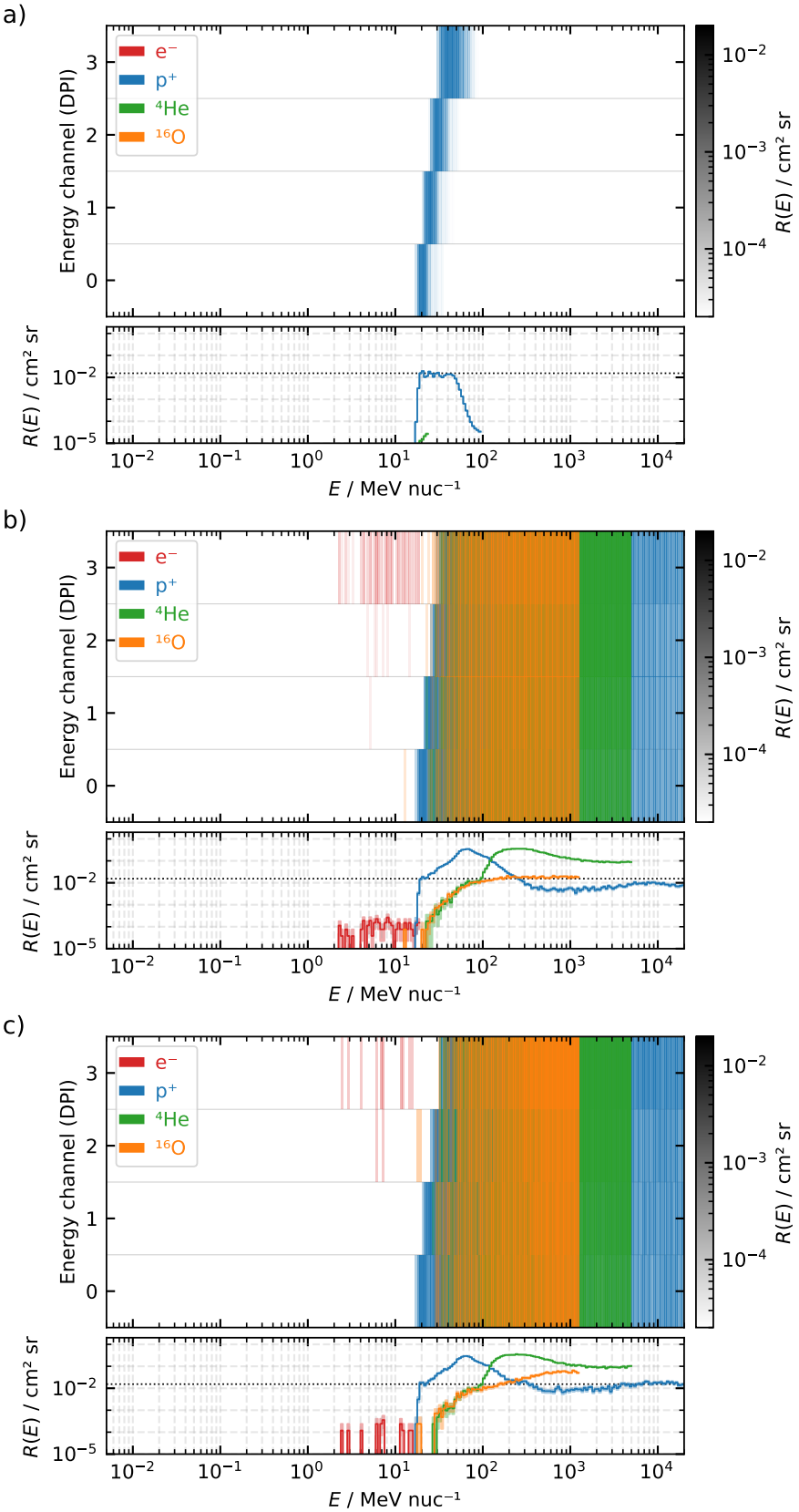

Figure 4.9: Energy response functions of the **NO_EPTP_p (ecliptic)** data product simulated with **setup-1** (a), **setup-2** (b) and **setup-3** (c).

4.3.2 *Directional response functions*

In addition to the energy response functions, the directional energy response functions provide information on the directions from which particles can generate valid event signals in EPT. The directional energy response functions and their statistical uncertainties are calculated using Eq. 3.13 and Eq. 3.16, respectively. Since the directional response has two additional dimensions that resolve the direction (θ and ϕ), a lower resolution of the energy E is used to maintain reasonable statistics. Here, the energy E of the simulated particles is resolved in only three broad energy bins. The energy bins are chosen in such a way that the first bin roughly matches the intended measuring range of EPT, the second bin covers energies at which the spacecraft shell primarily acts as shielding and the third bin includes all simulated energies above the second bin. For the direction, 16 uniform ϕ-bins and 60 uniform θ-bins are used. The directional energy response functions $A_\alpha(\theta, \phi, E)$ of the different energy channels (DPI) of each data product are combined into one directional energy response matrix $\mathbf{A}_\alpha(\theta, \phi, E)$ for each particle species α. Analogue to the total energy response functions, a total directional energy response function is calculated for each data product by summing up the directional energy response functions of all energy channels (DPI).
Additionally, a second total directional response function $A_\alpha(\theta, E)$ is determined for each data product, using the assumption that the ϕ dependence of the total directional response is negligible. This function is calculated by averaging the response over ϕ while using a finer binning for the θ-angle. It is used to compare the simulated directional response with the ideal response function of a detector with cylindrical geometry as described in Eq. 3.9.
For the sake of simplicity, only the total directional responses are presented in this work. In principle, the directional responses of the individual energy channels (DPI) of a data product can differ. However, a full description of the differences in the individual energy channels is beyond the scope here. Instead, only a general description of the directional response of the data products is given. Furthermore, only results from the simulations with setup-3 are presented, as it can be assumed that the simulation with the shell model provides the most realistic directional response functions. Finally, the directional response functions for helium and oxygen are also omitted since the proton response is sufficiently representative for the other ions.
A visual presentation of the total directional energy response function is still not straightforward, since the response depends on three different parameters at the same time. To illustrate the most important aspects of the response function, different visualisations are used here: For each energy bin, the total directional response $A(\theta, \phi)$ is presented in a 3D colormap and additionally in a Mollweide projection. The

coordinates used in all the visualisations refer to the simulation coordinate system shown in Fig. 4.2. For further guidance, a 15° wide ideal FOV of EPT is included in the visualisation, together with a red contour line that marks the directions occulted by the shell model. Moreover, the additional total response functions averaged over all ϕ-angles are shown for the three broad energy bins together with the ideal directional response.

Directional response functions for NO_EPT_mag

The directional response functions of the NO_EPT_mag data product for protons and electrons, obtained from the simulations with setup-3 are shown in Figs. 4.10 to 4.13. Figures 4.10 and 4.12 show the total response for electrons and protons, respectively. Each figure includes three rows displaying the average response to particles with energies in three broad energy bins. The two columns visualise the same response functions in a 3D presentation (left) and a Mollweide projection (right). Figures 4.11 and 4.13 show the total directional response in the three energy bins averaged over all ϕ-angles. The dotted lines show the ideal directional response of the EPT.

RESULTS FROM SETUP-3 For protons in the energy range $[0.05 - 6]$ MeV, the total directional response function of NO_EPT_mag simulated with setup-3 resembles an almost ideal directional response: There is no noticeable ϕ-dependency in the directional response for protons in this energy range (first row in Fig. 4.10) and $A(\theta)$ fits well to the ideal directional response (compare the dotted black and the green line in Fig. 4.11).
For protons in the energy range $[6 - 200]$ MeV, there is a response to particles from almost all directions except for those where the instrument is occulted by the spacecraft model. The response functions show a noticeable higher response for θ-directions $< 90°$ which correspond to proton trajectories that hit the detector from the magnet side (see the decreasing response with increasing θ-angle in Fig. 4.11).
In the upper energy range from $[0.2 - 20]$ GeV, the data product shows a response to particles from all directions. Due to the production of secondary particles, the detector has a slightly higher response to particles originating from directions that are occulted by the spacecraft compared to directions that are not occulted.
For electrons in the energy ranges $[20 - 400]$ keV and $[0.4 - 1]$ MeV, the total directional response functions show primarily a response to directions with $\theta < 80°$ (see Fig. 4.13). Thus, in these two energy ranges, the data product responds primarily to electrons that hit the detector from the magnet side. Above 1 MeV, the data product shows a response to electrons from almost all directions except some distinct directions where the instrument is occulted by the spacecraft model (see bottom row in Fig. 4.12).

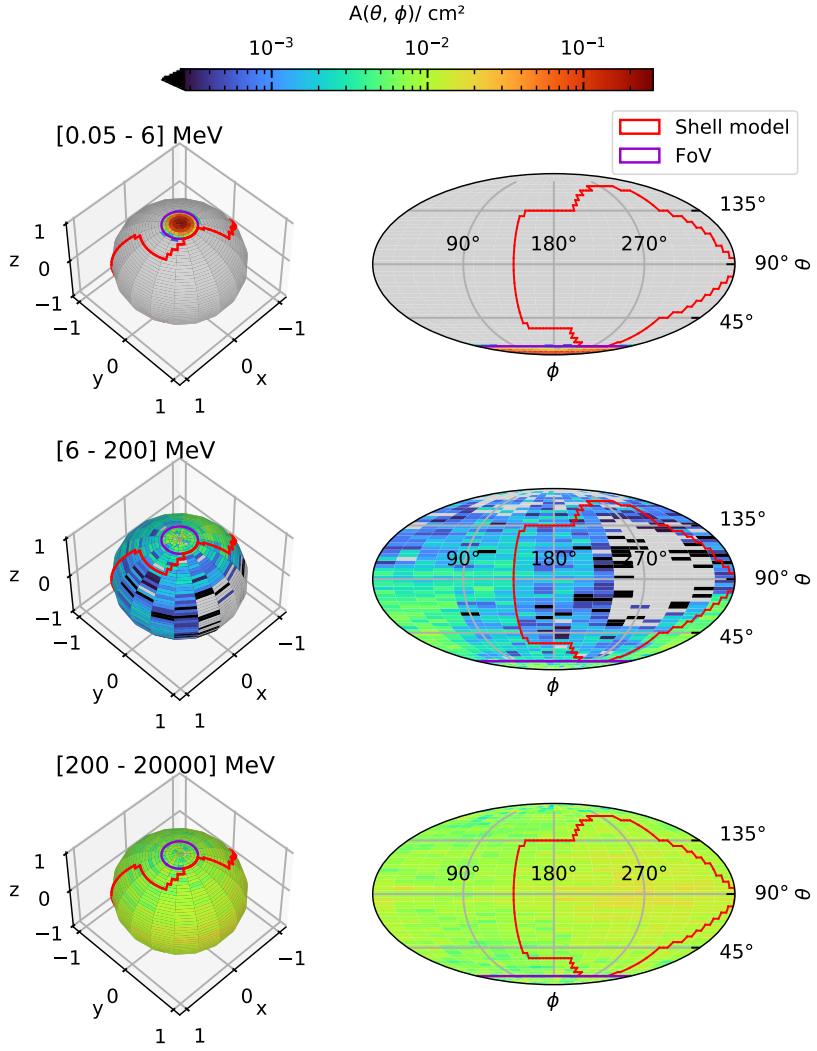

Figure 4.10: Directional response $A(\theta, \phi)$ of **NO_EPT_mag** for **protons** in three different energy ranges.

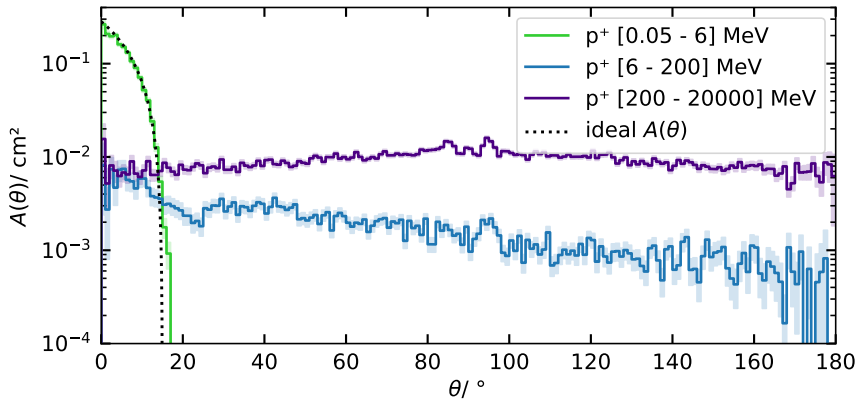

Figure 4.11: Directional response $A(\theta)$ of **NO_EPT_mag** for **protons** averaged over all ϕ-angles in three different energy ranges.

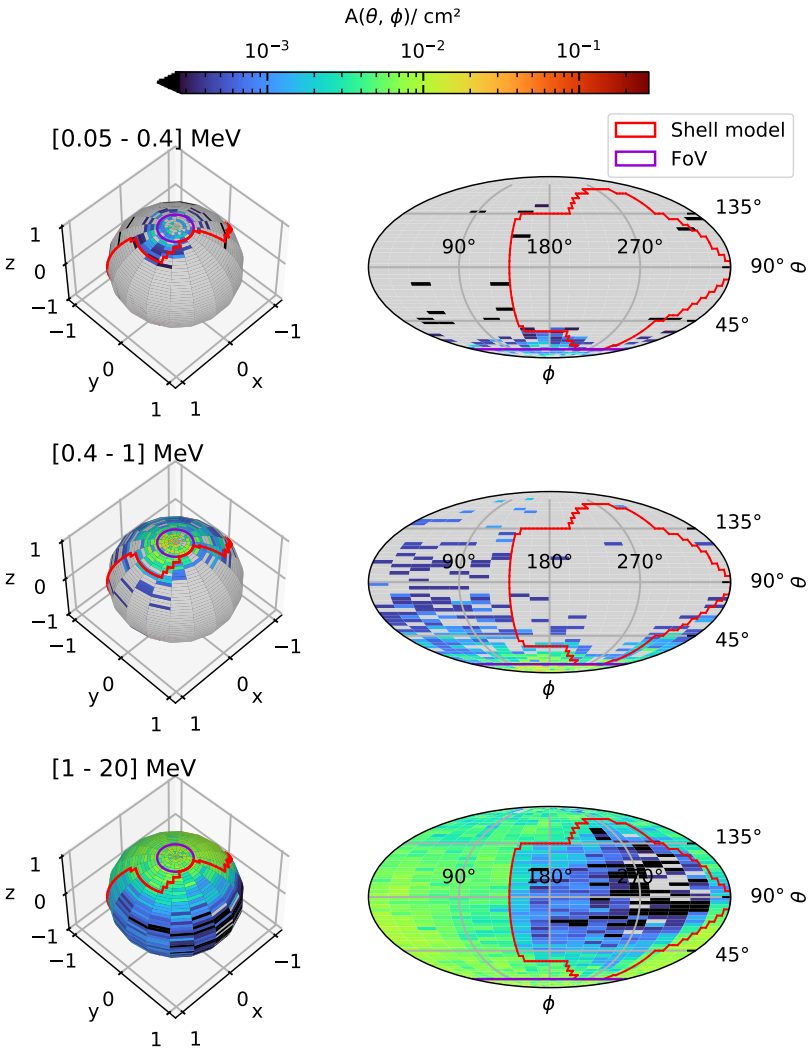

Figure 4.12: Directional response $A(\theta, \phi)$ of **NO_EPT_mag** for **electrons** in three different energy ranges.

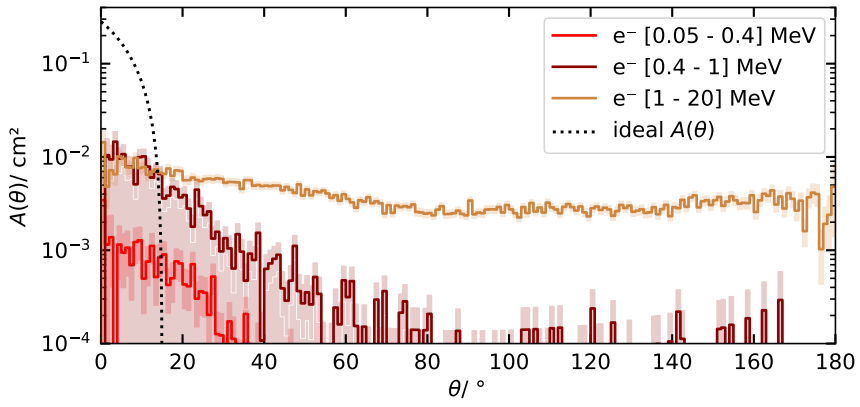

Figure 4.13: Directional response $A(\theta)$ of **NO_EPT_mag** for **electrons** averaged over all ϕ-angles in three different energy ranges.

Directional response functions for NO_EPT_foil

The directional response functions of the NO_EPT_foil data product for protons and electrons, obtained from the simulations with setup-3, are shown in Figs. 4.14 to 4.17. Figure 4.14 and Fig. 4.16 show the total directional response functions in three energy bins for electrons and protons, respectively. Figure 4.15 and Fig. 4.17 show the total directional response averaged over all ϕ-angles.

RESULTS FROM SETUP-3 For electrons in the energy range $[20 - 400]$ keV, the total directional response function of NO_EPT_foil simulated with setup-3 differs slightly from the response of an ideal detector. That is, there is a noticeable response to electrons from directions outside the nominal 15° wide FOV (see e.g. the response outside the magenta circle in figure 4.16, upper left panel). In fact, the directional response for electrons spreads over $\sim 60°$ in θ (from 180° to $\sim 120°$; see the bright red line in Fig. 4.17). The additional response to electrons outside the ideal FOV results from electrons that scatter in the aperture before they hit the detector, and also partially from electrons that generate secondary gamma rays in the aperture, which subsequently deposit energy in the detector. With increasing energy, the directional response extends over a wider θ-range. Above 1 MeV, the data product shows a response to electrons from almost all directions. However, the response is noticeably smaller for directions where the spacecraft occults the instrument (see bottom row in Fig. 4.16).
For protons in the energy range $[0.05 - 6]$ MeV, the total directional response is limited to the ideal FOV (compare e.g. response and magenta circle in the upper left panel in Fig. 4.14). In the energy range $[6 - 200]$ MeV, the data product shows a response to protons from almost all directions, but the response decreases with increasing θ angle (see green curve in Fig. 4.15) and the response is lower in directions at which the spacecraft occults the instrument (see second row in Fig. 4.14). Above 200 MeV, the data product shows a response to protons from all directions. As for the stopping particles in the magnet detector, the response is slightly higher in directions at which the instrument is occulted by the spacecraft due to an increased production of secondary particles.

Directional response for NO_EPTP_p (ecliptic)

The directional response functions of the NO_EPTP_p (ecliptic) data product for protons from the simulation with setup-3 are shown in Fig. 4.18 and Fig. 4.19. Since this data product counts penetrating events, the two centre segments measure in coincidence here. As neither of the two centre segments serves as an anti-coincidence, this data product will accept particles from both telescope sides. Again, note that the response functions here show the response of only one double-ended telescope.

RESULTS FROM SETUP-3 For protons in the energy range $[20 - 40]$ MeV, the total directional response of NO_EPTP_p (ecliptic) differs from the response of an ideal detector. There is a noticeable response to protons from directions outside the nominal 15° wide FOV (see e.g. the response outside the magenta circle in the upper row in Fig. 4.18). The response results from protons that are apparently able to penetrate the housing and make signals of valid penetrating events. The response is noticeable higher for θ-directions $< 90°$, which correspond to proton trajectories that hit the detector stack from the magnet side. The large differences in the response to protons from the magnet side (θ-directions $< 90°$) and protons from foil side θ-directions $> 90°$ (noticeable in Fig. 4.19) result from differences in the instrument housing on both sides. However, it should be mentioned again that the geometry in the simulation is a simplified representation of the actual instrument. Details in the real housing of EPT, which are not considered here, could further influence the response in certain directions through the housing.
In the energy range $[40 - 200]$ MeV, protons can penetrate the instrument housing and the data products show a response to almost all directions except a narrow angle range around $\theta = 90°$ (see Fig. 4.19) and some distinct directions occulted by the spacecraft. Above 200 MeV, the data product shows a response to protons from almost all directions. As for the two data products for stopping particles, the response is slightly higher in directions at which the instrument is occulted by the spacecraft.

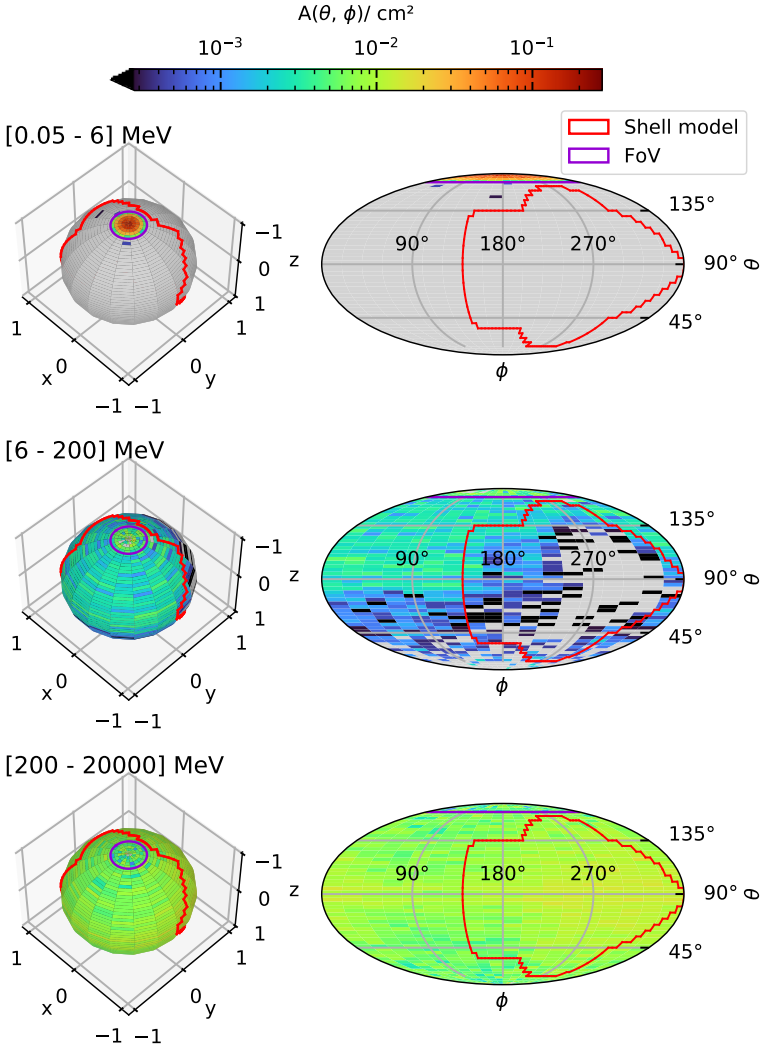

Figure 4.14: Directional response $A(\theta, \phi)$ of **NO_EPT_foil** for **protons** in three different energy ranges.

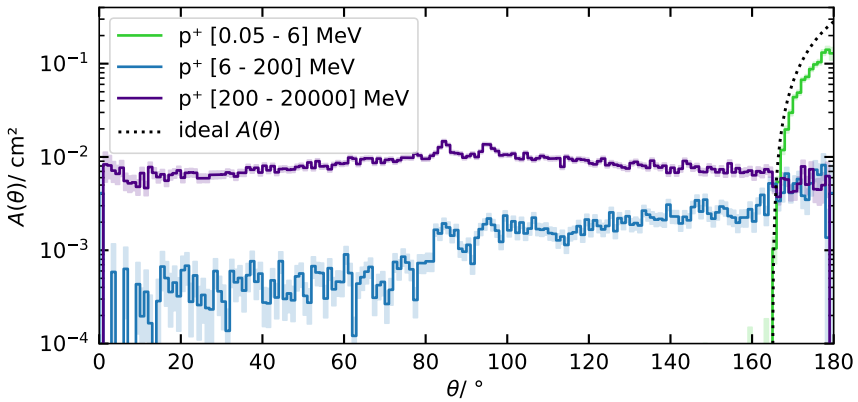

Figure 4.15: Directional response $A(\theta)$ of **NO_EPT_foil** for **protons** averaged over all ϕ-angles in three different energy ranges.

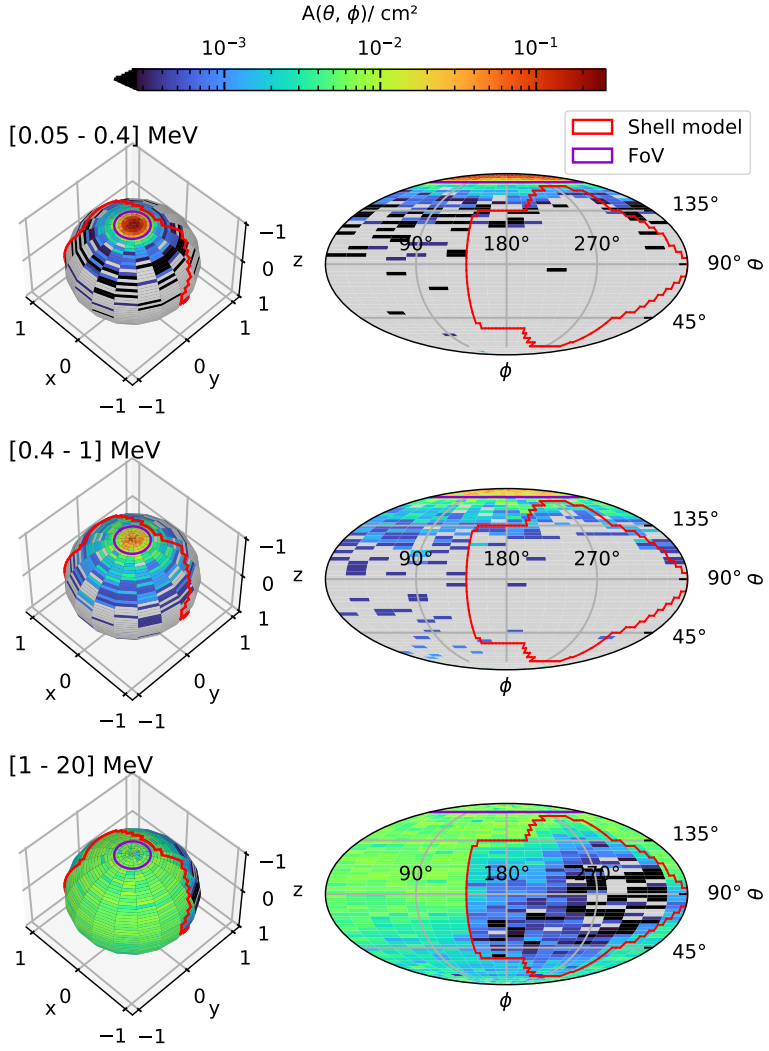

Figure 4.16: Directional response $A(\theta, \phi)$ of **NO_EPT_foil** for **electrons** in three different energy ranges.

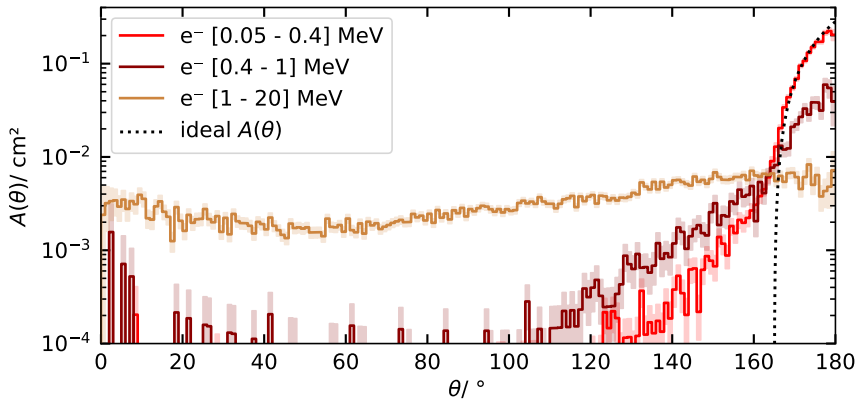

Figure 4.17: Directional response $A(\theta)$ of **NO_EPT_foil** for **electrons** averaged over all ϕ-angles in three different energy ranges.

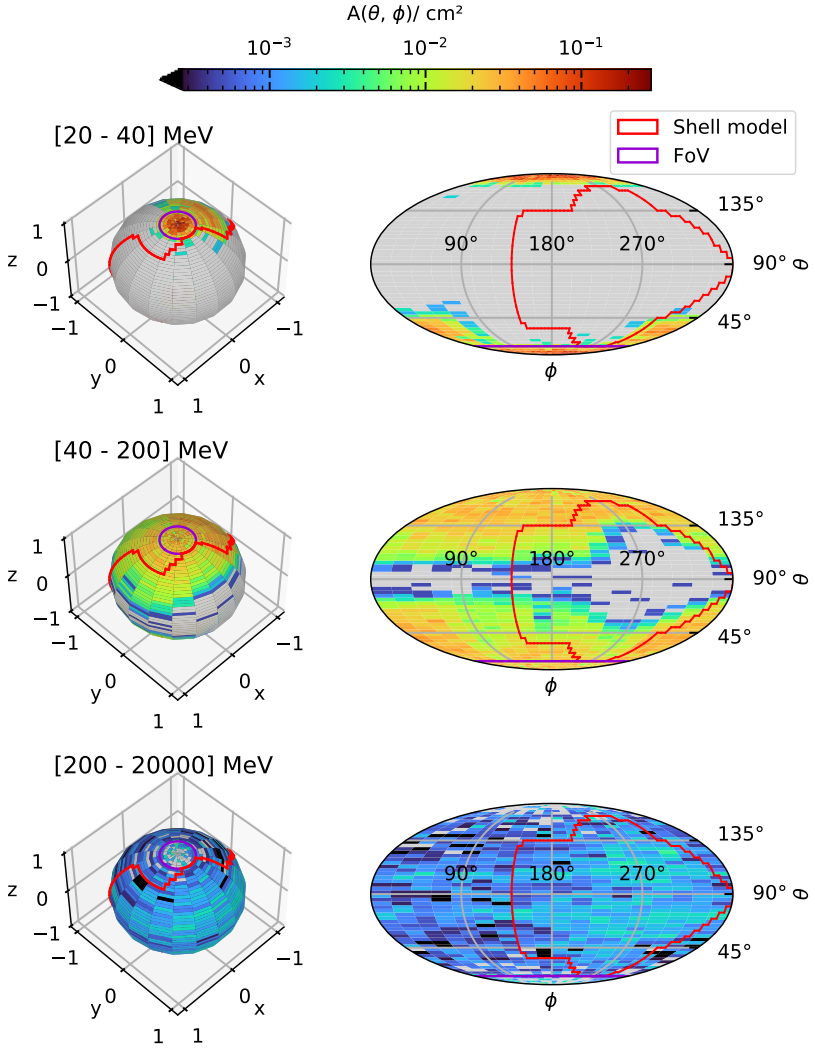

Figure 4.18: Directional response $A(\theta, \phi)$ of **NO_EPTP_p (ecliptic)** for **protons** in three different energy ranges.

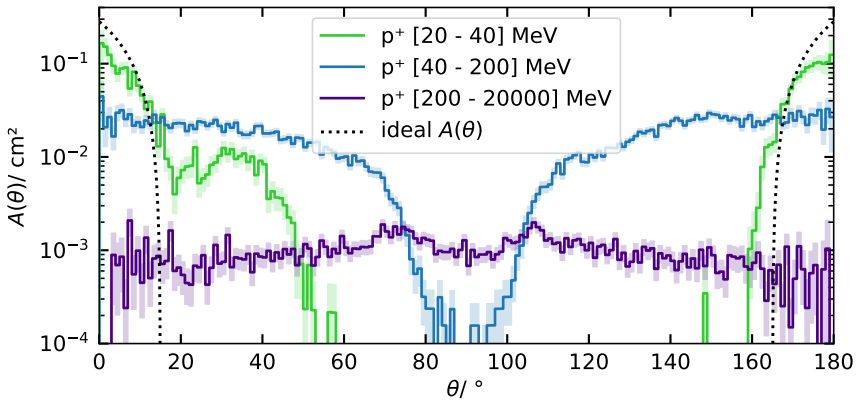

Figure 4.19: Directional response $A(\theta)$ of **NO_EPTP_p (ecliptic)** for **protons** averaged over all ϕ-angles in three different energy ranges.

4.4 DISCUSSION ON SIMULATION RESULTS

The results of the EPT detector response simulations can be summarised as follows: The energy response functions obtained from 4π simulations with the *EPT geometry* (setup-2) and the *EPT+Shell geometry* (setup-3) show that EPT has a considerably more complex response to ions and electrons than what was previously considered based on simulations limited to the aperture of the instrument (setup-1 and results from Rodríguez-Pacheco et al., 2020).
In general, the 4π simulations suggest a significantly larger response in all EPT data products to particles with sufficient energy to penetrate the instrument housing. As such, electrons with energies above a few hundred keV and ions with energies above ~ 20 MeV/nuc are able to produce unintended counts in the different data products. Since the response to these particles is relatively large (i.e. larger than the ideal geometry factor above certain energies), it must be assumed that such particles can contribute significantly to the measurements of EPT.
Simulations with the *EPT+Shell geometry* (setup-3) further suggest that the masses surrounding EPT, and in particular the spacecraft, shield the instrument from electrons and from ions with energies below a few hundred MeV/nuc. However, at energies above a few hundred MeV/nuc, the surrounding masses can increase the ion response due to the production of secondary particles.
The simulated directional energy response functions suggest an almost ideal directional response (as calculated from Eq. 3.9) for protons <6 MeV in the magnet detector. For the foil detector, the directional response for electrons <400 keV features a small but noticeable response outside the nominal FOV and thus it differs slightly from an ideal directional detector response.
At higher energies, the directional energy response functions show that the unwanted contamination of ions in the foil detector and electrons in the magnet detector is more likely when particles originate from the hemisphere into which the contaminated detector is looking. However, ions with energies well above 100 MeV/nuc and electrons with energies well above 1 MeV have a similar probability of contaminating the two detectors, almost independent of the initial particle direction.

The simulation results can have direct implications for the inversion and interpretation of EPT measurements, depending on the actual particle fluxes. For instance, the EPT magnet detector and the NO_EPT_mag data product were designed to primarily observe ions. Yet, the large response to electrons with energies above several hundred keV, which becomes evident in 4π simulations, makes it clear that a possible contribution of electrons in NO_EPT_mag should be considered during all periods with increased high-energy electron fluxes. Without taking

this electron response into account, the detector count rates could be misinterpreted as ion fluxes.
Furthermore, the directional energy response functions show an electron response outside the nominal FOV in the NO_EPT_foil data product. Although this response is small compared to the response within the FOV, it should be taken into account in all periods in which highly anisotropic fluxes are observed. Note, that in case of highly focused electron beams, counts can be registered in the detector even if the beam is completely outside the nominal FOV. Particular attention should be given to the directional response functions if one tries to compare the degree of anisotropy in different SEP events and especially if one compares observations from different instruments, as differences in the responses can significantly influence the observations (see Brüdern et al., 2022 for more details on this issue).
Moreover, the 4π simulations suggest that the energy channels (DPI) above channel 64 (deposited energy $> 6.5\,\mathrm{MeV}$) of the NO_EPT_mag data product have a considerable response to protons. Based on previous works and simulations restricted to the aperture, it was assumed that these channels respond solely to helium or heavier ions. Thus, the counts in these channels were attributed to heavier ions rather than protons. However, the results from 4π simulations show that this interpretation is not necessarily correct and that a possible contribution of protons in the upper channels of NO_EPT_mag must be considered.
Both the magnet and foil detectors have a response to $>20\,\mathrm{MeV/nuc}$ ions, which can cause unintended contamination of the measurements during all periods where the flux of such highly energetic ions shows a significant increase. Without appropriate consideration, the counts caused by $>$20MeV/nuc ions could be misinterpreted as ion and electron fluxes in the originally intended measuring range of $E < 6.3\,\mathrm{MeV}$ or $E < 450\,\mathrm{keV}$, respectively. Since the ion response increases further at even higher energies, the contribution of $>100\,\mathrm{MeV}$ particles (e.g. GCR particles) should also be considered.
The EPT penetrating data products have a complex response, as 4π simulations show. For example, the NO_EPTP_p (ecliptic) data product has four energy channels (DPI), which all respond to multiple particle species in a wide energy range. The inversion of the data product would thus require finding the energy-dependent flux of different particle species in wide energy ranges based on only four measured count rates. This represents a problem that is practically impossible to solve without further information. However, it may be possible to combine this data product of EPT with data products from the other EPD instruments. Using the response functions presented, the count rates in the data product could then be interpreted in a common approach together with other data products. Although a detailed discussion of the other penetrating data products of EPT has been omitted, similar consequences can be expected to apply to most of them.

Lastly, note that the accuracy of all the response functions presented here is limited. The response functions, and in particular the directional energy response functions, have limited statistics and thus considerable statistical uncertainties. Additionally, the simulations also have systematic uncertainties: Physical processes considered in the simulations are described by models with inherent limitations and the geometries used here are simplified representations of the actual instrument. The shell model is a particularly strong simplification of the actual spacecraft and other assemblies around EPT. In principle, the accuracy could be improved by re-running the simulations with more detailed models and additional computational resources to enhance the statistics. However, the results achieved here appear sufficient for the fundamental evaluation of the EPT response and the following interpretation of EPT measurements.

5 UNDERSTANDING EPT SCIENCE DATA

In the previous chapter, new EPT response functions were obtained from Geant4-based Monte Carlo simulations. This chapter will now describe in Sect. 5.1, how these response functions are used to perform a rudimentary inversion of the EPT measurements, which is used to calibrate the official scientific data.
Moreover, Sect. 5.2 shows how the response functions allow to estimate the GCR background in EPT and presents corresponding results. Finally, Sect. 5.3 elaborates on the electron contamination of the EPT magnet detector and shows, based on one example, how the contamination can be quantified.

5.1 EPT LEVEL-2 CALIBRATION

The EPT level-2 calibration is a rudimentary inversion of the count rates measured by EPT into differential electron and ion fluxes at different energies. It is used to generate the EPT level-2 data, which is one of the most important scientific EPD data sets available to the scientific community.
The general inversion problem has been described in Eq. 3.6 and Sect. 3.3. In order to simplify the inversion and to allow for a direct conversion from measured count rates to particle fluxes, several assumptions are made. Although these assumptions are not universally valid, they appear acceptable for the purpose of automatically obtaining a reasonable flux estimate from EPT count rates:

1. The observed flux is isotropic within a FOV. Under this assumption, the directional dependence of the response can be neglected and the energy response function $R(E)$ can be used instead of the directional energy response $A(E, \omega)$.
2. Each detector responds only to a single particle species. Under the assumption that the magnet detectors measure only protons and the foil detectors measure only electrons, the count rates in each detector can be inverted using a single response matrix for the corresponding particle species.
3. The flux of particles with energies above the intended measuring range is insignificant. Under this assumption, the response functions from simulations limited to the aperture (setup-1) can be used, which offer the best statistics (for details, see Sect. 4).
4. For the energy range in which an energy channel (DPI) has a response, it can be assumed that the energy spectrum is $J(E) \propto$

E^{-2} (a frequently observed spectral shape; see e.g. Krucker et al., 2009 or Dresing et al., 2020). Under this assumption, it is possible to convert the energy-dependent response $R(E)$ into a weighted mean response factor or a so-called effective geometry factor.

With assumptions 1 and 2 the count rate C measured in each energy channel can be described by

$$C = \int_0^\infty R(E)J(E)dE \,, \tag{5.1}$$

where $R(E)$ is the energy response function of the energy channel and $J(E)$ is the differential particle flux of the single species for which a response is considered.
For the level-2 calibration, an effective geometry factor $\overline{g}$ is sought so that the same count rate C can be calculated from a mean particle flux $\overline{J}$ in a given energy range between E_{low} and E_{high}:

$$C = \overline{J} \cdot \overline{g} \cdot (E_{\text{high}} - E_{\text{low}}) \,. \tag{5.2}$$

The mean particle flux is given by

$$\overline{J} = \frac{\int_{E_{\text{low}}}^{E_{\text{high}}} J(E)dE}{E_{\text{high}} - E_{\text{low}}} \tag{5.3}$$

and the effective geometry factor can be obtained by inserting Eqs. 5.1 and 5.3 in Eq. 5.2:

$$\overline{g} = \frac{\int_0^\infty R(E)J(E)dE}{\int_{E_{\text{low}}}^{E_{\text{high}}} J(E)dE} \,. \tag{5.4}$$

Using Eq. 5.4, an effective geometry factor can be calculated for any given energy dependence or spectral shape of $J(E)$. For $J(E) \propto E^{-2}$ (assumption 4), the effective geometry factor can be calculated as

$$\overline{g} = \frac{1}{E_{\text{low}}^{-1} - E_{\text{high}}^{-1}} \int_0^\infty \frac{R(E)}{E^2} dE. \tag{5.5}$$

Finally, the mean particle flux between E_{low} and E_{high} can be calculated by simply rearranging Eq. 5.2:

$$\overline{J} = \frac{C}{(E_{\text{high}} - E_{\text{low}}) \cdot \overline{g}}. \tag{5.6}$$

In principle, the equation above can be used to calculate an effective geometry factor for arbitrary energy limits E_{low} and E_{high}, which then would allow determining an average flux for any energy. However, this is only possible because a fixed spectral shape of $J(E)$ was assumed. If the actual spectral shape differs from the assumption, the effective geometry factor is no longer accurate and the fluxes determined from

it will be incorrect.
Yet, if the response is limited to a small energy range in which $J(E)$ does not change significantly, energy limits can be selected for which the effective geometry factor becomes nearly independent of the spectral shape.
For the EPT level-2 calibration, an attempt was made to define optimal energy limits. That is, E_{low} and E_{high} were selected for each energy channel (DPI) so that they correspond to the intersection of the response functions of successive energy channels (see Fig. 5.1). For the first and last energy channel E_{low} and E_{high} were chosen, respectively, so that they correspond to the point where the response reaches half its maximum. This way, the final energy limits create a continuous, non-overlapping binning of the energy, with the peak of each response residing between E_{low} and E_{high} for each energy channel. The effective geometry factors for these energy limits were determined using Eq. 5.5. Figure 5.1 shows an example with the energy limits and effective geometry factors defined for five consecutive energy channels (DPI) in the NO_EPT_foil data product. The final EPT level-2 calibration factors for all data products and corresponding response functions are publicly available in the Solar Orbiter data archive (*Solar Orbiter Archive* 2025).

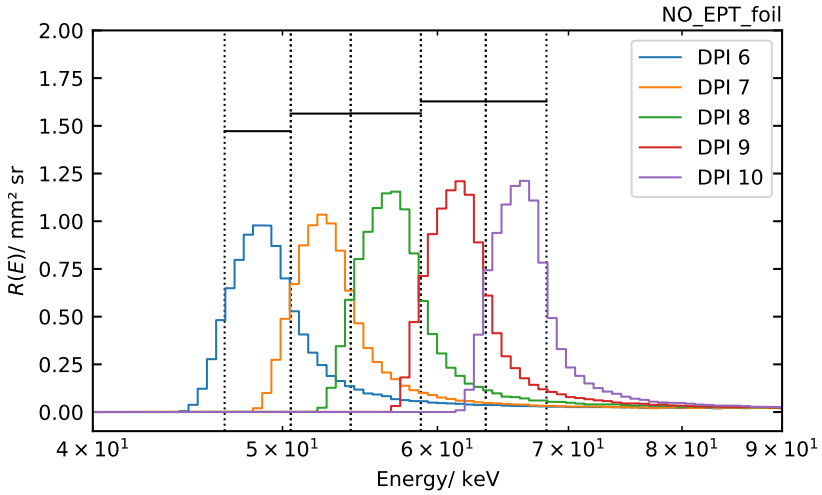

Figure 5.1: Energy response function of five DPIs of the NO_EPT_foil data product. Vertical dotted lines mark energy limits from the EPT level-2 calibration. Horizontal black bars show the effective geometry factors.

5.1.1 *Caveats of the level-2 data*

It is important to note that the EPT level-2 fluxes may be incorrect if one or more of the underlying assumptions are not applicable. As such,

the assumption of a spectral shape in the calculation of the effective geometry factors can introduce systematic errors if the actual spectral shape differs vastly. Nevertheless, these errors are usually small because the energy ranges in which the individual channels exhibit responses are small (<10 keV in the examples shown in Fig. 5.1).
A more problematic assumption is that each detector responds to only one particle species. Under this assumption, the level-2 fluxes will be incorrect during all periods in which more than one particle species contributes significantly to the count rates in a channel. This problem will be discussed in more detail in Sect. 5.3.
Moreover, the assumption that the flux of particles above the intended energy range can be neglected is also problematic. Although this assumption is justifiable during SEP events, when the energy-dependent particle flux and its relative contribution to the measured count rates decrease strongly with increasing energy, it is not universally valid. There are periods without SEP events during which the measured count rates of certain channels are dominated by high-energy ions well above the measurement range. The following section will present some corresponding examples. During such periods, the level-2 fluxes are incorrect.

Appendix D contains another chapter that addresses an additional detail of the EPT level-2 calibration. After the commissioning of EPT and the accumulation of several months of measurement data, it became evident that the original level-2 calibration suffered from issues caused by the onboard quantisation of the deposited energy and by certain non-linearities in the signal processing of EPT. The chapter in the appendix gives a detailed description of an optimisation that was developed to minimize the impact on the level-2 data.

5.2 GCR BACKGROUND IN EPT

EPT was built to measure SEP events during which the flux of energetic particles often increases by orders of magnitude over time periods of hours or days. But there are also other populations of energetic particles that will eventually be measured by EPT. GCR particles are one example for such an additional population. The flux of GCR particles is usually low compared to the SEP flux during an event, but GCR particles reach much higher energies (> GeV). The 4π simulations have shown that EPT has a fairly high response to ions >100 MeV/nuc (see Chap. 4). Thus, it must be assumed that the GCR will produce some non-negligible count rates in EPT, presumably in the form of a fairly constant background. This section presents an estimate of the actual contribution of GCR particles to the EPT measurements.
The GCR flux is widely independent of the SEP flux and has less temporal variation. However, as solar activity increases, so does the solar

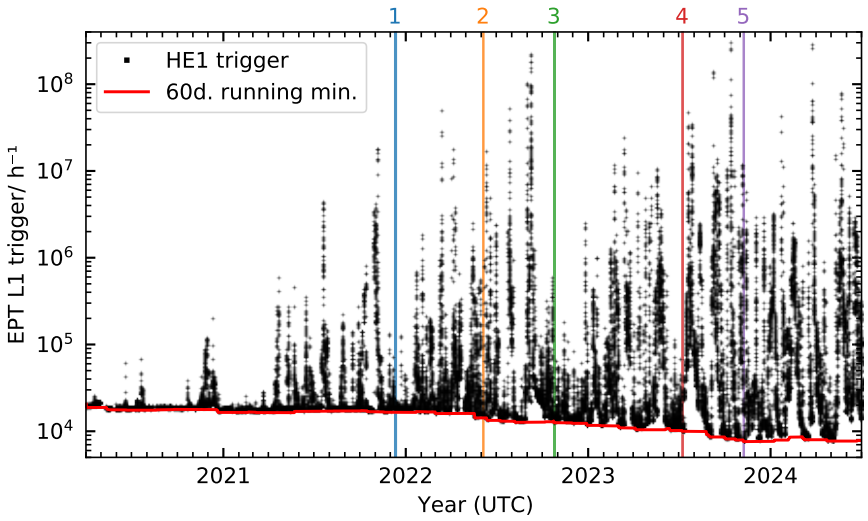

Figure 5.2: Time profile of the EPT level-1 trigger rate. The red line shows a 60-day running minimum. Vertical lines indicate five quiet time periods.

Table 5.1: List of five 'quiet' time periods during solar cycle 25.

No.	Start time (UTC)	End time (UTC)
1	2021-12-10 00:00	2021-12-13 00:00
2	2022-06-04 12:00	2022-06-06 02:00
3	2022-10-24 06:00	2022-10-27 00:00
4	2023-07-07 20:00	2023-07-10 00:00
5	2023-11-07 12:00	2023-11-09 06:00

modulation of the GCR and the increasing modulation causes a gradual decrease of the GCR flux in the inner heliosphere. Therefore, the expected GCR contribution to EPT measurements should be relatively constant with a gradual decrease while the activity of solar cycle 25 increases (maximum expected in 2025). During the course of the mission so far, the EPT level-1 trigger rates reflect a corresponding trend: Figure 5.2 shows the daily averaged sum of the level-1 trigger rates measured in the four EPT centre segments of HE1 between April 2020 and June 2024. As expected, the frequency of SEP events and thus the frequency of days with high trigger rates increases as solar cycle 25 progresses, but the rates on 'quiet' days, where no SEP events are observed, decrease over the years. In fact, a 60-day running minimum (shown as a red line) decreases from 20566 trigger/h to 7560 trigger/h between April 2020 and November 2023. Therefore, the background count rate appears to follow the decreasing GCR flux.

Given that the GCR flux is largely independent of the SEP flux, it can

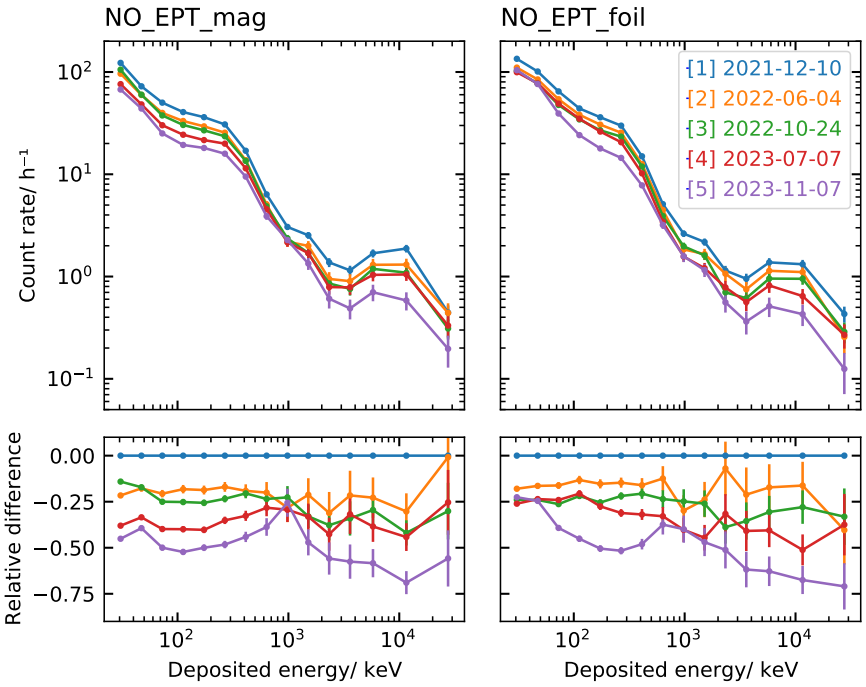

Figure 5.3: EPT 'quiet' time count rate spectra observed in the magnet detector (left panels) and in the foil detector (right panels). Lower panels show the relative differences to the spectrum observed in 2021 (blue lines).

be assumed that the relative contribution of the GCR to the EPT count rates is greatest when no SEP events are observed. Therefore, the GCR contribution during such 'quiet' time periods will be estimated here. For this purpose, several 'quiet' time periods throughout solar cycle 25 are identified. For each period, the flux of GCR protons, helium and oxygen is estimated using measurements from the HET sensor. Finally, the EPT response matrices are used to calculate GCR count rates in the different EPT data products.

In particular, five 'quiet' time periods are identified by visually inspecting the trigger rates and science data from HET, EPT and STEP. The 'quiet' time periods were selected according to the criteria that no signatures of SEP events were noticeable in any of the three sensors and that the trigger rates did not show any significant change during these periods. The resulting periods are listed in Tab. 5.1 and are further indicated by vertical lines in Fig. 5.2. Figure 5.3 shows the count rate spectra (level-1 data) observed during these five periods in the EPT sunward looking magnet and foil detectors (upper panels). The figure also shows the relative difference of each spectrum compared to the spectrum observed during the first period (bottom panels). For better illustration, several energy channels were combined in this figure.

In order to approximate the flux of GCR in the relevant energy range, the high-energy proton spectra measured by the HET sensor are

parametrised and extrapolated. For this purpose, the so-called force field solution (for a description see e.g. Moraal, 2013; Gleeson et al., 1968) is used here. The force field solution solves the 1D convection–diffusion transport equation for GCR in the heliosphere and can be used to calculate the modulation of the interstellar GCR spectrum for an observer at e.g. 1 AU. It can be used to parametrise the energy spectrum of GCR with a single free parameter, given a certain interstellar spectrum (an example of a similar application can be found in Usoskin et al., 2005). Following the force field solution, the differential particle flux of a species i at 1 AU is given by

$$J_i(E,\phi) = J_{\mathrm{LIS},i}(E+\Phi)\frac{E(E+2E_r)}{(E+\Phi)(E+\Phi+2E_r)}, \tag{5.7}$$

where $J_{\mathrm{LIS},i}$ is the local interstellar spectrum (LIS) that describes the energy-dependent differential flux of the species i in the local interstellar medium in units of $[1/(\mathrm{m}^2\ \mathrm{sr\ s\ GeV/nuc})]$, E is the kinetic energy, $\Phi = (Ze/A)\phi$ is the average energy loss per nucleon inside the heliosphere, Z is the charge number, A is the mass number, E_r is the rest mass of i and ϕ is the so-called modulation potential, which is the only explicit free parameter.
The LIS for protons is taken from Usoskin et al. (2005) and is given by

$$J_{\mathrm{LIS,p}}(E) = \frac{1.9\cdot 10^4 \cdot P(E)^{-2.78}}{1+0.4866\cdot P(E)^{-2.51}}, \tag{5.8}$$

where $P(E) = \sqrt{E(E+2E_r)}$. The same LIS is also used with a specific scaling to approximate the LIS of helium and oxygen. In particular, $J_{\mathrm{LIS,He}} = 0.05 \cdot J_{\mathrm{LIS,p}}$ (as suggested in Usoskin et al., 2005) and $J_{\mathrm{LIS,O}} = 0.0016 \cdot J_{\mathrm{LIS,p}}$. The factor of 0.0016 between the LIS of oxygen and protons was derived from the corresponding abundances measured in the local interstellar medium by VOYAGER 1 at 80 MeV/nuc (Cummings et al., 2016).
It should be mentioned that the assumption of the exact same spectral shape of the LIS for protons, helium and oxygen as well as the description of the GCR modulation by the force field solution are certainly substantial simplifications of the actual GCR physics. However, this approach is used here to obtain a simple approximation of the GCR flux in order to make an estimate of the expected count rates in EPT data products, without intending to further analyse the physics of the GCR. For this purpose, such a simple description of the GCR seems appropriate.
For each quiet time period, a modulation potential ϕ is determined by fitting $J_{\mathrm{p}}(E,\phi)$ to HET proton measurements. More specifically, a least square minimisation is used to estimate an optimal modulation potential that minimises the residuals between $J_{\mathrm{p}}(E,\phi)$ and the proton fluxes measured by HET (using the NO_HET_p_C data product while excluding the first five and last three energy channels, which suffer

from calibration issues). Figure 5.4 shows the HET measurements obtained during the five 'quiet' time periods together with the respective fit results of $J_p(E)$. The optimal modulation parameters as well as the reduced least squares derived from each minimisation are shown in the legend.

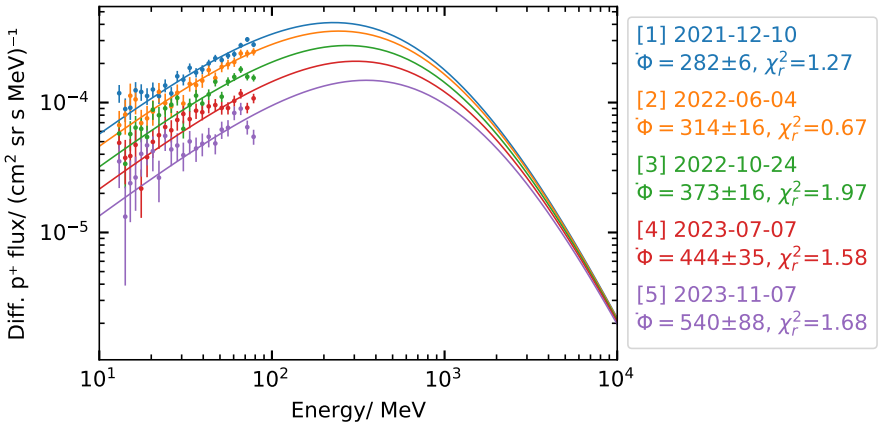

Figure 5.4: HET proton spectra observed during five 'quiet' time periods together with fit results from the force field solution.

The resulting proton spectra $J_p(E)$ can then be used to calculate the corresponding helium spectra $J_{He}(E)$ and oxygen spectra $J_O(E)$ for each period using the scaling factors mentioned above. In principle, one could also try to derive GCR helium and proton spectra directly from HET measurements, but for the short periods considered here the statistics were insufficient for such an approach.
Using $J_p(E)$, $J_{He}(E)$ and $J_O(E)$ of each period, count rates in EPT can be calculated from

$$\vec{C} = \mathbf{R}_p \cdot \vec{I}_p + \mathbf{R}_{He} \cdot \vec{I}_{He} + \mathbf{R}_O \cdot \vec{I}_O, \tag{5.9}$$

where $\vec{C} = (C_0, C_1, ..., C_n)$ is a vector with the count rates observed in n energy channels of one data product and $\mathbf{R}_p$, $\mathbf{R}_{He}$, $\mathbf{R}_O$ are the response matrices of this data product for the three considered particle species. $\vec{I}_p$, $\vec{I}_{He}$ and $\vec{I}_O$ are mean fluxes of the three particle species in the energy bins of the response matrices, which are calculated by multiplying the differential particle fluxes $J_p(E)$, $J_{He}(E)$ and $J_O(E)$ at the centre energy of each response bin with the energy width of the bin.
Here, the count rates in the 77 energy channels (DPIs) of the two main data products NO_EPT_mag and NO_EPT_foil are calculated using the response matrices derived from 4π simulations with the shell model (see Sect. 4.3). Figure 5.5 shows the resulting GCR count rates for the period 10. to 13. December 2021 together with the actual observed count rates during this period. To illustrate the contribution of the different particle species of the GCR, the figure includes the calculated count rates of the individual summands of Eq. 5.9 as well

as their total sum (black line). The errors were determined from the statistical uncertainties of the response matrices. The observations are shown together with their corresponding statistical uncertainties as dots with error bars. In the narrow panels, the relative deviation between the calculated and measured count rates in the individual energy channels (DPIs) are shown. Results for the other four periods can be found in Appendix F.

The results of this estimate on the GCR contribution to the EPT measurements can be can be described as follows: Protons are responsible for most of the total GCR count rates. The calculated GCR count rates in the two main data products of EPT are comparable to the ones observed in all energy channels (DPI) between channel 16 and 72 (deposited energy range $\sim$110 keV to $\sim$30 MeV). In the energy channels (DPI) below channel 16 ($\sim$110 keV) and above channel 72 ($\sim$30 MeV), the observed count rates are higher than the calculated GCR count rates.

Above channel 16, the spectral shapes of the calculated GCR rates agree well with the measured ones. This agreement is consistent for all five time periods and indicates that, despite all simplifications, the assumed GCR spectra and the simulated response functions produce reasonable estimates for the count rates measured in EPT.

The observed count rates in the magnet and the foil detector in the energy channels between channels 16 and 72 ($\sim$110 keV to $\sim$30 MeV deposited energy) can be fully explained by GCR particles. Count rates observed in channels above channel 72 (>30 MeV deposited energy) are slightly higher than the calculated GCR rates.

This discrepancy in the upper channels could be explained by the neglect of all species other than protons, helium and oxygen. In these channels, helium noticeably contributes to the total GCR count rate and it appears likely that further ion species could contribute as well.

The count rates observed in channels below channel 16 (<110 keV deposited energy) are significantly higher than the calculated rates from GCR. An interpretation of this discrepancy in the lower channels is not straight forward. Because it is present during all considered periods and both in the magnet and in the foil detectors, it is unlikely that the residual count rate, i.e. the count rate difference between the calculated GCR rate and the measured one, results from SEP event remnants.

One possible explanation could be that the residual count rate results from suprathermal particles. Observations of, e.g., suprathermal protons and electrons would be of scientific interest and in principle, one could derive a spectrum of these particles by subtracting the calculated GCR rates from the measured ones and then calibrate the residual count rate into particle fluxes. However, there is no certainty that the residual count rate is actually produced by suprathermal particles and there might be other explanations.

A second possible explanation is that the assumed GCR spectra and/or

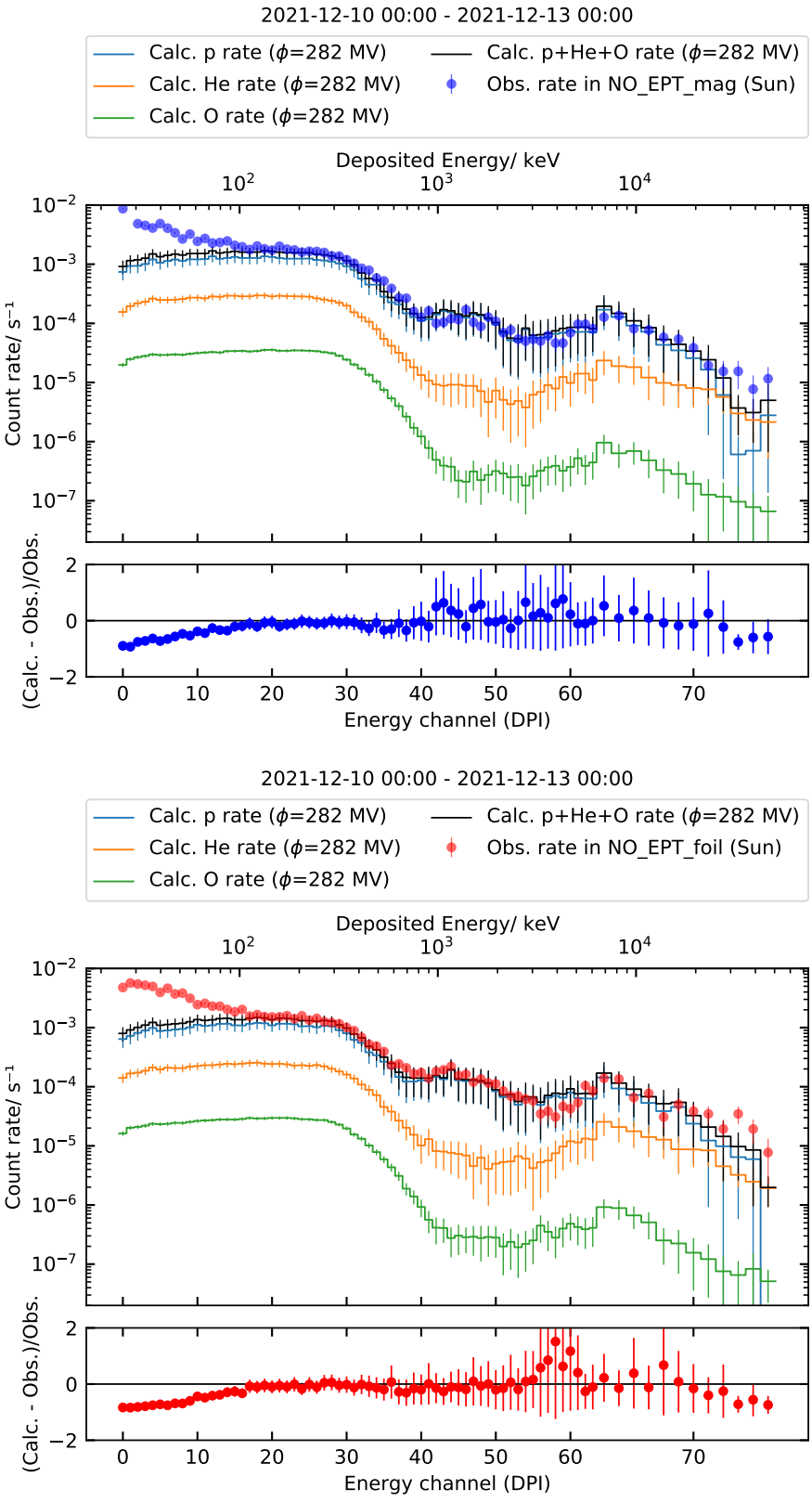

Figure 5.5: Comparison of the calculated GCR count rates and the observed count rates in the EPT magnet detector (top two panels) and the EPT foil detector (lower two panels).

the simulated response functions miss some relevant parts. For example, it might be possible that heavy GCR ions such as iron generate large numbers of γ-rays somewhere in a dense material of the spacecraft. These γ-rays could then create counts in the lower energy channels. In such a case, the count rates in the lowest energy channels of EPT could also be dominated by signals from GCR particles. In fact, the changes of the NO_EPT_mag spectra over time, shown in Fig. 5.3, may support this idea. If one compares the count rate spectra observed in December 2021 (blue line) and November 2023 (magenta line), a decrease of roughly 40 % is noticeable in all energy channels below several hundred keV. The relative changes in count rates observed below and above 110 keV appear similar and it seems that actually all energy channels follow the temporal changes in the GCR flux. This indicates that the lower channels are also dominated by GCR counts.
The NO_EPT_foil spectra, in contrast, show different temporal changes below and above 110 keV deposited energy. This might indicate that the lower channels in the foil detector of EPT are not dominated by GCR during 'quiet' times and rather contradicts the idea of a nearby source of gamma-rays. Ultimately, no unambiguous explanation for the count rates observed during 'quiet' times in the energy channels below 110 keV could be found here.
For future studies of 'quiet' time intervals, it might be worthwhile to determine the EPT responses to additional heavier ion species. While this could help to understand the count rates observed in the lower channels, it is out of the scope of this work.
Here, it can be concluded that the count rates in most energy channels of EPT are dominated by GCR counts during 'quiet' time periods. The GCR contribution should be considered in all studies of such periods. The next section takes a closer look at EPT observations during SEP events.

5.3 ELECTRON CONTAMINATION IN EPT

The magnet/foil-technique used in EPT has some well-known limitations. For example, the separation of different ion species is generally not possible and the separation of ions and electrons only works in certain energy ranges. Ions with energies above $\sim$400keV/nuc can penetrate the foil and generate signals in the foil detector and electrons with energies above 100 keV can scatter through the magnetic field and generate signals in the magnet detector.
Ideally, the contributions of electrons and ions should be taken into account equally for the inversion of the measurements in both detectors. However, considering multiple particle species with different response functions complicates the inversion of the measurement enormously and more complex inversion methods usually involve additional assumptions about the observed particle fluxes.

The rudimentary EPT level-2 calibration (described in Sect. 5.1) does not consider such contributions from multiple particle species. As a result, the fluxes in the level-2 data can be overestimated. Ions that contribute to the count rates measured in the foil detectors can lead to an overestimation of electron fluxes and electrons that contribute to the count rates measured in the magnet detectors can lead to an overestimation of the ion fluxes. Since the level-2 data is used by a broad scientific community, it is important to clearly describe the limitations of the data set to prevent misinterpretations.
As part of the SERPENTINE project (*SERPENTINE* 2020), the contamination of ions in the foil detector has been quantified and a data product was created that corrects the overestimation of electron fluxes due to ion contamination in the level-2 data. The corrected data is available as a level-3 data set (Espinosa Lara et al., 2024). However, the contamination of electrons in the magnetic detector has not yet been analysed and will be investigated here.

As a generic example, the electron contamination will be estimated for an SEP event observed on 24. February 2023. Figure 5.6 shows HET and EPT electron and ion fluxes (level-2 data) during the event. The ions show a clear signature of velocity dispersion in the dynamic spectrum (top panel) throughout the energy range of HET and EPT from $\sim 100\,\mathrm{MeV}$ down to $\sim 50\,\mathrm{keV}$. Below $\sim 1\,\mathrm{MeV}$, a second ion population is noticeable in the EPT measurements. This second population shows a flux increase that coincides with the increase in flux of near-relativistic electrons (shown in the second panel). For a duration of about eight hours after the event onset, the $453 - 1038\,\mathrm{keV}$ electron flux observed by the HET sensor (ch 0) shows an almost identical time profile as the $163 - 174\,\mathrm{keV}$ ion flux observed by EPT (ch 20) (see comparison of the two channels shown in the bottom panel).
The timing and correlation between the near-relativistic electrons observed by HET and the supposed low-energy ions ($< 1\,\mathrm{MeV}$) in EPT during this time period indicate that EPT actually observes electrons that were incorrectly calibrated into ion fluxes in the level-2 data.
To quantify the possible contribution of electrons in the sunward looking magnet detector and specifically in the NO_EPT_mag_S data product, the electron spectrum is estimated at each point in time and expected electron count rates in the magnet detector are calculated using the electron response matrices obtained from the 4π simulation with the shell model (see Sect. 4.3).
More specifically, the electron fluxes at the centre of the energy bins of the electron response matrix R_e are derived by logarithmically interpolating HET and EPT level-2 electron fluxes. To account for possible ion contamination in the foil detector, only the lowest 20 electron channels are used from EPT, which generally show a lower relative ion contamination compared to the higher channels. Below 1 MeV, the

EPT and HET fluxes observed in the sunward looking telescopes are used. Above 1 MeV, the HET electron fluxes from all four HET FOVs are averaged. This combination of directional and quasi-omni-directional electron fluxes is motivated by the directional energy response of the NO_EPT_mag data product (see Sect. 4.3.2). The directional electron response of the magnetic detector is mainly limited to the direction in which the detector is looking below 1 MeV, while above 1 MeV there is a response to electrons from almost all directions.
From the interpolated differential electron fluxes, mean electron fluxes $\vec{I}_e$ are calculated by multiplying the interpolated differential particle flux in each bin with the energy width of the bin. Count rates $\vec{C} = (C_0, C_1, ..., C_n)$ in the n energy channels are then calculated from

$$\vec{C} = \mathbf{R}_e \cdot \vec{I}_e. \tag{5.10}$$

Uncertainties $\vec{\Delta C}$ are calculated likewise based on the statistical uncertainties of the response matrix $\mathbf{\Delta R}_e$.
The resulting calculated electron count rates are shown together with the actual measured count rates in Fig. 5.7. The figure shows the measured count rates in all energy channels (DPI) (top panel), the calculated electron count rates in all energy channels (second panel), a direct comparison of the measured and calculated count rates in some arbitrary energy channels (here channel 15 to 20) as a time profile and a direct comparison of the count rate spectrum averaged over an arbitrary time interval from 21:00 to 21:30 UT (bottom panel).
The results can be described as follows: During the first $\sim$ 8 h after the event onset, there is a good agreement between the observed count rates and the calculated electron rates in the lowest 42 energy channels of the NO_EPT_mag_S data product. The time profiles of the observed count rates and the calculated electron count rates appear quite similar (comparing magenta and blue lines in the third panel of Fig. 5.7). During the time interval from 21:00 to 21:30 UT, the calculated electron count rate spectrum agrees well with the observed spectrum in all energy channels (DPI) up to channel 42. Above channel 50 ($\sim$ 2 MeV deposited energy), the calculated electron count rate is zero. Thus, the count rates above channel 50 were most likely generated by ions.
It can be concluded that electrons can significantly influence the count rates observed in the magnet detector. In the presented example the count rates observed during the first hours of the event, below channel 42, can be fully explained by electron contamination. This contribution is not considered in the EPT level-2 data and can cause a significant overestimate in the EPT level-2 ions fluxes. For all events with electron flux increases well above 100 keV similar contamination should be expected. Particular attention should be paid to this effect when determining the arrival times of ions. Due to the contamination of the electrons in the magnetic detector, it may appear as if low-energy ions reach the spacecraft quite early during an SEP event, whereas, in fact,

the signal is produced by electrons.
By using EPT and HET electron measurements, together with the response matrices calculated in this work, it is in general possible to quantify the electron contribution in the magnet detector. Eventually, the presented method could be used to develop an algorithm that systematically corrects the electron contribution in the magnet detector. However, this would require a reliable estimate of the electron flux in the relevant energy range, which is unfortunately not always available. Due to the limited FOVs of EPT and HET the actual electron flux can be underestimated in case of high anisotropic distributions. In principle, an electron beam can generate counts in a magnetic detector without being directly observed in one of the FOVs. In this case, there is no way to properly determine the electron flux. Moreover, there are certain periods during which the HET electron measurements are not reliable due to calibration problems.
Therefore, it is currently only possible to evaluate the electron contribution on an event-by-event basis. For each period, the reliability of the estimated electron flux should be evaluated. If the electron fluxes are reliable, the method described here can be used to quantify their contribution in the magnet detector.
So far, this work has described the instrument response of EPT and some important instrumental effects. The following part will focus on the scientific analysis of SEP events.

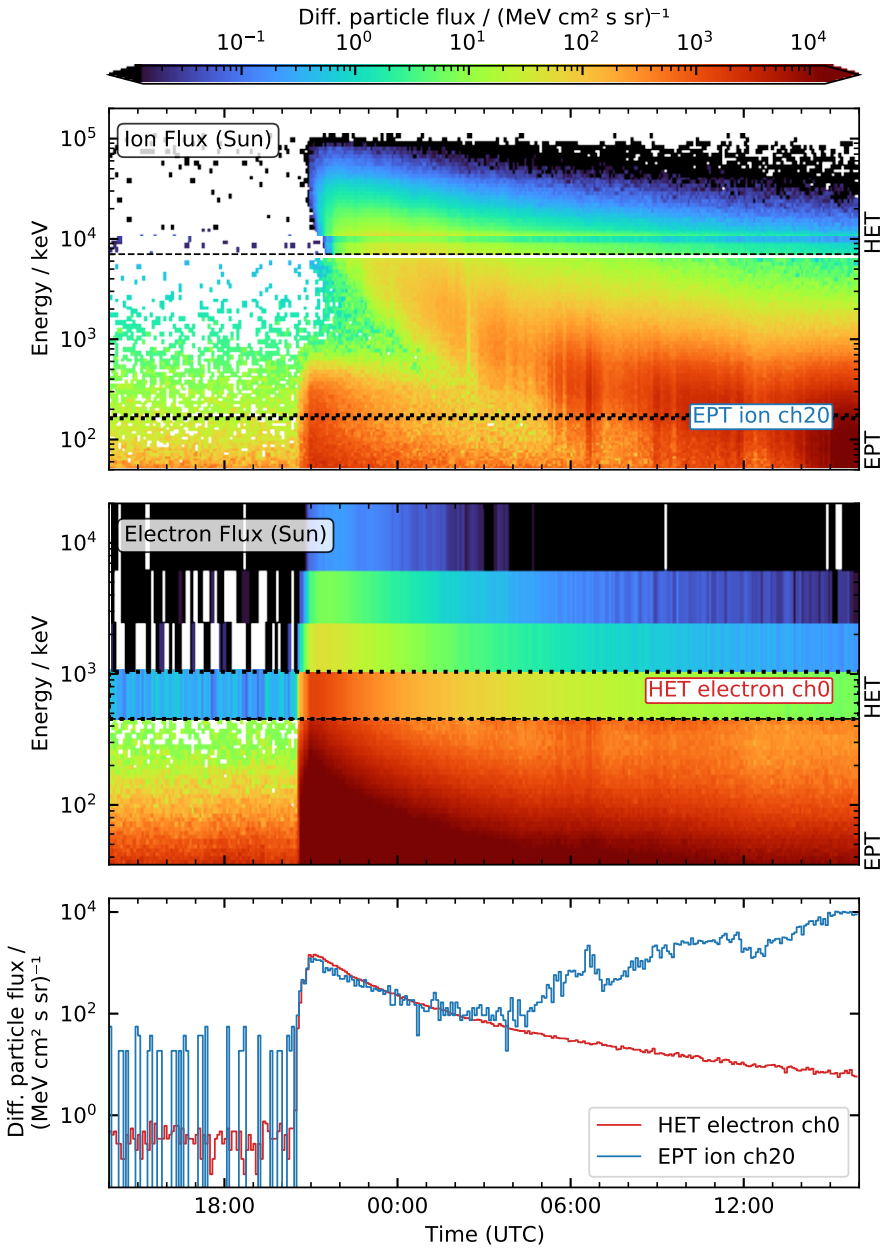

Figure 5.6: Electron and ion fluxes observed by EPT and HET during an SEP event on 2023-02-24. The top panel shows the dynamic ion spectrum measured by EPT and HET. The second panel shows a dynamic electron spectrum measured by the two sensors. The bottom panel compares the first HET electron channel (ch 0: 453 – 1038 keV) with one EPT ion channel (ch 20: 163 – 174 keV).

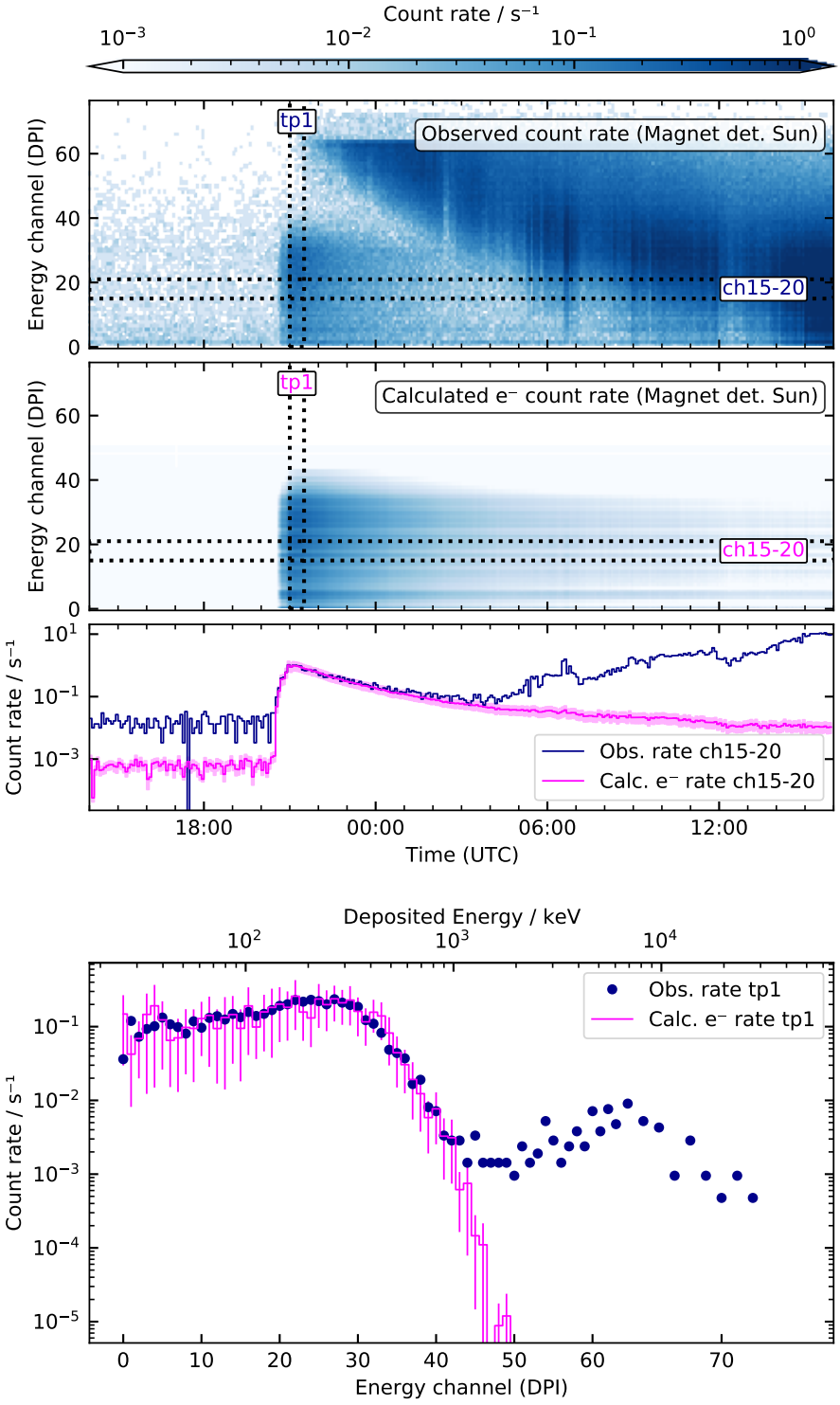

Figure 5.7: Comparison of the measured count rates and calculated electron count rates in the EPT sunward looking magnet detector (NO_EPT_mag_S) for an SEP event observed on 2023-02-24. From top to bottom the panels show the measured count rate in a dynamic spectrum, the calculated electron count rate in a dynamic spectrum, the calculated and measured count rates summed over five energy channels (channel 15 to 20) as a time profile and the calculated and measured count rate spectra averaged over a 30 minute time period (tp1). The energy channels used in the time profiles as well as the time range used for the spectra are highlighted in the dynamic spectra.

Part III

OBSERVATIONS OF SOLAR ENERGETIC PARTICLES

6

WIDESPREAD SEP EVENTS

In the endeavour to understand solar energetic particle events, so-called widespread SEP events pose a particular challenge. In widespread events, particles spread over large parts of the inner heliosphere. Occasionally, energetic particles of a single event can be observed around the entire Sun (see e.g. Gómez-Herrero et al., 2015). The observations of such events raise a fundamental question – How do SEPs manage to spread over such a wide space?

Frequently discussed explanations include extended particle sources such as CME-driven shocks (Cliver et al., 1995), an effective particle transport in the corona (Reinhard et al., 1974) and interplanetary particle transport perpendicular to the magnetic field (Wibberenz et al., 2006; Dröge et al., 2010). Unfortunately, it can be quite difficult to attribute certain SEP characteristics observed in situ to either specific properties of the source or to a particular transport process. In some cases multiple event scenarios with various source and transport processes are proposed as explanations for the same in situ observations (for example in Gómez-Herrero et al., 2015 and Prise et al., 2014).

However, with a larger number of observers, it is possible to place additional constraints on many event scenarios. For example, the arrival times of the SEPs at different locations in the heliosphere can be analysed and their delays can be used, e.g. to constrain the duration of the interplanetary transport or the source expansion.

The first widespread SEP event observed by Solar Orbiter on 20 November 2020 offers a great opportunity to study an event that filled almost the entire inner heliosphere with SEPs which were observed by four different spacecraft. In a corresponding event study (included in the following section), the in situ SEP observations of these four spacecraft are compared with remote sensing observations of the solar source. Particular attention is given to anisotropies in the particle fluxes and to the timing of electrons and protons.

Although the study does not reach a clear conclusion about the cause of the wide spread of SEPs in this particular event, it presents different interpretations of the observations and discusses two extreme scenarios.

In the first scenario, it is considered that particles are accelerated and released by a single expanding source, i.e. a shock wave, that causes the wide particle spread. This scenario seems likely, as both an EUV wave and a CME were observed during the event. The observed EUV wave expanded far around the Sun and, assuming that it tracks the front of a shock wave, its spatial extent could explain the wide spread

of SEPs. However, in this particular event, no clear correlation was found between the arrival time of the EUV wave and the injection of SEPs at the magnetic footpoints of the four spacecraft at the Sun. Possible explanations for the poor correlation between the EUV wave and injection times are discussed in the paper. In a later study of the same event, Kouloumvakos et al. (2022) calculated the kinetics of the shock in the upper corona using a 3D model. They concluded that the shock wave likely plays a crucial role in the spread of the SEPs in this event.

In the second scenario, efficient cross-field transport of particles is discussed as the dominant process leading to the broad particle spread. The different onset times of electrons and protons observed at all four spacecraft might well be compatible with such a scenario when different diffusion speeds for electrons and protons are considered. Here, observations of large anisotropies pose strong constraints on the location where the spreading occurs, placing it close to the Sun rather than in the interplanetary medium.

Ultimately, the study emphasises how valuable the additional SEP observations from Solar Orbiter are and what constraints may be set for different scenarios that try to explain widespread SEP events.

A&A 656, A20 (2021)
https://doi.org/10.1051/0004-6361/202140937

Astronomy & Astrophysics
Special issue

Solar Orbiter First Results (Cruise Phase)

The first widespread solar energetic particle event observed by Solar Orbiter on 2020 November 29

A. Kollhoff[1], A. Kouloumvakos[2], D. Lario[3], N. Dresing[4], R. Gómez-Herrero[5], L. Rodríguez-García[5], O. E. Malandraki[6], I. G. Richardson[3,7], A. Posner[8], K.-L. Klein[9], D. Pacheco[1], A. Klassen[1], B. Heber[1], C. M. S. Cohen[10], T. Laitinen[11], I. Cernuda[5], S. Dalla[11], F. Espinosa Lara[5], R. Vainio[4], M. Köberle[1], R. Kühl[1], Z. G. Xu[1], L. Berger[1], S. Eldrum[1], M. Brüdern[1], M. Laurenza[12], E. J. Kilpua[13], A. Aran[14], A. P. Rouillard[2], R. Bučík[15], N. Wijsen[16], J. Pomoell[13], R. F. Wimmer-Schweingruber[1], C. Martin[1], S. I. Böttcher[1], J. L. Freiherr von Forstner[1], J.-C. Terasa[1], S. Boden[1], S. R. Kulkarni[1], A. Ravanbakhsh[1], M. Yedla[1], N. Janitzek[17], J. Rodríguez-Pacheco[5], M. Prieto Mateo[5], S. Sánchez Prieto[5], P. Parra Espada[5], O. Rodríguez Polo[5], A. Martínez Hellín[5], F. Carcaboso[5], G. M. Mason[18], G. C. Ho[18], R. C. Allen[18], G. Bruce Andrews[18], C. E. Schlemm[18], H. Seifert[18], K. Tyagi[18], W. J. Lees[18], J. Hayes[18], S. D. Bale[19], V. Krupar[20,3], T. S. Horbury[21], V. Angelini[21], V. Evans[21], H. O'Brien[21], M. Maksimovic[9], Yu. V. Khotyaintsev[22], A. Vecchio[23], K. Steinvall[22,24], and E. Asvestari[13]

(Affiliations can be found after the references)

Received 30 March 2021 / Accepted 24 May 2021

ABSTRACT

Context. On 2020 November 29, the first widespread solar energetic particle (SEP) event of solar cycle 25 was observed at four widely separated locations in the inner ($\lesssim$1 AU) heliosphere. Relativistic electrons as well as protons with energies >50 MeV were observed by Solar Orbiter (SolO), Parker Solar Probe, the Solar Terrestrial Relations Observatory (STEREO)-A and multiple near-Earth spacecraft. The SEP event was associated with an M4.4 class X-ray flare and accompanied by a coronal mass ejection and an extreme ultraviolet (EUV) wave as well as a type II radio burst and multiple type III radio bursts.

Aims. We present multi-spacecraft particle observations and place them in context with source observations from remote sensing instruments and discuss how such observations may further our understanding of particle acceleration and transport in this widespread event.

Methods. Velocity dispersion analysis (VDA) and time shift analysis (TSA) were used to infer the particle release times at the Sun. Solar wind plasma and magnetic field measurements were examined to identify structures that influence the properties of the energetic particles such as their intensity. Pitch angle distributions and first-order anisotropies were analyzed in order to characterize the particle propagation in the interplanetary medium.

Results. We find that during the 2020 November 29 SEP event, particles spread over more than 230° in longitude close to 1 AU. The particle onset delays observed at the different spacecraft are larger as the flare–footpoint angle increases and are consistent with those from previous STEREO observations. Comparing the timing when the EUV wave intersects the estimated magnetic footpoints of each spacecraft with particle release times from TSA and VDA, we conclude that a simple scenario where the particle release is only determined by the EUV wave propagation is unlikely for this event. Observations of anisotropic particle distributions at SolO, Wind, and STEREO-A do not rule out that particles are injected over a wide longitudinal range close to the Sun. However, the low values of the first-order anisotropy observed by near-Earth spacecraft suggest that diffusive propagation processes are likely involved.

Key words. Sun: particle emission – Sun: heliosphere – Sun: coronal mass ejections (CMEs) – Sun: flares – interplanetary medium

1. Introduction

Solar energetic particle (SEP) events observed by widely separated spacecraft have led to fundamental questions about the underlying processes responsible for the wide spread of energetic particles in the heliosphere. During the Solar Terrestrial Relations Observatory (STEREO) era, different possible explanations for this wide extent of SEPs had been considered (e.g., Rouillard et al. 2012; Gómez-Herrero et al. 2015; Lario et al. 2014, 2017; Zhang et al. 2021, and references therein). The possibility of extended particle sources was discussed even earlier. For example, Cliver et al. (1995) and Torsti et al. (1999) proposed that coronal and interplanetary shocks driven by coronal mass ejections (CMEs) could accelerate and inject particles over large regions in the heliosphere (also see Kouloumvakos et al. 2019). Transport processes are another candidate suggesting that particles originating from even a narrow source could propagate to distant heliolongitude either in the corona or in interplanetary space (e.g., Reinhard & Wibberenz 1974; Jokipii 1966). Differences in solar wind conditions can produce variations in particle onset delays and intensity–time profiles observed even between locations with small longitudinal separations (e.g., Klassen et al. 2016; Pacheco et al. 2017). Turbulence-induced particle diffusion perpendicular to the magnetic field within the interplanetary medium has been discussed by, for example, Wibberenz & Cane (2006) and Zhang et al. (2009) and has been supported by multiple modeling efforts (e.g., Dröge et al. 2010; Wang et al. 2012). It has also been shown that the magnetic field line meandering associated with turbulence can give rise to efficient non-diffusive propagation across the average magnetic field

(Laitinen et al. 2016). Other possible phenomena that may help particle propagation across the field include guiding center drifts (Marsh et al. 2013; Dalla et al. 2013; Wijsen et al. 2020) and propagation along the heliospheric current sheet (Battarbee et al. 2018).

As examples of studies of such widespread events Dresing et al. (2012) concluded, for a widespread SEP event observed on 2010 January 17, that large delays of the observed particle onsets and weak particle anisotropies are consequences of strong perpendicular diffusion in the interplanetary medium (Dröge et al. 2010). In contrast, the clear anisotropies observed during a widespread event on 2011 November 3 disfavor a major role for perpendicular transport in the interplanetary medium and rather suggest that particles spread quickly close to the Sun (Gómez-Herrero et al. 2015). Different delays in the observed particle onset times at different spacecraft have been attributed to either the time the shock needs to intersect with the field lines connected to the individual spacecraft (e.g., Malandraki et al. 2009; Park et al. 2013) or to the time required for interplanetary cross-field diffusion (Dröge et al. 2010).

Multi-spacecraft observations are essential for determining the properties of widespread SEP events. In particular, the STEREO mission with its two spacecraft, equipped with both in situ particle instruments and remote sensing instruments, has made major contributions to understanding these events. With the new era of spacecraft, including Parker Solar Probe (PSP, Fox et al. 2016) and Solar Orbiter (SolO, Müller et al. 2020), we have a great opportunity to clarify the processes leading to the broad particle spread.

In this paper, we illustrate the potential of these new spacecraft by combining observations from SolO, PSP, STEREO-A and multiple near-Earth spacecraft of the first widespread SEP event of solar cycle 25. For the first time, it is possible to compare and combine energetic particle observations from four different locations $\lesssim$1 AU with a wide longitudinal separation.

In Sect. 2, we introduce the different instruments and data sets used in this study. Section 3 provides an overview of the particle observations at the different locations while detailed descriptions of in situ and remote sensing observations are given in Sect. 4. Analysis of the SEP onsets are presented in Sect. 5 together with anisotropy studies. Finally we summarize and discuss the observations in the context of two extreme scenarios in Sect. 6.

2. Instrumentation

This study uses data from instruments on board SolO, PSP, STEREO-A, SOlar and Heliospheric Observatory (SOHO), Global Geospace Science Wind satellite (Wind), and Advanced Composition Explorer (ACE) as well as measurements from Earth-based instruments and simulation data. Below we provide a succinct summary of the main data sets used here.

SolO: We utilize energetic particle measurements from the Energetic Particle Detector (EPD, Rodríguez-Pacheco et al. 2020) Supra Thermal Electron and Proton (STEP) instrument, Electron Proton Telescope (EPT), and High Energy Telescope (HET) for electrons in the energy range from a few keV to a few MeV and ion measurements obtained from the STEP, EPT, and HET from a few keV to above 100 MeV nucleon^{-1}. While the majority of EPD's data products perform as expected, there are still some unsettled calibration issues. A more detailed description of the instrument performance is given in Wimmer-Schweingruber et al. (2021). For this study we mostly avoided the use of data products with pending calibration issues. An exception are the differential electron and proton fluxes from HET which are only used for the determination of onset times and the evaluation of electron anisotropies.

Differential ion fluxes from STEP and EPT were calculated by applying proton geometry factors and are labeled as proton fluxes in this work. However, both instruments do not directly distinguish between different ion species (Rodríguez-Pacheco et al. 2020). We note that STEP electron measurements can have large uncertainties if increased ion fluxes were observed in the same energy range at the same time. EPT electron measurements are known to be affected by ions with energies above 400 keV (the possible contribution of ions is well known from similar instruments such as STEREO/SEPT (see Wraase et al. 2018) or ACE/EPAM (Marhavilas et al. 2015).

Magnetic field measurements were obtained from the Solar Orbiter magnetometer (MAG, Horbury et al. 2020). Unfortunately, the Solar Wind Analyser (SWA, Owen et al. 2020) on board SolO was not operational during the event. Instead, solar wind speed and plasma density were obtained by using measurements from the Radio and Plasma Waves (RPW, Maksimovic et al. 2020) instrument. We obtained the electron density (n_e) from the probe-to-spacecraft potential (V_{PSP}) measured by RPW. As the spacecraft floating potential is reached when the total current to the spacecraft is zero, that is when the photo-electron emission from the spacecraft is balanced by the plasma electron current, we derived an approximate dependence of n_e on V_{PSP}. Then, we calibrated the electron density by using the electron plasma frequency derived from the high-frequency electric field spectrum (for more details see Khotyaintsev et al. 2021). In order to estimate the SW speed, we applied the deHoffmann–Teller (HT) analysis (Khrabrov & Sonnerup 1998) to electric and magnetic field data. The method used is described in detail in Steinvall et al. (2021) and is summarized here. The goal of HT analysis is to find the velocity (relative to the spacecraft) of the frame in which the electric field is zero. In the solar wind, where magnetic fluctuations due to current sheets and magnetohydrodynamic (MHD) turbulence are abundant, the HT velocity $\boldsymbol{v}_{HT}$ is a good estimate of the solar wind velocity. We obtained a series of radial solar wind speeds by repeatedly applying the HT analysis on one-hour intervals of the electric field $\boldsymbol{E}$ and magnetic field $\boldsymbol{B}$ data, moving the centre of the interval in 10-min steps, keeping velocities where $-(\boldsymbol{v}_{HT} \times \boldsymbol{B})_y$ was in good agreement with E_y. Finally, we averaged the velocities over six-hour intervals to reduce noise.

L1-Missions: We utilize particle observations from the Electron Proton Helium INstrument (EPHIN, Müller-Mellin et al. 1995) and from the High Energy Detector (HED) of the Energetic and Relativistic Nuclei and Electron experiment (ERNE, Torsti et al. 1995) on board the SOHO, 3D Plasma and Energetic Particle Investigation (3DP, Lin et al. 1995) on board Wind, and Electron Proton Alpha Monitor (EPAM, Gold et al. 1998) on board ACE. Solar wind plasma and magnetic field observations were taken from the Solar Wind Experiment (SWE, Ogilvie et al. 1995) and Magnetic Field Investigation (MFI, Lepping et al. 1995) on board Wind. Furthermore, we used coronagraph images from the Large Angle and Spectrometric Coronagraph (LASCO)-C2 on board SOHO. While in-depth reviews of the proton and helium fluxes measured by SOHO/EPHIN have been performed in recent years (e.g., Kühl & Heber 2019), the electron measurements are yet to be optimized in the same manner. In particular, the complex energy-dependent response of the electron channels and the resulting spectral shape dependency of the applied response factor has to be taken into account in order to provide an absolute flux

number. While this issue is shared with all instruments performing electron measurements in this energy range, it is unfortunately often neglected. To avoid feigning an uncertainty which is yet to be quantified, we preferred to present count rates rather than physical flux numbers. The onset determination of the EPHIN electrons performed in this paper is not affected by this.

STEREO-A: We use particle measurements from the HET (von Rosenvinge et al. 2008), the Solar Electron Proton Telescope (SEPT, Müller-Mellin et al. 2008), and the Suprathermal Electron Telescope (STE, Lin et al. 2008), radio observations from the Radio and Plasma Wave Investigation on the STEREO Mission (SWAVES, Bougeret et al. 2008), EUV images from the Sun Earth Connection Coronal and Heliospheric Investigation (SECCHI) – The Extreme-Ultraviolet-Imager (EUVI) as well as coronagraph images from SECCHI – The Coronagraph COR2 (COR2; Howard et al. 2008). As for EPT, SEPT ion fluxes are calculated by applying proton geometry factors and are labeled as proton fluxes here. We note that SEPT electron measurements are affected by ions with energies above 400 keV (Wraase et al. 2018). Magnetic field and solar wind plasma measurements were obtained from the Magnetic Field Experiment (MAG) and the Plasma and Suprathermal Ion Composition experiment (PLASTIC, Galvin et al. 2008). We note that for this study we use preliminary level 2 data from PLASTIC as no further evaluated data was available for the time period considered here.

PSP: Particle observations by PSP were provided by the Integrated Science Investigation of the Sun (IS⊙IS, McComas et al. 2016). IS⊙IS is made up of two Energetic Particle Instruments (EPI), covering the low (EPI-Lo) and high (EPI-Hi) portions of the energetic particle distribution. EPI-Hi is further comprised of three telescopes: two Low Energy Telescopes (one double ended with apertures labeled LETA and LETB, the other single ended and labeled LETC) and a double ended High Energy Telescope (with apertures called HETA and HETB). The data shown in Fig. 1 are from EPI-Lo and HET (averaged over HETA and HETB). It should be noted that complete calibration of the instruments' responses to electrons have not been completed, so currently only count rates are available.

Ground-based and Earth orbit observations: We use radio observations from the Compound Astronomical Lowcost Low-frequency Instrument for Spectroscopy and Transportable Observatory (CALLISTO) instruments in Glasgow, Heiterswil (Switzerland) and Trieste in the 45–81 MHz range (Benz et al. 2005) and from the Observations Radio pour Fedome et l'Etude des Eruptions Solaires (ORFEES) in Nançay in the range 144–1000 MHz. In addition, we utilize images from the Solar Ultraviolet Imager (SUVI, Vasudevan et al. 2019) of the Geostationary Operational Environmental Satellite (GOES) and Atmospheric Imaging Assembly (AIA, Lemen et al. 2011) on board the Solar Dynamics Observatory (SDO).

Solar Wind Simulations: We use the Wang–Sheeley–Arge (WSA)-ENLIL+Cone model (ENLIL model, Odstrčil et al. 1996; Arge & Pizzo 2000; Odstrcil 2003; Arge et al. 2004) to model the changing solar wind conditions at the time of the SEP event, including propagation of the associated CME, and to derive the interplanetary magnetic field (IMF lines as an alternative to using nominal Parker spiral field lines. This is a global 3D MHD model[1] that generates a time-dependent background characterization of the heliosphere outside of 21.5 $R_\odot$. The simulation uses a time-dependent sequence of daily-updated Global Oscillations Network Group (GONG) magnetograms as a base,

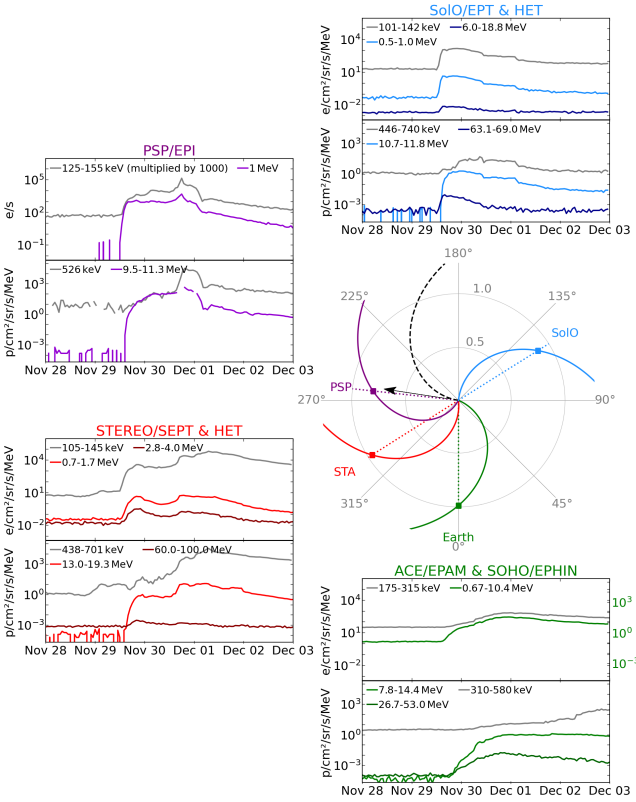

Fig. 1. Overview of the 2020 November 29 SEP event: *middle right panel* shows the orbital locations of PSP (magenta point), SolO (blue point), STEREO-A (red point), and near-Earth spacecraft (green point) as seen from the north ecliptic. Nominal interplanetary magnetic field (IMF) lines connecting each spacecraft with the Sun considering the solar wind speeds listed in Table 1 are shown in corresponding colors. The black arrow indicates the location of the active region associated with the event (E98 seen from the Earth). Surrounding panels illustrate hourly-averaged proton fluxes (*lower panels*) and electron fluxes (*upper panels*) observed by the different spacecraft.

into which high density structures are injected to model solar wind disturbances. We use the graduated cylindrical shell (GCS) model (Thernisien et al. 2006; Thernisien 2011) to reconstruct the CMEs injected in the ENLIL model (see details in Nieves-Chinchilla et al., in prep.). As well as modeling the heliospheric structure, ENLIL provides the magnetic footpoints and the IMF lines passing through the different spacecraft, so the magnetic field lines length can be estimated. The data derived from the modeled IMF lines at the SEP onset time is summarized in Table 1. The input parameters and results of the model are available on the Community Coordinated Modeling Center (CCMC) website[2].

3. Energetic particle increase on 2020 November 29

Figure 1 shows an overview of the particle observations from 2020 November 28 to 2020 December 3 collected by SolO (top right panel), PSP (top left panel), STEREO-A (bottom left panel), and by near-Earth spacecraft (bottom right panel). Each panel shows intensity–time profiles of electrons (upper portion of the panels) and protons (lower portion of the panels) as observed by the EPI-Lo (gray) and EPI-Hi (magenta)

[1] https://ccmc.gsfc.nasa.gov/models/modelinfo.php?model=ENLIL%20with%20Cone%20Model

[2] https://ccmc.gsfc.nasa.gov/database_SH/Laura_Rodriguez-Garcia_031321_SH_1.php

Table 1. Spacecraft locations, magnetic field footpoints, IMF path length (L) and longitudinal separation (ΔLon.) from the flare location (HGC: 249° longitude; −23° latitude).

Location [a]				Magnetic field footpoints [a]								
				Parker spiral					ENLIL [b]			
Spacecraft/Body	r (AU)	Lon.	Lat.	Vsw(km s^{-1})	Lon.	Lat.	ΔLon.	L(AU)	Lon.	Lat.	ΔLon.	L(AU)
STEREO-A	0.96	290°	7°	361	355°	7°	106°	1.15	344°	6°	95°	1.16
Earth	0.99	348°	1°	358	55°	1°	166°	1.18	44°	1°	155°	1.24
PSP	0.81	251°	4°	295 [b]	319°	4°	69°	0.98	298°	4°	49°	0.94
Solar orbiter	0.88	110°	−5°	417 [b]	162°	−5°	−88°	1.0	145°	−6°	−104°	0.94

Notes. [a]Coordinates are given in the Carrington Heliographic (HGC) system. [b]ENLIL values are taken from simulation on 29/11/2020 at 13:00 UT. Path length calculated for ENLIL magnetic field lines assume a radial extension from 21.5 $R_\odot$ to 1 $R_\odot$.

detectors of IS⊙IS on board PSP, the EPT (gray) and HET (blue) on board SolO, the SEPT (gray) and HET (red) on board STEREO-A, EPAM (gray) on board ACE, and Electron Proton Helium INstrument (EPHIN) (green) on board SOHO.

The view of the ecliptic plane from solar north (middle right panel of Fig. 1) illustrates the spacecraft locations on November 29 at 13:00 UT close to the time when the onset of the large SEP event was observed. These spacecraft covered a longitude span of ∼238° and clearly observed intensity increases of protons at energies >50 MeV and electrons at energies >1 MeV.

In the middle right panel, we also show nominal Parker spiral IMF lines connecting each spacecraft with the Sun. These lines are calculated using the one hour averaged solar wind speed measured near the event onset time by the STEREO/PLASTIC and the WIND/SWE. Because PSP solar wind data are not available at the time of writing, and the solar wind analyzer on SolO/SWA was not operational, speeds obtained from ENLIL simulation are used instead.

The SEP event was associated with an M4.4 soft X-ray flare that occurred at NOAA active region (AR) 12790, located just behind the east limb as seen from Earth. The flare started at 12:34 UT and peaked at 13:11 UT. STEREO-A/EUVI images at 13:00 UT show that the flare was located at E98S23 (in Stonyhurst Heliographic (HGS) coordinates). The black arrow in the middle right panel of Fig. 1 indicates the longitudinal location of this solar flare. The locations of the different spacecraft and their magnetic footpoints as well as the longitudinal separations between the footpoints and the flare location are given in Table 1. Additionally, as further discussed in Sect. 4.2, the SEP event was associated with the eruption of a fast and relatively wide CME, an EUV-wave expanding in the low corona, and a white-light shock wave observed higher in the corona seen by STEREO-A/COR2 and SOHO/LASCO-C2.

4. Observations

4.1. In situ observations

Figure 2 shows, from top to bottom, near-relativistic electron intensities, ion intensities, magnetic field magnitude, magnetic field elevation and azimuth angles in the spacecraft centered Radial-Tangential-Normal (RTN) coordinate system, and the solar wind proton speed and density as measured by, from left to right, SolO, STEREO-A, and near-Earth spacecraft at L1.

The electron and high-energy (≳12 MeV) proton intensity profiles at SolO show a rapid rise shortly after the parent solar eruption (indicated by the vertical arrow in the top panels of Fig. 2) followed by a gradual decay. Such intensity–time profiles are typical of SEP events that originate from western longitudes relative to the observing spacecraft (Cane et al. 1988). At about ∼11 UT on November 30, electron and ≳500 keV ion intensities drop abruptly in association with the passage of an enhanced magnetic field structure. This structure is most likely a corotating interaction region (CIR) formed by the interaction of a faster solar wind stream with the preceding slower solar wind (indicated by CIR in the third panel of the left column in Fig. 2). Unfortunately, the limited Radio and Plasma Waves (RPW) data cannot confirm the expected transition in solar wind speed at SolO, but this was evident when the same CIR passed Earth on November 21 (not shown here). The abrupt changes in the particle intensities occur in the vicinity of magnetic field sector boundary crossings and the stream interface (indicated by the first dashed vertical line in the left panels of Fig. 2 coinciding with a drop in the solar wind density within the CIR). The ion intensities at even lower energies (≲500 keV) either plateau at their maximum intensities or keep increasing after the passage of this CIR structure. Such a low-energy ion intensity enhancement suggests that either the CIR affected the transport of low-energy SEPs injected at the time of the solar eruption or that these low-energy ions were locally accelerated in the CIR.

Another abrupt change in the particle intensities at SolO occurs early on December 1 (second dashed vertical line in the left panels of Fig. 2) when intensities decrease, except for the lowest energy (≲20 keV) protons, which show a large increase. This intensity change also appears to be associated with an abrupt plasma density decrease, but the absence of a magnetic field enhancement makes it unclear whether this was also a stream interface within a CIR. However, the limited speed estimates from RPW on December 2 appear to be consistent with the presence of a higher speed stream following a CIR. The lower energy ions were sufficiently intense that they contaminated the electron observations made by SolO/STEP during the periods indicated by the gray traces on the top left panel of Fig. 2.

Another point to note is the presence of multiple sector boundary crossings for around a day ahead of the CIR on November 30, including during the early stages of the SEP event, indicating that SolO was close to the heliospheric plasma sheet at this time, with possible implications for SEP transport. Thus, the SolO observations suggest that the arrival of energetic particles at the spacecraft depends on the region where they are accelerated and the influence of solar wind structures on their transport in the inner heliosphere, and that both of these factors depend on the energy of the particles (e.g., Wijsen et al. 2021).

Particle intensities at STEREO-A (center column of Fig. 2) also increase shortly after the occurrence of the solar eruption

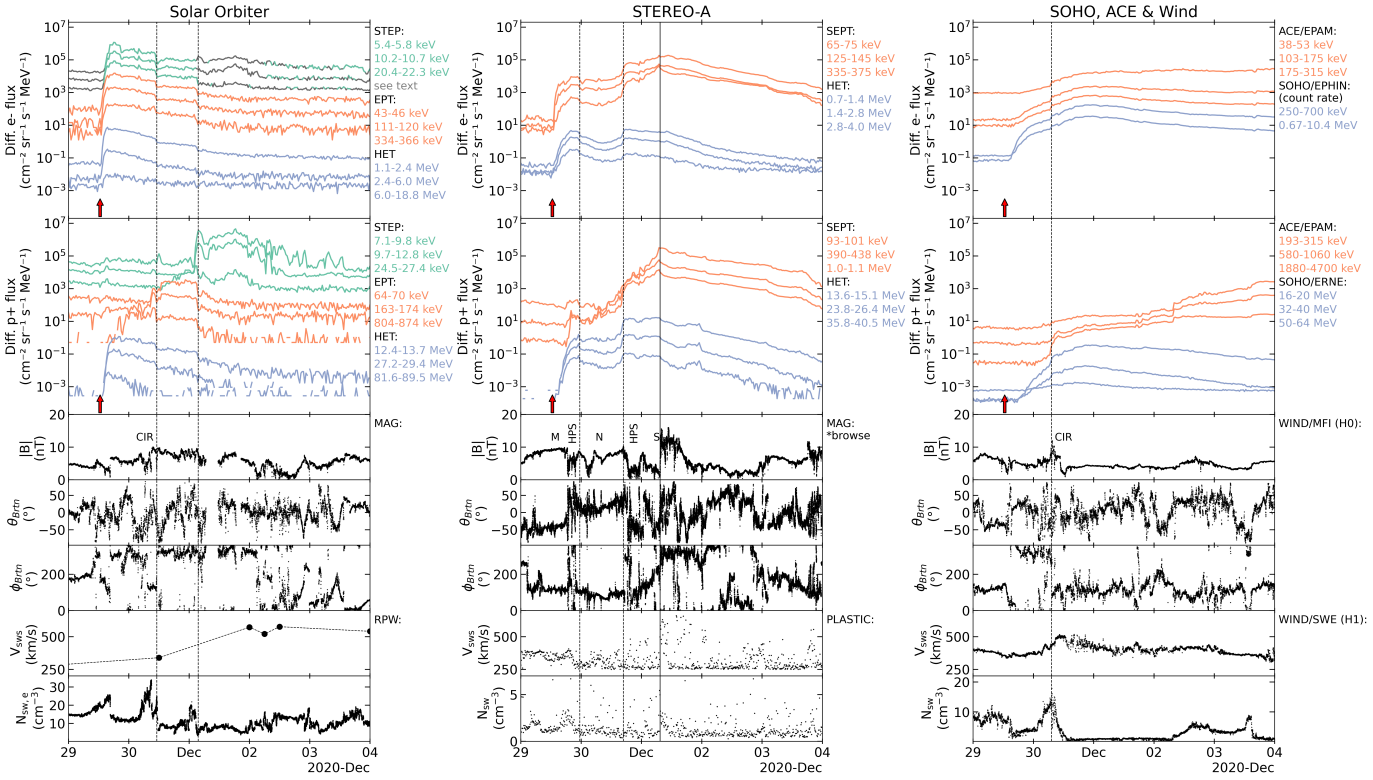

Fig. 2. Time profiles of in situ observations from SolO (*left panel*), STEREO-A (*central panel*), and SOHO, ACE at L1 (*right panel*). Shown *from top to bottom* are electron fluxes at multiple energies, proton fluxes at multiple energies, magnetic field magnitude, elevation and azimuth angles of the magnetic field vector in RTN coordinates, solar wind speed, and solar wind density. Vertical dashed lines indicate times of abrupt changes in particle intensity. The solid line at STEREO-A indicates passage of a probable shock. Gray lines in the STEP data indicate time periods without clear electron measurements and should be interpreted as an upper limit for the electron flux.

and decay more slowly, but their profiles are more irregular than at SolO. The onset of the event occurs just before the trailing edge of an enhanced, inward-polarity magnetic field structure indicated by "M"; note also that the low-energy ($\lesssim$2 MeV) ion intensities are already elevated prior to the event onset. Uncertainty in the STEREO-A/PLASTIC preliminary solar wind plasma data used in this figure does not allow a complete characterization of structure M, but the observation of a similar structure by PSP on November 27 and at L1 on December 4 (not shown here) suggests that this was a corotating structure. Intervals of depressed magnetic field intensity including multiple sector boundaries that are likely to be encounters with the heliospheric plasma sheet (HPS) are also prominent features of the solar wind at STEREO-A during the SEP event.

After several magnetic field sector boundary crossings (first dashed line in the center column in Fig. 2), the electron and high-energy ($\gtrsim$13 MeV) proton intensities decrease during the passage of a region of predominantly enhanced ($\sim$10 nT) magnetic field with a northward orientation, indicated by "N" in the middle column of Fig. 2. The second vertical dashed line in the center column of Fig. 2 indicates the end of this structure and re-entry into the HPS. The intensities of both electrons and protons at all energies abruptly increase at this time, consistent with a spatial modulation due to the local solar wind structure. The low-energy ($\lesssim$4 MeV) ion intensities peak with the arrival of a probable interplanetary shock (to be confirmed when the final plasma data become available) at 07:25 UT on December 1 that presumably was driven by the halo CME on 29 November (the average shock transit speed from the Sun to STEREO-A is $\sim$930 km s^{-1}). Thus, the STEREO-A observations also show the clear influence of local solar wind structures on the SEP intensities.

Particle intensities observed by near-Earth spacecraft (right panel in Fig. 2) show a more gradual increase with an onset that is substantially delayed with respect to the other spacecraft (see Sect. 5.1). Similar to the rising phase of the event at SolO, a CIR (indicated by "CIR") ahead of a modest high-speed stream affects the intensity profiles. In particular, an abrupt intensity increase during the rising phase of the SEP event is associated with the passage of a true sector boundary crossing (indicated by the vertical dashed line in the right column of Fig. 2), as verified by a reversal of Wind 3DP suprathermal electron flow relative to the magnetic field direction (not shown here). A further abrupt increase in the low energy proton intensity on December 2 is associated with an increase in density that may indicate the trailing edge of the stream.

Thus, Fig. 2 shows that the SEP intensity–time profiles observed by SolO, STEREO-A, and near-Earth spacecraft were also affected by the passage of local solar wind structures. In most cases, these appear to be corotating features but their possible observation by the different spacecraft, and potential influence of transient structures, requires further analyses of the solar wind data and modeling of these structures in the inner heliosphere.

The SEP intensity-profiles observed at PSP (top left panel Fig. 1) are studied in detail by Cohen et al. (2021). Although there appears to be a small shock and possibly an ICME observed by PSP prior to the Nov 29 event (due to the slower CME launched late on November 26), there is no corresponding SEP signature. The 10 MeV proton intensity and 1 MeV electron

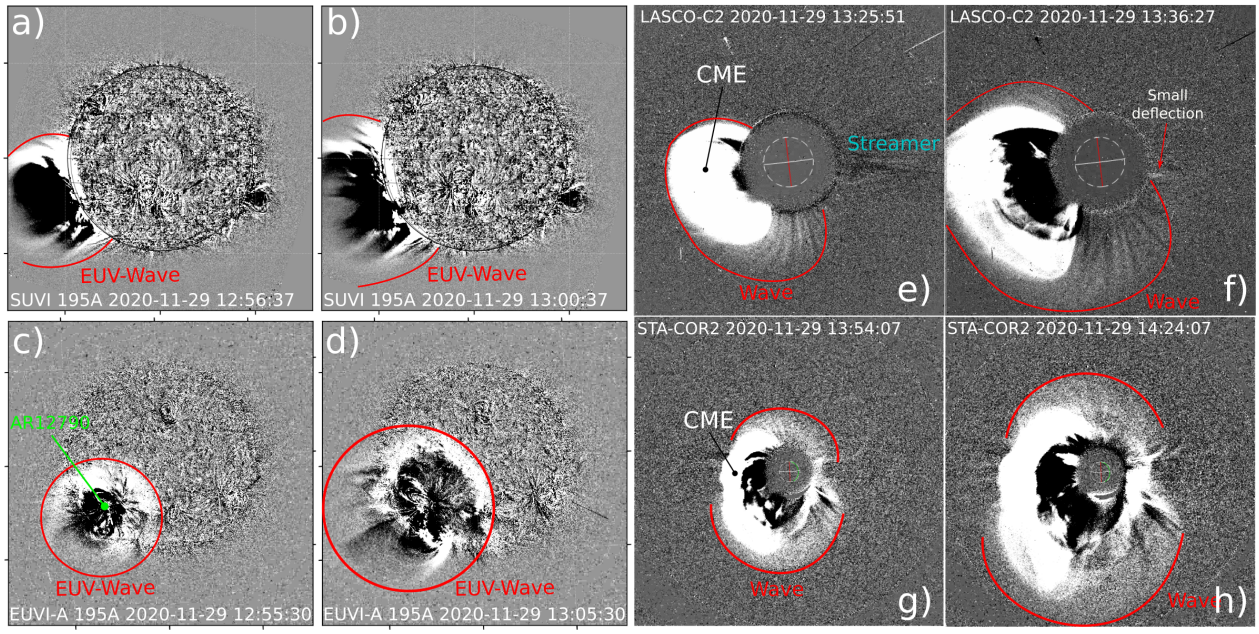

Fig. 3. Remote sensing observations of the EUV wave, the CME, and the white-light shock wave from two different viewpoints. *Panels a–d*: EUV running-difference images recorded nearly simultaneously from SUVI (*a and b*) and STEREO-A EUVI (*c and d*) at 195 Å during the early stages of the EUV wave expansion in the low corona. The EUV wave front is labeled and outlined with the red lines. *Panels e–h*: running-difference images in white-light from SOHO/LASCO-C2 (*e and f*) and STEREO-A/COR2 (*g and h*). The CME is labeled and the white-light shock wave is labeled and outlined with red lines.

count rate rise fairly quickly after the type III radio burst associated with the M4.4 solar flare at ~13:11 UT on November 29, while the 0.5 MeV protons and 150 keV electrons show a more gradual increase. The region around the shock (which arrives at PSP on November 30, 18:35 UT) is sufficiently turbulent that the 0.5 MeV protons are well confined and strongly peak at the time of the shock passage. Surprisingly, the peak in the electron count rates (for the two energy channels shown in Fig. 1) is coincident with the shock arrival. It is unlikely that these are locally accelerated by the shock; possibly, they are a trapped population due to the narrowing region between the two ICMEs. After the passage of the shock and sheath region, the SEP intensity drops dramatically as PSP enters the ICME, as is often seen in magnetic clouds (see details in Cohen et al. 2021).

4.2. Remote sensing observations

Previous studies (see, e.g., Park et al. 2013) have proposed that widespread SEP events are associated with EUV waves propagating far from the parent active region, or by extended CME-driven shocks, which inject particles onto field lines that are poorly connected to the active region. For this event, EUV observations of the low corona show that an EUV wave was launched in connection with the solar flare from NOAA AR 12790. The EUV wave appears as a circular wave expanding away from the AR and lasting for more than one hour. During this time it covers a large distance over the visible disk as seen from STEREO-A. Figure 3 shows running-difference images of SUVI (panels a and b) and STEREO-A EUVI (panels c and d) at 195 Å taken at an early stage of the EUV wave expansion with the front of the EUV wave indicated in the images. The EUV observations show that the wave forms at ~12:47 UT, two minutes after the hard X-ray onset time from SOHO/EPHIN (see Fig. 4). We measured that the EUV wave propagates on the solar disk with an average speed of 500 km s^{-1}. North and northwest of the AR as seen from STEREO-A, the wave seems to be brighter and stronger and can be clearly traced until ~13:30 UT in SUVI images, when located near central meridian as viewed from Earth. After this time, it is difficult to trace the propagation of the wave on the visible disk.

White-light coronagraphic observations recorded a fast and relatively wide CME together with a shock wave observed as a bright front around the CME. Figure 3 shows running-difference images from SOHO/LASCO-C2 (panels e and f) and STEREO-A/COR2 (panels g and h) with the front of the shock wave indicated and CME labeled. The CME emerges above the eastern limb in the SOHO/LASCO-C2 images at ~13:26 UT. From the viewpoint of STEREO-A/COR2, it is observed as a Halo-CME. The CME first appears in the COR2 images at ~13:24 UT. The LASCO-C2 image in panel f also shows a small streamer deflection at the west limb, suggesting that the pressure wave associated with the CME probably reached very distant locations relative to the flare higher in the corona. From a 3D reconstruction of the CME and the white-light shock wave we estimate that at the radial direction the CME propagates at an average speed of ~1500 km s^{-1} while the shock wave propagates faster with a speed of around 1800 km s^{-1}. Both the CME and the white-light shock wave seem to decelerate above ~10 $R_\odot$. A detailed analysis of the CME and the associated shock wave kinematics will be presented in a subsequent study.

4.3. Radio and X-ray observations

Solar radio and X-ray emissions provide insight into particle acceleration at and near the Sun in this event. X-ray light curves and dynamic radio spectrograms are displayed in Fig. 4. The top panel shows GOES observations in the nominal wavelength band 0.1−0.8 nm (photon energies 2−12 keV). The time derivative of the soft X-ray emission during its rise phase, plotted by the red curve, is a well-known proxy of the hard X-ray emission from nonthermal electrons and was recently proposed to be a proxy of

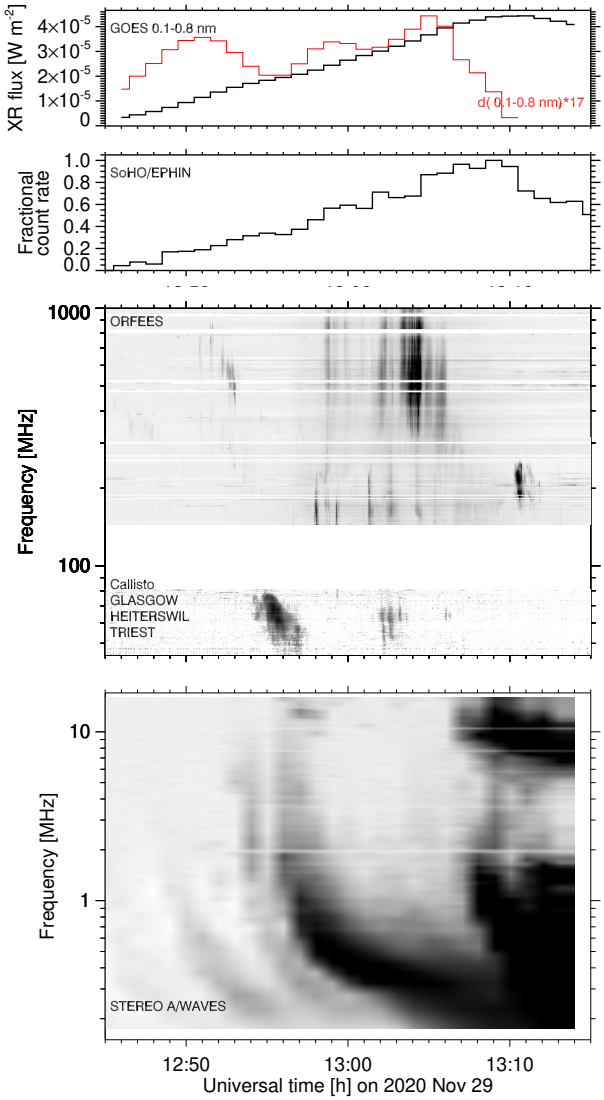

Fig. 4. Time history of the X-ray emission and dynamic spectrograms of the 2020 November 29 solar burst. *From top to bottom*: (1) time history in soft X-rays and its time derivative (red); (2) count rate time history due to hard X-rays in the SOHO/EPHIN detector; dynamic radio spectrograms in the frequency ranges (3) 144−1000 MHz, (4) 41−85 MHz, (5) 0.15−16 MHz.

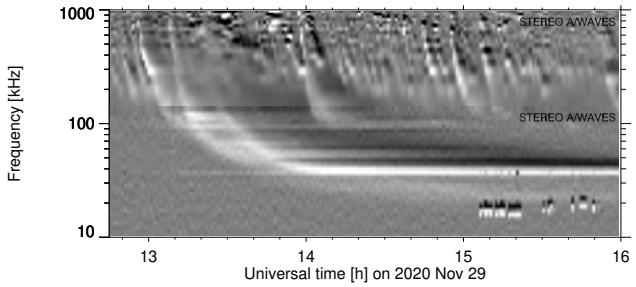

Fig. 5. Frequency-difference spectrum observed by STEREO-A in the range (0.01−1) MHz (the plotted range is ±7.5%) in the 2020 November 29 solar event.

the injection function of solar energetic electrons into the heliosphere (Steyn et al. 2020). Its time variation indicates different episodes of electron acceleration during the flare. The second panel from top shows the response to somewhat harder X-rays in the count rate of detector-A from SOHO/EPHIN, which is sensitive to photons with energies in the order of tens of keV (Kühl et al. 2020). As for the soft X-ray light curve, the rise time profile at EPHIN shows little structure, probably due to the fact that the footpoints of the hard X-ray source, which usually show time fluctuations, are occulted to observers on the Sun-Earth line in this event.

Dynamic spectra of the radio emission from the low corona (1000 MHz) to 0.13 AU (0.15 MHz) are displayed in the three bottom panels of Fig. 4. Bursts at dm-m-wavelengths (1000−45 MHz) accompany the hard X-ray emission. Three time periods can be distinguished:

Firstly, the emission between 12:51 and 12:58 UT consists of an initial faint feature between 950 and 350 MHz with evidence of two bands (central panel). The bands start to drift toward lower frequencies at 12:51:30 UT and fade near 12:53 UT. In the 81−45 MHz band (second from bottom) a type II burst is observed between 12:54 and 12:57 UT. The emission between 350 and 950 MHz is probably an early manifestation of the disturbance that later shows up as the type II burst, that is similar to a precursor as identified by Klassen et al. (1999). The type II burst continues down to 10 MHz and ends there near 12:58 UT. On its low-frequency side it is accompanied by type III bursts observed by STEREO-A (bottom panel).

Secondly, after the type II precursor the radio spectrum consists of a series of short broadband bursts between 12:57 and 13:08 UT. They start above 1000 MHz together with a new rise in the soft X-ray derivative and extend down to 45 MHz, possibly to 14 MHz. They have some spectral structure with distinct emissions above and below 300 MHz during the first minutes. These bursts differ from type III bursts in that they have a well-defined low-frequency cutoff and show no evidence of a drift toward lower frequencies or of a temporal broadening at low frequencies. They are broadband pulsations, that is, a typical fine structure of type IV bursts (see Aurass et al. 2003, and references therein).

Lastly, no later emission is detected by the spectrographs in the 1000−45 MHz band. At frequencies below 16 MHz, that is, at decameter-to-hectometer (DH) wavelengths, strong emission starts at 13:06 UT with a well-defined low-frequency edge near 5 MHz. It continues until 13:40, with a drift of the low-frequency edge toward lower frequencies, and is followed until 14 UT by a patch of radio emission at similar wavelengths but without a systematic drift. PSP observed the same spectral feature until 13:40. The drifting burst between 13:06 and 13:40 UT is a type II burst. On its low-frequency side it is accompanied by type III bursts. While they overlap in time with the initial phase of the type II burst, they start at higher frequencies above the 16 MHz limit of the STEREO/WAVES receiver.

A dynamic spectrogram at frequencies below 1 MHz is displayed in Fig. 5. It shows the relative difference between flux densities in adjacent frequencies (i.e., the difference divided by the average). White shading marks regions where the flux density increases with increasing frequency. At frequencies above 150 kHz the type III bursts related to the eruptive events are mixed with an unrelated type III storm, while at lower frequencies only type III bursts from the eruptive event are seen. Continuous type III bursts through the band are seen near 1 MHz during the dm-m-wave type II burst (12:50–12:58) and at the start of the DH type II burst (13:08) and at lower frequencies (300 kHz) near 13:20 UT. These type III bursts behave differently at low frequencies: the one accompanying the early meter-wave type II burst merges near 100 kHz with the later one that

has a steeper leading edge in the dynamic spectrogram. The low-frequency edge of the second type III burst continues down to about 20 kHz, as shown by the white halo on the low-frequency side of the type III spectrum. As it reaches 20 kHz near 15:05 UT, several intense packets of Langmuir waves are observed until 15:50 UT. They demonstrate that the spacecraft intercepts at least some of the electron beams producing the type III burst. STEREO-A is hence connected to the source region of these electron beams, launched in the corona during the DH type II burst. The travel time to 1 AU between 13:06 and 15:05 UT corresponds to an average exciter speed of $8.4 \times 10^{-2}c$ traveling 1.2 AU, which is slow (energy 2 keV), but still consistent with the energy range usually quoted for the electron beams generating Langmuir waves at 1 AU (Ergun et al. 1998). The onset of the Langmuir waves is consistent with the first arrival of electrons near 5 keV at STEREO-A (Fig. 6). The low-frequency behavior of the previous type III burst, together with the fact that Wind/WAVES does not detect this type III burst, suggests that the electron beams accelerated at the meter-wave type II shock traveled along a different path, which was not intercepted by STEREO-A. While STEREO-A detected Langmuir waves, demonstrating a magnetic connection to the source region of the electrons despite the large longitudinal distance of the nominal Parker spiral from the flare site (see Table 1), none were seen at Wind, PSP (Bale, priv. comm.) or SolO (Maksimovic, priv. comm.).

5. Analysis of SEP onsets

5.1. Timing of energetic particles and velocity dispersion analysis

In order to estimate the solar release time of the energetic particles we have performed the so-called time shift analysis (TSA) and the velocity dispersion analysis (VDA). Both methods are commonly used to identify the release time of energetic particles at the Sun (see, e.g., Krucker et al. 1999; Gómez-Herrero et al. 2021) and multiple studies (e.g., Lintunen & Vainio 2004; Saiz et al. 2005; Vainio et al. 2013; Laitinen et al. 2015) have discussed the uncertainties and limitations of these methods. We note that the VDA uncertainties assumed here are valid only under the assumption that there is negligible cross-field diffusion.

The VDA is based on the assumptions that particles with different energies are injected at the same time and that the first arriving particles travel nearly scatter-free along the same path to the observer. From the arrival times of particles with different energies both the effective path length and the common solar injection time can be derived. The two parameters are often obtained by a linear fit of the onset times plotted vs. particle velocities given in c/v. The TSA assumes that the particles propagate scatter-free along a given path length. Individual solar release times for particles with different velocities are then obtained by time shifting the arrival time to $t_{\mathrm{rel.}} = t_{\mathrm{arr.}} - L/v$.

Both methods require accurate arrival times of the first particles reaching the observer. These times are usually identified from intensity–time-profiles using different methods such as the so-called 3σ-method (see, e.g., Krucker et al. 1999), the Poisson-CUSUM method (see, e.g., Huttunen-Heikinmaa et al. 2005; Xu et al. 2020) or by simply identifying the onset by eye. Onset times determined with these methods are usually delayed compared to the actual arrival of the first particles since the measured signal has to rise above a certain background first before it becomes detectable. The delay of the onset times can

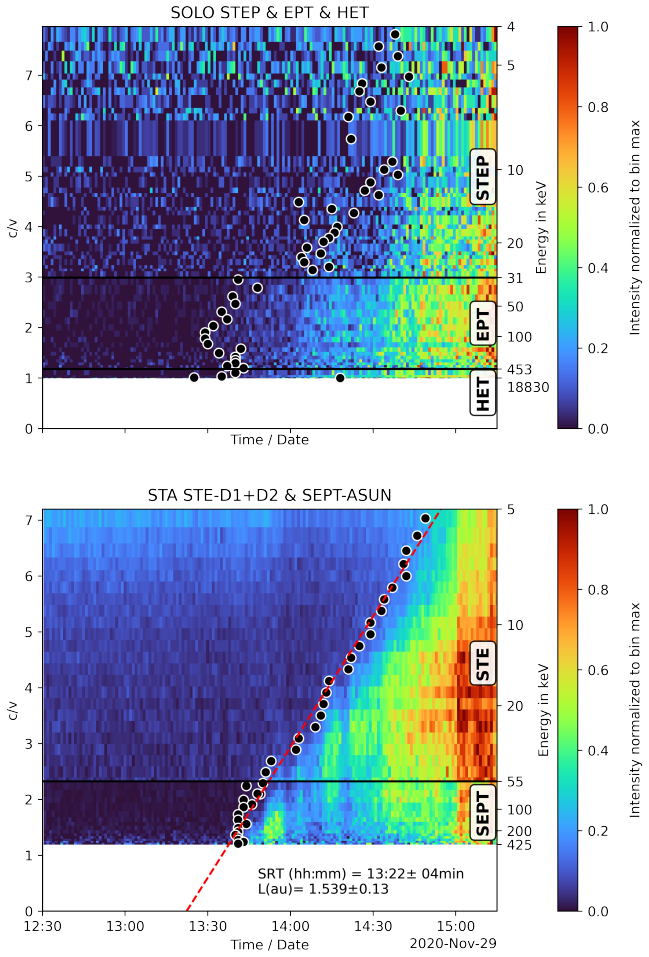

Fig. 6. 60 second time resolution c/v vs. time plots for electrons observed by SolO STEP, EPT, and HET (*top panel*) and STEREO STE D1 + D2 and SEPT-ASUN (*bottom panel*). The color scale represents intensities normalized to maximum intensity in the respective energy channel. Black horizontal lines separate the instruments. Black Points mark the onset times derived with the Possion-CUSUM method. The red dashed line in the *bottom panel* represents the linear fit for VDA.

be made worse by low statistics, gradual increases, or high pre-event backgrounds from either instrumental effects or from pre-occuring events. Additionally, instruments with limited fields-of-view (FOV), not covering a full 4π solid angle, may not observe the actual arrival of the first particles if the magnetic field vector and the resulting particle trajectories are outside of the FOV.

It is important to note that while the above effects cause delays to the observed onsets, assessing their influence on the determination of the particle solar release times is not as straightforward. The delays on observed onsets are typically different for different energies, which may cause the VDA-derived solar release times to be early as well as delayed with respect to the real release time (Laitinen et al. 2015).

In general, the results of VDA should be interpreted with caution. The fundamental assumptions of a simultaneous injection of particles with different energies as well as their scatter-free transport may not apply for specific events.

Scattering in the interplanetary medium can broaden the intensity time profiles observed far from the source and the following slower rise of the observed particle intensities tends to cause significant delayed onset detection. Thus, if strong

scattering is involved in the particle transport, the solar injection times, and path lengths determined by VDA can have significant errors (Laitinen et al. 2015).

To overcome uncertainties in the onset determination Zhao et al. (2019) proposed an extension to the VDA where they considered the times when the flux reached certain ratios of the peak flux instead of the onset times. While this extension would allow us to avoid uncertainties in the onset determination, its application is impracticable for the here discussed event. Given the long rising phase of particle intensities and the modulation of the time profiles by transient structures the unambiguous determination of the relevant peak fluxes in different energy channels is not possible for the here discussed event.

In this work, we apply the VDA only for measurements that show a prompt and clear increase above the background intensities during the early rise phase. Yet, a detailed deconvolution and quantification of the potential sources of errors in the VDA is not feasible with the data presented here. Further studies including simulations of the SEP transport have to confirm the solar release and injection times derived for this event by VDA.

Here we use the Poisson-CUSUM and the 3σ-Method to derive onset times. We applied the Poisson-CUSUM method to data sets with low statistics where the 3σ-Method would require extensive down-sampling of the native time or energy resolution. The 3σ-Method was applied to time profiles with higher statistics.

Considering first VDA, Fig. 6 shows the c/v vs. time plots for electron measurements from STEP, EPT, and HET on SolO (upper panel) as well as STE and SEPT on STEREO-A (lower panel). The colorbar shows the intensity normalized to the maximum intensity in each energy channel. The black horizontal lines separate the individual instruments and the black points mark the onset times of each energy channel derived with the Poisson-CUSUM method.

For STEREO-A we combine measurements from the SEPT-ASUN telescope, that is pointing away from the Sun, together with measurements from the D1 and D2 detectors of Suprathermal Electron Telescope (STE). These apertures were chosen because they share a common FOV and were aligned close to the local magnetic field direction during this time period. Therefore, they likely observed the earliest electrons arriving at the spacecraft. A further description of the multi-sector measurements is given in Sect. 5.2.

VDA results using the onset times determined for SEPT and STE are included in the lower panel of Fig. 6. The red dashed line represents a linear fit through the onset times for the various energy channels starting at 5 keV. The fit yields a solar release time of 13:22 UT ±4 min as well as an effective path length of (1.54 ± 0.13) AU. 3σ fitting errors were determined by bootstrapping the fit with random samples of half the data points.

While the onset times derived from STEREO-A electron observations follow a clear dispersion and are in general agreement with the linear fit shown, onset times derived from SolO electron observations in the top panel of Fig. 7 are more ambiguous. The flux increase observed by SolO/STEP, SolO/EPT, and SolO/HET is not as prompt and well defined as the equivalent STEREO-A observations. The smaller geometry factors of SolO/EPT and SolO/STEP compared to those of STEREO/SEPT and STEREO/STE generally lead to worse statistics while observing similar differential fluxes. The onset times derived from SolO/STEP are inconsistent with the SolO/EPT onsets and likely too late. This discrepancy is probably related to the slightly gradual increase of the event and the different signal-to-background ratios of the two instruments. Also, the onset times

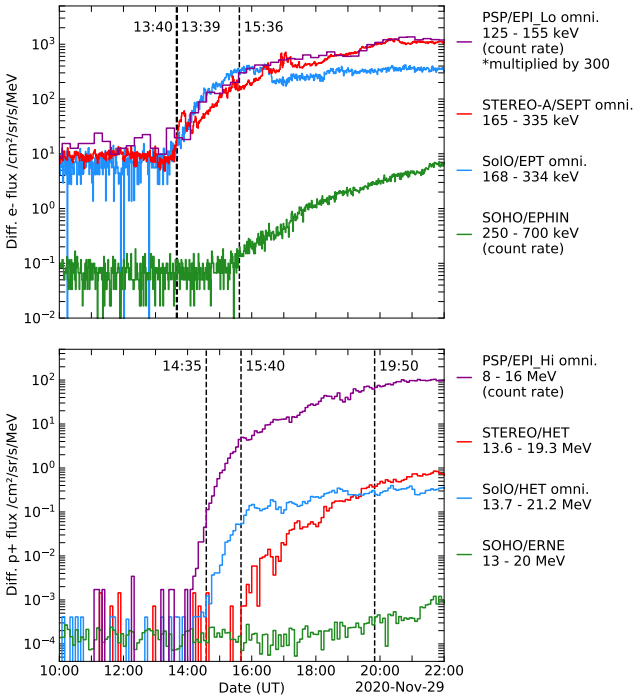

Fig. 7. Electron and proton fluxes observed during the onset phase. *Top panel*: 1-min averaged electron fluxes observed by SolO/EPT, STEREO-A/SEPT, and SOHO/EPHIN together with 15-min averaged electron count rates measured by PSP/EPI-Lo. *Bottom panel*: 10-min averaged proton fluxes observed by SolO/HET, STEREO/HET, SOHO/ERNE and proton count rates measured by PSP/EPI-Hi. 3σ onset times are marked by dashed lines.

of >200 keV electrons observed by SolO/EPT are seemingly too late compared to onset times at lower energies. This is likely related to the worse signal-to-background ratio present at higher energies. The onset times derived from SolO/HET observations suffer also from generally low statistics.

The large uncertainties of the onset times determined from SolO observations prevented us from performing a VDA on these data sets. Instead we used the earliest observed onset of relativistic electrons at 13:25 UT seen by HET at 2.4−6.0 MeV and a path length of 0.94 AU determined from ENLIL (Table 1) to estimate a solar release time of 13:17 UT using TSA. Similar restrictions also prevented us from performing VDA for near-Earth observations, where the actual onset times are difficult to determine from the slow, gradual flux increase.

Figure 7 shows omni-directional electron (top panel) and proton (bottom panel) intensity–time profiles at the different spacecraft during the event onset. The omni-directional profiles are obtained by combining multiple energy channels and measurements from the different telescopes of each instrument. Onset times identified by the 3σ-Method are shown in dashed lines. The onset times of near-relativistic electrons (125−335 keV) observed by SolO at 13:40 ± 11 min and STEREO-A at 13:39 ± 1 min are almost identical. The onset of 250−700 keV electrons observed by SOHO at 15:36 ± 19 min is delayed by about two hours compared to the onsets at STEREO-A and SolO.

The onset times determined from ∼13 to 21 MeV protons measurements by SolO, STEREO-A, and SOHO are 14:35 ± 5 min (SolO), 15:40 ± 11 min (STEREO-A) and 19:50 ± 5 min (SOHO). The given uncertainties are estimated by the difference of 3σ and 5σ onset times. If both of these onset times

Table 2. Timeline of the 2020 November 29 SEP event.

Date	Estimated solar release time (UT)	Delay w.r.t. Type III(1) (min)	Observed onset time (UT)	Observation	Instrument	Mission
29/11	12:26	−19	12:34	M4.4 X-ray flare onset	GOES	GOES
29/11	12:37	−8	12:45	Hard X-ray onset	EPHIN	SOHO
29/11	12:43	−1	12:51	dm-m-λ type II	ORFEES	Earth
29/11	12:45	0	12:53	DH type III(1)	WAVES	STA
29/11	12:58	+13	13:06	DH type II	WAVES	STA
29/11	12:58	+13	13:06	DH type III(2)	WAVES	STA
29/11	13:03	+18	13:11	M4.4 X-ray flare max	GOES	GOES
29/11	13:17	+32	13:25	CME	COR2	STA
29/11	13:19 ± 5 min TSA	+34	13:28 ± 5 min [(c)]	>0.5 MeV *e*- onset	EPI-Hi	PSP
29/11	13:22 ± 4 min VDA	+37	13:39 ± 1 min	165−335 keV *e*- onset	SEPT	STA
29/11	13:17 ± 11 min TSA [(a)(b)]	+32	13:40 ± 11 min	168−334 keV *e*- onset	EPT	SolO
29/11	15:24 ± 19 min TSA [(a)]	+159	15:36 ± 19 min	250−700 keV *e*- onset	EPHIN	SOHO
29/11	13:15 VDA [(c)]	+30	14:30 ± 5 min [(c)]	8.0−16.0 MeV *p* onset	EPI-Hi	PSP
29/11	13:53 ± 5 min TSA [(a)]	+68	14:35 ± 5 min	13.7−21.2 MeV *p* onset	HET	SolO
29/11	14:47 ± 10 min TSA [(a)]	+122	15:40 ± 10 min	13.6−19.3 MeV *p* onset	HET	STA
29/11	18:54 ± 5 min TSA [(a)]	+369	19:50 ± 5 min	13.0−20.0 MeV *p* onset	ERNE	SOHO

Notes. [(a)]Assuming the path length from ENLIL simulations listed in Table 1. [(b)]The onset of 165−334 keV electrons observed by EPT is likely too late due to a low signal-to-background ratio. Here we are using the earliest onset time of relativistic electrons (2.4−6.0 MeV) observed by HET at 13:25 UT for the TSA. [(c)]Values for PSP were taken from Cohen et al. (2021).

are identical, the uncertainty is determined by the time resolution of the data used.

The proton onset determined from STEREO/HET could also include a delay because the single STEREO/HET telescope was not oriented along IMF at this time and may not have detected the first arriving particles.

The corresponding injection times of these particles obtained by TSA, while assuming a path length of 0.94 AU for PSP, 0.94 AU for SolO, 1.16 AU for STEREO-A, and 1.24 AU for near-Earth missions, are given in Table 2. We note that the combination of energy channels introduces additional uncertainties in the determination of the particle velocities. Here we use the velocity corresponding to the geometrical mean of these particle energy ranges.

Further we note that the path lengths used here are a simple estimate for the actual path traveled by the particles. As studied by Chhiber et al. (2021) and Laitinen & Dalla (2019) the turbulent meandering of field lines can cause a significant lengthening of the IMF path lengths. Conversely, Laitinen & Dalla (2019) found that, in certain constellations, a meandering field line could also establish a magnetic connection that is shorter than the nominal Parker spiral length. Other factors such as the gyration of particles that propagate with an effective pitch angle of $\cos(\theta) \neq \pm 1$ will additionally extend the actual path length (see, e.g., Chhiber et al. 2021).

Obviously, the potential discrepancies between the path lengths assumed here and the actual lengths would directly translate to uncertainties in the solar release times determined by TSA. As the determination of an accurate path length is difficult, we restrict our analysis to the path length determined from ENLIL simulations. Additional Monte Carlo simulations of the magnetic field lines and of particle trajectories, considering the solar wind turbulence, might yield better approximations for the actual path length. These analyses however are beyond the scope of this work and will be the subject of future studies.

The release times of SEPs observed by PSP are studied in detail by Cohen et al. (2021). Unfortunately, the EPI-Hi ion intensity vs. energy data are only available on an hourly cadence during this event. Such coarse time resolution makes onset analysis impractical for calculating particle solar release times. There is, however, a sample of individual ion measurements recorded by EPI-Hi with 1-min time resolution that can be used in inverse velocity analysis. For this, the inverse velocity of each ion was calculated and plotted vs. the particle observation time. A clear edge to the distribution was then fitted by eye to obtain a path length and a solar release time at 13:15 ± 4 min UT (see Cohen et al. 2021, for details).

Since the determination of the electron EPI instrument response has not been completed, similar analysis of the electron events is not possible. There are electron count rates at 1-min time resolution available from PSP/EPI-Hi/HET, but only categorized by which detector the particle stopped in. This is difficult to convert to an energy range due to the significant variation in incident angles as well as due to scattering in the instrument. However, given that HET's response is primarily to electrons >0.5 MeV, the velocity dispersion of these electrons is fairly small. By examining the onset of these 1-min rates, we estimate the electron onset time to be 13:28 ± 5 min UT.

5.2. Anisotropies

The two top panels of Fig. 8 show the pitch angle distribution (PAD) of near-relativistic (left) and relativistic (right) electrons observed by SolO/EPT and HET, respectively. We note that the SolO/HET PAD is a data product that is not available from any other present heliospheric spacecraft. Corresponding to the energy range shown in the top left panel, the bottom panels show the PADs observed by STEREO A/SEPT (left) and Wind/3DP (right). The first order anisotropy is presented in the bottom panels of Fig. 8. In case of the four-sector telescopes, the anisotropies were determined using the summation method described by Brüdern et al. (2018). For Wind's eight-sector measurements an integration of the fitted PAD was used (e.g., Dresing et al. 2014). It shows that Wind observes only a very weak anisotropy due to anti-sunward propagating electrons with an average value of $\langle A \rangle = 0.3$ for the first hour of the event. However, this weak anisotropy lasts from the time of the onset around 16 UT on November 29 until

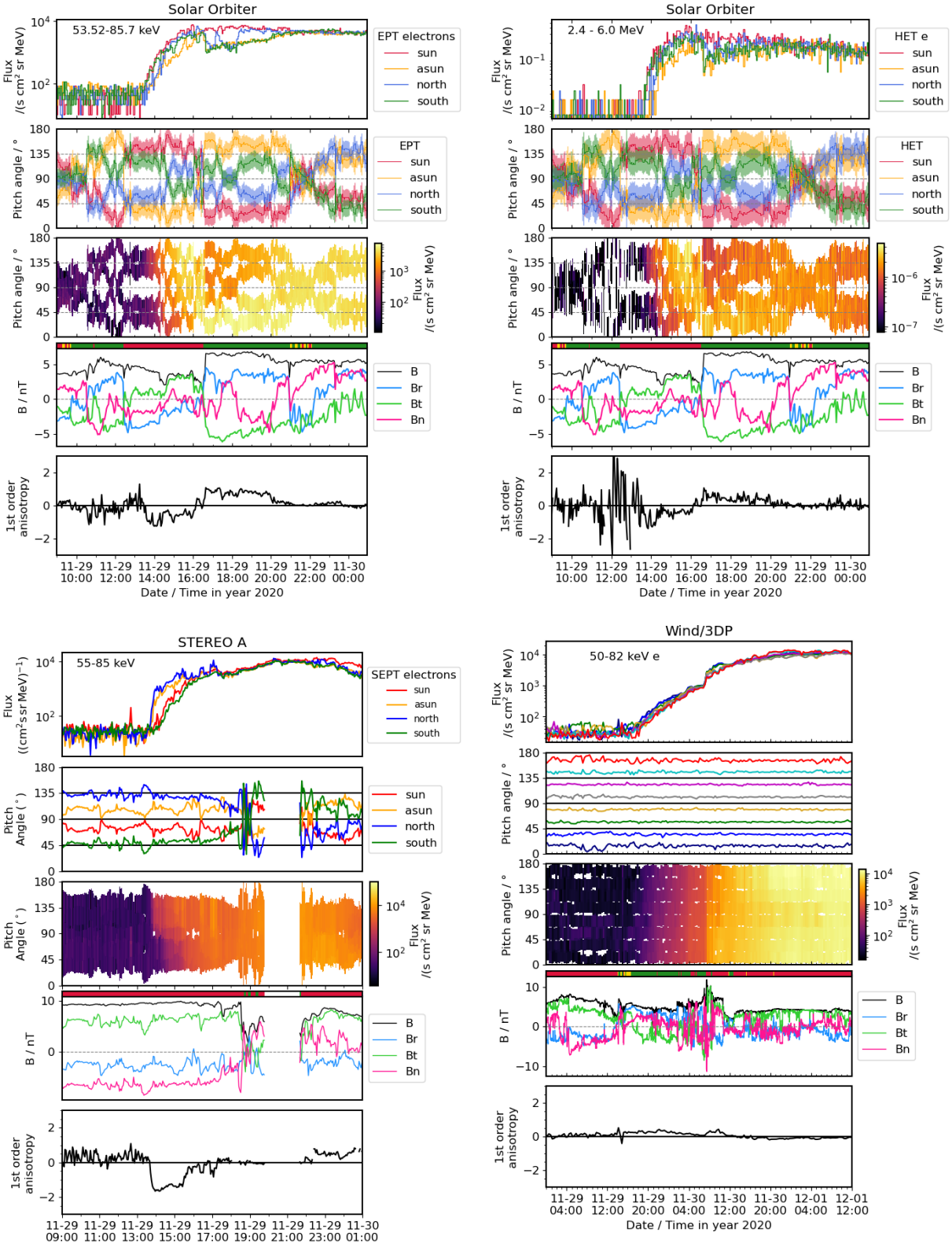

Fig. 8. Pitch angle distributions of energetic electrons observed by SolO/EPT (*top left*), SolO/HET (*top right*), STEREO A/SEPT (*bottom left*), and Wind/3DP (*bottom right*). *Top panels*: sectored electron fluxs of ~50−80 keV (bottom figures and top left figure) and 2.4−6.0 MeV (*top right*, HET) observed in the four viewing directions of the telescopes (in case of STEREO and SolO) or binned into eight sectors for Wind. *Second panel*: corresponding pitch angles covered by the different viewing directions or sectors, *third panel*: pitch angle distributions of the electrons (flux in color coding). *Fourth panel*: magnetic field magnitude and RTN components and *bottom panel*: first order anisotropy. The colored band on top of the magnetic field panel denotes the in situ magnetic field polarity with red (green) marking negative (positive) polarity and yellow denoting unclear polarity periods. We note the longer time period of the figure showing Wind data.

almost 10 UT on November 30. While the anisotropy during the beginning of the event is caused by anti-sunward propagating electrons, the anisotropic period from ~07 to ~10 UT on November 30 is caused by sunward propagating electrons as illustrated by the opposite (negative) field polarity during this period. The long-rise time of the event together with the weak anti-sunward anisotropy early in the event suggest a prolonged injection close to the Sun, whereas the short interval with weak sunward anisotropy might result from local effects produced by the CIR identified in the right column of Fig. 1. Presumably, the injection region on the Sun did not extend toward the magnetic footpoint of Wind at the Sun as this would likely result in a larger anisotropy at the spacecraft. A certain amount of perpendicular diffusion might therefore be involved in transporting the particles to the spacecraft. However, detailed transport modeling would be needed to specify the relative contributions of interplanetary transport versus injection size and duration.

SolO observes a stronger anisotropy which is expected due to its much smaller longitudinal separation angle to the parent solar active region as compared with Wind (see Table 1). The absolute value of the first order anisotropy at MeV energies observed by SolO/HET (Fig. 8, top right, bottom panel) is slightly smaller ($\langle A \rangle = -0.7$ for the first hour) than at near-relativistic energies measured by EPT ($\langle A \rangle = -0.8$, Fig. 8, top left, bottom panel). This is expected because of the energy dependent diffusion coefficient leading to stronger interplanetary scattering for higher energy electrons (Dröge 2003; Agueda et al. 2014; Strauss et al. 2020). We note that the sign of the first order anisotropy depends on the polarity of the magnetic field and all nonzero anisotropy shown in Fig. 8 is due to anti-sunward propagating electrons except the short period of sunward propagating electrons at Wind as discussed above. Therefore, the switch of negative to positive anisotropy observed by SolO at ~16:30 UT is only caused by the change of magnetic field polarity, yielding a duration of more than seven hours which supports the hypothesis of a temporally extended electron injection already suggested by the Wind observations. The largest anisotropy is observed by STEREO/SEPT with a mean value of $\langle A \rangle = -1.4$ during the first hour of the event. The duration of nonzero anisotropy of only about three hours is shorter than at the other spacecraft. However, the vanishing anisotropy could also be due to limited pitch angle coverage, which decreases throughout the event. The large anisotropy observed at STEREO-A is surprising because this spacecraft is far separated (~95°) from the parent active region at the Sun. However, in the light of the detection of local Langmuir waves at STEREO a large anisotropy is expected (see Sect. 4.2). The large longitudinal range covered by STEREO A, SolO, and Wind, showing significant and partially even high electron anisotropies, suggests a spatially extended electron injection or distribution close to the Sun like the class-2 events of Dresing et al. (2014). The observation of anti-sunward directed anisotropies in regions of different field polarity (as indicated by the red and green color bands in Fig. 8) suggest that the injection of particles occurred on both sides of the heliospheric current sheets. There is the possibility that the extent of the distribution of electrons injected close to the Sun was not as large as the longitudinal range spanned by the observers (as perpendicular transport is likely involved in the particle spread), but it is likely far larger than that provided by a flare injection only.

6. Summary and discussion

On 2020 November 29, a solar energetic particle event was observed by spacecraft near Earth (SOHO, ACE, and Wind) and by STEREO-A, PSP, and SolO at widely separated locations spanning ~230° in heliolongitude and 0.81–0.99 AU in heliocentric distance, providing the first opportunity to study a widespread SEP event using such a constellation of four observers. This study summarizes the observations at the different spacecraft and also highlights the capabilities of the new generation of instruments on SolO.

Remote sensing observations show that the SEP event was associated with a partially occulted M4.4 X-ray flare located in NOAA active region 12 790 just behind the east limb as observed from Earth (E98). The flare was accompanied by an EUV wave that expanded away from the AR and covered a large portion of the visible solar disk seen by STEREO-A and Earth. Coronagraphic observations show a fast (1500 km s^{-1}) and relatively wide CME originating from the same AR and a fast CME-driven shock wave. Type II and multiple type III radio emissions are evidence for the propagation of the CME-driven shock wave and the release of electrons into interplanetary space.

In situ particle observations by four widely separated observers give evidence for the wide spread of SEPs. As summarized in Fig. 1, energetic protons with energies extending to >50 MeV and near-relativistic and relativistic electrons rapidly filled the inner heliosphere following the solar event. The onset times determined for near-relativistic electrons and tens of MeV protons, as well as the resulting solar release times determined by VDA and TSA, show a dependence on the longitudinal separation between the solar event and the footpoint of the magnetic field connecting to the spacecraft, as has been previously reported for similar widespread events (e.g., Dresing et al. 2012; Lario et al. 2017; Richardson et al. 2014). The differences in the particle onset and release times at the four locations are presumably determined by, and provide constraints on, particle acceleration and transport processes and require further investigation. Here, we briefly consider two examples of how to interpret these onset and release times that indicate the value of combining observations of widespread SEP events from multiple spacecraft.

In our first interpretation, we compare the solar release times of electrons and ions observed by the different spacecraft with the propagation of the EUV wave. Figure 9 presents a timeline of the events in Table 2. It shows the angular distance of the EUV wave from the AR (⋆ markers), which is determined "by eye" from SDO/AIA and STEREO-A/EUVI images. The vertical bars show the angular distance of the spacecraft magnetic field footpoints from the AR from Table 1 assuming Parker spiral field lines; the widths of the bars assume an uncertainty of ±5°. The electron (proton) release times for each spacecraft, inferred from TSA or VDA (with the 1 AU light travel time added), are also shown by × and + markers, respectively.

Comparing the release times of the energetic particles for each spacecraft with the arrival times of the EUV wave at the corresponding field line footpoints, we do not find a clear relationship between these times. The electron release times determined by TSA for PSP (connected around 70° from the AR) do appear to coincide with the arrival of the EUV wave at the respective field line footpoint. For SolO, the magnetic footpoint is behind the east limb, preventing us from determining a direct connection of the EUV wave extension to the magnetic footpoint. For an EUV wave speed of 500 km s^{-1} the electron release times determined by TSA for SolO (connected around 90° from the AR) would also coincide with the arrival of the EUV wave to the magnetic footpoint. For STEREO-A it is, again, difficult to trace the EUV wave to the spacecraft footpoint. Moreover, Fig. 9 suggests

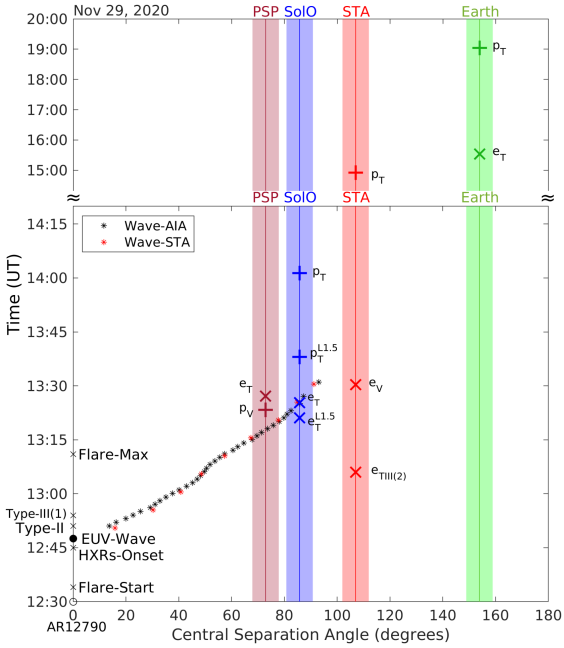

Fig. 9. Comparison of the inferred particle release times with the arrival time of the EUV wave at the spacecraft field line footpoints. The ⋆ markers show the angular distance of the EUV wave from the AR. The release times for electrons and protons are shown by × and + markers for each spacecraft. The angular distance of the magnetic footpoint from the active region for each spacecraft is shown by the vertical bars, which assume an uncertainty of ±5 deg.

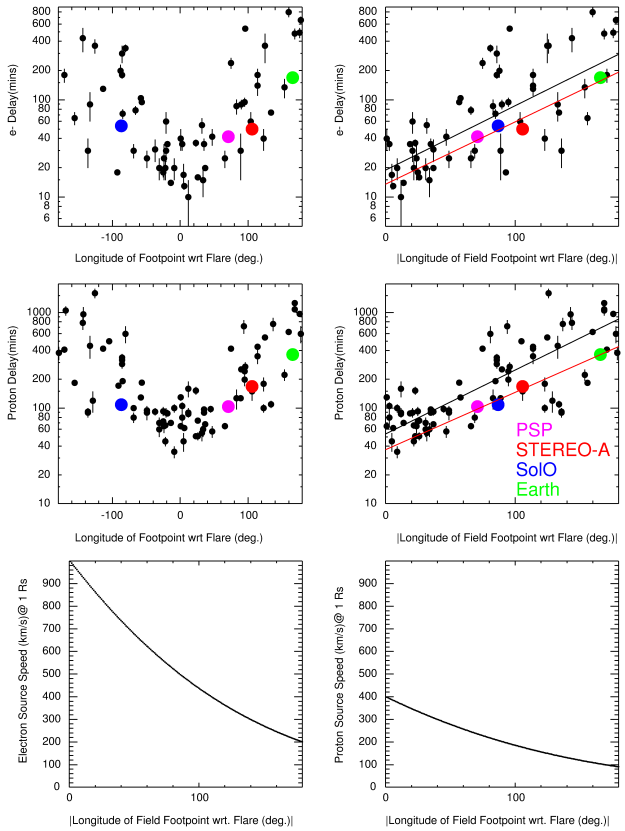

Fig. 10. Comparison of electron (*top panels*) and proton (*middle panels*) onset delays vs. connection angle for the November 2020 SEP event (colored circles, indicating the observing spacecraft) with those for ∼0.7−4 MeV electrons and 14−24 MeV protons in the cycle 24 SEP events observed at both STEREO spacecraft and near the Earth discussed by Richardson et al. (2014) (black circles). The *bottom panels* show the "source speeds" from the flare to the field line footpoint as a function of connection angle for electrons (*left*) and protons inferred from the November 2020 event onset delays.

that the electron release may have happened before the EUV wave reached the STEREO-A footpoint. Another consideration for STEREO-A is that the second type III radio burst (Sect. 4.3), starting at 13:06 UT, that later reaches the local plasma frequencies at STEREO-A, indicates that some electrons were released onto the field line connecting to STEREO-A prior to the release time determined by VDA (see the marker labeled with $e_{\mathrm{TIII}(2)}$). Considering observations near Earth, we find no obvious evidence that indicates that the EUV wave reached the magnetic footpoint. Even if a magnetic connection was established close to the solar surface, the electron release time would be considerably delayed relative to the intersection of the wave with the field line footpoint. For the proton release times, their relation with the arrival of the EUV wave at the footpoints of the different spacecraft seems to be worse. At PSP, the proton release time may be consistent, within errors, with the arrival of the EUV wave at the field line footpoint, whereas at SolO the release times are ∼15−35 min later. At Earth, even if a connection was established close to the solar surface, the proton release times would be significantly delayed from the extrapolated arrival time of the wave at the field line footpoint.

There are several possible scenarios that could help to account for the above discrepancies. The presence of open magnetic field lines rooted in the active region, that strongly diverge with height, could help to account for the early electron arrival at STEREO-A, since the electrons could be rapidly transported longitudinally in the corona over several tens of degrees (Klein et al. 2008; Klassen et al. 2018). The significant anisotropy of the first arriving electrons and the detection of Langmuir waves at STEREO-A are complementary pieces of evidence that non-nominal magnetic connections are an important element of this widespread event. To account for the delayed proton release times, a possibility is that the properties of the shock and ambient medium affect the acceleration of electrons and protons differently. Another explanation could be a prolongation of the path length for protons caused by a turbulent random-walk or by the meandering of field lines in the corona and interplanetary space, as modeled by Laitinen & Dalla (2019). This would increase the proton path lengths from those assumed in TSA and would hence reduce the time differences between the proton release times and the EUV wave connection times. Application of this model considerably reduces the time difference for SolO (see markers labeled with $p_{\mathrm{T}}^{\mathrm{L1.5}}$ and $e_{\mathrm{T}}^{\mathrm{L1.5}}$ in Fig. 9 which assume a prolonged path length of 1.5 AU) but not for STEREO-A. In summary, the actual particle acceleration and release processes are likely to be far more complex than assumed in constructing Fig. 9, and further detailed modeling is required to evaluate each of those aspects.

In our second interpretation, we compare the observed electron and proton onset delays in the November 2020 event with observations of similar SEP events during solar cycle 24, and consider the implications of a simple interpretation of these delays. Richardson et al. (2014) examined the connection-angle dependence of electron and proton delays, derived from observed particle event onset times relative to the onset of the associated type III radio emissions, for a sample of SEP events observed at both STEREOs and near-Earth spacecraft in solar cycle 24. Figure 10 compares these results with the similar

delays during the November 2020 event. The top left panel shows (black circles) the near-relativistic electron delays vs. connection angle for the cycle 24 events (where the connection angle is positive if the spacecraft field line footpoint is to the west of the flare), illustrating the general increase in the onset delay with increasing connection angle. The colored circles show the similar results for the November 2020 event, based on information from Table 1. The top right panel shows the same results plotted vs. the absolute value of the connection angle together with the log-linear fits for all the cycle 24 events and for the November 2020 event. We note that the electron delays in the 29 November 2020 event are similarly ordered by increasing connection angle. They are slightly lower than the average for the cycle 24 events. In particular, the electron onset delay for perfect connection (zero connection angle) inferred from the fit (red line) to the observations for the 29 November 2020 event is 14 ± 4 min, which is comparable to the intervals between the solar release and event onset times in Table 2 inferred from VDA or TSA. The similar delay for the cycle 24 events (black line showing the corresponding fit) is 19 ± 4 min.

Similar plots for protons are shown in the middle row of Fig. 10, where the cycle 24 results are for 14−24 MeV protons. Again, the delays for the 29 November 2020 event are within the same range but are also less than the average values based on the log-linear fit. The proton onset delay for perfect connection is 37 ± 6 min compared to 54 ± 5 min for the cycle 24 events (again obtained from the fit). The significance of these shorter delays is unclear. They may be simply due to event-to-event variations or possibly associated with long-term variations in the particle mean free paths (e.g., Dröge et al. 2016) since the cycle 24 events were observed close to solar maximum, while the 29 November 2020 event is early in cycle 25; this requires further investigation. The locations of PSP and SolO inside 1 AU (Table 1) are also not taken into consideration here, but the differences in particle path lengths are unlikely to be sufficient to account for the differences in these delays.

The bottom panels assume (as in Richardson et al. 2014) a simple scenario in which the onset delay at the spacecraft is the sum of a longitudinally-independent particle travel time from the Sun to the spacecraft, given by the delay at zero connection angle as discussed above, and a delay attributed to the time a particle source moving away from the flare at the solar surface, or, alternatively, a particle diffusion process, takes to reach the footpoint of the field line connected to the spacecraft. The electron and proton source speeds for the 29 November 2020 event in the bottom panels are the average speeds required for the electron or proton source to reach a given connection angle, based on the respective log-linear fits in the middle row of the figure. As in Richardson et al. (2014), these speeds decline with increasing connection angle and are higher for electrons than for protons, reflecting the smaller onset delays for electrons. In this simple scenario, the different source speeds suggest that the electron and proton onset delays cannot be accounted by a connection to a single particle source moving away from the solar event near the Sun. On the other hand, a particle speed dependent diffusion process for electrons and protons could account for the observed onset delays. Despite the simplicity of this analysis, the onset times for all four spacecraft involved (including SolO connected to the opposite side of the flare than the other spacecraft) are so well aligned that any combination of three spacecraft allows the onset time at the fourth to be determined with good accuracy. Moreover, onset delays for all near-ecliptic locations around the Sun can be inferred from the fit. Thus, a new capability to make such onset time projections is demonstrated using these first observations of an SEP onset by four in-ecliptic, near-1-AU spacecraft in widely-separated locations with accurate timing.

Further insight into the particle acceleration and transport is provided by the solar radio emissions accompanying this SEP event. The type II radio emissions give evidence for the propagation of a CME-driven shock wave, and multiple type-III radio bursts for multiple releases of energetic electrons into interplanetary space. Type III bursts at the time of the early meter-wave type II burst (type III(1) in Table 2) emanate from the type II lane and are likely accelerated at the shock. These electrons do not seem to reach STEREO A. The type III bursts after 13:06 UT (type III(2) in Table 2) start at higher frequencies than the simultaneous type II burst at decametric-hectometric wavelengths, suggesting that the corresponding electrons, which are detected at STEREO A, come from some acceleration process behind the shock.

A possibility is that they are released from closed structures of the CME as it interacts and reconnects with ambient open field lines. Similar processes resulting in onset delays and long lasting injections were discussed, for instance, by Klein et al. (2005), Dresing et al. (2018) and Pacheco et al. (2019). As already mentioned, the observation of local Langmuir waves and clear velocity-dispersed electron onsets at STEREO-A indicate that the spacecraft directly intercepted some of the electron beams producing the type III burst. This indicates that the spacecraft was directly connected to the source region of at least one of the electron beams despite its wide separation from the initial flare location.

The in situ observations presented in Sect. 4.1 indicate that the propagation of particles can also be influenced by solar wind structures. SolO, STEREO-A and near-Earth spacecraft show features in the SEP intensity–time profiles that are associated with the passage of local solar wind structures, including sector boundaries, that in most cases are likely to be corotating features. This suggests that the large scale 'background' solar wind structures play a role in determining how the particle intensities vary with time at a particular spacecraft, whether by changing the spacecraft connection to the particle source and/or influencing the transport of particles in the inner heliosphere. This requires further study, for example by modeling the structures present in the ambient solar wind, their relationship to the transient structures associated with prior solar eruptions, and their impact on field line connections and particle transport.

This initial examination of the observations presented in this study suggests that aspects of the 2020 November SEP event are both consistent and inconsistent with two idealized extreme scenarios of particle acceleration and transport in such widespread events. In one scenario, SEPs are accelerated along a broad CME shock front with particle propagation mainly parallel to the magnetic field. The longitudinal breadth of the particle distribution arises from the wide acceleration source, and the observed particle onset delays are due to the source reaching the field lines connected to the individual spacecraft. While there is no direct evidence for this scenario in the particle observations as they are presented in Fig. 9, the actual acceleration process could be more complex than assumed when constructing this figure: the longitudinal spreading of the CME shock would be more rapid higher in the middle corona than close to the surface, explaining why the EUV wave expansion might not accurately indicate when magnetic connection of the coronal shock to the observer is established (Zhu et al. 2018). As shown by Posner et al. (1997) and Miteva et al. (2014), the EUV wave expansion speeds may be too low to account for the onset of electron fluxes.

Different acceleration efficiencies for electrons and protons at quasi-parallel and quasi-perpendicular shocks could then explain the different delays for the two species if a shock connection has been established. However, the long onset delays observed at L1 do seem incompatible with the time taken for the shock to expand as far as the L1 connected field line. More detailed analysis of the shock wave driven by the CME and its particle acceleration efficiency is clearly required before concluding whether this scenario is applicable to this event.

In another scenario, efficient cross-field transport of particles could be the dominant process, so that a narrow source could lead to broad longitudinal particle spread at 1 AU. The different onset times of electrons and protons at all four spacecraft, as well as the different "source speeds" for the two species in Fig. 10, might well be compatible with such a scenario. The low values of the first order anisotropy obtained from near-Earth observations together with the more gradual flux increase observed near Earth suggest that cross-field transport is likely involved in the particle spread. However, the relatively large anisotropies measured at SolO and STEREO-A pose strong constraints on the location where the spreading occurs, placing it close to the Sun rather than in the interplanetary medium. Thus, simulations of coronal and interplanetary particle transport are needed to clarify if this scenario is fully consistent with the observations.

Clearly, these two scenarios represent idealized extremes, and a combination of these scenarios might account for the widespread 2020 November 29 SEP event. The observations and simple analyses presented here cannot rule out a scenario in which an expanding source and perpendicular particle transport are both involved in the particle spread. More detailed studies, using 3D models that assume an expanding particle source and incorporate various transport processes, may lead to a plausible explanation for this event.

In conclusion, this initial study of the 2020 November 29 SEP event demonstrates the value of combining observations from multiple spacecraft in the inner heliosphere, together with remote sensing observations, in helping to understand processes of particle acceleration and transport in widespread SEP events. It also demonstrates some of the capabilities of the new instrumentation on SolO. We anticipate that further opportunities to study SEP events using such observations will arise as solar cycle 25 progresses toward maximum and that in particular, interesting observations from unique viewpoints will be available as PSP approaches closer to the Sun and SolO climbs to higher latitudes.

Acknowledgements. Solar Orbiter is a space mission of international collaboration between ESA and NASA, operated by ESA. The CAU Kiel team acknowledges support from the German Federal Ministry for Economic Affairs and Energy, the German Space Agency (Deutsches Zentrum für Luft- und Raumfahrt e.V., DLR) under grants 50OT0901, 50OT1202, 50OT1702, and 50OT2002. A.K. acknowledges financial support from the ANR COROSHOCK project (ANR-17-CE31-0006-01). D.L. acknowledges support from NASA-HGI grant NNX16AF73G and the NASA Program NNH17ZDA001N-LWS. This study has received funding from the European Union's Horizon 2020 research and innovation programme under grant agreement No. 101004159 (SERPENTINE). The U. Turku team acknowledges funding by the Academy of Finland (Grant No. 336809). The UAH team acknowledges financial support by the Spanish Ministerio de Ciencia, Innovación y Universidades FEDER/MCIU/AEI Projects ESP2017-88436-R and PID2019-104863RB-I00/AEI/10.13039/501100011033. L.R.G. is also supported by the European Space Agency, under the ESA/NPI program, and acknowledges the work performed by Laura Balmaceda and Hebe Cremades in the 3D reconstruction of the CMEs used in the ENLIL simulation. ENLIL simulation results have been provided by the Community Coordinated Modeling Center at NASA Goddard Space Flight Center (GSFC) through their public Runs on Request system (http://ccmc.gsfc.nasa.gov; run IDs Laura_Rodriguez-Garcia_031321_SH_1). The WSA model was developed by C. N. Arge, currently at GSFC, and the ENLIL Model was developed by D. Odstrcil, currently at George Mason University. We thank the STEREO: SECCHI, S/WAVES; SOHO: LASCO; Wind/WAVES; and SDO/AIA teams for providing the data used in this study. The STEREO SECCHI data are produced by a consortium of RAL (UK), NRL (USA), LMSAL (USA), GSFC (USA), MPS (Germany), CSL (Belgium), IOTA (France), and IAS (France). SOHO is a mission of international cooperation between ESA and NASA. The SDO/AIA data are provided by the Joint Science Operations Center (JSOC) Science Data Processing (SDP). We thank the radio monitoring service at LESIA (Observatoire de Paris) for providing value-added data that have been used for this study. The ORFEES radio-spectrograph (Observations Radio pour FEDOME et l'Etude des Eruptions Solaires) is the result of a partnership between Paris Observatory and the French Air Force. CALLISTO is a radio spectrograph network organized by the Institute of Astronomy, ETH Zurich and FHNW Windisch, Switzerland. We acknowledge data from the instruments in Glasgow (UK), Heiterswil (Switzerland), and Trieste (Italy). The RPW instrument has been designed and funded by CNES, CNRS, the Paris Observatory, The Swedish National Space Agency, ESA-PRODEX and all the participating institutes. I.G.R. acknowledges support from NASA programs NNH19ZDA001N-HSR and NNH19ZDA001N-LWS, and the STEREO mission. IRFU team acknowledges support from the Swedish National Space Agency grant 20/136. A.A. acknowledges the support of the Spanish Ministerio de Ciencia e Innovación (MICINN) under grant PID2019-105510GB-C31 and through the 'Center of Excellence María de Maeztu 2020-2023' award to the ICCUB (CEX2019-000918- M). F.C. acknowledges the financial support by the Spanish MINECO-FPI-2016 predoctoral grant with FSE. E.A. would like to acknowledge the financial support by the Academy of Finland (Postdoctoral Grant No 322455). V.K. acknowledges the support by NASA under grants 18-2HSWO218_2-0010 and 19-HSR-19_2-0143. Solar Orbiter magnetometer operations are funded by the UK Space Agency (grant ST/T001062/1). T.S.H. is supported by STFC grant ST/S000364/1. T.L. and S.D. acknowledge support from the UK Science and Technology Facilities Council (STFC; grant ST/R000425/1).

References

Agueda, N., Klein, K.-L., Vilmer, N., et al. 2014, A&A, 570, A5
Arge, C. N., & Pizzo, V. J. 2000, J. Geophys. Res., 105, 10465
Arge, C. N., Luhmann, J. G., Odstrcil, D., Schrijver, C. J., & Li, Y. 2004, J. Atmos. Solar-Terrest. Phys., 66, 1295
Aurass, H., Klein, K., Zlotnik, E. Y., & Zaitsev, V. V. 2003, A&A, 410, 1001
Battarbee, M., Dalla, S., & Marsh, M. S. 2018, ApJ, 854, 23
Benz, A. O., Monstein, C., & Meyer, H. 2005, Sol. Phys., 226, 143
Bougeret, J. L., Goetz, K., Kaiser, M. L., et al. 2008, Space Sci. Rev., 136, 487
Brüdern, M., Dresing, N., Heber, B., et al. 2018, Cent. Eur. Astrophys. Bull., 42, 2
Cane, H. V., Reames, D. V., & von Rosenvinge, T. T. 1988, J. Geophys. Res., 93, 9555
Chhiber, R., Matthaeus, W. H., Cohen, C. M. S., et al. 2021, A&A, 650, A26
Cliver, E. W., Kahler, S. W., Neidig, D. F., et al. 1995, Proc. 24th Int. Cosmic Ray Conf., 4, 257
Cohen, C. M. S., Christian, E. R., Cummings, A. C., et al. 2021, A&A, 656, A29 (SO Cruise Phase SI)
Dalla, S., Marsh, M. S., Kelly, J., & Laitinen, T. 2013, J. Geophys. Res. (Space Phys.), 118, 5979
Dresing, N., Gómez-Herrero, R., Klassen, A., et al. 2012, Sol. Phys., 281, 281
Dresing, N., Gómez-Herrero, R., Heber, B., et al. 2014, A&A, 567, A27
Dresing, N., Gómez-Herrero, R., Heber, B., et al. 2018, A&A, 613, A21
Dröge, W. 2003, ApJ, 589, 1027
Dröge, W., Kartavykh, Y. Y., Klecker, B., & Kovaltsov, G. A. 2010, ApJ, 709, 912
Dröge, W., Kartavykh, Y. Y., Dresing, N., & Klassen, A. 2016, ApJ, 826, 134
Ergun, R. E., Larson, D., Lin, R. P., et al. 1998, ApJ, 503, 435
Fox, N. J., Velli, M. C., Bale, S. D., et al. 2016, Space Sci. Rev., 204, 7
Galvin, A. B., Kistler, L. M., Popecki, M. A., et al. 2008, Space Sci. Rev., 136, 437
Gold, R. E., Krimigis, S. M., Hawkins, I. S. E., et al. 1998, Space Sci. Rev., 86, 541
Gómez-Herrero, R., Dresing, N., Klassen, A., et al. 2015, ApJ, 799, 55
Gómez-Herrero, R., Pacheco, D., Kollhoff, A., et al. 2021, A&A, 656, L3 (SO Cruise Phase SI)
Horbury, T. S., OBrien, H., Carrasco Blazquez, I., et al. 2020, A&A, 642, A9
Howard, R. A., Moses, J. D., Vourlidas, A., et al. 2008, Space Sci. Rev., 136, 67
Huttunen-Heikinmaa, K., Valtonen, E., & Laitinen, T. 2005, A&A, 442, 673
Jokipii, J. R. 1966, ApJ, 146, 480
Khotyaintsev, Yu. V., Graham, D. B., Vaivads, A., et al. 2021, A&A, 656, A19 (SO Cruise Phase SI)

Khrabrov, A. V., & Sonnerup, B. U. 1998, Analysis Methods for Multi-Spacecraft Data, 1, 221
Klassen, A., Aurass, H., Klein, K.-L., Hofmann, A., & Mann, G. 1999, A&A, 343, 287
Klassen, A., Dresing, N., Gómez-Herrero, R., Heber, B., & Müller-Mellin, R. 2016, A&A, 593, A31
Klassen, A., Dresing, N., Gómez-Herrero, R., Heber, B., & Veronig, A. 2018, A&A, 614, A61
Klein, K. L., Krucker, S., Trottet, G., & Hoang, S. 2005, A&A, 431, 1047
Klein, K.-L., Krucker, S., Lointier, G., & Kerdraon, A. 2008, A&A, 486, 589
Kouloumvakos, A., Rouillard, A. P., Wu, Y., et al. 2019, ApJ, 876, 80
Krucker, S., Larson, D. E., Lin, R. P., & Thompson, B. J. 1999, ApJ, 519, 864
Kühl, P., & Heber, B. 2019, Space Weather, 17, 84
Kühl, P., Heber, B., Gómez-Herrero, R., et al. 2020, J. Space Weather Space Clim., 10, 53
Laitinen, T., & Dalla, S. 2019, ApJ, 887, 222
Laitinen, T., Huttunen-Heikinmaa, K., Valtonen, E., & Dalla, S. 2015, ApJ, 806, 114
Laitinen, T., Kopp, A., Effenberger, F., Dalla, S., & Marsh, M. S. 2016, A&A, 591, A18
Lario, D., Raouafi, N. E., Kwon, R.-Y., et al. 2014, ApJ, 797, 8
Lario, D., Kwon, R.-Y., Richardson, I. G., et al. 2017, ApJ, 838, 51
Lemen, J., Title, A., Akin, D., et al. 2011, Sol. Phys., 275, 17
Lepping, R. P., Acũna, M. H., Burlaga, L. F., et al. 1995, Space Sci. Rev., 71, 207
Lin, R. P., Anderson, K. A., Ashford, S., et al. 1995, Space Sci. Rev., 71, 125
Lin, R., Curtis, D., Larson, D., et al. 2008, Space Sci. Rev., 136, 241
Lintunen, J., & Vainio, R. 2004, A&A, 420, 343
Maksimovic, M., Bale, S. D., Chust, T., et al. 2020, A&A, 642, A12
Malandraki, O. E., Marsden, R. G., Lario, D., et al. 2009, ApJ, 704, 469
Marhavilas, P., Malandraki, O., & Anagnostopoulos, G. 2015, Planet. Space Sci., 117, 192
Marsh, M. S., Dalla, S., Kelly, J., & Laitinen, T. 2013, ApJ, 774, 4
McComas, D., Alexander, N., Angold, N., et al. 2016, Space Sci. Rev., 204, 187
Miteva, R., Klein, K.-L., Kienreich, I., et al. 2014, Sol. Phys., 289, 2601
Müller, D., St. Cyr, O. C., Zouganelis, I., et al. 2020, A&A, 642, A1
Müller-Mellin, R., Kunow, H., Fleissner, V., et al. 1995, Sol. Phys., 162, 483
Müller-Mellin, R., Böttcher, S., Falenski, J., et al. 2008, Space Sci. Rev., 136, 363
Odstrcil, D. 2003, AdSpR, 32, 497
Odstrčil, D., Smith, Z., & Dryer, M. 1996, Geophys. Res. Lett., 23, 2521
Ogilvie, K. W., Chornay, D. J., Fritzenreiter, R. J., et al. 1995, Space Sci. Rev., 71, 55
Owen, C. J., Bruno, R., Livi, S., et al. 2020, A&A, 642, A16
Pacheco, D., Agueda, N., Gómez-Herrero, R., & Aran, A. 2017, J. Space Weather Space Clim., 7, A30
Pacheco, D., Agueda, N., Aran, A., Heber, B., & Lario, D. 2019, A&A, 624, A3
Park, J., Innes, D. E., Bucik, R., & Moon, Y.-J. 2013, ApJ, 779, 184
Posner, A., Bothmer, V., Kunow, H., et al. 1997, Eur. Space Agency Spec. Publ., 415, 377
Reinhard, R., & Wibberenz, G. 1974, Sol. Phys., 36, 473
Richardson, I. G., von Rosenvinge, T. T., Cane, H. V., et al. 2014, Sol. Phys., 289, 3059
Rodríguez-Pacheco, J., Wimmer-Schweingruber, R. F., Mason, G. M., et al. 2020, A&A, 642, A7
Rouillard, A. P., Sheeley, N. R., Tylka, A., et al. 2012, ApJ, 752, 44
Saiz, A., Evenson, P., Ruffolo, D., & Bieber, J. W. 2005, ApJ, 626, 1131
Steinvall, K., Khotyaintsev, Yu. V., Cozzani, G., et al. 2021, A&A, 656, A9 (SO Cruise Phase SI)
Steyn, R., Strauss, D. T., Effenberger, F., & Pacheco, D. 2020, J. Space Weather Space Clim., 10, 64
Strauss, R. D., Dresing, N., Kollhoff, A., & Brüdern, M. 2020, ApJ, 897, 24
Thernisien, A. 2011, ApJS, 194, 33
Thernisien, A. F. R., Howard, R. A., & Vourlidas, A. 2006, ApJ, 652, 763
Torsti, J., Valtonen, E., Lumme, M., et al. 1995, Sol. Phys., 162, 505
Torsti, J., Kocharov, L., Teittinen, M., et al. 1999, J. Geophys. Res., 104, 9903
Vainio, R., Valtonen, E., Heber, B., et al. 2013, J. Space Weather Space Clim., 3, A12
Vasudevan, G., Shing, L., Mathur, D., et al. 2019, Design and On-orbit Calibration of the Solar Ultraviolet Imager (SUVI) on the GOES-R Series Weather Satellite, 276
von Rosenvinge, T. T., Reames, D. V., Baker, R., et al. 2008, in The High Energy Telescope for STEREO, ed. C. T, Russell (New York: Springer), 391
Wang, Y., Qin, G., & Zhang, M. 2012, ApJ, 752, 37
Wibberenz, G., & Cane, H. V. 2006, ApJ, 650, 1199
Wijsen, N., Aran, A., Sanahuja, B., Pomoell, J., & Poedts, S. 2020, A&A, 634, A82
Wijsen, N., Samara, E., Aran, A., et al. 2021, ApJ, 908, L26
Wimmer-Schweingruber, R. F., Janitzek, N. P., Pacheco, D., et al. 2021, A&A, 656, A22 (SO Cruise Phase SI)
Wraase, S., Heber, B., Böttcher, S., et al. 2018, A&A, 611, A100
Xu, Z., Guo, J., Wimmer-Schweingruber, R. F., et al. 2020, ApJ, 902, L30
Zhang, M., Qin, G., & Rassoul, H. 2009, ApJ, 692, 109
Zhang, J., Temmer, M., Gopalswamy, N., et al. 2021, Progr. Earth Planet. Sci., 8, 56
Zhao, L., Li, G., Zhang, M., et al. 2019, ApJ, 878, 107
Zhu, B., Liu, Y. D., Kwon, R.-Y., & Wang, R. 2018, ApJ, 865, 138

[1] Institut für Experimentelle und Angewandte Physik, Christian Albrechts-Universität zu Kiel, Kiel, Germany
e-mail: kollhoff@physik.uni-kiel.de
[2] IRAP, Université Toulouse III – Paul Sabatier, CNRS, CNES, Toulouse, France
[3] NASA Goddard Space Flight Center, Heliophysics Science Division, Greenbelt, MD 20771, USA
[4] Department of Physics and Astronomy, University of Turku, 20014 Turku, Finland
[5] Universidad de Alcalá, Alcalá de Henares, Spain
[6] National Observatory of Athens, IAASARS, Metaxa and Vas. Pavlou str., Pedeli 15236, Athens, Greece
[7] Department of Astronomy, University of Maryland, College Park, MD 20742, USA
[8] NASA/HQ, 300 Hidden Figures Way SW, Washington, DC 20546, USA
[9] LESIA, Observatoire de Paris, Université PSL, CNRS, Sorbonne Université, Université de Paris, 5 Place Jules Janssen, 92195 Meudon, France
[10] California Institute of Technology, Pasadena, CA, USA
[11] University of Central Lancashire, Lancashire, UK
[12] Institute for Space Astrophysics and Planetology, INAF, Roma, Italy
[13] University of Helsinki, Helsinki, Finland
[14] Dep. Física Quàntica i Astrofísica, Institut de Ciències del Cosmos (ICCUB), Universitat de Barcelona (IEEC-UB), Barcelona, Spain
[15] Southwest Research Institute, San Antonio, TX 78238, USA
[16] Centre for mathematical Plasma-Astrophysics, Department of Mathematics, KU Leuven, Celestijnenlaan 200B, 3001 Leuven, Belgium
[17] European Space Astronomy Center, Villanueva de la Cañada, 28692 Madrid, Spain
[18] Johns Hopkins University, Applied Physics Laboratory, Laurel, MD, USA
[19] Department of Physics and Space Sciences Laboratory, University of California, Berkeley, CA 94720, USA
[20] Goddard Planetary Heliophysics Institute, University of Maryland, Baltimore County, Baltimore, MD, USA
[21] Department of Physics, Imperial College London, London SW7 2AZ, UK
[22] Swedish Institute of Space Physics (IRF), Uppsala 75121, Sweden
[23] Radboud Radio Lab, Department of Astrophysics, Radboud University, Nijmegen, The Netherlands
[24] Space and Plasma Physics, Department of Physics and Astronomy, Uppsala University, Uppsala 75120, Sweden

7

SEP OBSERVATIONS AT DIFFERENT SOLAR DISTANCES

When SEPs arrive at Earth, they have already propagated vast distances through interplanetary space. During their transport, the properties of the particle population change due to processes such as diffusion, focusing in a divergent magnetic field and scattering at magnetic field irregularities (see e.g. Jokipii, 1966). As a result, it is generally difficult to relate the properties of in situ observations of SEPs to properties of their distant source. For instance, linking the injection time of particles at the Sun to the particle arrival times at 1 AU can be quite difficult due to the influence of the interplanetary transport (see e.g. Agueda et al., 2009 and references therein).

Multi-spacecraft observations at different distances from the Sun offer the opportunity to directly study the influence of transport processes (for some examples see Wibberenz et al., 2006; Rodríguez-García et al., 2023). The unique orbit of Solar Orbiter provides excellent possibilities to compare SEP observations at varying heliocentric distances with observations at ~ 1 AU.

In a corresponding study (following in this section), observations of 25 near-relativistic electron events from Solar Orbiter's EPT are compared with similar observations from SEPT onboard the STEREO-A spacecraft and observations from the Three-Dimensional Plasma and Energetic Particle Investigation (3DP) onboard the Wind spacecraft. The study compares several event characteristics such as onset times, peak fluxes and maximum anisotropies – which were determined with commonly used routines – for events where the observers featured similar magnetic connections to the Sun.

The study shows a wide event-to-event variability in the radial dependency of the parameters. While the observed peak intensities tend to follow, on average, an R^{-3}-dependency (similar to the theoretical predictions of diffusive particle transport; see e.g. Vainio et al., 2007), other parameters such as the maximum anisotropy do not show such clear radial dependence.

Several possible explanations for the wide event-to-event variability are discussed. As such, limitations in the methods used to determine event parameters are pointed out and additional problems, including the unknown conditions in the interplanetary medium, are considered. Ultimately, the study concludes that simple event parameters such as onset times (in omnidirectional particle fluxes) and maximum anisotropies – determined with commonly used methods – are likely insufficient for a direct comparison between different instruments.

For future studies it is suggested to consider pitch-angle-dependent fluxes from the different observers while taking into account the directional response functions and individual backgrounds of the different instruments.

A&A 675, A155 (2023)
https://doi.org/10.1051/0004-6361/202345955

Astronomy & Astrophysics
Special issue

Solar Orbiter First Results (Nominal Mission Phase)

Multi-spacecraft observations of near-relativistic electron events at different radial distances

A. Kollhoff[1], L. Berger[1], M. Brüdern[1], N. Dresing[2], S. Eldrum[1], S. Fleth[1], R. Gómez-Herrero[3], B. Heber[1], P. Kühl[1], D. Pacheco[1], L. Rodríguez-García[3], J. Rodríguez-Pacheco[3], R. F. Wimmer-Schweingruber[1], and Z. Xu[1]

[1] Institute of Experimental and Applied Physics, Kiel University, Christian-Albrechts-Platz 4, 24118 Kiel, Germany
e-mail: kollhoff@physik.uni-kiel.de
[2] Department of Physics and Astronomy, 20014 University of Turku, Finland
[3] Universidad de Alcalá, Space Research Group (SRG-UAH), Plaza de San Diego s/n, 28801 Alcalá de Henares, Madrid, Spain

Received 20 January 2023 / Accepted 29 May 2023

ABSTRACT

Aims. We study the radial evolution of near-relativistic solar energetic electron (SEE) events observed by at least two spacecraft at different heliocentric distances and with small separation angles between their magnetic footpoints at the Sun.
Methods. We identified SEE events for which Solar Orbiter and either Wind or STEREO-A had a small longitudinal separation (<15°) between their nominal magnetic footpoints. For the approximation of the footpoint separation, we followed a ballistic back-mapping approach using in situ solar wind speed measurements. For all the SEE events that satisfied our selection criteria, we determined the onset times, rise times, peak fluxes, and peak values of the first-order anisotropy for electrons in the energy range from ~50−85 keV. We compared the event parameters observed at different spacecraft and derived exponential indices α_p for each parameter p, assuming an R^{α}-dependence on the heliocentric distance R.
Results. In our sample of SEE events, we find strong event-to-event variations in the radial dependence of all derived parameters. For the majority of events, the peak flux decreases with increasing radial distance. For the first-order anisotropy and the rise time no clear radial dependence was found. The derived onset delays observed between two spacecraft were found to be too long to be explained by ideal Parker spirals in multiple events.
Conclusions. The rudimentary methods presented in this study lead to event parameters with large uncertainties. The absence of a clear radial dependence on the first-order anisotropy and the rise time as well as the ambiguous onset timing of the SEE events found in this study could be the result of general limitations in the methods we used. Further studies, including analyses of the directional fluxes and transport simulations that take the individual instrument responses into account, would allow a better interpretation of the radial evolution of SEE events.

Key words. Sun: particle emission – Sun: activity

1. Introduction

In the age of space probes, solar energetic particle (SEP) events are a frequently observed phenomenon. Enhancements of energetic particles with near-relativistic and sometimes even relativistic energies were observed by a number of scientific space missions, such as Helios (Mueller-Mellin et al. 1982), Ulysses (Wenzel et al. 1992), the SOlar and Heliospheric Observatory (SOHO; Domingo et al. 1995), Wind (Acuña et al. 1995), the Solar Terrestrial Relations Observatory (STEREO; Russell 2008), and more recently, the Parker Solar Probe (PSP; Fox et al. 2016) and Solar Orbiter (Müller 2020). Since the first observations, attempts have been made to explain the phenomenon in as much detail as possible. However, the physical processes involved in SEP acceleration and in their propagation through the heliosphere are not yet fully understood.

Observations of near-relativistic electron events provide an important contribution to the understanding of these fundamental questions. Because of their high speed, near-relativistic electrons are good tracers of the associated solar source. Additionally, they are detected quite frequently. For instance, the ongoing STEREO mission has observed more than 1000 near-relativistic electron events so far (reported in the SEPT Online Event List 2022)[1] and therefore provides a sufficient sample for statistical studies, such as Dresing et al. (2020).

The event properties measured at a spacecraft generally depend on the acceleration at the source, the injection process, the transport of particles to the observer, and finally, the characteristics of the observing instrument. In order to disentangle these interrelated processes, a good understanding of the involved transport processes is crucial. Theoretical studies of the interplanetary transport, such as those by Jokipii (1966), form the basis for a series of numerical simulations that try to reproduce the in situ observations of the event properties (e.g., Agueda et al. 2009; Strauss et al. 2017).

For near-relativistic electrons, it is generally assumed that particles are injected into the interplanetary space with a nearly isotropic velocity distribution (e.g., Dröge et al. 2016; Strauss & Fichtner 2015). After their injection, the electrons propagate through interplanetary space, guided by the interplanetary magnetic field. The Lorentz force that acts on the electrons forces them to gyrate along the magnetic field. With respect to the local magnetic field vector $\boldsymbol{B}$, the instantaneous velocity vector $\boldsymbol{v}$ of the particle can be described by the pitch-angle θ (which

[1] http://www2.physik.uni-kiel.de/stereo/downloads/sept_electron_events.pdf

is the angle between $\boldsymbol{B}$ and $\boldsymbol{v}$), a gyro-phase, and the speed of the particle. For a large population of electrons, the gyro-phase is often neglected, which means that an equal representation of all gyro-phases in the population is assumed. The velocity distribution of a large electron population is therefore usually only characterised by its speed $|\boldsymbol{v}|$ and the pitch-angle distribution.

The isotropic pitch-angle distribution of a freshly injected particle population is influenced by different transport processes. For example, the diverging magnetic field introduces forces that focus the population along the magnetic field. Close to the Sun, where the gradients in the magnetic field are large, focusing almost immediately transforms the isotropic injection into an anisotropic pitch-angle distribution. The effect of focusing can be counteracted by scattering processes. Pitch-angle scattering, for instance, is a process where the pitch-angle of an electron undergoes stochastic changes due to particle-wave interactions with turbulence and irregularities in the magnetic field. Efficient pitch-angle scattering can lead to a diffusive propagation of the population along the magnetic field and to an isotropisation of the distribution (e.g., Jokipii 1966). Processes that cause a diffusive particle transport perpendicular to the magnetic field are discussed for example by Dröge et al. (2010).

The exact interplay of the different transport processes is complex. In the cases of focusing and pitch-angle scattering, it is often difficult to say which process predominates at a given radial distance. Numerous studies showed that the efficiency of both processes varies with radial distance. For example, the focusing length, a parameter to describe the efficiency of the focusing, strongly decreases with radial distance due to the decreasing local gradients of the magnetic field strength (e.g., He & Wan 2012). Studies such as Wibberenz et al. (1989) discussed the potential radial dependence of the mean free path, a parameter used to describe the efficiency of scattering.

Depending on the transport processes and the relative location to the source, observable event properties such as the arrival time of the particles, omni-directional intensities, and the anisotropy of the particle population may vary. With a single point of observation in interplanetary space, it is often difficult to conclude where and how strongly focusing and pitch-angle scattering influence these parameters. Multi-spacecraft observations can provide additional constraints. For example, under ideal conditions, where two spacecraft at different radial distances are well connected by the interplanetary magnetic field, the differences in the observations at the two spacecraft may be used to analyse different effects of transport processes.

Studies that used data from the Helios era, such as Wibberenz & Cane (2006), showed a strong radial and longitudinal dependence of the peak intensity and quantitatively confirmed the spatial diffusion of electrons. Rodríguez-García et al. (2023) recently confirmed in a larger statistical study that included recent data from Solar Orbiter that the peak intensity observed in close nominally magnetically connected spacecraft at different radial distances agrees on average with a dependence on R^{-3}. The same dependence can also be derived from theoretical considerations under the assumption of a diffusive particle transport (e.g., Vainio et al. 2007). Furthermore, Rodríguez-García et al. (2023) also showed that for a large sample of events, the near-relativistic electron spectra are harder on average close to the Sun. Both studies improved the general understanding of the involved transport processes.

In this study, we analyse a sample of near-relativistic electron events observed by Solar Orbiter and either STEREO-A or Wind. In particular, we selected solar energetic electron (SEE) events for which a significant increase in the ~50−85 keV electron flux was observed at two spacecraft. Similar to the study by Rodríguez-García et al. (2023), we analyse the radial dependence of the peak intensity in our sample. In addition to this, we examine other event parameters, such as onset times, anisotropies, and the slopes of the flux increase around the onset, in order to identify possible radial dependences.

In Sects. 2 and 3 we describe the data sets we used in this study, the event selection, and the SEE event parameters derived for this study. In Sect. 4 we analyse the radial dependencies of these parameters. Section 5 summarises and discusses our results.

2. Instrumentation

For this study, we used near-relativistic electron, magnetic field, and solar wind measurements from Solar Orbiter, the Solar Terrestrial Relations Observatory (STEREO)-A, and the Global Geospace Science satellite Wind (WIND). From Solar Orbiter, we used the electron measurements from the Electron Proton Telescope (EPT), which is part of the Energetic Particle Detector (EPD; Rodríguez-Pacheco et al. 2020); solar wind speed measurements from the Solar Wind Analyser (SWA; Owen et al. 2020); and magnetic field measurements from the Solar Orbiter magnetometer (MAG; Horbury et al. 2020). From STEREO-A, we used electron measurements from the Solar Electron Proton Telescope (SEPT; Müller-Mellin et al. 2008). Solar wind data were obtained from the Plasma and Suprathermal Ion Composition experiment (PLASTIC; Galvin et al. 2008), and magnetic field data were taken from the Magnetic Field Experiment (Acuña et al. 2008). From Wind, we used electron observations made by the 3DP (3DP; Lin et al. 1995). The solar wind speed and magnetic field data were taken from the Solar Wind Experiment (SWE; Ogilvie et al. 1995) and the Magnetic Field Investigation (MFI; Lepping et al. 1995).

3. Event selection and determination of parameters

We identified time periods during which the magnetic footpoint of Solar Orbiter at the Sun presumably had a small longitudinal separation angle (<15°) to the magnetic footpoints of either Wind or STEREO-A. The separation angle was estimated by ballistic back-mapping assuming an ideal Parker spiral and using two-hour-averaged solar wind speed measurements around the onset at the different spacecraft. For time periods for which no solar wind speed observation was available, we approximated a possible range of separation angles for solar wind speeds ranging from 300 to 500 km s^{-1}.

Figure 1 shows an overview of the near-relativistic electron observations made by Solar Orbiter, Wind, and STEREO-A in the top three panels. The presented fluxes are multi-channel averages, weighted with the energy width of the individual channels. The fourth and fifth panels show the heliocentric distances of the different spacecraft and the approximate longitudinal footpoint separation angles between Solar Orbiter and Wind or STEREO-A. The dots in the lowest panel show the footpoint separation angles approximated by using solar wind speed measurements from the different spacecraft.

In this study, we specifically focused on the time period between the fourth and fifth perihelion of Solar Orbiter (September 2021–March 2022). This period is indicated in Fig. 1 by the vertical dashed lines. During this period, the orbit of Solar Orbiter enabled a particularly good connection to the other near 1 au spacecraft mentioned above. Within this time period, we identified all near-relativistic electron events that satisfied the following two selection criteria: (a) A clear flux increase of ~50−85 keV electrons at Solar Orbiter and a clear flux increase

Fig. 1. Overview of multi-spacecraft near-relativistic electron observations made between 2020 February 28 and 2022 September 1. From top to bottom, the panels show ~49.7–85.6 keV electron fluxes measured by Solar Orbiter/EPT, 55–85 keV electron fluxes measured by STEREO-A/SEPT, 50–82 keV electron fluxes measured by Wind/3DP, the heliocentric distance of all three spacecraft, and the longitudinal separation of the magnetic footpoints between Solar Orbiter and STEREO-A (orange) as well as between Solar Orbiter and Wind (green). The dots in the lowest panel show the separation angle approximated by using solar wind speed measurements from the different spacecraft, and the coloured areas show the minimum and maximum separation angle estimated for arbitrary solar wind speeds ranging from 300 to 500 km s^{-1}.

of ~50–85 keV electrons at either Wind, STEREO-A, or both; and (b) a longitudinal separation smaller than 15° of the nominal magnetic footpoints between Solar Orbiter and Wind or STEREO-A.

Following the criteria discussed above, we found 25 SEE events, which are listed in Tables 1 and 2. As in the 4 SEE events observed on 2022 January 16, January 18, February 13, and March 7, our selection criteria are satisfied by Wind and STEREO-A at the same time. These 4 events appear in both tables.

To characterise the electron events, we determined a set of seven SEE event parameters: Onset time, slope of the early flux increase, separation angle of the magnetic foot-point, time of maximum, rise time, peak flux, and the first-order anisotropy. These parameters were determined for each electron event in our sample. Detailed descriptions of all parameters are given below.

3.1. Onset time

We approximated the arrival time of the first electrons of each SEE event at each spacecraft by determining the time when the ~50–80 keV electron flux rose above the mean pre-event background plus three standard deviations. In particular, we used the following routine. (1) We calculated the moving mean $\bar{f}_i$ and moving standard deviation σ_i in a two-hour window from $t_i - 120$ min, t_i for the ~55–80 keV electron flux. (2) We defined an onset at t_i if two consecutive three-minute-averaged flux values rose by more than three standard deviations ($f_{i+1} > \bar{f}_i + 3 \cdot \sigma_i$ and $f_{i+2} > \bar{f}_i + 3 \cdot \sigma_i$).

The 120-min background averages and the three-minute averages used here were assumed to provide a reasonable compromise between time resolution and statistical uncertainty. We note that the derived onset times we obtained following the process described above are only a rough estimate for the actual arrival time of the first electrons. The onset time found with the routine strongly depends on the instrument response, pre-event background, and pitch-angle coverage. In addition, gradual flux increases result in systematically delayed onset times because undetectable flux increases will raise the detection threshold.

3.2. Slope of the early flux increase

In order to describe how prompt a flux increase was after its onset, we determined the slope $m = (I_{+9\,\mathrm{min}} - I_{-3\,\mathrm{min}})/12$ min in a [−3min, +9min] interval around

the onset. $I_{-3\,\mathrm{min}}$ and $I_{+9\,\mathrm{min}}$ are three-minute-averaged omni-directional flux values observed three minutes before and nine minutes after the onset time.

We note that there is no general prediction of how exactly the flux increase develops around the onset. The increase rate is most likely not constant over time, and the slope derived in a 12-min-interval is therefore a somewhat arbitrary parameter. However, for the presented sample of events, this interval (3 min before the onset to 9 min after the onset) does not exceed the rise phase of any of the events in our sample. For shorter time intervals, the statistical uncertainties in the flux measurements would significantly increase the uncertainty in the slope parameter.

In this study, the estimated slope only serves as a simple assessment of how prompt the flux increase was, regardless of the observed peak flux.

3.3. Separation angle of the magnetic footpoints

For each event, we approximated the longitudinal separation angle between the magnetic footpoints of the spacecraft. We neglected the latitudinal separation of the magnetic footpoints because all spacecraft were close to the ecliptic plane (heliographic latitudes lower than ±5°) in the time period of interest. To determine the longitudinal magnetic footpoint separation angle, we used the following procedure. (1) We determined each spacecraft position at the time of the onset. (2) We determined the two-hour-averaged solar wind speed around the onset time at each spacecraft. (3) We calculated the longitudinal back-mapping angle β as $\beta = \omega_\odot \cdot r_{\mathrm{spacecraft}}/v_{\mathrm{sw}}$, where $r_{\mathrm{spacecraft}}$, v_{sw} and $\omega_\odot$ are the radial distance of the spacecraft, the solar wind speed at the time of the onset, and the solar angular velocity for a sidereal rotation period of 25.38 days, respectively. (4) We calculated the longitudinal footpoint separation at the Sun $\Delta\Phi_{\mathrm{FP}}$ as the angle between the back-mapped longitudes $\Phi_{\mathrm{FP}} = \Phi - \beta$ of the two spacecraft, where Φ is the longitude of the spacecraft, and β is the back-mapping angle.

We note that the separation angles were determined assuming an ideal Parker field and that significant deviations from this ideal scenario can occur, for example, due to the influence of interplanetary structures and the complex structure of the coronal magnetic field below the solar wind source surface.

3.4. Time of maximum and SEE peak flux

We determined the highest omni-directional (all-sector-averaged) flux values observed during each event together with the time when the maximum was reached. For this purpose, we used the following procedure. (1) We calculated 15-min running averages of the ~55−80 keV electron flux. (2) We determined the highest value of the 15-min-averaged flux in an interval of $[t_{\mathrm{onset}}, t_{\mathrm{onset}} + 300\,\mathrm{min}]$ after the SEE event onset. This value was then defined as the peak flux. (3) We determined the time when the highest 15-min-averaged flux was observed. This time was then taken as the time of maximum. (4) We defined the time between onset and time of maximum as the rise time.

By using 15-min-averages, we intended to reduce the statistical uncertainties. A similar timescale for the determination of peak intensities was used for example by Dresing et al. (2020). The 300-min window used as a limit to determine the time of maximum was introduced in order to prevent the method from detecting subsequent events. The specific value of 300 min was chosen after a visual inspection of the event sample. We note that the observed omni-directional peak flux and time of maximum depend on the exact pitch-angle coverage of the instrument. A further discussion of this aspect is given in Sect. 4.

3.5. Maximum first-order anisotropy

We used the sector intensities observed by the different instruments and the measurements of the local magnetic field vectors to calculate the peak value of the first-order anisotropy for each SEE event. We used the following procedure. (1) We calculated one-minute-averaged magnetic field vectors and sector intensities for each spacecraft. (2) For the four-sector measurements by STEREO-A/SEPT and Solar Orbiter/EPT, we estimated the first-order anisotropy A^1 using the following equation:

$$A^1 = 3\frac{\sum_{i=1}^{4} \delta\mu_i \cdot \mu_i \cdot I(\mu_i)}{\sum_{i=1}^{4} \delta\mu_i \cdot I(\mu_i)}, \tag{1}$$

where $I(\mu_i)$, μ_i, and $\delta\mu_i$ are the observed intensities of sector i, the cosine of the pitch-angle of the central pointing axes of sector i, and the range in μ-space covered by sector i, respectively. Equation (1) was proposed by Brüdern et al. (2018) in order to reliably determine the first-order anisotropy in case of four-sector measurements. For Wind/3DP, we calculated the first-order anisotropy for eight-sector measurements by the following equation:

$$A^1 = 3\frac{\sum_{i=1}^{8} \mu_i \cdot I(\mu_i)}{\sum_{i=1}^{8} I(\mu_i)}, \tag{2}$$

where $I(\mu_i)$ and μ_i are the observed intensities of sector i and the pitch-angle of the inverted central pointing axes of sector i, respectively. The first-order anisotropy for Wind was calculated without considering the actual pitch-angle coverage of the individual sectors $\delta\mu_i$ because the exact coverage could not be identified. (3) We calculated a three-minute moving average of the first-order anisotropy and determined its highest value. This value was then selected as the maximum first-order anisotropy. We note that the maximum value of the anisotropy observed also depends on the exact pitch-angle coverage of the instrument. Again, this is further discussed in Sect. 4.

4. Analysis

We analysed the event parameters derived from the 25 near-relativistic SEE events listed in Tables 1 and 2. For each SEE event, the date of the observation is given in the first column, and the next three columns of the tables list the spacecraft position in Stonyhurst coordinates. The radial distance, R (1), is given in astronomical units; the longitude, Φ (2), and latitude, Θ (3), are given in degrees. The onset time, t_{onset} (4), and the time at which the peak flux was observed, $t_{I_{\mathrm{max}}}$ (6), are given with an approximate uncertainty of ±3 min, which was estimated based on the time averages used here. The peak flux, I_{max} (5), is given in units of electrons per (cm^2 sr s MeV). The solar wind speed, v_{sw} (7), at the time of the onset is given in km s^{-1}. The maximum values of the first-order anisotropy, A^1_{max} (8), are unitless. The slope of the flux increase around the onset, m (9), is given in units of electrons per (cm^2 sr s^2 MeV). The separation angle between the magnetic footpoints at the Sun, $\Delta\Phi_{\mathrm{FP}}$ (10), is given in degrees.

Table 1. All selected SEE events with a small longitudinal separation between the magnetic footpoints of Solar Orbiter and STEREO-A.

Date	Solar Orbiter EPT									STEREO-A SEPT										3DP
	R au	Φ °	Θ °	t_{onset} UT	I_{max} [(b)]	$t_{I_{max}}$ UT	v_{sw} km s^{-1}	A^1_{max}	m [(c)]	R au	Φ °	Θ °	t_{onset} UT	I_{max} [(b)]	$t_{I_{max}}$ UT	v_{sw} km s^{-1}	A^1_{max}	m [(c)]	$\Delta\Phi_{FP}$ °	Seen
	(1)	(2)	(3)	(4)	(5)	(6)	(7)	(8)	(9)	(1)	(2)	(3)	(4)	(5)	(6)	(7)	(8)	(9)	(10)	(11)
26 Sep. 21	0.61	−29.1	1.9	11:57	1.03E+03	12:48	363	...	3.74E−01	0.96	−39.9	6.8	12:27	4.79E+01	16:15	395	0.7	7.85E−03	7.2	y
27 Sep. 21	0.62	−27.8	2.0	11:54	1.75E+03	13:06	308	...	4.44E−01	0.96	−39.8	6.9	12:00	6.11E+02	13:12	375	−1.8	2.46E−02	1.4	y
28 Sep. 21	0.62	−26.8	2.0	06:54	1.57E+03	07:21	312	...	2.84E−01	0.96	−39.7	6.9	07:36	2.27E+02	08:27	357	−0.2	4.32E−02	3.1	y
9 Oct. 21	0.68	−14.8	2.3	06:42	2.53E+04	06:54	367	2.7	9.07E−01	0.96	−38.9	7.3	06:48	4.32E+04	07:45	388	1.6	6.55E−02	−8.9	n
16 Jan. 22	0.94	−16.1	−1.2	20:18	2.90E+02	20:42	524 [(a)]	−0.6	5.66E−02	0.97	−34.8	−0.8	20:21	3.50E+02	20:51	461	−0.9	4.37E−02	−11.3	y
18 Jan. 22	0.93	−16.5	−1.4	17:54	1.76E+04	18:36	513	...	1.44E+00	0.97	−34.8	−1.1	18:00	1.26E+04	19:03	397	−0.2	1.43E−01	−3.1	y
20 Jan. 22	0.92	−16.9	−1.4	06:30	4.90E+04	09:36	495	−1.2	2.07E−01	0.97	−34.7	−1.3	06:21	1.10E+04	07:21	362	−0.9	1.14E−01	1.9	y
30 Jan. 22	0.86	−18.4	−2.0	23:42	3.90E+02	02:30	468	1.3	7.07E−02	0.97	−34.6	−2.5	23:48	2.16E+02	03:33	415	0.5	1.31E−02	−4.3	y
3 Feb. 22	0.83	−18.7	−2.3	21:27	6.05E+02	00:45	538	...	7.32E−02	0.97	−34.6	−3.1	21:00	8.64E+02	21:18	483	−1.3	4.07E−02	−4.6	n
10 Feb. 22	0.78	−18.4	−2.7	03:06	5.61E+01	06:30	565	−1.2	4.06E−02	0.97	−34.5	−3.8	03:30	1.15E+01	04:45	559	0.7	8.57E−03	−7.4	n
13 Feb. 22	0.75	−17.9	−2.9	03:21	3.22E+02	07:09	306 [(a)]	−1	5.87E−02	0.97	−34.5	−4.2	04:36	1.38E+02	08:12	377	−0.4	7.20E−03	−13.7	n
5 Mar. 22	0.51	−2.3	−4.3	23:54	6.81E+03	00:00	423	−1.8	1.02E+00	0.97	−34.1	−6.1	00:15	7.42E+01	00:18	449	−1.8	9.11E−02	−8.8	n
7 Mar. 22	0.49	0.5	−4.3	15:09	3.83E+02	15:18	306	−0.8	1.93E−01	0.97	−34.0	−6.2	15:39	2.45E+01	17:00	354	−1.5	2.30E−02	−7.0	n
8 Mar. 22	0.49	1.6	−4.3	05:00	3.09E+02	05:27	293	−1.2	6.75E−02	0.97	−34.0	−6.3	05:30	2.83E+01	06:00	329	−1.4	1.58E−02	−4.1	n
10 Mar. 22	0.45	7.3	−4.3	20:45	4.72E+03	21:24	299	−2.8	4.84E−02	0.97	−33.9	−6.4	21:39	1.73E+02	00:51	309	−1.2	1.33E−02	−1.1	y
14 Mar. 22	0.41	18.0	−4.1	17:54	1.01E+03	21:42	385	−1.3	1.26E−01	0.97	−33.8	−6.7	18:33	2.24E+02	22:12	363	−0.4	3.22E−02	−12.2	n
18 Mar. 22	0.36	33.7	−3.4	22:09	1.80E+03	22:09	397	2.5	7.96E+00	0.97	−33.7	−6.9	22:42	1.25E+02	22:57	317	0.8	2.90E−02	−14.8	n

Notes. A description of the parameters is given in Sect. 3. [(a)]No solar wind data were available around the onset. [(b)](cm^2 sr s MeV)$^{-1}$. [(c)](cm^2 sr s^2 MeV)$^{-1}$.

Table 2. All SEE events with a small longitudinal separation between the magnetic footpoints of Solar Orbiter and Wind.

Date	Solar Orbiter EPT									Wind 3DP										SEPT
	R au	Φ °	Θ °	t_{onset} UT	I_{max} [(b)]	$t_{I_{max}}$ UT	v_{sw} km s^{-1}	A^1_{max}	m [(c)]	R au	Φ °	Θ °	t_{onset} UT	I_{max} [(b)]	$t_{I_{max}}$ UT	v_{sw} km s^{-1}	A^1_{max}	m [(b)]	$\Delta\Phi_{FP}$ °	Seen
	(1)	(2)	(3)	(4)	(5)	(6)	(7)	(8)	(9)	(1)	(2)	(3)	(4)	(5)	(6)	(7)	(8)	(9)	(10)	(11)
1 Nov. 21	0.83	−1.7	2.1	01:51	7.60E+04	02:54	355[a]	−1.4	1.32E+00	0.99	0.0	4.4	02:42	6.38E+03	06:30	411	−0.5	2.42E−01	3.9	y
9 Nov. 21	0.88	0.0	1.9	17:21	1.79E+03	19:27	399	0.5	7.21E−02	0.99	0.0	3.5	17:18	2.60E+03	18:21	360	1.5	1.32E−01	13.3	y
4 Dec. 21	1.00	−2.2	1.0	07:54	3.69E+02	07:57	445	...	5.02E−01	0.99	0.0	0.5	07:54	2.89E+02	08:03	471	1.6	1.49E−01	−1.7	y
4 Dec. 21	1.00	−2.3	1.0	13:33	3.28E+03	13:39	406	2.6	3.02E+00	0.99	0.0	0.4	13:30	9.94E+03	13:51	451	1.7	1.26E+00	−4.8	y
5 Dec. 21	1.01	−2.7	0.9	19:48	5.50E+02	22:57	467	...	2.15E−01	0.99	0.0	0.3	19:48	5.15E+02	23:36	455	1	2.00E−01	3.1	n
6 Dec. 21	1.01	−2.9	0.9	05:54	1.48E+03	06:09	480	...	8.61E−01	0.99	0.0	0.2	05:54	2.69E+03	06:09	466	1.5	1.24E+00	3.3	y
1 Jan. 22	1.00	−11.7	−0.4	14:00	1.30E+02	14:00	576	1.4	2.78E−01	0.98	0.0	−3.1	13:57	6.93E+02	13:57	571	2.5	1.30E+00	11.6	n
16 Jan. 22	0.94	−16.1	−1.2	20:18	2.90E+02	20:42	524 [(a)]	−0.6	5.66E−02	0.98	0.0	−4.7	20:54	7.52E+01	22:21	593	−0.4	3.67E−02	12.7	y
18 Jan. 22	0.93	−16.5	−1.4	17:54	1.76E+04	18:36	513	...	1.44E+00	0.98	0.0	−4.9	17:57	1.11E+04	20:00	594	−2.2	4.01E−01	12.6	y
13 Feb. 22	0.75	−17.9	−2.9	03:21	3.22E+02	07:09	306 [(a)]	−1	5.87E−02	0.99	0.0	−6.7	02:27	1.03E+04	04:15	514	−2.3	8.43E−01	4.9	y
7 Mar. 22	0.49	0.5	−4.3	15:09	3.83E+02	15:18	306	−0.8	1.93E−01	0.99	0.0	−7.3	16:15	3.97E+01	18:30	454	−0.8	1.31E−02	13.5	y
21 Mar. 22	0.34	44.3	−2.7	05:39	8.56E+03	07:00	272	1.7	9.50E−01	1.00	0.0	−7.0	06:06	1.36E+03	06:33	316	2.1	1.97E−01	2.3	y

Notes. A description of the parameters is given in Sect. 3. [(a)]No solar wind data were available around the onset. [(b)](cm^2 sr s MeV)$^{-1}$. [(c)](cm^2 sr s^2 MeV)$^{-1}$.

The last Col. (11) indicates whether a significant flux increase was observed at all three spacecraft.

If no value for the first-order anisotropy is given, the parameter could not be determined due to lack of magnetic field data. For four SEE events, indicated with an [(a)] in the table, no solar wind data were available from Solar Orbiter around the onset of the event. In this case, we used the nearest observed solar wind speed for the back-mapping. Figure 2 shows an example of the determined event parameters and the corresponding observations for the event observed on 2022 March 19.

In four SEE events, our selection criteria presented in Sect. 3 were satisfied by STEREO-A and Wind simultaneously, meaning that all three spacecraft presented close nominal magnetic footpoint locations. For the 29 pairs of observation points (Tables 1 and 2 together), we analysed the event parameters in terms of their radial gradients. In particular, we determined the gradient of the peak intensity, first-order anisotropy, slope of the early flux increase, and rise time. Figure 3 shows a summary of the event parameters vs. the radial distance for each spacecraft.

Following former studies such as Rodríguez-García et al. (2023) and theoretical considerations (e.g., given by Vainio et al. 2007), we characterised the radial gradient of the omnidirectional peak intensity by the exponential index α_I, given by

$$\alpha_I = \frac{\log(I_1/I_2)}{\log(R_1/R_2)}, \tag{3}$$

where I_1 and I_2 are the peak intensities observed at the two spacecraft, and R_1 and R_2 are the corresponding radial distances of the spacecraft. For the other SEE event parameters, we determined the exponential indices in an analogous way, in order to characterise the radial gradients of the first-order anisotropy (α_A), the slope of the early flux increase (α_m), and the rise time (α_T). The exponential indices derived from the 25 SEE events for the different parameters analysed here are listed in Tables 3 and 4.

Because of the various uncertainties in the event parameters discussed in Sects. 3 and 5, small changes in event parameters

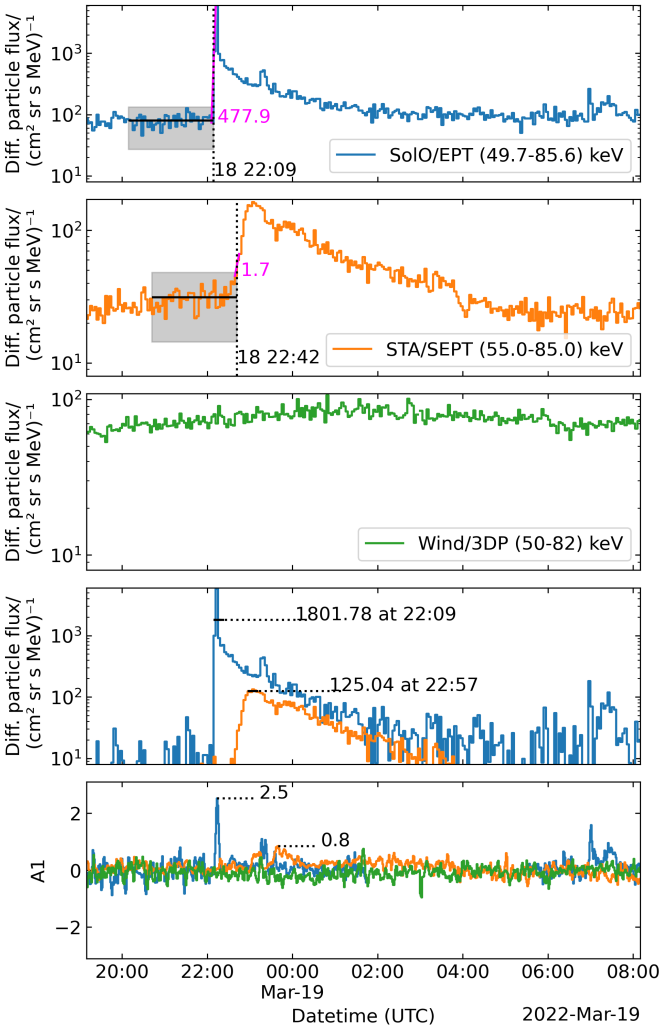

Fig. 2. Time profiles used to determine the event parameters shown for the event observed on 2022 March 18. From top to bottom: near-relativistic electron fluxes observed by Solar Orbiter/EPT (heliocentric distance of 0.36 AU at 22:09 UT on March 18), STEREO-A/SEPT (heliocentric distance of 0.97 AU at 22:42 UT on March 18), and Wind/3DP, the background-subtracted fluxes, and the first-order anisotropy. The black lines and grey areas in the first two panels identify the mean of the pre-event background and the $\pm 3\sigma$ levels. The dotted lines identify the onset times. The values in the fourth panel are the 15-min-averaged background-subtracted peak fluxes. The values in the bottom panel are three-minute-averaged values of the maximum first-order anisotropy.

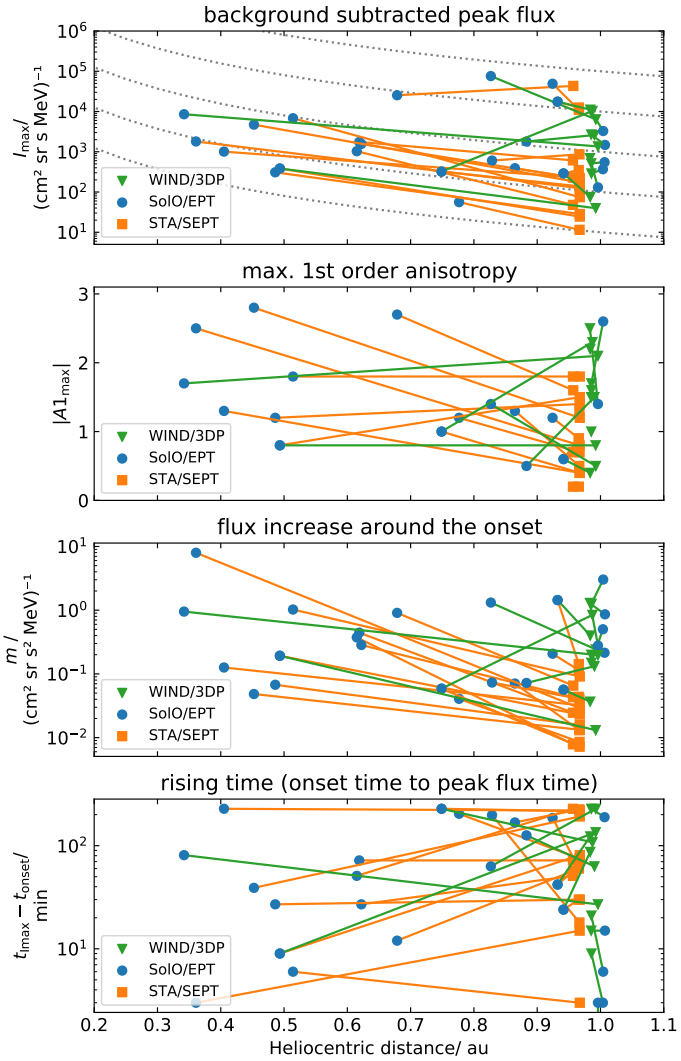

Fig. 3. Radial dependence of the peak intensity, maximum first-order anisotropy, flux increase around the onset, and the time to maximum. Observations made by Solar Orbiter/EPT, Wind/3DP, and STEREO-A/SEPT are shown as blue circles, green triangles, and orange squares, respectively. The solid lines connect observations of the same event. The line colours correspond to the marker colours of the 1 au spacecraft. The dotted lines in the top panel show a dependence on $I \propto R^{-3}$.

over short radial distances cannot be resolved by our analysis. Therefore, we restricted our further analysis to events for which the radial distance between the spacecraft was greater than 0.1 au. The remaining events are still affected by the same uncertainties, but the same errors ΔI_1 and ΔI_2 of the parameters I_1 and I_2 will yield a smaller error $\Delta\alpha_I$ of the gradient α_I at larger radial separations. Following the error propagation of Eq. (3) and neglecting the errors of the spacecraft positions, the error of the gradient is given by

$$\Delta\alpha_I = \left|\frac{\Delta I_1}{I_1 \log(R_1/R_2)}\right| + \left|\frac{\Delta I_2}{I_2 \log(R_1/R_2)}\right|. \quad (4)$$

Although no exact values for ΔI_1 and ΔI_2 could be determined here, Eq. (4) shows that the error $\Delta\alpha_I$ becomes increasingly larger for decreasing radial separations as $\log(R1/R2)$ approaches zero.

In 17 out of 25 SEE events, Solar Orbiter had a radial distance ≥0.1 au with respect to the other spacecraft. In 2 of these 17 events, STEREO-A and Wind satisfied our selection criteria simultaneously. For the total of 19 pairs of observations, we found 15 cases in which the peak intensity decreases with increasing radial distance. In 8 out of 15 cases in which we were able to determine the first-order anisotropy, the maximum value of the anisotropy decreases with increasing radial distance. The slope of the early flux increase decreases in 17 out of 19 cases, and the rise time increases in 10 out of 19 cases.

In the SEE event on 2022 February 13, the gradients α_I, α_{A^1}, and α_m determined between Solar Orbiter (R = 0.77 au) and Wind (R = 0.99 au) contradict the corresponding gradients derived for the same event between Solar Orbiter and STEREO-A (R = 0.97 au). During the SEE event, Wind observed the highest fluxes and first-order anisotropy, followed by Solar Orbiter.

The lowest fluxes and first-order anisotropy were observed by STEREO-A. This SEE event is also one of the cases for which no solar wind speed measurement was available for Solar Orbiter. The footpoint separation was estimated with a solar wind speed of 306 km s^{-1}. The estimated longitudinal separation angles were +4.9° between Solar Orbiter and Wind and −13.7° between Solar Orbiter and STEREO-A.

An unambiguous identification of the solar source was not possible for this event. However, one potential candidate is the class C6.2 flare that appeared at the NOAA active region AR12941 around 01:47 UT, located N29W38 as seen from Earth. When we assume that this is the actual source, Wind would have the closest longitudinal connection to the source, followed by Solar Orbiter, while STEREO-A would have the largest longitudinal separation to the source. In this constellation, perpendicular transport might be the dominant process that effects the SEE event parameter here. Even though we limited our sample to events where the estimated footpoints were closely spaced, the 2022 February 13 event indicates that the actual source separation still plays a significant role. Further discussion of the influence of the source separation can be found in Rodríguez-García et al. (2023).

A clear identification of the source location for all events considered here is beyond the scope of this study. For future studies, a selection of events that are well connected to the source might reduce the influence of longitudinal transport effects, and radial dependences would likely become more prominent.

In addition to the four parameters discussed above, we also compared the timing of the electron arrival at the different spacecraft. We performed this analysis with the full sample of events, including events with $dR < 0.1$ au. Figure 4 shows the difference in the onset times versus the heliocentric distance between the spacecraft, together with estimates for the onset delays, assuming that all particles travel along an ideal Parker spiral. For the estimates, we assumed a solar wind speed of 250 km s^{-1} and arbitrarily chosen pitch-angles from 0° to 89°. These estimates are intended to represent extreme cases for particularly long path lengths along an ideal Parker spiral. We calculated the delay of ideal propagating particles, T, by

$$T = \frac{L}{\cos\alpha}\frac{1}{c}\frac{1}{\sqrt{1-\frac{1}{(1+E/(m_0c^2))^2}}}, \quad (5)$$

where L is the Parker spiral length between Solar Orbiter and a spacecraft located at 1 au, α is the pitch-angle, c is the speed of light, m_0 is the electron rest mass, and E is the kinetic energy.

For our sample, the majority of events show onset delays that are significantly larger than the expected delays for particles propagating along an ideal Parker spiral. Even when we assume that all observed particles maintained an arbitrary pitch-angle of 70°, the observed onset delays are too long. In five events, we found onset delays >40 min between the spacecraft. With a relativistic speed of ∼0.52 au min^{-1} for 55 keV electrons, these delays would correspond to path lengths >2 au. The exact cause for the long onset delays cannot be determined with certainty here.

A comparison of the ratio of the peak intensities at the different spacecraft with the onset delays in each event is shown in Fig. 5. The clear correlation between these two quantities might be an indication for the systematic errors introduced by the procedure used to determine the onsets. The smaller the flux increase, the longer the time the flux needs to emerge from the pre-event background to become detectable. For the majority of events, the outer spacecraft observed a significantly smaller flux increase than the inner spacecraft. Therefore, the systematic error in the onset detection at the outer spacecraft would often be greater. Larger errors at the outer spacecraft directly translate into an increased delay between the onsets that are detected at the two spacecraft. A critical discussion of the use of the onset determination method is given in the discussion.

Table 3. Exponential indices for the radial gradients in the event parameters observed by STEREO-A and Solar Orbiter.

	STEREO-A – Solar Orbiter				
Date	ΔR/ au	α_I	α_{A^1}	α_m	α_T
26. Sep. 21 11:57	0.34	−6.95	...	−8.75	3.39
27. Sep. 21 11:54	0.34	−2.42	...	−6.64	0.00
28. Sep. 21 06:54	0.33	−4.49	...	−4.38	1.48
9. Oct. 21 06:42	0.28	1.55	−1.52	−7.65	4.53
16. Jan. 22 20:18	0.02	7.55	16.04	−10.23	8.83
18. Jan. 22 17:54	0.03	−9.40	...	−65.36	11.46
20. Jan. 22 06:30	0.04	−33.93	−6.53	−13.59	−25.70
30. Jan. 22 01:54	0.10	−5.32	−8.59	−15.19	2.63
3. Feb. 22 21:27	0.14	2.32	...	−3.81	−15.56
10. Feb. 22 03:06	0.19	−7.24	−2.46	−7.09	−4.56
13. Feb. 22 04:48	0.22	−3.31	−3.58	−8.21	−0.21
5. Mar. 22 23:54	0.45	−7.15	0.00	−3.83	−1.10
7. Mar. 22 15:09	0.47	−4.08	0.93	−3.16	3.26
8. Mar. 22 05:06	0.48	−3.47	0.22	−2.11	0.15
10. Mar. 22 21:03	0.51	−4.35	−1.12	−1.70	2.10
14. Mar. 22 17:54	0.56	−1.73	−1.35	−1.57	−0.05
18. Mar. 22 22:10	0.61	−2.71	−1.16	−5.70	1.6

Table 4. Exponential indices for the radial gradients in the event parameters observed by Wind and Solar Orbiter.

	Wind – Solar Orbiter				
Date	ΔR/ au	α_I	α_{A^1}	α_m	α_T
1. Nov. 21 01:51	0.17	−13.55	−5.63	−9.27	7.04
9. Nov. 21 17:21	0.11	3.23	9.57	5.27	−6.04
4. Dec. 21 07:54	−0.02	13.36	...	66.25	−60.06
4. Dec. 21 12:48	−0.02	−59.14	22.66	46.82	−66.80
5. Dec. 21 19:48	−0.02	3.14	...	3.42	−8.90
6. Dec. 21 05:54	−0.02	−27.46	...	−16.67	0.00
1. Jan. 22 14:00	−0.01	−130.63	−45.31	−120.57	0.00
16. Jan. 22 20:18	0.04	−30.78	−9.26	−9.89	29.41
18. Jan. 22 17:54	0.05	−8.46	...	−23.75	19.93
13. Feb. 22 04:48	0.24	12.55	3.01	9.64	−2.70
7. Mar. 22 15:09	0.50	−3.24	0.00	−3.85	3.88
21. Mar. 22 05:39	0.65	−1.72	0.20	−1.47	−1.03

5. Summary and discussion

We have analysed 25 near-relativistic electron events that were observed by Solar Orbiter EPD/EPT in the time between the fourth and fifth perihelion of Solar Orbiter. Our selection included only events that were also observed by Wind/3DP or STEREO-A/SEPT. We further limited the sample to events for which the different spacecraft featured a similar magnetic connection to the Sun, where the nominal magnetic footpoints of the spacecraft were separated by less than 15 deg in longitude.

For the given event sample, we determined a set of SEE event parameters using routines that are well established in the energetic particle community. These parameters include the onset

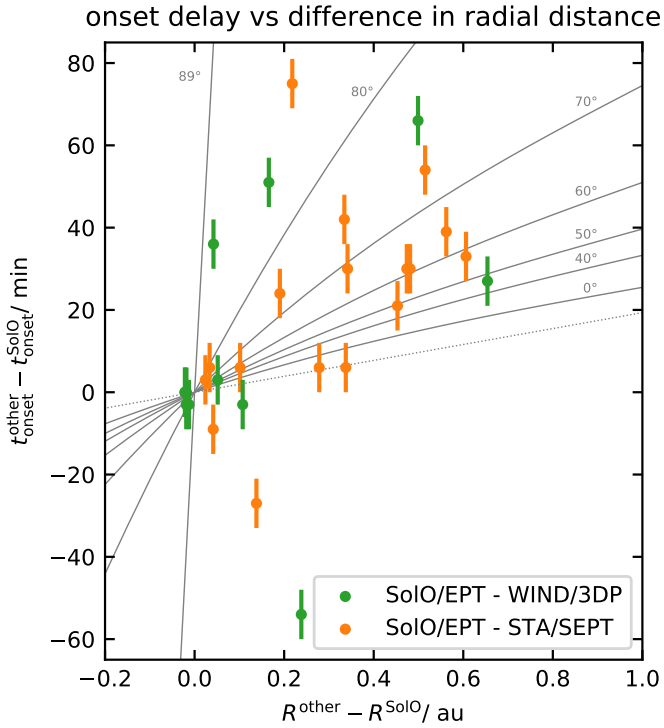

Fig. 4. Timing difference between the onsets observed by Solar Orbiter and STEREO-A/Wind vs. the difference in their radial distance. The dotted line shows the ideal travel time for radially propagating 55 keV electrons. The solid lines show the ideal travel time assuming the electrons travel along a Parker spiral (v_{sw} = 250 km s^{-1}), with various constant pitch-angles ranging from of 0° to 89°.

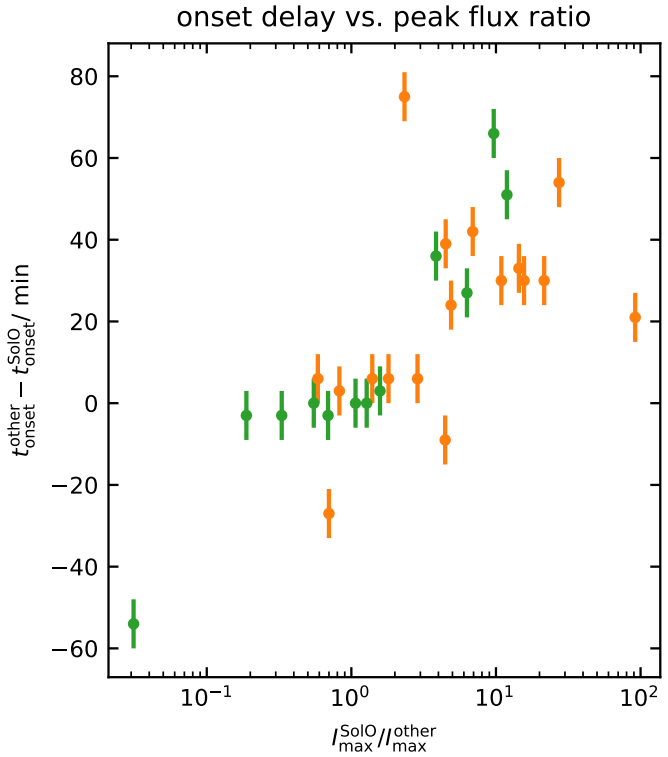

Fig. 5. Onset delay observed between Solar Orbiter and STEREO-A (orange) and Solar Orbiter and Wind (green) vs. the ratio of the observed peak fluxes.

time of the flux increase, the slope of the early flux increase, the peak flux and time of maximum, and the maximum value of the first-order anisotropy. Comparing the event parameters derived for the same SEE event by different observers at different locations, we find a wide variability in the SEE parameters and their corresponding gradients in radial direction.

A statistical evaluation of the SEE parameters with respect to their radial dependences shows the following tendencies: In 15 out of 17 cases, the peak intensity decreases with increasing radial distance. The maximum value of the first-order anisotropy decreases in 8 out of 15 cases with increasing radial distance. The slope of the early flux increase decreases in 17 out of 19 cases, and the rise time increases in 10 out of 19 cases with increasing radial distance.

Comparing the relative onset times of electrons at the different spacecraft, we again find a wide variability. For the majority of events, the derived delays are significantly larger than estimates based on ideal Parker spirals. The derived onset delays also show a correlation with the ratio of the peak intensities between the two spacecraft.

The long onset delays and the absence of clear radial dependences in the first-order anisotropy and the rise time point to limitations of the analysis methods. The rudimentary approaches for determining event parameters chosen in this study are most likely insufficient to accurately characterise the radial evolution of SEE events.

For example, the assumption of an ideal Parker field is not generally valid, and the complexity of the coronal magnetic field was not considered here. The deviation of our estimates from the real magnetic footpoints could be one crucial driver for the large variability in the radial gradients we found. In addition, all parameters used here are strongly dependent on the exact instrument response. The sensitivity and background of the different instruments influence, for example, how fast a certain flux increase can be detected (e.g., Laitinen et al. 2015). The different instruments also have unique directional particle acceptances that directly translate into different pitch-angle coverage and pitch-angle responses. The observed peak intensity, the slope of the early flux increase, and the observed anisotropy will depend on these directional responses. For instance, an unfavourable pitch-angle coverage, for which none of the EPT telescopes looks along the magnetic field, could lead to the observation of a low peak intensity and low anisotropy because the instrument looked past an ambient particle beam.

The strong changes in the event parameters and the enormous gradients ($|\alpha| > 10$) observed in events where Solar Orbiter had a small radial separation ($\Delta R < 0.1$ au) from the other spacecraft are a finding that particularly requires discussion. For spacecraft that supposedly have a similar magnetic connection to the Sun and about the same radial distance, we expected minor changes in the event parameters. In contradiction to this, we find events with extremely large indices at these constellations in our sample (e.g., the SEE events on 2022 January 20 and 2022 January 30). For these unexpected observations, we consider two possible explanations here.

First, the instrumental differences mentioned above might affect the results. In our study, we used sector-averaged fluxes as an estimate for the pitch-angle-averaged (omni-directional) flux. However, the sectors of EPT, SEPT, and 3DP usually cover different pitch-angle ranges. We note that in particular the sectors of SEPT have a different pointing than the sectors of EPT because the STEREO-A spacecraft was rolled during its solar superior

conjunction (from January to August 2015). Furthermore, the exact pitch-angle response will differ between the instruments. Thus, the sector-averaged fluxes from the three instruments are averages over different limited pitch-angle ranges with individual weights. During anisotropic time periods, these different averages are not directly comparable (e.g., Fig. 6 by Bruedern et al. 2022). The sector averages used in this study can only be used as a rough estimate for the full 180° pitch-angle-averaged flux. This limitation will not only affect peak intensities, but also increase the times and the slope of the flux increase observed around the onset. In addition, the maximum anisotropy that can be observed will also depend on the exact pitch-angle coverage of the instruments (e.g., Bruedern et al. 2022). The large differences in the event parameters between the observations of Wind/3DP and Solar Orbiter/EPT observations during Solar Orbiter EGAM (events around December 2021 to January 2021) are another indication of the limited comparability of the event parameters derived from the sector-averaged (omni-directional) intensities. The differences in the individual events are currently under investigation, and their interpretation is beyond the scope of this work. Detailed event studies as well as a cross validation of the instrument calibrations will be needed in order to understand and explain the observed differences. A discussion of how sufficiently the inter-calibration can affect the derived radial gradients of the peak intensity can be found in Rodríguez-García et al. (2023). For all events with significant anisotropies, a comparison of pitch-angle-dependent intensities would clearly be more suitable. A detailed analysis of the pitch-angle coverage and the pitch-angle response of each instrument would most likely increase the precision of our analysis. However, an analysis like this was beyond the scope of this study, and the essential magnetic field data necessary for a pitch-angle-dependent study were not available for several events.

Second, the interplanetary context is a possible explanation for some differences. For events for which two spacecraft are located in flux tubes that are similarly situated but different, any differences in the event parameters might be observed despite the small spacecraft separation. An example for this type of observation was reported by Klassen et al. (2016) and was further analysed by Pacheco et al. (2017).

Further studies are needed to take all these effects into account. In particular, simulations of the individual events that take into account the exact instrument responses would help to separate the instrumental influence and the actual influence of the involved transport processes on the observations. The benefits of this approach are for example shown in Agueda et al. (2008).

For the long onset delays found in this study, we consider the following three possible explanations.

First, the actual path lengths might be significantly longer than those estimated by a Parker spiral. This might be the case if the magnetic footpoints are subject to strong meandering, for example (e.g., Laitinen & Dalla 2019). In this case, the estimated magnetic footpoints would also be affected because the intrinsic assumption of an ideal Parker field would not be fulfilled.

Second, if the electrons are subject to substantial scattering between the observers, a longer onset delay might be expected. If almost none of the electrons propagate scatter free, there is no meaningful definition of a path length.

Third, the method for determining the onsets has well-known limitations (see e.g., Saiz et al. 2005; Laitinen et al. 2015). For small and/or gradual flux increases, the procedure often yields times that are significantly delayed with respect to the arrival time of the first particles, and high pre-event backgrounds will lead to even longer delays. The correlation of the onset delay with the ratio of the peak fluxes shown in Fig. 5 is an indication for such a systematic uncertainty.

The limitations of the onset determination method we used mean that it is highly questionable whether this simple method is sufficient to resolve timing differences of several minutes. For further analysis, we suggest an evaluation of the pitch-angle dependent fluxes to determine the onset times, as well as a detailed comparison of the detection thresholds of the different instruments.

In conclusion, this study presents a series of near-relativistic electron events and shows the wide event-to-event variability in the radial dependence of commonly used SEE event parameters. As a possible explanation for the wide variability, we specifically pointed out the limitations of the parameters and described the potential shortcomings in the methods we used to derive these parameters. For future studies of the radial evolution of SEE events, we recommend to consider pitch-angle dependent fluxes in order to overcome some of the critical problems with the parameters we used here.

Acknowledgements. Solar Orbiter is a mission of international cooperation between ESA and NASA, operated by ESA. This work was supported by the German Space Agency (Deutsches Zentrum für Luft- und Raumfahrt, e.V., (DLR)) under grant number 50OT2002. N.D. is grateful for support by the Academy of Finland (SHOCKSEE, grant no. 346902). This work received funding from the European Union's Horizon 2020 research and innovation program under grant agreement No. 101004159 (SERPENTINE). The UAH team acknowledges the financial support by the Spanish Ministerio de Ciencia, Innovación y Universidades FEDER/MCIU/AEI Projects ESP2017-88436-R and PID2019-104863RB-I00/AEI/10.13039/501100011033.

References

Acuña, M., Ogilvie, K., Baker, D., et al. 1995, Space Sci. Rev., 71, 5
Acuña, M. H., Curtis, D., Scheifele, J. L., et al. 2008, Space Sci. Rev., 136, 203
Agueda, N., Vainio, R., Lario, D., & Sanahuja, B. 2008, ApJ, 675, 1601
Agueda, N., Lario, D., Vainio, R., et al. 2009, A&A, 507, 981
Brüdern, M., Dresing, N., Heber, B., et al. 2018, Cent. Eur. Astrophys. Bull., 42, 2
Bruedern, M., Berger, L., Heber, B., et al. 2022, in 44th COSPAR Scientific Assembly. Held 16–24 July, 44, 1298
Domingo, V., Fleck, B., & Poland, A. I. 1995, Sol. Phys., 162, 1
Dresing, N., Effenberger, F., Gómez-Herrero, R., et al. 2020, ApJ, 889, 143
Dröge, W., Kartavykh, Y. Y., Klecker, B., & Kovaltsov, G. A. 2010, ApJ, 709, 912
Dröge, W., Kartavykh, Y. Y., Dresing, N., & Klassen, A. 2016, ApJ, 826, 134
Fox, N. J., Velli, M. C., Bale, S. D., et al. 2016, Space Sci. Rev., 204, 7
Galvin, A. B., Kistler, L. M., Popecki, M. A., et al. 2008, Space Sci. Rev., 136, 437
He, H.-Q., & Wan, W. 2012, ApJ, 747, 38
Horbury, T. S., Obrien, H., Carrasco Blazquez, I., et al. 2020, A&A, 642, A9
Jokipii, J. R. 1966, ApJ, 146, 480
Klassen, A., Dresing, N., Gómez-Herrero, R., Heber, B., & Müller-Mellin, R. 2016, A&A, 593, A31
Laitinen, T., & Dalla, S. 2019, ApJ, 887, 222
Laitinen, T., Huttunen-Heikinmaa, K., Valtonen, E., & Dalla, S. 2015, ApJ, 806, 114
Lepping, R. P., Acũna, M. H., Burlaga, L. F., et al. 1995, Space Sci. Rev., 71, 207
Lin, R. P., Anderson, K. A., Ashford, S., et al. 1995, Space Sci. Rev., 71, 125
Mueller-Mellin, R., Green, G., Iwers, B., et al. 1982, Data Processing for a Cosmic ray Experiment Onboard the Solar Probes HELIOS 1 and 2: Experiment 6, Final Report, Oct. 1981 Kiel Univ. (Germany). Inst. für Reine und Angewandte Kernphysik
Müller, D., St. Cyr, O. C., Zouganelis, I., , et al. 2020, A&A, 642, A1
Müller-Mellin, R., Böttcher, S., Falenski, J., et al. 2008, Space Sci. Rev., 136, 363
Ogilvie, K. W., Chornay, D. J., Fritzenreiter, R. J., et al. 1995, Space Sci. Rev., 71, 55
Owen, C. J., Bruno, R., Livi, S., et al. 2020, A&A, 642, A16

Pacheco, D., Agueda, N., Gómez-Herrero, R., & Aran, A. 2017, J. Space Weather Space Clim., 7, A30
Rodríguez-Pacheco, J., Wimmer-Schweingruber, R. F., Mason, G. M., et al. 2020, A&A, 642, A7
Rodríguez-García, L., Gómez-Herrero, R., Dresing, N., et al. 2023, A&A, 670, A51 (SO Nominal Mission Phase SI)
Russell, C. T. 2008, The STEREO Mission (New York: Springer)
Saiz, A., Evenson, P., Ruffolo, D., & Bieber, J. W. 2005, ApJ, 626, 1131
SEPT Online Event List 2022, STEREO Electron Event List
Strauss, R. D., & Fichtner, H. 2015, ApJ, 801, 29
Strauss, R. D. T., Dresing, N., & Engelbrecht, N. E. 2017, ApJ, 837, 43
Vainio, R., Agueda, N., Aran, A., & Lario, D. 2007, in Space Weather: Research Towards Applications in Europe 2nd European Space Weather Week (ESWW2), ed. J. Lilensten, Astrophys. Space Sci. Lib., 344, 27
Wenzel, K. P., Marsden, R. G., Page, D. E., & Smith, E. J. 1992, A&AS, 92, 207
Wibberenz, G., & Cane, H. V. 2006, ApJ, 650, 1199
Wibberenz, G., Kecskeméty, K., Kunow, H., et al. 1989, Sol. Phys., 124, 353

SUMMARY AND OUTLOOK

8

SUMMARY AND OUTLOOK

This thesis is dedicated to the study of solar energetic particle events. With a focus on measurements from EPT on Solar Orbiter, it shows how measurements of the instruments can be interpreted, what instrumental effects may influence the observations and how EPT may help to shed light on open scientific questions regarding SEPs. The aim of this thesis was to answer three fundamental questions.

1. How exactly does EPT respond to directional and energy-dependent fluxes of energetic particles in space? As a basis for the scientific interpretation of the EPT measurements, the detector response functions were determined from Monte Carlo simulations. In a series of simulations the directional energy response of the instrument has been characterised. It has been shown that EPT has a considerable response to particles with energies above the intended measuring range. Further, it was investigated how different masses in the vicinity of the instrument, in particular the spacecraft, affect the instrument response functions. With a simplified spacecraft model it could be demonstrated that the additional masses in the vicinity of the instrument not only function as a shielding – instead they also increase the response to ions with energies above several hundred MeV/nuc. The response functions obtained here are now being used to calibrate the public scientific data of EPT. The quality of the scientific data was further improved by analysing and correcting onboard quantisation errors and nonlinearities in the onboard signal processing of EPT.
2. What instrumental effects must be considered when analysing EPT measurements? Using the simulated response functions, several questionable observations of EPT could be understood. As such, it has been shown that the background in EPT and its variation with time can be explained by high-energy galactic cosmic rays. During periods without SEP events, the count rates in most energy channels of EPT can be fully explained by galactic cosmic ray counts. In addition, it was shown how high-energy electrons can contaminate the EPT ion detector. While the uppermost energy channels – those measuring ions above 2 MeV – are generally free from electron signals, the lower channels can be severely contaminated by electrons. The presented results help to prevent misinterpretations in future studies, for example when analysing arrival times of the ions during an SEP event observed by EPT.

3. How can measurements from EPT be combined with observations made by other spacecraft to study the sources of SEPs and the SEP propagation in interplanetary space? In two publications, measurements of EPT were compared with measurements from other instruments on different spacecraft, enabling a direct comparison of the SEP distribution at various locations throughout the heliosphere. The first publication is devoted to the question of how SEPs manage to fill large parts of the inner heliosphere during widespread SEP events. For the first widespread event observed by Solar Orbiter, different event scenarios were discussed as possible explanations, including a single large source and effective particle transport close to the Sun. Different observational constraints, resulting from the timing of electrons and protons and the observed anisotropies, were discussed. The second publication focuses on the influence of interplanetary transport processes on near-relativistic electron observations. Observations of the same event at different solar distances were compared using event parameters that are commonly used to characterise SEP events. The results show a wide event-to-event variability in the radial dependency of the parameters. As a possible explanation for this variability, limitations of the chosen parameters, instrumental differences and the unknown condition in the interplanetary medium were discussed.

In conclusion, this work has contributed substantially to a better understanding of EPT measurements and provides a basis for the generation of scientifically usable data. It has also shown how EPT measurements can be used to further our understanding of SEP events and has made a scientific contribution to this endeavour.

Based on the results of this work, several additional studies can be motivated: With the response functions determined here, it is possible to identify periods in which the scientific data of EPT is contaminated by unintended particle species or by particles with energies above the expected measuring range. The results can be used, for example, to generate quality flags that indicate such contamination to scientific users. In addition, correction methods can be developed which automatically correct contamination and generate corrected data sets.
The obtained directional response functions allow for a more detailed interpretation of measurements of anisotropic particle fluxes. Future studies can use the directional response functions to derive a better measure of the anisotropy of the observed particle flux. An example of such an application can be found in Brüdern et al. (2022).
For detailed multi-spacecraft studies it is advisable to compare the presented energy and directional response functions of EPT with the corresponding functions of the other instruments. This should clarify whether and to what extent differences in observations of the SEP

event can be explained by differences in the response functions.

As a final note, it should be mentioned that this work's focus on instrumental effects and limitations of EPT should not obscure the fact that EPT generally provides excellent data with high scientific value. With the increasing activity of solar cycle 25 and the change in Solar Orbiter's orbit towards higher latitudes, many more promising EPT observations are to be expected in the upcoming years.

APPENDIX

A

EPT DATA PRODUCTS

Table A.1 lists all data products generated by EPT for the current onboard software configuration (internal version number v10). Table A.2 further explains the EPT COUNTERs that are part of the housekeeping data. Table A.3 further explains the analogue frontend readout (ARB) packets, which are also part of the housekeeping.

Table A.1: List of all EPT data products (onboard configuration version 10).

Data	APID	Cadence/s	Description
Low-Latency Science Data (0x31)			
LL_EPT_e	0x331	30	Counts foil det., 8 DPI per direction
LL_EPT_i	0x331	30	Counts mag det., 18 DPI per direction
LL_EPT_T_e	0x331	5	Counts foil det., 1 DPI per direction
LL_EPT_T_i	0x331	5	Counts mag det., 2 DPI per direction
Nominal Science Data (0x51)			
NO_EPT_mag	0x351	1	Counts mag det., 77 DPI per direction
NO_EPT_foil	0x351	1	Counts foil det., 77 DPI per direction
NO_EPTP_e	0x351	5	Counts of penetrating event, 2 DPI
NO_EPTP_p	0x351	5	Counts of penetrating event, 12 DPI
NO_EPTP_he3	0x351	30	Counts of penetrating event, 5 DPI
NO_EPTP_he4	0x351	30	Counts of penetrating event, 5 DPI
NO_EPTP_he	0x351	30	Counts of penetrating event, 6 DPI
Burst Mode (1) Data (0x61)			
B1_EPT_mag	0x361	10	Counts mag det., 48 DPI per direction
B1_EPTP_he3	0x361	5	Counts of penetrating events, 5 DPI
Housekeeping Data (0x48)			
ARB 0x820c	0x848	60	L1 tigger, HK, ARB clock
ARB 0x81e7	0x848	3600	L1 trigger, PEEKB/A/S, L1 thresh, L2 logic, ARB Filter
REG 0x007f	0x848	600	Register readout
COUNTER 0x40000	0x548	600	Digital board counter (16)
COUNTER 0x40030	0x548	600	Digital board counter (16)
COUNTER 0x40090	0x548	600	Digital board counter (16)
COUNTER 0x400a0	0x548	3600	Digital board counter (12)
COUNTER 0x400c0	0x548	3600	Digital board counter (8)
EEPROM 0xf00000	0x548	3600	EEPROM Readout (chunk)
TABLE 0x202c2000	0x548	3600	CONFIG Table Readout (chunk)
PHA Data (0x54)			
PHA Buffer 0	0x354	300	PHA buffer with invalid events
PHA Buffer 1	0x354	300	PHA buffer with penetrating events
PHA Buffer 2	0x354	300	PHA buffer with stopping events

Table A.2: Description of the HET/EPT housekeeping data. The table describes the digital board counter readout. The counters are transmitted in chunks in the packets COUNTER 0x04000, COUNTER 0x400030, COUNTER 0x0400a0 and COUNTER 0x00400c0 (see Tab. A.1).

Index	Description
Digital board counters and frontend L2 triggers	
0	×1 triggers lost on the analog board.
1	×2 triggers lost on the analog board.
2	×4 triggers lost on the analog board.
3	×8 triggers lost on the analog board.
4	×16 triggers lost on the analog board.
5	×32 triggers lost on the analog board.
6	×64 triggers lost on the analog board.
7	×128 triggers lost on the analog board.
8	l2 #0 triggers.
9	l2 #1 triggers.
10	l2 #2 triggers.
11	l2 #3 triggers.
12	l2 #4 triggers.
13	l2 #5 triggers.
14	l2 #6 triggers.
15	l2 #7 triggers.
Digital Board Counters, SEU Errors	
16	Counter memory uncorrectable seu errors.
17	Telemetry fifo uncorrectable seu errors.
18	l3 register uncorrectable seu errors.
19	Data product schedule uncorrectable seu errors.
20	l3 trigger code uncorrectable seu errors.
21	pps schedule uncorrectable seu errors.
22	(unused) reserved for frontend seu errors.
23	sram uncorrectable seu errors.
24	Counter memory single bit seu errors.
25	Telemetry fifo single bit seu errors.
26	l3 register single bit seu errors.
27	Data product schedule single bit seu errors.
28	l3 trigger code single bit seu errors.
29	pps schedule single bit seu errors.

Table A.2 – continued from previous page

Index	Description
30	(unused) reserved for frontend seu errors.
31	sram single bit seu errors.
Digital Board Counters, communication	
32	pps accepted.
33	pps received via message.
34	pps received via 1 Hz clock from icu.
35	Data product packets.
36	Memory readout packets.
37	Register readout packets.
38	Frontend readout packets.
39	Packet collisions.
40	messages received from icu.
41	messages executed from pps schedule.
42	eeprom bytes written.
43	eeprom bytes read or written.
44	atbrk received, errors 8
45	Lost analog board sync., errors 8
46	Unused.
47	Unused.
Digital Board, Trigger Counters	
48	Lost events received from the frontend.
49	Data products encoded.
50	l3 trigger started.
51	pha records stored/counted.
52	Histogram windows computed.
53	Histogram bin increments.
54	Triggers received for class 0.
55	Triggers received for class 1.
56	Triggers received for class 2.
57	Triggers received for class 3.
58	tfifo put while pushing.
59	tfifo init while sending.
60	Window sum valid.
61	Floating point result valid.
62	log 2 (c) result valid.
63	Compression result valid.

Table A.2 – continued from previous page

Index	Description
Digital Board, uart	
64	Valid bytes received.
65	Invalid bytes received (stop bit missing).
66	Messages received.
67	Message header format errors.
68	Message timeouts.
69	crc errors.
70	fifo uncorrectable seu errors.
71	fifo single bit seu errors.
72	Streaming mode: packet lost.
73	Streaming mode: packet init.
74	Streaming mode: packet submit.
75	Streaming mode: packet put.
76	Unused.
77	Unused.
78	Unused.
79	Unused.

Table A.3: Description of the HET/EPT housekeeping data. The table describes the analog frontend readout. The data is transmitted in the packet ARB 0x820c (see Tab. A.1).

Name	Description
sc 00	l1 trigger counter channel 0.
sc 01	l1 trigger counter channel 1.
⋮	
sc 29	l1 trigger counter channel 29.
hk 400	het preamp temperature
hk 500	ept preamp temperature
hk 401	het Vref, +2.5 V
hk 501	ept sensor temperature
hk 402	het sensor temperature 1
hk 502	ept Vfet/2, +5 V
hk 403	het Vfet/2, +5 V
hk 503	ept Vana/2, +6 V
hk 404	het sensor temperature 2
hk 504	ept Vref, +2.5 V
hk 405	Shaper Vcc/2, +5 V
hk 505	Bias Current
hk 406	Power board temperature
hk 506	Bias Voltage
hk 407	Analog board temperature
hk 507	Digital board temperature

B

IN-FLIGHT CONFIGURATION CHANGES

Since the commissioning of EPT, several in-flight configuration changes have been made. Although most of the changes had little or no impact on the EPT science data, there are some changes that should be noted:

1. Feb. - May 2020: In order to investigate the noise level in the EPT SSDs, the EPT configuration was patched several times and the level-1 thresholds were subsequently lowered from $\sim 25\,\mathrm{keV}$ to $\sim 15\,\mathrm{keV}$. The thresholds were finally set back to $\sim 25\,\mathrm{keV}$.

2. Apr. 29, 2020: In order to increase the PHA statistics, the HET-/EPT configuration was patched and the PHA cadence was increased from 3600s to 600s.

3. Aug. 19, 2020: In order to increase the PHA statistics, the HET-/EPT configuration was patched and the PHA cadence was increased from 600s to 300s.

4. Mar. 24, 2021: Upload of a complete new HET/EPT configuration (v09). In the new configuration, the nominal science data products of EPT were redefined with an increased time resolution and with a wider coverage in deposited energy. Data products that became obsolete due to the changes were removed. A threshold in the EPT l3-trigger was increased in order to exclude minimal ionising particles from the penetrating PHA buffer. Corresponding events were moved to the invalid buffer.

5. Dec 4, 2021: In order to discriminate events that result from cross-talk in the detectors, the EPT l1/l2-trigger logic was changed in a configuration patch (v09.2). After the patch, events with significant signals in the outer segments will be further processed and should now be discriminated by the l3 instead of l2 trigger.

6. Apr. 15, 2024: Along with some changes in the HET logic, the EPT l3 trigger was adjusted in order to improve the handling of negative A-values. Negative A-values can occur when signals from different particles follow each other too quickly or through signal cross-talk in the different segments. Previously, they were interpreted as 0. Due to the adjustment, negative signals are interpreted as positive pulse heights. This patch also introduced a bug that sets the temperature calibration to $-37.3^{\circ}\mathrm{C}$. The bug was later fixed in the configuration v10.

7. Jun. 17, 2024: Upload of a complete new HET/EPT configuration (v10). The configuration incorporated some previous patches and fixed the bug that caused the incorrect temperature calibrations. The configuration also included another fix for a bug in the EPT l3 trigger, where under certain conditions negative A-values were still interpreted as 0.

With the exception of change 4., where data products were redefined, the changes are hardly recognisable in the science data. However, the changes in 5. have reduced the background in the science data ever so slightly (by a few percent depending on the detector) and the changes in 2., 3. and 4. have improved the PHA coverage for the scientifically relevant events. Figure B.1 shows the hourly averaged PHA coverage (number of PHA words divided by the total number of events) from HE1 in a timeline with vertical lines marking the in-flight configuration changes of EPT.

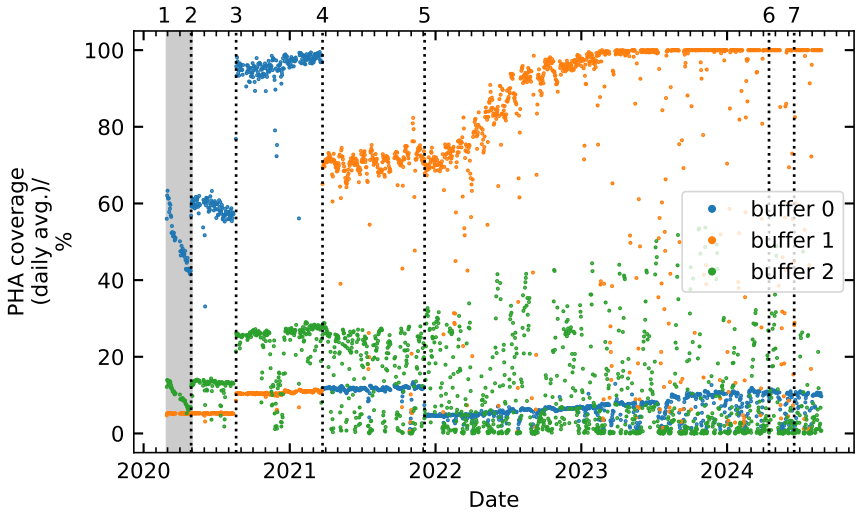

Figure B.1: PHA coverage of HE1. The three colors show the PHA coverage for invalid (buffer 0), stopping (buffer 2) and penetrating events (buffer 1) over time. Vertical lines identify configuration changes.

In 5., the level-1/2 trigger logic of EPT was reconfigured during the in-flight configuration update (version 9.2). Before the patch, both EPT l2-triggers required that none of the outer segments had a level-1 trigger bit set. This logic caused an error, in which events with a large energy deposition in the outer segments were initially vetoed by the level-2 trigger, but subsequently the event created another signal in a centre segment through electronic cross talk. In order to eliminate these cross talk events, patch 9.2 changed the level-1/2 trigger logic in way that any signal >1 MeV in an outer segment will also cause a level-2 trigger. Due to this expansion of the level-2 trigger, most crosstalk signals will fall within the coincidence window of the original large

signal. Thus, both signals can be attributed to the same event and the event can later be identified as invalid by the level-3 trigger. Table B.1 lists the level-2 trigger conditions before and after the patch.

Table B.1: EPT level-1 trigger thresholds and level-2 trigger conditions before and after EPT configuration patch 9.2 (2021-12-04).

Before patch 9.2:

Det.	l1 Thr.	l2 Trig.	Condition
C1-4	25 keV	0	any(C1,C2) & none(A1,A2)
A1-4	60 keV	1	any(C3,C4) & none(A3,A4)

After patch 9.2:

Det.	l1-Thr.	l2 Trig.	Condition
C1-4	25 keV	0	any(C1,C2,A1,A2)
A1-4	1 MeV	1	any(C3,C4,A3,A4)

C

EPT RESPONSE FUNCTIONS

Figures C.1 to C.9 show EPT response matrices determined from Geant4-based Monte Carlo simulations. The figures show the results obtained with different simulation setups, including simulations limited to the instrument aperture (setup-1), 4π simulations (setup-2) and 4π simulations with a spacecraft model (setup-3). The details of the simulations are described in Chapter 4.
Figs. C.1 to C.3 show the response of the NO_EPT_mag data product (stopping particles in the magnet detectors).
Figs. C.4 to C.6 show the response of the NO_EPT_foil data product (stopping particles in the foil detectors).
Figs. C.7 to C.9 show the response of the NO_EPTP_p (ecliptic) data product (penetrating protons).
In addition to the response matrices, Figs. C.10, C.11 and C.12 show direct comparisons of the total response functions obtained from the different simulation setups for the NO_EPT_mag, NO_EPT_foil and NO_EPTP_p (ecliptic) data product, respectively.

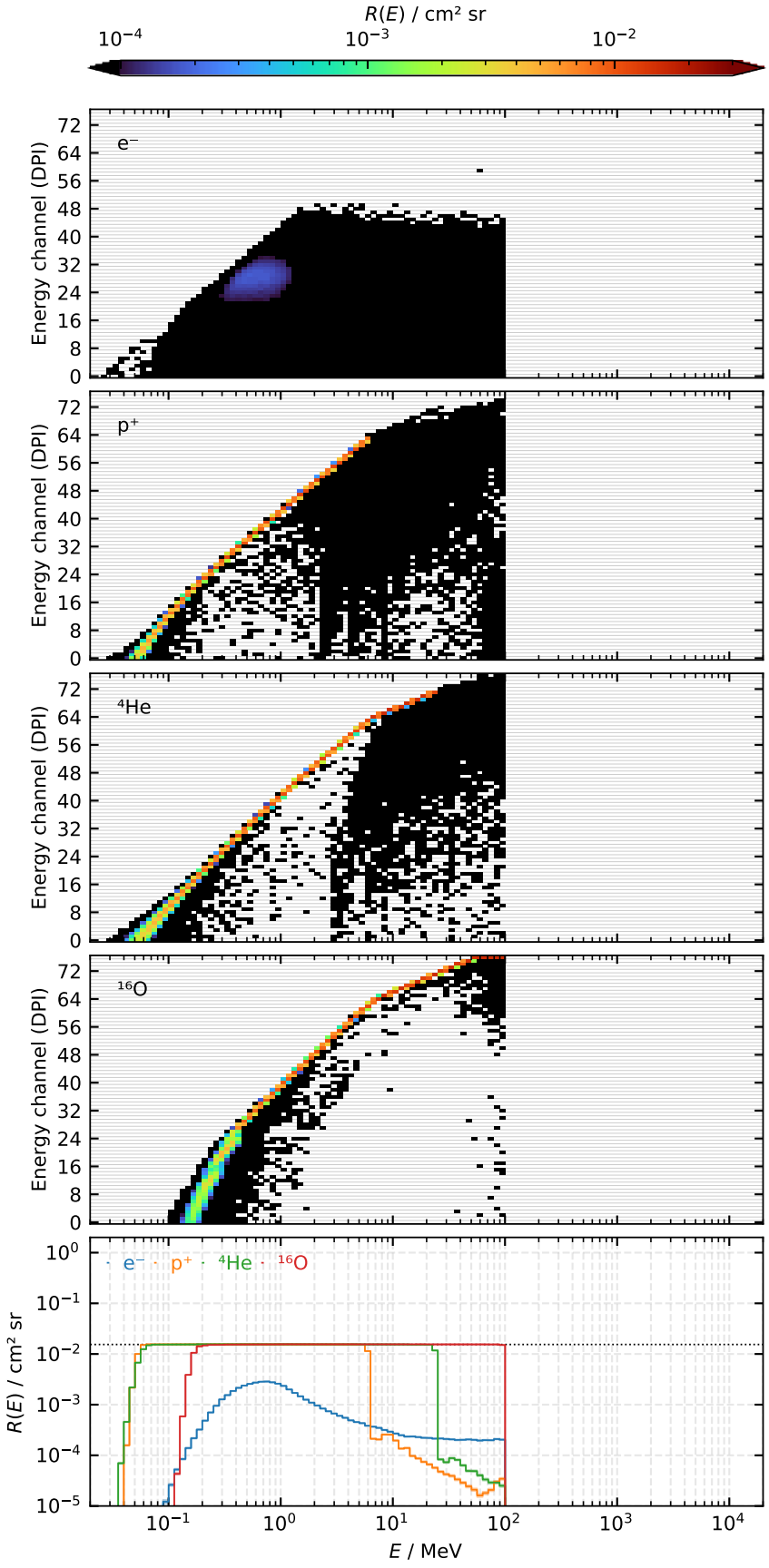

Figure C.1: Response matrices and total response of the **NO_EPT_mag** data product obtained from aperture simulations (setup-1).

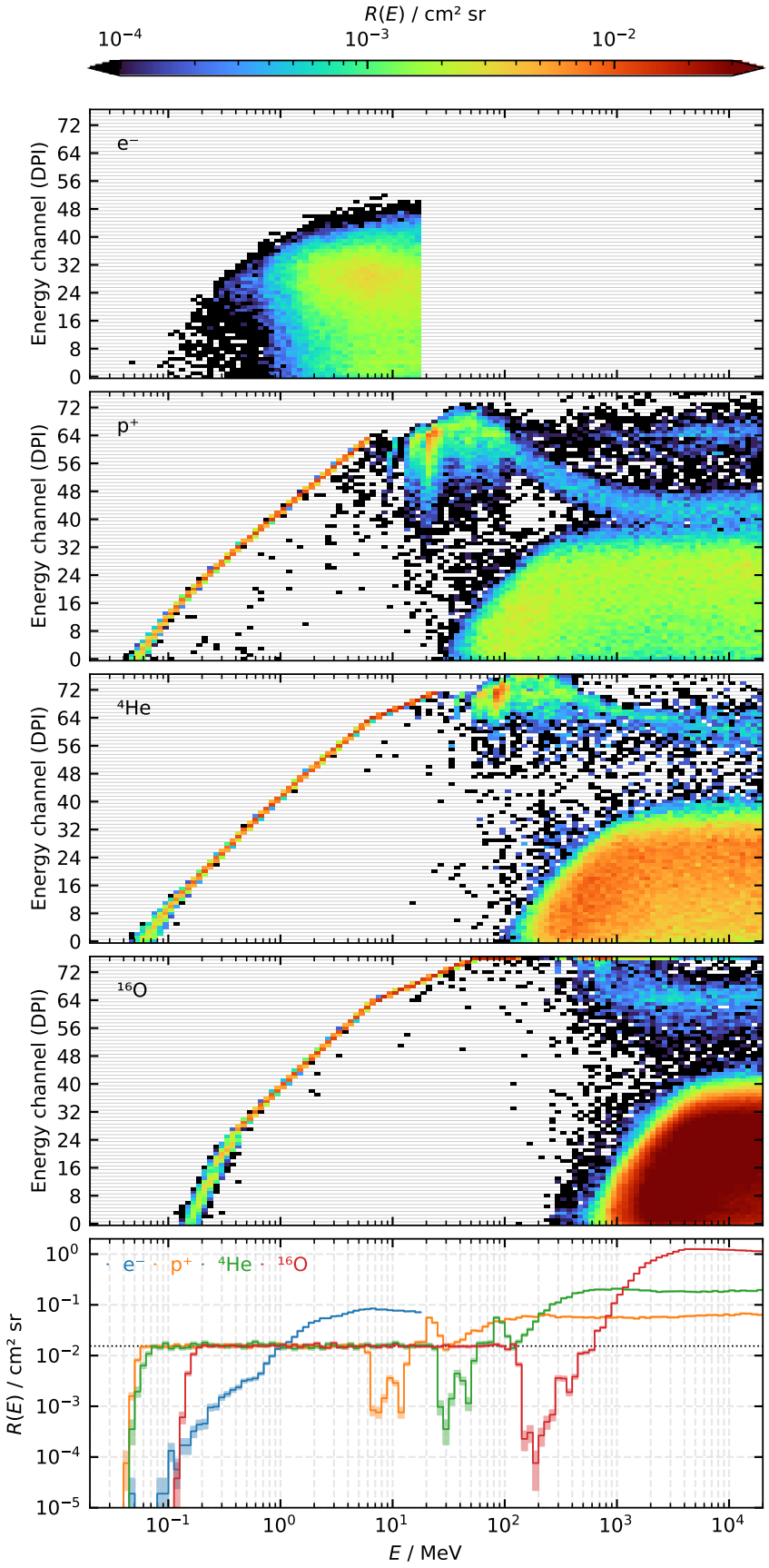

Figure C.2: Response matrices and total response of the **NO_EPT_mag** data product obtained from 4π simulations (setup-2).

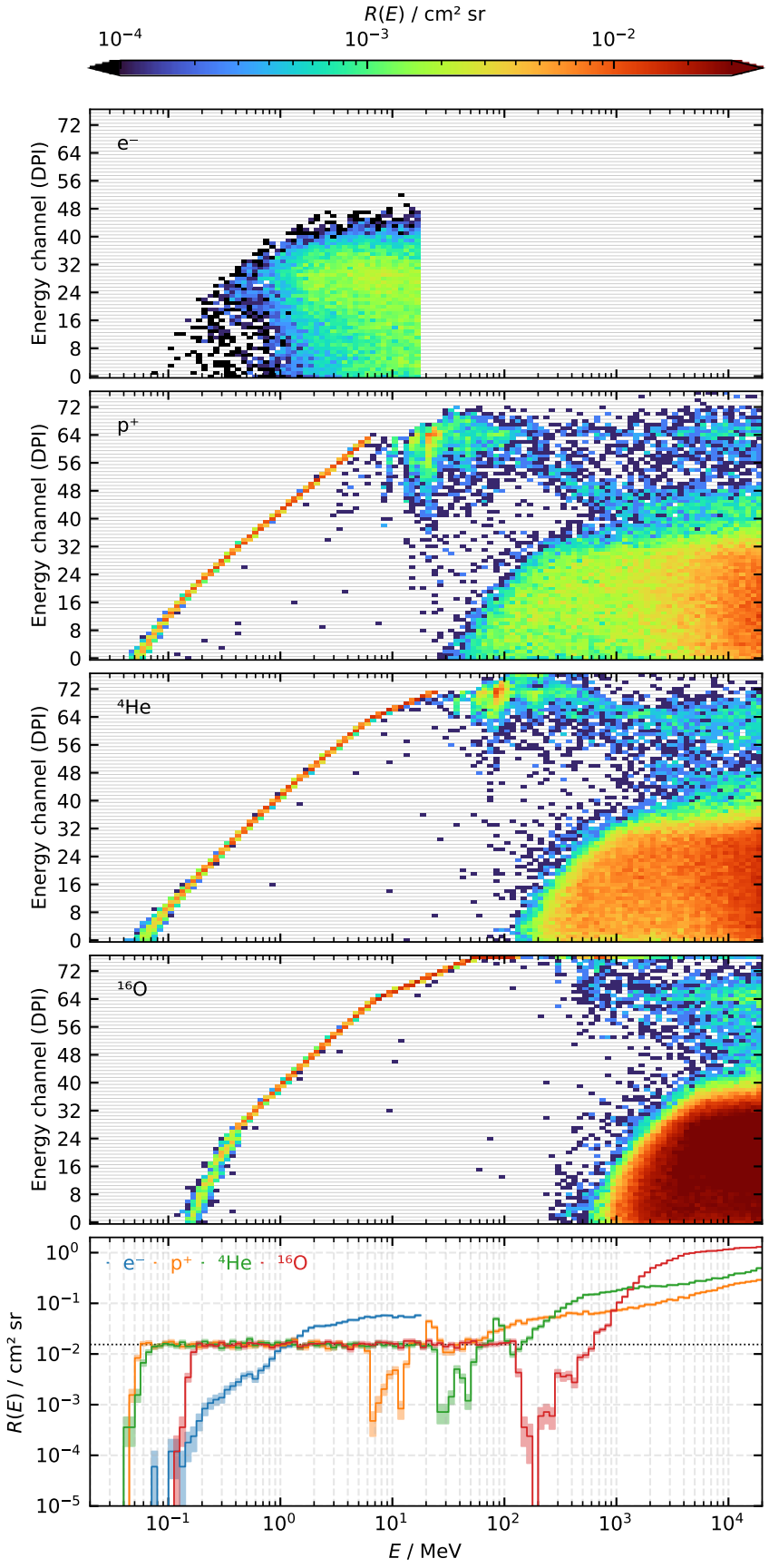

Figure C.3: Response matrices and total response of the **NO_EPT_mag** data product obtained from 4π simulations with the spacecraft model (setup-3).

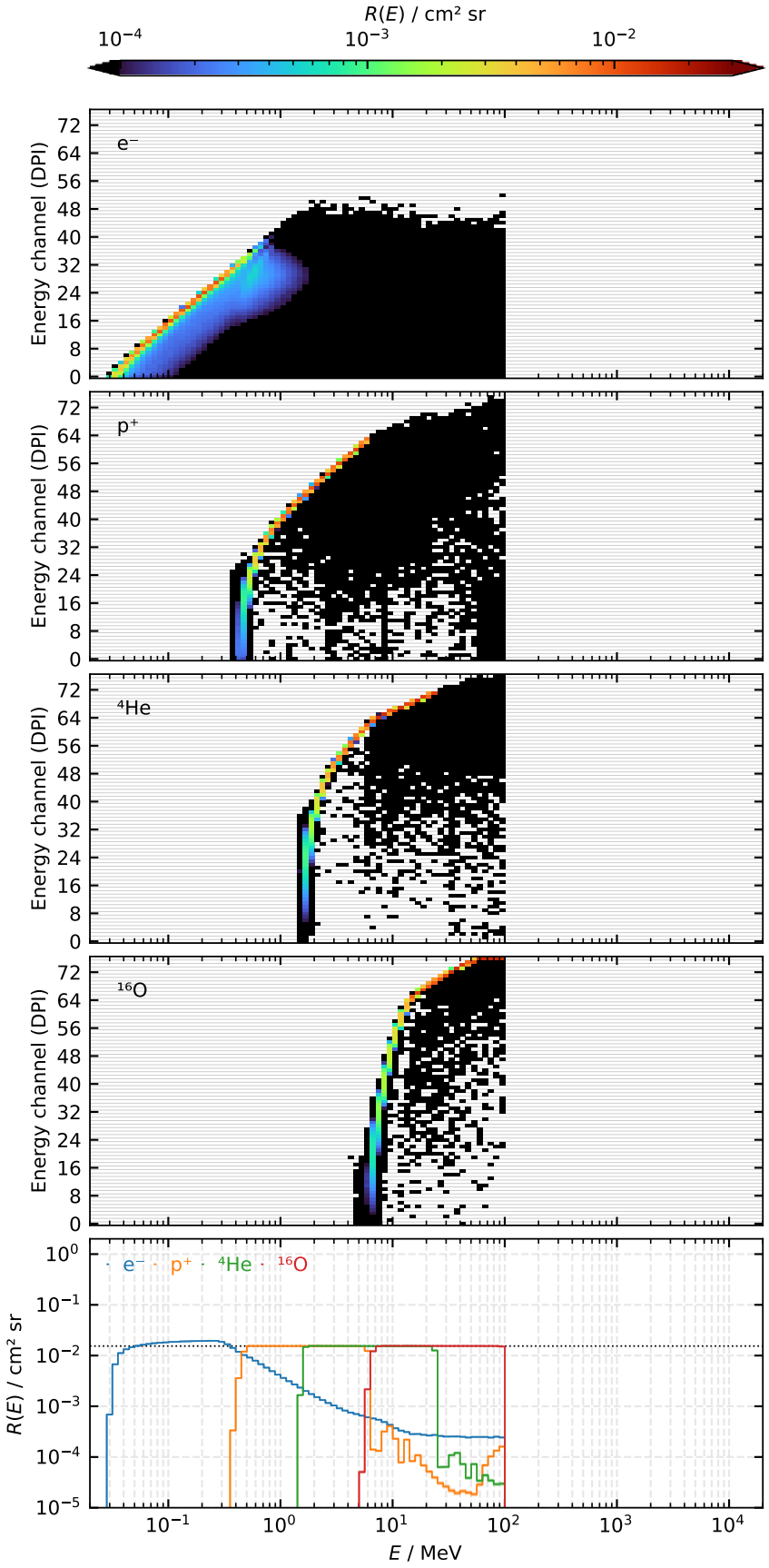

Figure C.4: Response matrices and total response of the **NO_EPT_foil** data product obtained from aperture simulations (setup-1).

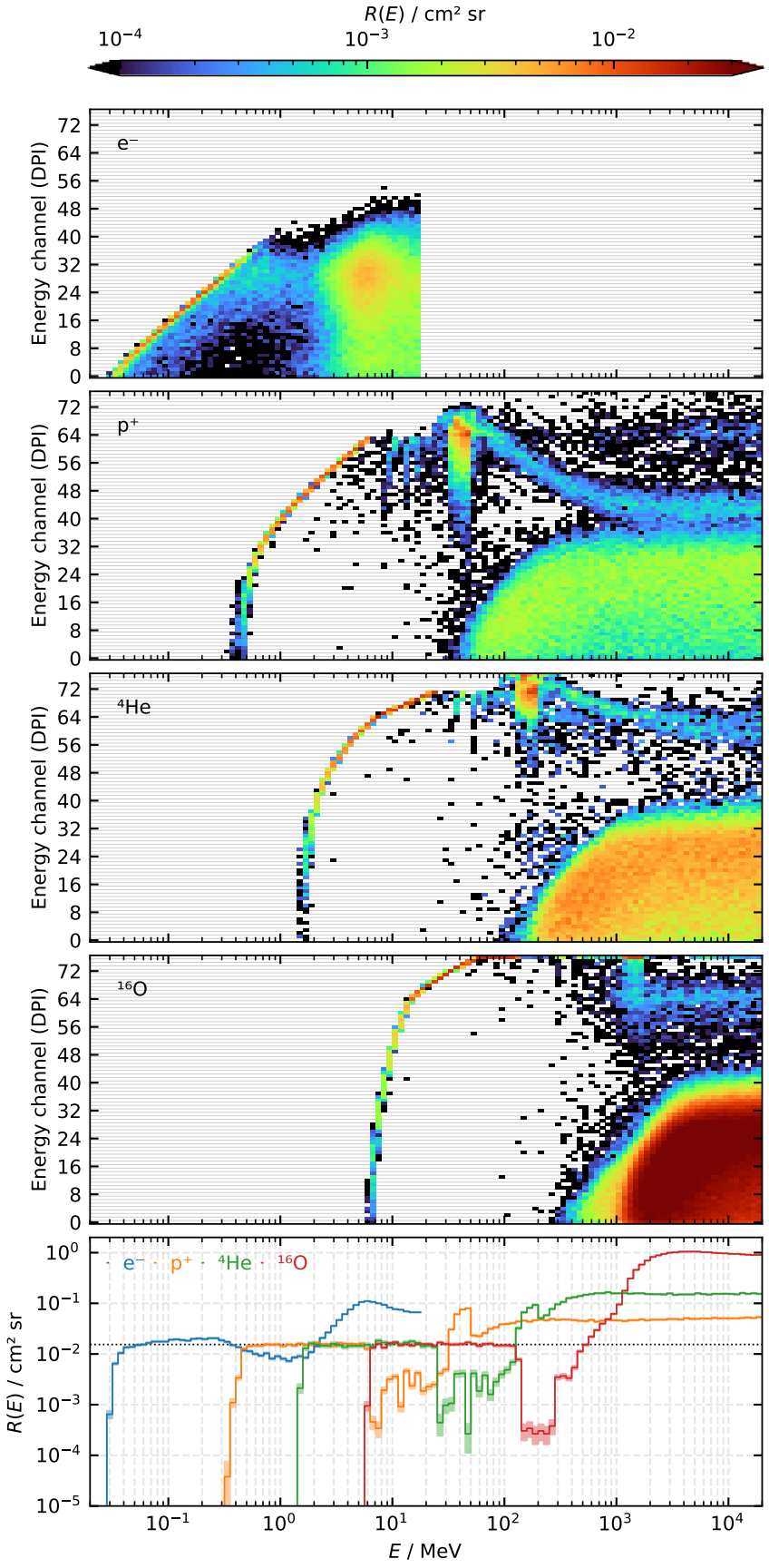

Figure C.5: Response matrices and total response of the **NO_EPT_foil** data product obtained from 4π simulations (setup-2).

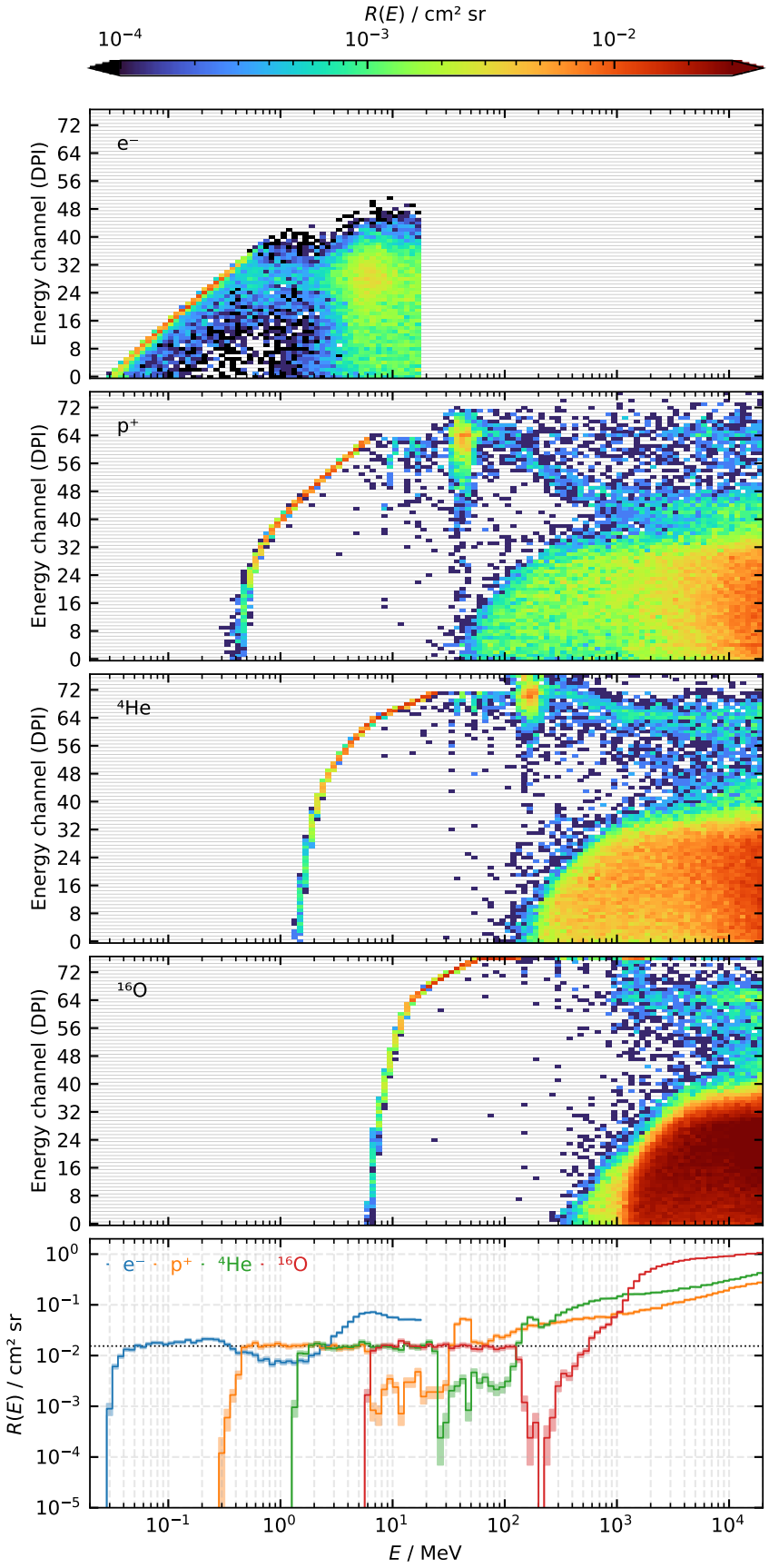

Figure C.6: Response matrices and total response of the **NO_EPT_foil** data product obtained from 4π simulations with the spacecraft model (setup-3).

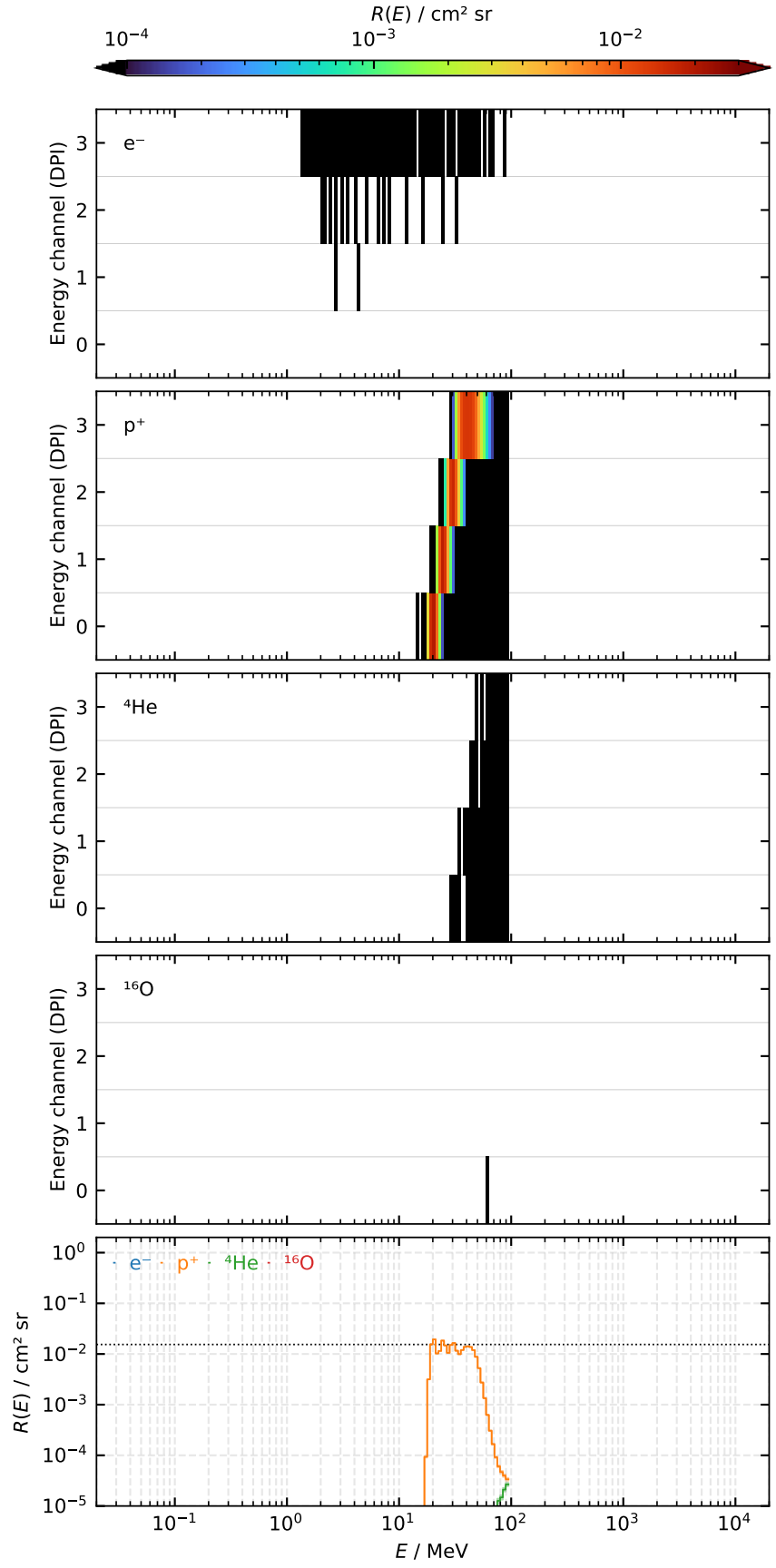

Figure C.7: Response matrices and total response of the **NO_EPTP_p (ecliptic)** data product obtained from aperture simulations (setup-1).

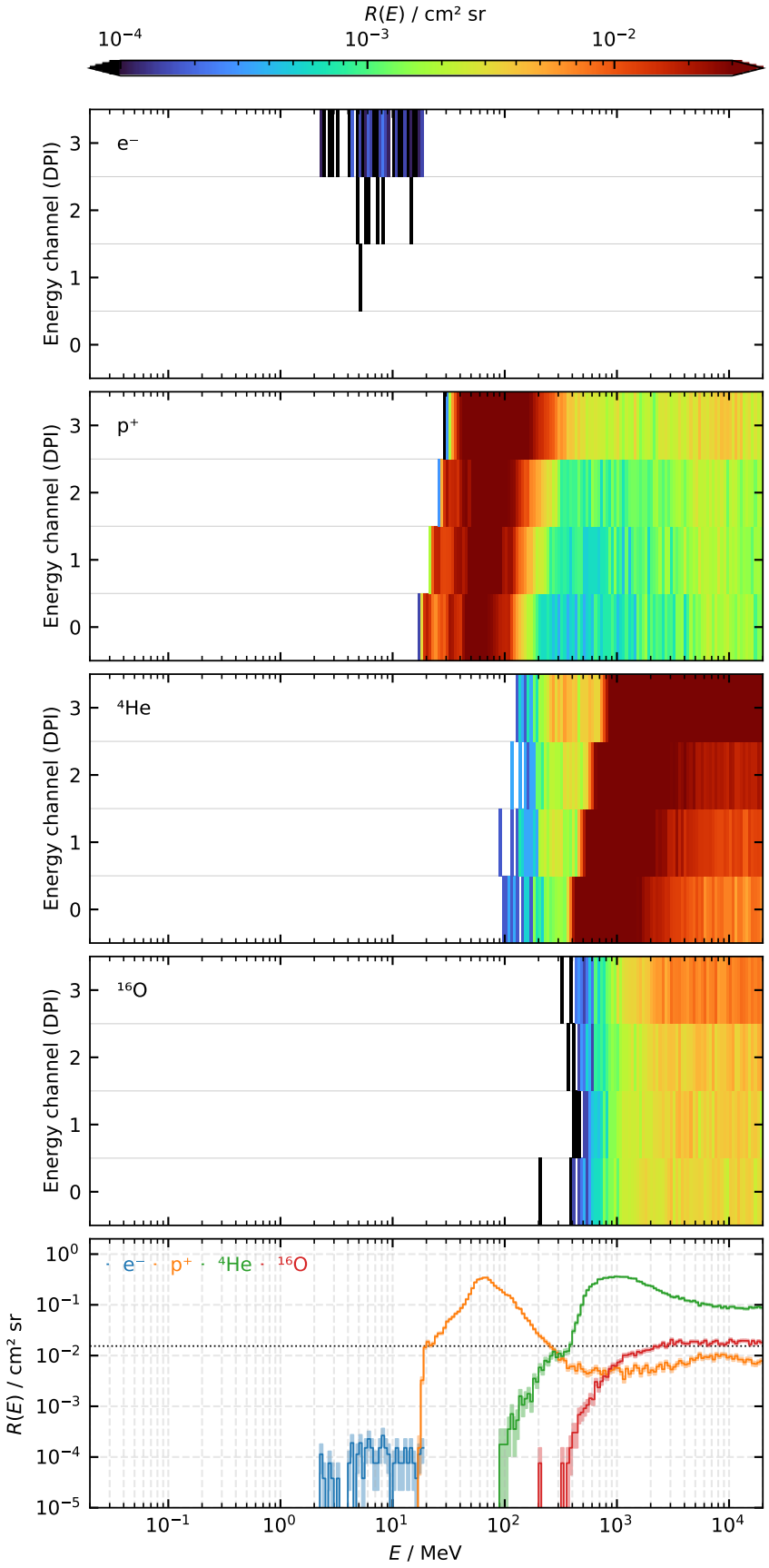

Figure C.8: Response matrices and total response of the **NO_EPTP_p (ecliptic)** data product obtained from 4π simulations (setup-2).

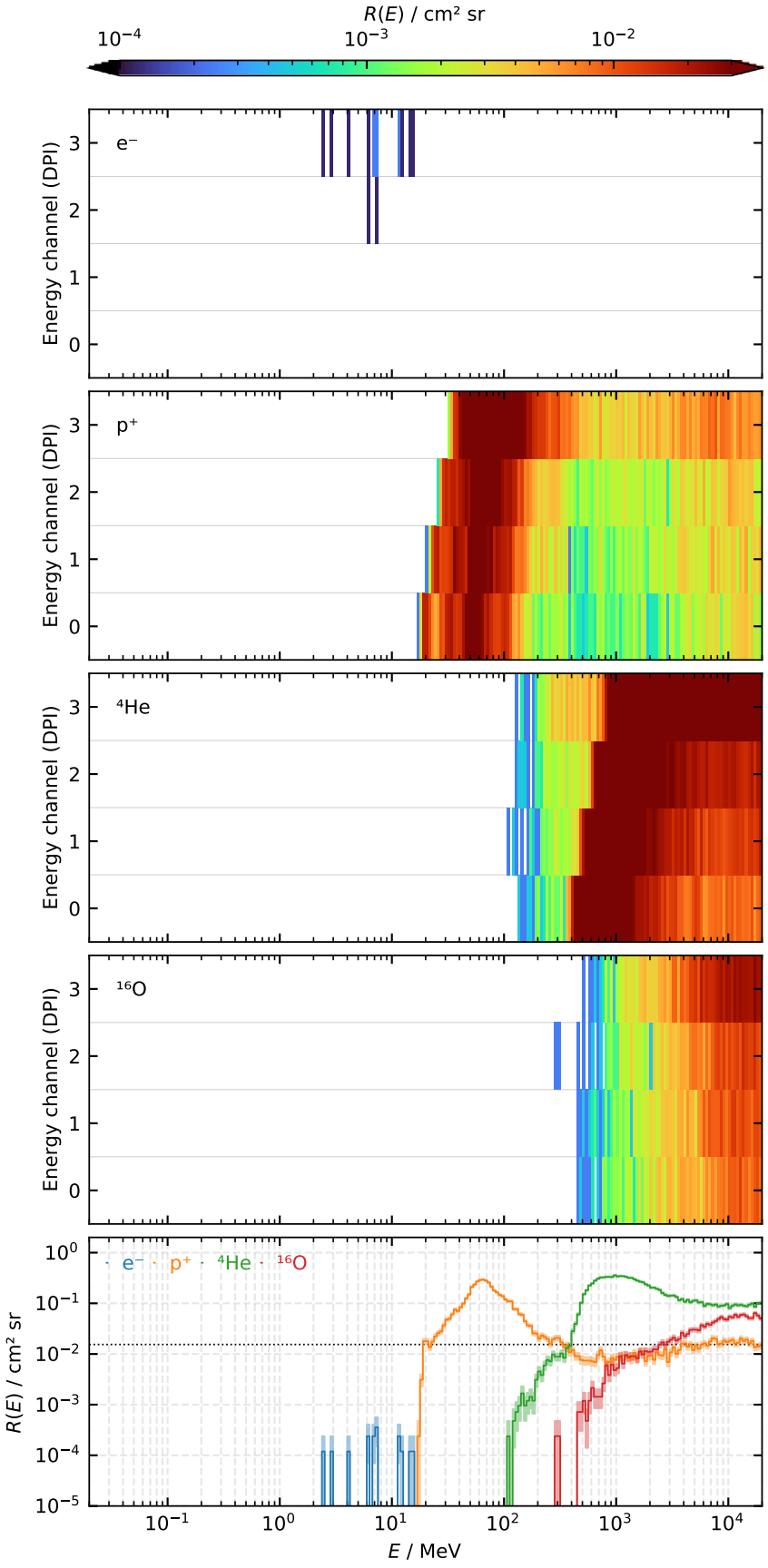

Figure C.9: Response matrices and total response of the **NO_EPTP_p (ecliptic)** data product obtained from 4π simulations with the spacecraft model (setup-3).

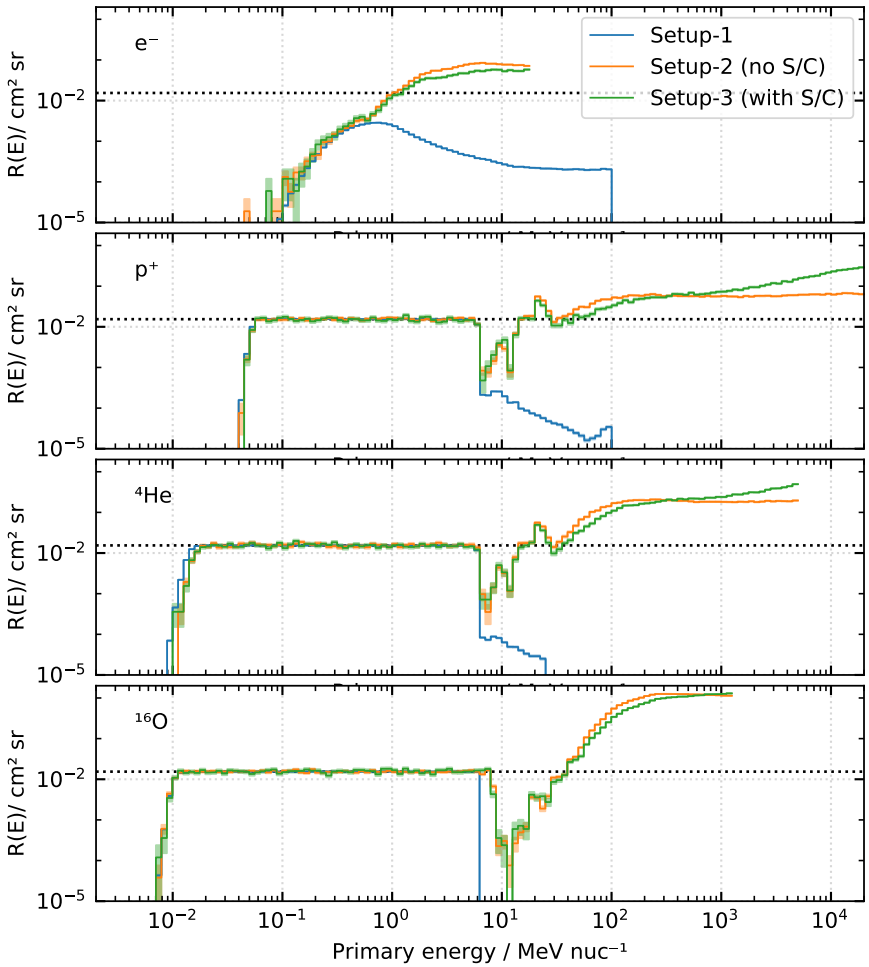

Figure C.10: Total energy response functions of the **NO_EPT_mag** data product obtained from simulations limited to the aperture (setup-1), 4π simulations without the spacecraft model (setup-2) and with the spacecraft model (setup-3). The panels show, from top to bottom, the response for electrons, protons, helium and oxygen.

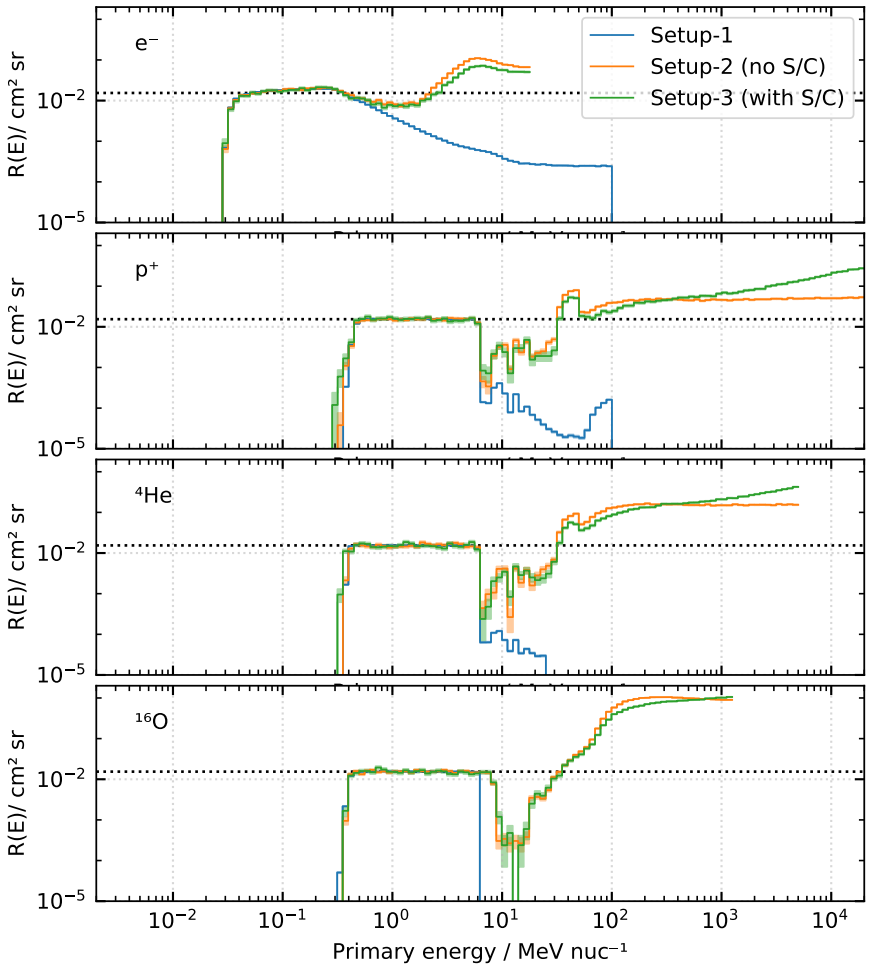

Figure C.11: Total energy response functions of the **NO_EPT_foil** data product obtained from simulations limited to the aperture (setup-1), 4π simulations without the spacecraft model (setup-2) and with the spacecraft model (setup-3). The panels show, from top to bottom, the response for electrons, protons, helium and oxygen.

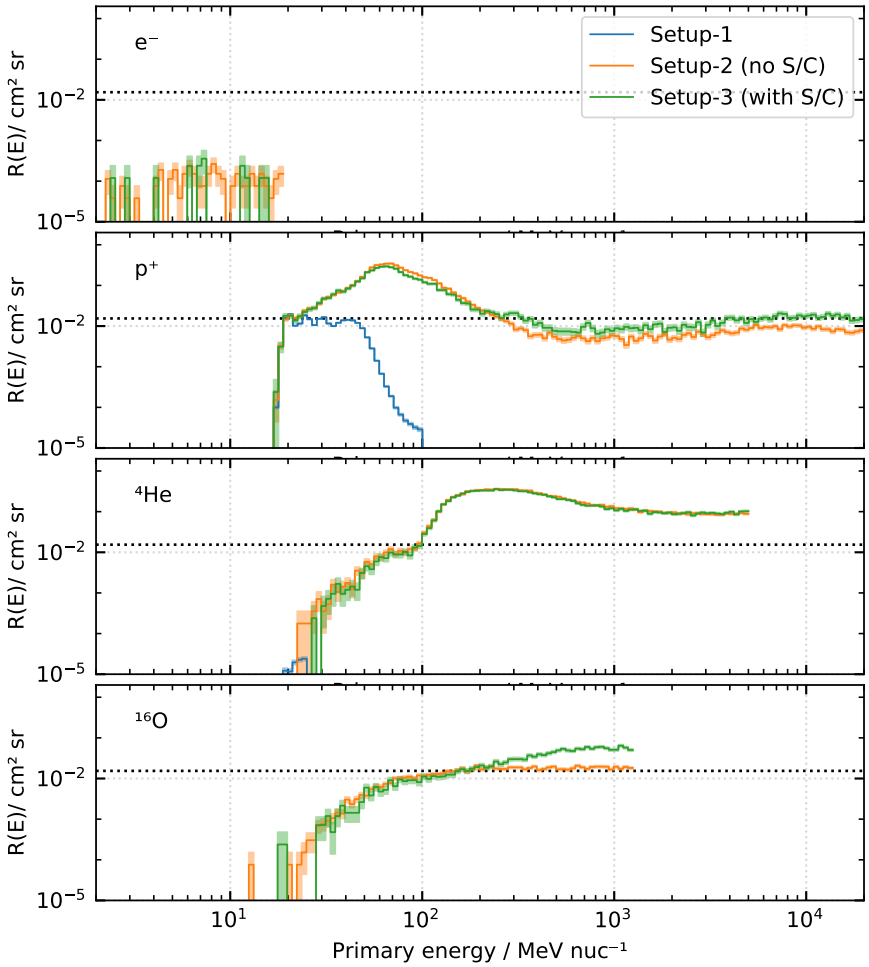

Figure C.12: Total energy response functions of the **NO_EPTP_p (ecliptic)** data product obtained from simulations limited to the aperture (setup-1), 4π simulations without the spacecraft model (setup-2) and with the spacecraft model (setup-3). The panels show, from top to bottom, the response for electrons, protons, helium and oxygen.

D

OPTIMISATION OF THE LEVEL-2 CALIBRATION

After the commissioning of EPT and the accumulation of several months of measurement data, some irregularities in the level-2 calibration became evident. The calibrated particle fluxes obtained with the initial level-2 calibration showed anomalous fluctuations between consecutive energy channels. An example of these fluctuations is shown in the left panel in Fig. D.1. The fluctuations are most prominent in the spectrum of the southward looking telescope below 100 keV where they produce a noticeable zigzag pattern in the spectrum. The pattern occurred independently of the selected time period and could be reproduced in a similar form for almost all periods if sufficient statistics were available.
It is now clear that the onboard quantisation of the deposited energy and nonlinearities in the signal processing were responsible for the fluctuations in the level-2 data. Since such fluctuations may lead to incorrect interpretations of the scientific data, for example when anisotropies are calculated in individual channels, the calibration had to be corrected. In the following, the deficits of the initial calibration (version v02) are described and an optimisation is presented, which resulted in the currently used level-2 calibration (version v03). The right panel of Fig. D.1 shows the improvements of the revised calibration.
The inaccuracies in the v02 calibration mainly resulted from unique quantisations of the deposited energy in the different detectors. The detector-specific quantisations cause the data products to have different effective energy limits for the different detectors. These differences were not properly taken into account in the v02 calibration. In addition, the transformation from the actual deposited energy to the digital onboard measure of the deposited energy (A-value) exhibits differential nonlinearities. These differential nonlinearities can further shift the effective energy limits of the data products and had to be considered.

D.0.1 *Onboard quantisation of the deposited energy*

The electronics in EPT generate a voltage pulse from an energy deposition in a detector which is continuously digitised and processed by the digital filter (see Sect. 3.2.2 for a detailed description). The maximum of the digitised and filtered pulse heights is used as a digital measure (A-value) of the deposited energy. The transform function from deposited energy to an A-value is unique for each detector and has a temperature dependency. In other words, every detector per-

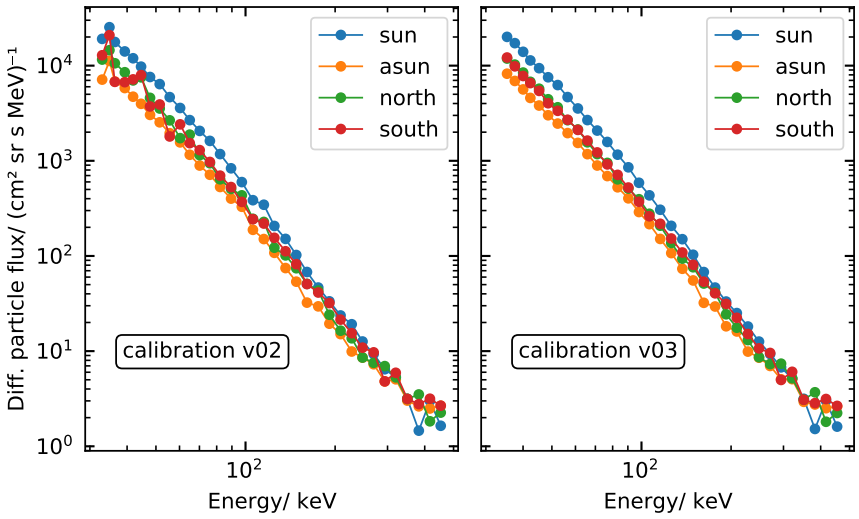

Figure D.1: Comparison of the EPT v02 and v03 level-2 data. Left panel shows the calibrated electron fluxes in each telescope (calibration v02) observed on 2022-13-01 between 07:00 UT and 12:00 UT. The right panel shows the same data calibrated with the updated v03 calibration.

forms a unique quantisation of the deposited energy. Yet, the onboard processing of EPT uses the same histogram bins for all detectors to count the digitised energy depositions. This causes unique quantisation errors for each detector. Figure D.2 illustrates the problem, using two detectors of HE1 as an example.

The quantisation of the actual deposited energy into the onboard pulse height measure (A-value) is shown in panel a). Due to differences in the electronics, the analogue pulse height and its digital measurement (A-value) differ in detectors C2 and C3 for the same deposited energy. Because the transformation also has a a temperature dependence, panel a) will look different for varying unit temperatures. To compensate the differences, an individual A-value-to-keV calibration is used for each detector to calibrate A-values into discrete onboard energy values (shown in panel b)). The onboard energy values are counted in onboard l3 histograms, which are uniform for all detectors (i.e. same energy edges for all detectors). Since the quantisation of the energy is individual, a different number of onboard energy values may fall into the same bin in the different l3 histograms of the respective detectors (see panel c)). For example, l3 histogram bin 62 will count two onboard energy values from detector C2, but only one from detector C3 in the example in Fig D.2 panel c). Thus, the l3 histogram bin 62 is effectively wider for detector C2 than C3. The differences in the effective energy limits propagate directly into the data product items (DPIs), as these are simply sums of certain l3 histogram bins (see panel d)). The full transform function from deposited energy to a certain DPI is therefore unique for each detector (shown in panel e)).

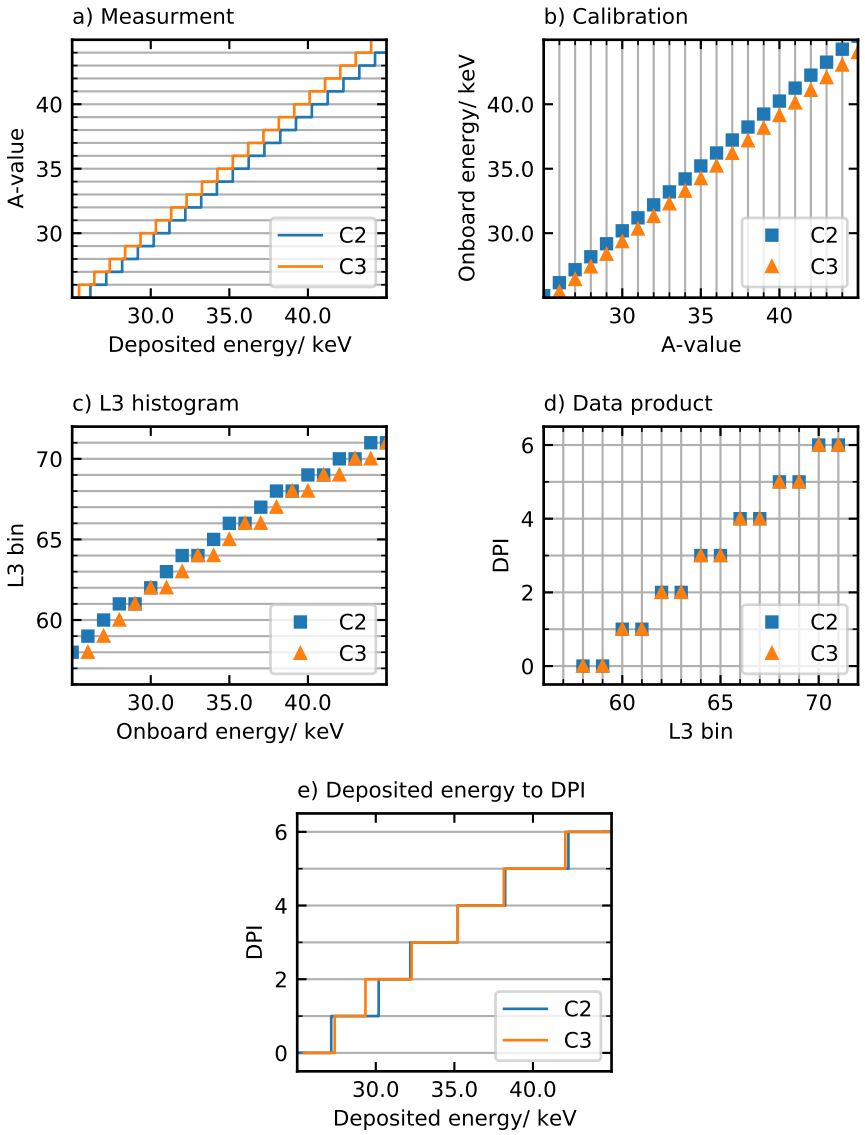

Figure D.2: Illustration of the detector-specific quantisation of the deposited energy in EPT. a) shows the quantisation in measurement of the deposited energy, b) shows the calibration of A-values to discrete onboard energies, c) shows the binning of onboard energy values in the l3 histogram, d) shows the combination of l3 bins to data product items and f) shows the resulting transform function of deposited energy to data product item (DPI).

The unique quantisation of each detector can be determined by modelling the onboard calculations, while taking into account the onboard accuracy and arithmetic. As a result, an exact mapping of A-values to DPIs can be calculated for each detector and each temperature calibration. Figure D.3 shows the resulting mapping for the first 8 DPI of the NO_EPT_foil data product. In principle, this mapping could be used together with the individual A-value-to-keV calibrations to derive effective deposited energy limits for each DPI for each detec-

tor and temperature. However, there are differential nonlinearities in the transformation of deposited energy to A-values that further shift the actual energy limits. These differential nonlinearities cannot be simulated and must be determined separately.

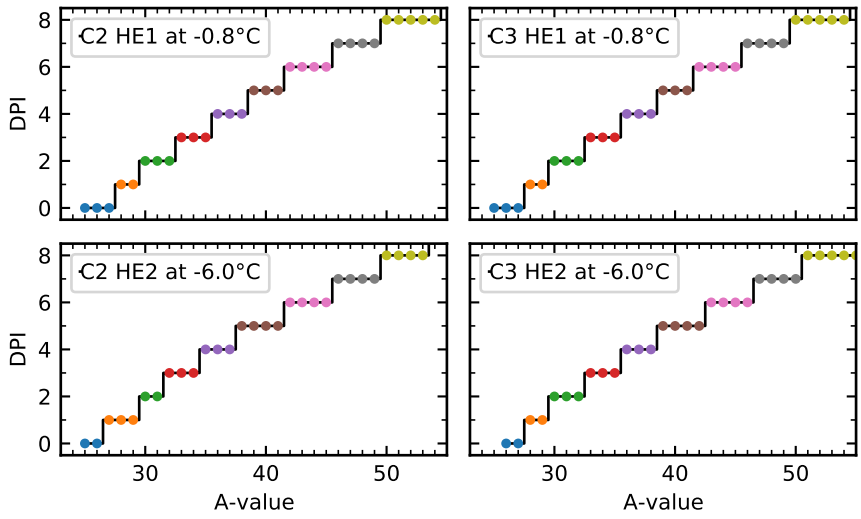

Figure D.3: Detector-specific mapping of A-values to DPIs for the NO_EPT_foil data product. Each panel shows the unique mapping of one of EPT's eight detectors for a HE1 temperature configuration of $-0.8°$ C and HE2 temperature configuration of $-6.0°$ C. Points mark individual A-values. The colour indicates the mapping to a specific DPI.

D.0.2 *Differential nonlinearities in the signal processing*

An investigation of the EPT PHA data has shown that the transformation of the deposited energy into A-values suffers from differential nonlinearitys (DNLs). Figure D.4 illustrates the general nature of these DNLs. The transfer function from deposited energy to A-values is not given by uniform steps as one would expect from an ideal quantisation (black line in Fig. D.4). Instead, the width in deposited energy varies between consecutive A-values (red line Fig. D.4). The deviation from the ideal transformation function are the DNLs that need to be characterised in order to get an accurate mapping between deposited energy and A-values.
Identifying the underlying cause of the DNLs in EPT is difficult. Partially they are likely to result from the limited resolution of the ADC in combination with the operation of the digital filter. The digitisation of the shaped voltage pulses to multiple ADC values and the subsequent calculation of a linear combination with a set of coefficients in the digital filter (for a detailed description see again Sect. 3.2.2) will inevitably lead to some DNLs. But other factors may also play a role. The position

of the base line, which is the voltage behind the analogue chain that is present when no particle is measured, the noise on the shaped pulse signal and the phase between the shaped pulse and ADC clock are some examples of possible factors that could affect the DNLs. Given the large number of possible factors, an analytical determination of the DNLs seems unpromising, thus an empirical estimation is preferred.

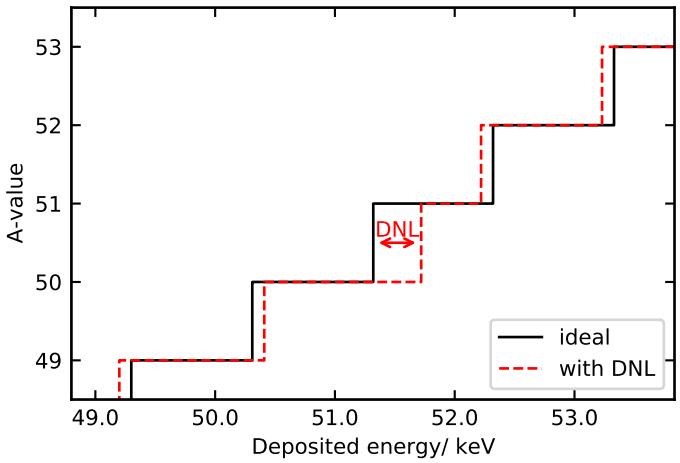

Figure D.4: Illustration of differential nonlinearity in the quantisation of the deposited energy. The black line shows an ideal linear quantisation. The red line illustrates the actual quantisation with DNLs in EPT.

Unfortunately, the DNLs in EPT were not characterised pre-flight. On ground, the DNLs could have been measured with a signal generator, which simulates the analogue chain with well-defined pulses. By linearly ramping up the pulse height in the generator, a quasi-scan of the deposited energy can be performed. Then the DNLs can be derived from the frequencies of measured A-values. An example of such a pre-flight characterisation of DNLs can be found in (Müller-Mellin et al., 2008, Sect. 4.1), where the DNLs in SEPT were determined.
For EPT, the DNLs can now only be characterised by analysing in-flight data. With the PHA data it is possible to determine the frequency of individual A-values, but in difference to a pre-flight calibration the actual frequency of the signal in deposited energies is not known. Nevertheless, under some assumptions, the DNLs may be determined solely from the frequencies of the measured A-values. To do so, it is assumed that the spectrum of the measured particles has a continuous smooth distribution in deposited energy that is described locally by a power-law. Additionally, it is assumed that the DNLs of consecutive A-values add up to approximately zero over larger A-value ranges (e.g. more than 20 A-values). Using these assumptions, the measured frequencies N of the A-values can be smoothed with local power-law fits in order to obtain ideal frequencies $<N>$ that a detector without DNLs would observe. From the ratio between the smoothed frequen-

cies and the actual measured ones, the DNLs can be characterised by calculating a DNL factor $a = <N> / N$ for each A-value.
Figure D.5 shows the frequency of individual A-values that occurred in the PHA data over a time period of nine months (January 3, 2022 to October 3, 2023). Due to the DNLs, the frequencies of consecutive A-values vary significantly, i.e. by values much larger than $\sqrt{N}$, which is expected from Poisson counting statistics.

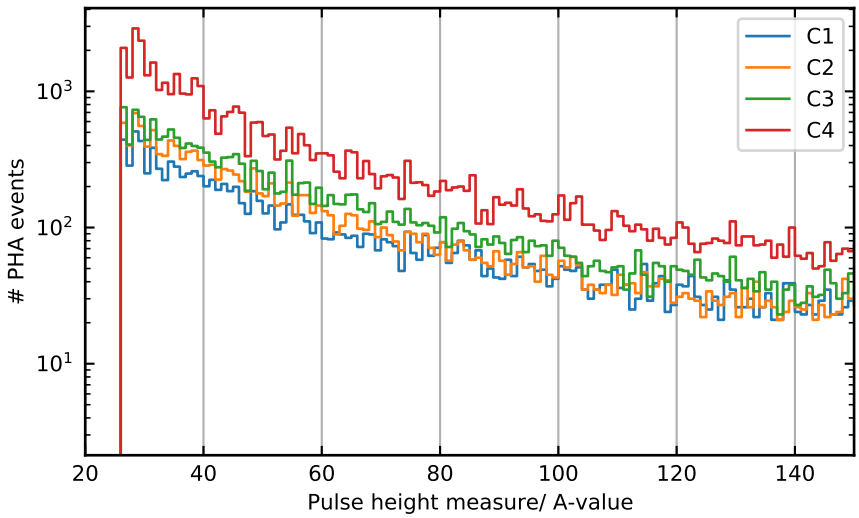

Figure D.5: EPT PHA spectra with fluctuations between consecutive A-values due to DNLs. Created with data gathered by the four HE1 detectors between 2022-01-03 and 2022-10-03.

Figure D.6 shows the smoothing of a PHA spectrum used for the determination of the DNLs. The smoothed A-values are determined by local fits. For each A-value, a fit of the function $N(A) = a \cdot A^b$ is performed in a range of ± 10 A-values around the respective A-value. The smoothed frequency is then given by the function value for the respective A-value. The edges of the spectrum present an exception: Here, the fit range is limited by an edge and thus will be asymmetric around the respective A-value. For example, the smoothed frequency of the A-value 27 is derived from a local fit in the A-value range 25 to 35, since 25 is the lower edge of the PHA spectrum.
As the exact cause of the DNLs is not known, it cannot be ruled out that the DNLs change over the mission. Du to ageing of the detectors, leakage currents and the noise in the detectors might increase over time. In principle, this could change the pattern of the DNLs.
In addition, the DNLs appear to have a strong temperature dependency. Figure D.7 compares the DNLs determined from different PHA spectra that were recorded at different times and at different instrument temperatures. While there are clear differences in the DNLs in the spectra recorded at different instrument temperatures, the DNLs in the spectra recorded at different times (months apart) but at a similar temperature,

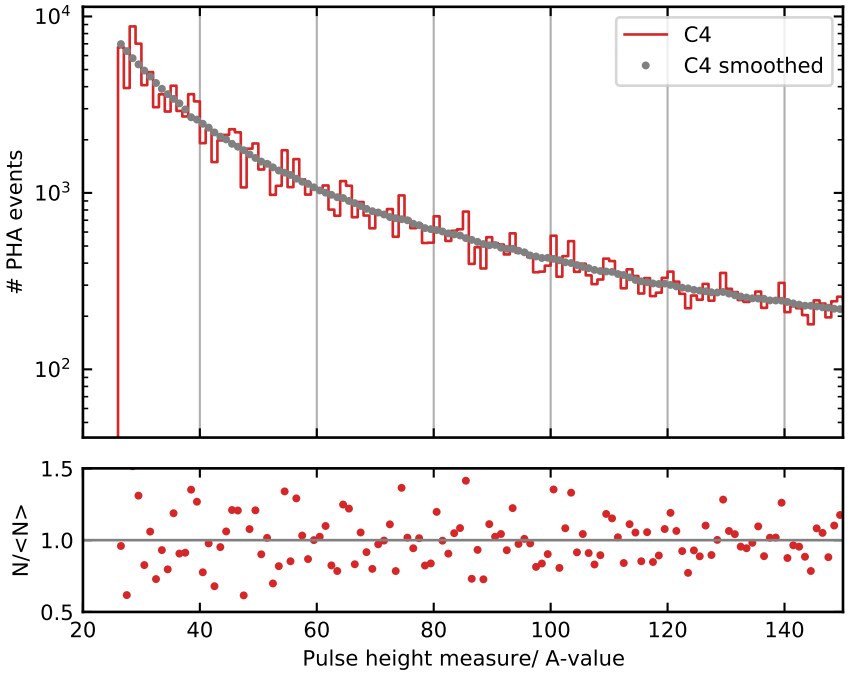

Figure D.6: Example of an EPT PHA spectrum smoothed with local power-law fits (top panel). The ratio of the measured frequency N and the smoothed frequency $<N>$ (bottom panel) is used to characterise the DNLs.

show similar patterns. Thus, the effect of the temperature on the DNLs is currently more important than the ageing effect. This may change over the ongoing mission and therefore, changes in the DNLs over time should be monitored occasionally.

Since March 2022, both EPT units are heated to almost constant temperatures and previous temperature variations related to the orbit and the thermal emission of neighbouring instruments are significantly lower now. As a result, since March 2022, it is possible to characterise the DNLs with a single set of DNL factors. Before March 2022, the DNL pattern was constantly altered due to temperature changes, which makes it practically impossible to determine reliable DNL factors for this period.

To optimisation the level-2 data, a set of DNL factors was derived from the PHA data accumulated between March 2022 to February 2023. The factors were derived by performing a bootstrap test, which can be used to determine not only mean DNL factors for the given time period but also a measure for their accuracy.

In the considered period, EPT has recorded over 76000 PHA buffers for stopping events. The majority of these buffers were filled up to their 1 kB limit and contained 43 PHA words of stopping events. For the bootstrap test, 20000 PHA buffers are drawn with replacement from the 76000 buffers to generate new samples of the data. In total, 100

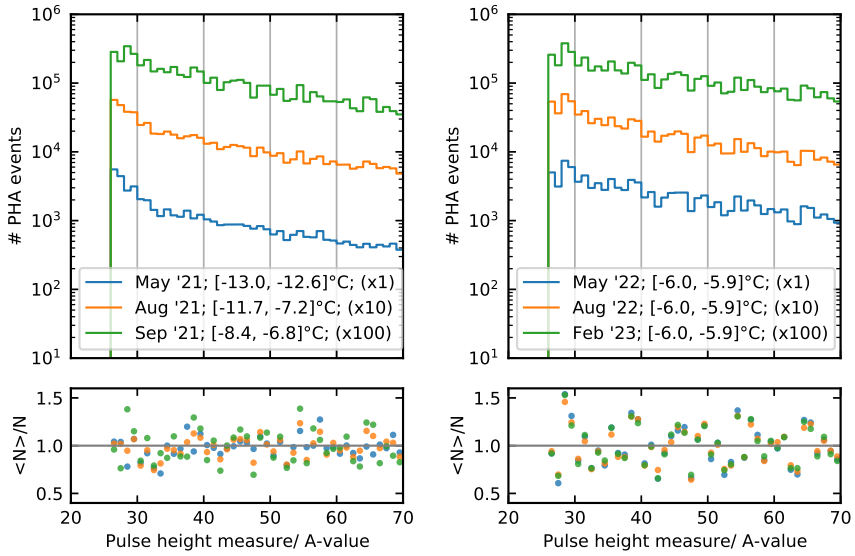

Figure D.7: Comparison of the DNL pattern in different time periods and at different temperatures. The left panels show PHA spectra and DNL factors from three different periods that were measured at different instrument temperatures. The corresponding temperature ranges are given in the legend. The right panels show PHA spectra and DNL factors from three different periods that were measured after March 2022 at almost constant instrument temperatures.

new samples of the data are generated in this way. For each new sample, a PHA spectrum is generated using all PHA words in the sample. Next, the spectrum is smoothed and DNL factors are determined by calculating the ratio of smoothed to measured events. The DNL factor derived from one sample and for one A-value represents one bootstrap estimate here. The distribution of all 100 bootstrap estimates are then analaysed separately for each A-value. As an example, Figure D.8 shows the distribution of the bootstrap estimates for eight different A-values. The mean values present the final DNL factors, while the 95%-confidence levels are used as a measure for the uncertainty. The confidence levels are quite narrow for lower A-values but increase for larger ones. The reason for this are the lower statistics of higher A-values in the PHA data. Fortunately, the DNL of higher A-values is not very relevant, since high A-values are generally gathered in wider DPIs in the final science data. Thus, larger A-values are always combined with several other A-values in one DPI and their DNLs will tend to compensate each other. Following the initial assumption, the DNLs from a large number of A-values will add up to zero and therefore the DNL of large A-values (e.g. >200) are assumed to be irrelevant here. Using the method described, DNL factors are determined for all eight EPT centre detectors.

Finally, the DNL factors obtained for the different detectors are mul-

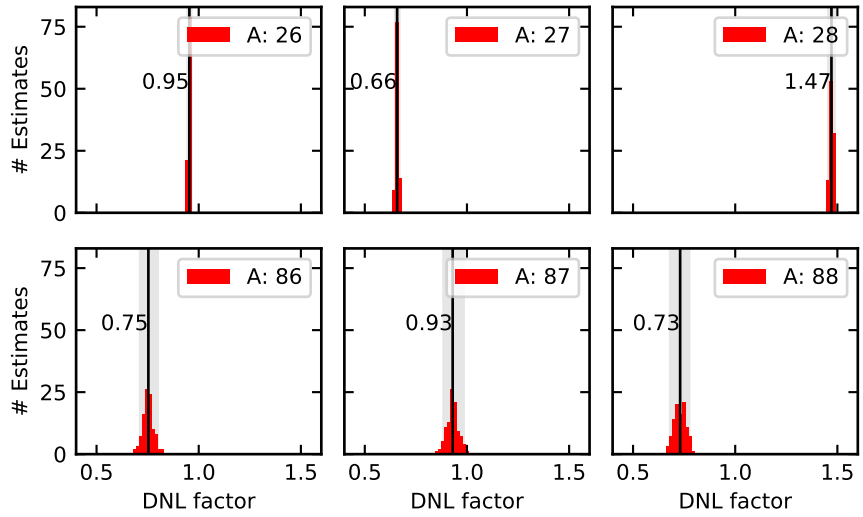

Figure D.8: Example of the distribution of bootstrap estimates of DNL factors for different A-values in one detector. Vertical black lines show mean values, grey shaded areas indicate 95%-confidence intervals.

tiplied with the corresponding energy calibration factors and the A-value-to-DPI mapping (described in the previous section) is used to determine effective deposited energy limits of each DPI for each detector. The final effective energy limits are tabulated in the appendix E.

Using these effective deposited energy limits, detector-specific response functions can be calculated from the Monte Carlo simulations. Figure D.9 shows an example for the response functions of the DPIs of the NO_EPT_foil data product. The important difference of these v03 response functions in comparison to the previously used ones (v02) is that now all DPIs have detector-specific response functions. The detector differences can be seen e.g. by comparing the response functions of DPI 2 (first orange line on the left in each panel) in the different detectors in Fig. D.9.

From the new response functions, new level-2 calibration factors (v03) are derived for the two main data products NO_EPT_mag and NO_EPT_foil. The method for determining the primary energy limits E_{low} and E_{high} has been slightly adjusted so that the calibration provides the same energy limits for all four viewing directions: The energy limits for the NO_EPT_mag DPIs were determined from the HE1 C4 response functions (sunward looking magnet detector) at a temperature configuration of $-6.0°$C, following the procedure described in Sect. 5.1. The energy limits for the NO_EPT_foil DPIs were determined from the HE1 C2 response functions (sunward looking foil detector) at a temperature configuration of $-6.0°$C. With the primary energy limits set, detector-specific effective geometry factors $\overline{g}$ are then calculated

for each detector using the individual response functions. The final level-2 v03 calibration factors are tabulated in the appendix E. The black vertical lines in Fig. D.9 show the energy limits determined from the response functions of the sunward looking detector. The horizontal black lines show the corresponding effective geometry factor for each detector.

Finally, it should be noted that it may seem questionable why the differences in the response functions of the individual detectors are only taken into account by different geometry factors in the level-2 calibration and not by different primary energy limits. This is only possible by assuming a certain spectral shape and may lead to additional systematic errors in the calibrated level-2 fluxes. However, this way the calibration produces a data set that is easier to analyse, as fluxes observed in the different telescopes can be directly compared in the same energy range.

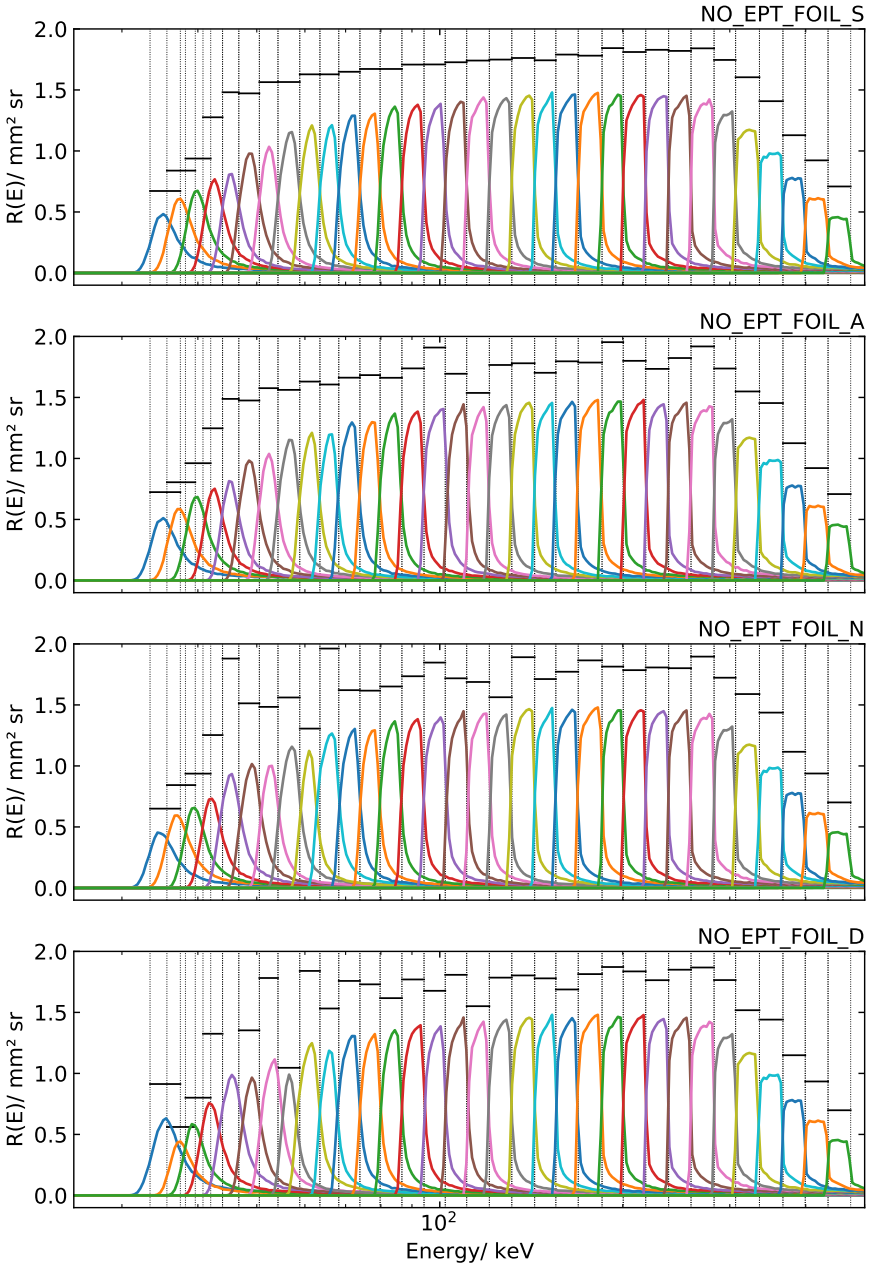

Figure D.9: Response functions of the NO_EPT_foil data product used in the level-2 v03 calibration. The four panels show the response functions of the four EPT foil detectors. Black vertical lines show the primary energy edges of the calibration, which are the same for all four detectors. Horizontal black lines show the effective mean geometry factors for each channel.

E

EPT CALIBRATION

EPT A-VALUE-TO-KEV CALIBRATION

The EPT level-3 trigger calibrates A-values to keV. The calibration is unique for each detector and has a temperature dependency. Calibration factors were calculated for each detector for discrete temperature values. Table E.1 lists the factors for the different detectors and for discrete temperatures. The factors used onboard can be set from ground via commanding, according to the observed unit temperatures.

Table E.1: List of EPT A-value-to-keV calibration factors.

Unit & Detector		Temp./°C										
		−37.3	−31.5	−24.9	−17.7	−11.6	−6	−0.8	4.4	9.8	15.4	21.6
HET/EPT1	C4	0.995	0.999	1.002	1.005	1.007	1.008	1.009	1.009	1.009	1.009	1.008
	A4	0.989	0.993	0.996	0.999	1.001	1.002	1.003	1.003	1.003	1.003	1.002
	C3	0.976	0.980	0.983	0.986	0.988	0.989	0.990	0.990	0.990	0.990	0.989
	A3	0.990	0.994	0.997	1.000	1.002	1.003	1.004	1.004	1.004	1.004	1.003
	C2	0.978	0.982	0.985	0.988	0.990	0.991	0.992	0.992	0.992	0.992	0.991
	A2	0.999	1.003	1.006	1.009	1.011	1.012	1.013	1.013	1.013	1.013	1.012
	C1	0.991	0.995	0.998	1.001	1.003	1.004	1.005	1.005	1.005	1.005	1.004
	A1	0.974	0.978	0.981	0.984	0.986	0.987	0.988	0.988	0.988	0.988	0.987
HET/EPT2	C4	0.982	0.984	0.984	0.985	0.985	0.985	0.984	0.983	0.982	0.981	0.979
	A4	0.995	0.997	0.997	0.998	0.998	0.998	0.997	0.996	0.995	0.994	0.992
	C3	0.976	0.978	0.978	0.979	0.979	0.979	0.978	0.977	0.976	0.975	0.973
	A3	0.996	0.998	0.998	0.999	0.999	0.999	0.998	0.997	0.996	0.995	0.993
	C2	1.004	1.006	1.006	1.007	1.007	1.007	1.006	1.005	1.004	1.003	1.000
	A2	0.995	0.997	0.997	0.998	0.998	0.998	0.997	0.996	0.995	0.994	0.992
	C1	0.988	0.990	0.990	0.991	0.991	0.991	0.990	0.989	0.988	0.987	0.985
	A1	1.035	1.036	1.037	1.038	1.038	1.038	1.037	1.036	1.035	1.033	1.031

A-VALUE AND DEPOSITED ENERGY RANGES

Due to a detector-specific and temperature-depended onboard quantisation of the deposited energy and differential nonlinearities in the signal processing of EPT, the EPT data products feature unique A-value and deposited energy limits for each detector. The tables on the following four pages list the corresponding A-values ranges and deposited energy ranges for the 77 DPI of the NO_EPT_mag/foil data products for all detectors and two different temperatures. For details see Sect. D.

Table E.2: A-value ranges and DNL-corrected deposited energy ranges for the 77 DPI of the NO_EPT_foil/mag data products. The given ranges are specific for the HE1 detectors at a temperature configuration of -11.6°C.

	A-value range				Deposited energy range/ keV			
DPI	C1	C2	C3	C4	C1	C2	C3	C4
0	25 – 26	25 – 27	25 – 27	25 – 26	25.1 – 27.0	24.7 – 27.4	24.7 – 27.3	25.2 – 27.1
1	27 – 29	28 – 29	28 – 29	27 – 29	27.0 – 30.3	27.4 – 29.9	27.3 – 29.9	27.1 – 30.6
2	30 – 31	30 – 32	30 – 32	30 – 31	30.3 – 32.3	29.9 – 32.8	29.9 – 32.7	30.6 – 32.6
3	32 – 34	33 – 35	33 – 35	32 – 34	32.3 – 35.1	32.8 – 35.7	32.7 – 35.7	32.6 – 35.1
4	35 – 37	36 – 38	36 – 38	35 – 37	35.1 – 38.0	35.7 – 38.8	35.7 – 38.7	35.1 – 38.1
5	38 – 41	39 – 41	39 – 41	38 – 41	38.0 – 42.2	38.8 – 41.9	38.7 – 41.8	38.1 – 42.5
6	42 – 45	42 – 45	42 – 45	42 – 45	42.2 – 46.2	41.9 – 45.8	41.8 – 45.7	42.5 – 46.4
7	46 – 49	46 – 49	46 – 50	46 – 49	46.2 – 50.2	45.8 – 49.8	45.7 – 50.7	46.4 – 50.5
8	50 – 53	50 – 54	51 – 54	50 – 53	50.2 – 54.0	49.8 – 54.8	50.7 – 54.7	50.5 – 54.0
9	54 – 58	55 – 59	55 – 59	54 – 58	54.0 – 59.3	54.8 – 59.8	54.7 – 59.7	54.0 – 59.4
10	59 – 63	60 – 64	60 – 64	59 – 63	59.3 – 64.0	59.8 – 64.7	59.7 – 64.5	59.4 – 64.1
11	64 – 69	65 – 70	65 – 70	64 – 69	64.0 – 70.1	64.7 – 70.5	64.5 – 70.4	64.1 – 70.4
12	70 – 75	71 – 76	71 – 76	70 – 75	70.1 – 76.3	70.5 – 76.6	70.4 – 76.5	70.4 – 76.7
13	76 – 82	77 – 83	77 – 83	76 – 82	76.3 – 83.2	76.6 – 83.6	76.5 – 83.4	76.7 – 83.4
14	83 – 90	84 – 91	84 – 92	83 – 90	83.2 – 91.2	83.6 – 91.3	83.4 – 92.2	83.4 – 91.5
15	91 – 98	92 – 99	93 – 100	91 – 98	91.2 – 99.1	91.3 – 99.3	92.2 – 100.2	91.5 – 99.4
16	99 – 107	100 – 109	101 – 109	99 – 107	99.1 – 108.2	99.3 – 109.1	100.2 – 109.0	99.4 – 108.6
17	108 – 117	110 – 118	110 – 118	108 – 116	108.2 – 118.3	109.1 – 118.2	109.0 – 117.9	108.6 – 117.7
18	118 – 127	119 – 129	119 – 129	117 – 127	118.3 – 128.3	118.2 – 129.0	117.9 – 128.8	117.7 – 128.6
19	128 – 139	130 – 141	130 – 141	128 – 138	128.3 – 140.6	129.0 – 141.0	128.8 – 140.9	128.6 – 139.8
20	140 – 151	142 – 153	142 – 153	139 – 150	140.6 – 152.4	141.0 – 152.8	140.9 – 152.5	139.8 – 152.0
21	152 – 165	154 – 167	154 – 167	151 – 164	152.4 – 166.5	152.8 – 166.7	152.5 – 166.3	152.0 – 166.1
22	166 – 181	168 – 183	168 – 184	165 – 180	166.5 – 182.5	166.7 – 182.5	166.3 – 183.1	166.1 – 182.2
23	182 – 197	184 – 199	185 – 200	181 – 196	182.5 – 198.6	182.5 – 198.4	183.1 – 198.9	182.2 – 198.3
24	198 – 215	200 – 218	201 – 218	197 – 214	198.6 – 216.6	198.4 – 217.2	198.9 – 216.7	198.3 – 216.4
25	216 – 234	219 – 237	219 – 237	215 – 233	216.6 – 235.7	217.2 – 236.0	216.7 – 235.4	216.4 – 235.6
26	235 – 255	238 – 258	238 – 259	234 – 254	235.7 – 256.7	236.0 – 256.8	235.4 – 257.2	235.6 – 256.7
27	256 – 279	259 – 282	260 – 283	255 – 278	256.7 – 280.8	256.8 – 280.5	257.2 – 280.9	256.7 – 280.9
28	280 – 303	283 – 307	284 – 307	279 – 301	280.8 – 304.9	280.5 – 305.3	280.9 – 304.6	280.9 – 304.0
29	304 – 331	308 – 335	308 – 336	302 – 329	304.9 – 333.0	305.3 – 333.0	304.6 – 333.2	304.0 – 332.2
30	332 – 363	336 – 367	337 – 368	330 – 361	333.0 – 365.1	333.0 – 364.7	333.2 – 364.8	332.2 – 364.4
31	364 – 394	368 – 400	369 – 400	362 – 393	365.1 – 396.1	364.7 – 397.3	364.8 – 396.5	364.4 – 396.7
32	395 – 430	401 – 436	401 – 437	394 – 428	396.1 – 432.2	397.3 – 433.0	396.5 – 433.0	396.7 – 431.9
33	431 – 468	437 – 474	438 – 475	429 – 466	432.2 – 470.4	433.0 – 470.6	433.0 – 470.6	431.9 – 470.2
34	469 – 510	475 – 517	476 – 518	467 – 508	470.4 – 512.5	470.6 – 513.2	470.6 – 513.0	470.2 – 512.4
35	511 – 558	518 – 565	519 – 566	509 – 556	512.5 – 560.6	513.2 – 560.7	513.0 – 560.5	512.4 – 560.8
36	559 – 606	566 – 614	567 – 615	557 – 603	560.6 – 608.7	560.7 – 609.2	560.5 – 608.9	560.8 – 608.1
37	607 – 662	615 – 670	616 – 672	604 – 659	608.7 – 664.9	609.2 – 664.6	608.9 – 665.2	608.1 – 664.5
38	663 – 726	671 – 735	673 – 736	660 – 722	664.9 – 729.1	664.6 – 729.0	665.2 – 728.4	664.5 – 727.9
39	727 – 789	736 – 800	737 – 801	723 – 786	729.1 – 792.3	729.0 – 793.3	728.4 – 792.6	727.9 – 792.4
40	790 – 861	801 – 872	802 – 874	787 – 858	792.3 – 864.5	793.3 – 864.6	792.6 – 864.7	792.4 – 864.8
41	862 – 937	873 – 949	875 – 951	859 – 933	864.5 – 940.7	864.6 – 940.8	864.7 – 940.8	864.8 – 940.4
42	938 – 1021	950 – 1034	952 – 1036	934 – 1016	940.7 – 1024.9	940.8 – 1024.9	940.8 – 1024.8	940.4 – 1023.9
43	1022 – 1117	1035 – 1131	1037 – 1133	1017 – 1112	1024.9 – 1121.2	1024.9 – 1120.9	1024.8 – 1120.6	1023.9 – 1120.6
44	1118 – 1212	1132 – 1228	1134 – 1230	1113 – 1207	1121.2 – 1216.5	1120.9 – 1217.0	1120.6 – 1216.4	1120.6 – 1216.2
45	1213 – 1324	1229 – 1341	1231 – 1344	1208 – 1318	1216.5 – 1328.8	1217.0 – 1328.8	1216.4 – 1329.0	1216.2 – 1328.0
46	1325 – 1452	1342 – 1471	1345 – 1473	1319 – 1446	1328.8 – 1457.2	1328.8 – 1457.5	1329.0 – 1456.5	1328.0 – 1456.9
47	1453 – 1580	1472 – 1600	1474 – 1603	1447 – 1573	1457.2 – 1585.5	1457.5 – 1585.2	1456.5 – 1584.9	1456.9 – 1584.7
48	1581 – 1723	1601 – 1745	1604 – 1749	1574 – 1716	1585.5 – 1728.9	1585.2 – 1728.7	1584.9 – 1729.1	1584.7 – 1728.7
49	1724 – 1875	1746 – 1899	1750 – 1903	1717 – 1867	1728.9 – 1881.4	1728.7 – 1881.2	1729.1 – 1881.3	1728.7 – 1880.8
50	1876 – 2042	1900 – 2069	1904 – 2073	1868 – 2034	1881.4 – 2048.9	1881.2 – 2049.5	1881.3 – 2049.2	1880.8 – 2048.9
51	2043 – 2234	2070 – 2263	2074 – 2267	2035 – 2224	2048.9 – 2241.4	2049.5 – 2241.5	2049.2 – 2240.9	2048.9 – 2240.2
52	2235 – 2425	2264 – 2457	2268 – 2461	2225 – 2415	2241.4 – 2432.9	2241.5 – 2433.5	2240.9 – 2432.5	2240.2 – 2432.5
53	2426 – 2649	2458 – 2683	2462 – 2688	2416 – 2637	2432.9 – 2657.6	2433.5 – 2657.3	2432.5 – 2656.8	2432.5 – 2656.0
54	2650 – 2904	2684 – 2942	2689 – 2947	2638 – 2892	2657.6 – 2913.3	2657.3 – 2913.6	2656.8 – 2912.6	2656.0 – 2912.8
55	2905 – 3160	2943 – 3200	2948 – 3207	2893 – 3146	2913.3 – 3170.0	2913.6 – 3169.0	2912.6 – 3169.5	2912.8 – 3168.5
56	3161 – 3447	3201 – 3491	3208 – 3498	3147 – 3432	3170.0 – 3457.9	3169.0 – 3457.1	3169.5 – 3456.9	3168.5 – 3456.5
57	3448 – 3750	3492 – 3798	3499 – 3806	3433 – 3734	3457.9 – 3761.7	3457.1 – 3761.0	3456.9 – 3761.2	3456.5 – 3760.5
58	3751 – 4085	3799 – 4138	3807 – 4146	3735 – 4068	3761.7 – 4097.7	3761.0 – 4097.5	3761.2 – 4097.1	3760.5 – 4096.8
59	4086 – 4469	4139 – 4526	4147 – 4535	4069 – 4449	4097.7 – 4482.8	4097.5 – 4481.6	4097.1 – 4481.4	4096.8 – 4480.4
60	4470 – 4852	4527 – 4914	4536 – 4924	4450 – 4830	4482.8 – 4866.9	4481.6 – 4865.7	4481.4 – 4865.7	4480.4 – 4864.1
61	4853 – 5298	4915 – 5366	4925 – 5377	4831 – 5275	4866.9 – 5314.2	4865.7 – 5313.1	4865.7 – 5313.2	4864.1 – 5312.1
62	5299 – 5809	5367 – 5884	5378 – 5895	5276 – 5784	5314.2 – 5826.6	5313.1 – 5825.9	5313.2 – 5824.9	5312.1 – 5824.6
63	5810 – 6320	5885 – 6401	5896 – 6414	5785 – 6292	5826.6 – 6339.1	5825.9 – 6337.6	5824.9 – 6337.6	5824.6 – 6336.1
64	6321 – 7501	6402 – 7597	6415 – 7612	6293 – 7468	6339.1 – 7523.5	6337.6 – 7521.6	6337.6 – 7521.1	6336.1 – 7520.1
65	7502 – 8938	7598 – 9052	7613 – 9070	7469 – 8899	7523.5 – 8964.6	7521.6 – 8961.8	7521.1 – 8961.5	7520.1 – 8960.9
66	8939 – 10598	9053 – 10733	9071 – 10755	8900 – 10551	8964.6 – 10629.3	8961.8 – 10625.8	8961.5 – 10626.1	8960.9 – 10624.2
67	10599 – 12641	10734 – 12803	10756 – 12828	10552 – 12585	10629.3 – 12678.2	10625.8 – 12674.9	10626.1 – 12674.0	10624.2 – 12672.2
68	12642 – 15003	12804 – 15195	12829 – 15225	12586 – 14937	12678.2 – 15046.9	12674.9 – 15042.7	12674.0 – 15041.9	12672.2 – 15040.3
69	15004 – 17876	15196 – 18105	15226 – 18141	14938 – 17798	15046.9 – 17928.1	15042.7 – 17923.3	15041.9 – 17922.6	15040.3 – 17920.9
70	17877 – 21196	18106 – 21468	18142 – 21510	17799 – 21103	17928.1 – 21257.6	17923.3 – 21252.3	17922.6 – 21250.8	17920.9 – 21248.5
71	21197 – 25282	21469 – 25606	21511 – 25657	21104 – 25171	21257.6 – 25355.3	21252.3 – 25348.4	21250.8 – 25347.6	21248.5 – 25344.4
72	25283 – 30006	25607 – 30391	25658 – 30451	25172 – 29875	25355.3 – 30092.8	25348.4 – 30085.0	25347.6 – 30083.6	25344.4 – 30080.6
73	30007 – 35752	30392 – 36211	30452 – 36282	29876 – 35596	30092.8 – 35855.2	30085.0 – 35846.2	30083.6 – 35844.0	30080.6 – 35840.8
74	35753 – 42392	36212 – 42936	36283 – 43021	35597 – 42207	35855.2 – 42514.2	35846.2 – 42503.2	35844.0 – 42501.4	35840.8 – 42497.1
75	42393 – 50564	42937 – 51213	43022 – 51314	42208 – 50343	42514.2 – 50709.6	42503.2 – 50696.4	42501.4 – 50693.9	42497.1 – 50688.8
76	50565 – 125134	51214 – 126739	51315 – 126990	50344 – 124588	50709.6 – 125492.8	50696.4 – 125458.6	50693.9 – 125453.6	50688.8 – 125442.4

Table E.3: A-value ranges and DNL-corrected deposited energy ranges for the 77 DPI of the NO_EPT_foil/mag data products. The given ranges are specific for the HE1 detectors at a temperature configuration of -6.0°C.

	A-value range				Deposited energy range/ keV			
DPI	C1	C2	C3	C4	C1	C2	C3	C4
0	25 – 26	25 – 27	25 – 27	25 – 26	25.1 – 27.1	24.8 – 27.4	24.7 – 27.3	25.2 – 27.1
1	27 – 29	28 – 29	28 – 29	27 – 29	27.1 – 30.4	27.4 – 29.9	27.3 – 29.9	27.1 – 30.7
2	30 – 31	30 – 32	30 – 32	30 – 31	30.4 – 32.4	29.9 – 32.8	29.9 – 32.7	30.7 – 32.6
3	32 – 34	33 – 35	33 – 35	32 – 34	32.4 – 35.1	32.8 – 35.8	32.7 – 35.7	32.6 – 35.1
4	35 – 37	36 – 38	36 – 38	35 – 37	35.1 – 38.0	35.8 – 38.9	35.7 – 38.8	35.1 – 38.1
5	38 – 41	39 – 41	39 – 41	38 – 41	38.0 – 42.3	38.9 – 41.9	38.8 – 41.8	38.1 – 42.6
6	42 – 45	42 – 45	42 – 45	42 – 45	42.3 – 46.3	41.9 – 45.9	41.8 – 45.8	42.6 – 46.4
7	46 – 49	46 – 49	46 – 49	46 – 49	46.3 – 50.3	45.9 – 49.9	45.8 – 49.8	46.4 – 50.6
8	50 – 53	50 – 54	50 – 54	50 – 53	50.3 – 54.0	49.9 – 54.8	49.8 – 54.7	50.6 – 54.1
9	54 – 58	55 – 59	55 – 59	54 – 58	54.0 – 59.4	54.8 – 59.8	54.7 – 59.7	54.1 – 59.5
10	59 – 63	60 – 64	60 – 64	59 – 63	59.4 – 64.0	59.8 – 64.7	59.7 – 64.6	59.5 – 64.1
11	64 – 69	65 – 70	65 – 70	64 – 69	64.0 – 70.2	64.7 – 70.6	64.6 – 70.5	64.1 – 70.5
12	70 – 75	71 – 76	71 – 76	70 – 75	70.2 – 76.4	70.6 – 76.7	70.5 – 76.6	70.5 – 76.8
13	76 – 82	77 – 83	77 – 83	76 – 82	76.4 – 83.3	76.7 – 83.7	76.6 – 83.5	76.8 – 83.5
14	83 – 90	84 – 91	84 – 91	83 – 90	83.3 – 91.3	83.7 – 91.4	83.5 – 91.4	83.5 – 91.6
15	91 – 98	92 – 99	92 – 100	91 – 98	91.3 – 99.2	91.4 – 99.4	91.4 – 100.4	91.6 – 99.5
16	99 – 107	100 – 108	101 – 109	99 – 107	99.2 – 108.3	99.4 – 108.2	100.4 – 109.1	99.5 – 108.7
17	108 – 116	109 – 118	110 – 118	108 – 116	108.3 – 117.5	108.2 – 118.3	109.1 – 118.1	108.7 – 117.8
18	117 – 127	119 – 129	119 – 129	117 – 126	117.5 – 128.4	118.3 – 129.2	118.1 – 129.0	117.8 – 127.9
19	128 – 139	130 – 141	130 – 141	127 – 138	128.4 – 140.8	129.2 – 141.1	129.0 – 141.1	127.9 – 140.0
20	140 – 151	142 – 153	142 – 153	139 – 150	140.8 – 152.6	141.1 – 153.0	141.1 – 152.6	140.0 – 152.2
21	152 – 165	154 – 167	154 – 167	151 – 164	152.6 – 166.7	153.0 – 166.9	152.6 – 166.5	152.2 – 166.3
22	166 – 181	168 – 183	168 – 183	165 – 180	166.7 – 182.8	166.9 – 182.8	166.5 – 182.3	166.3 – 182.4
23	182 – 197	184 – 199	184 – 200	181 – 196	182.8 – 198.8	182.8 – 198.6	182.3 – 199.1	182.4 – 198.6
24	198 – 215	200 – 217	201 – 218	197 – 214	198.8 – 216.9	198.6 – 216.5	199.1 – 216.9	198.6 – 216.7
25	216 – 234	218 – 237	219 – 237	215 – 233	216.9 – 236.0	216.5 – 236.3	216.9 – 235.7	216.7 – 235.9
26	235 – 254	238 – 258	238 – 258	234 – 253	236.0 – 256.1	236.3 – 257.1	235.7 – 256.5	235.9 – 256.0
27	255 – 278	259 – 282	259 – 283	254 – 277	256.1 – 280.2	257.1 – 280.9	256.5 – 281.2	256.0 – 280.2
28	279 – 302	283 – 306	284 – 307	278 – 301	280.2 – 304.3	280.9 – 304.7	281.2 – 305.0	280.2 – 304.4
29	303 – 330	307 – 335	308 – 335	302 – 329	304.3 – 332.4	304.7 – 333.4	305.0 – 332.7	304.4 – 332.6
30	331 – 362	336 – 367	336 – 368	330 – 361	332.4 – 364.5	333.4 – 365.1	332.7 – 365.3	332.6 – 364.9
31	363 – 394	368 – 399	369 – 400	362 – 392	364.5 – 396.6	365.1 – 396.9	365.3 – 397.0	364.9 – 396.2
32	395 – 430	400 – 435	401 – 436	393 – 428	396.6 – 432.8	396.9 – 432.5	397.0 – 432.6	396.2 – 432.5
33	431 – 468	436 – 474	437 – 475	429 – 466	432.8 – 471.0	432.5 – 471.2	432.6 – 471.2	432.5 – 470.8
34	469 – 509	475 – 516	476 – 517	467 – 507	471.0 – 512.1	471.2 – 512.8	471.2 – 512.7	470.8 – 512.1
35	510 – 557	517 – 565	518 – 566	508 – 555	512.1 – 560.3	512.8 – 561.4	512.7 – 561.2	512.1 – 560.5
36	558 – 605	566 – 613	567 – 614	556 – 603	560.3 – 608.5	561.4 – 609.0	561.2 – 608.6	560.5 – 608.9
37	606 – 661	614 – 670	615 – 671	604 – 658	608.5 – 664.8	609.0 – 665.5	608.6 – 665.0	608.9 – 664.3
38	662 – 725	671 – 734	672 – 736	659 – 722	664.8 – 729.0	665.5 – 728.9	665.0 – 729.3	664.3 – 728.8
39	726 – 788	735 – 799	737 – 800	723 – 785	729.0 – 792.3	728.9 – 793.3	729.3 – 792.6	728.8 – 792.4
40	789 – 860	800 – 872	801 – 873	786 – 857	792.3 – 864.6	793.3 – 865.7	792.6 – 864.8	792.4 – 864.9
41	861 – 936	873 – 948	874 – 950	858 – 932	864.6 – 940.9	865.7 – 941.0	864.8 – 941.0	864.9 – 940.6
42	937 – 1019	949 – 1033	951 – 1035	933 – 1015	940.9 – 1024.2	941.0 – 1025.2	941.0 – 1025.1	940.6 – 1024.2
43	1020 – 1115	1034 – 1130	1036 – 1132	1016 – 1111	1024.2 – 1120.6	1025.2 – 1121.4	1025.1 – 1121.0	1024.2 – 1121.0
44	1116 – 1211	1131 – 1227	1133 – 1229	1112 – 1206	1120.6 – 1217.0	1121.4 – 1217.5	1121.0 – 1217.0	1121.0 – 1216.8
45	1212 – 1322	1228 – 1340	1230 – 1343	1207 – 1317	1217.0 – 1328.5	1217.5 – 1329.5	1217.0 – 1329.7	1216.8 – 1328.7
46	1323 – 1450	1341 – 1469	1344 – 1472	1318 – 1444	1328.5 – 1457.0	1329.5 – 1457.4	1329.7 – 1457.3	1328.7 – 1456.7
47	1451 – 1577	1470 – 1598	1473 – 1601	1445 – 1571	1457.0 – 1584.5	1457.4 – 1585.3	1457.3 – 1584.9	1456.7 – 1584.8
48	1578 – 1721	1599 – 1744	1602 – 1747	1572 – 1714	1584.5 – 1729.1	1585.3 – 1730.0	1584.9 – 1729.4	1584.8 – 1728.9
49	1722 – 1872	1745 – 1897	1748 – 1901	1715 – 1865	1729.1 – 1880.8	1730.0 – 1881.6	1729.4 – 1881.7	1728.9 – 1881.1
50	1873 – 2039	1898 – 2067	1902 – 2071	1866 – 2032	1880.8 – 2048.5	1881.6 – 2050.1	1881.7 – 2049.8	1881.1 – 2049.5
51	2040 – 2231	2068 – 2260	2072 – 2265	2033 – 2222	2048.5 – 2241.3	2050.1 – 2241.4	2049.8 – 2241.7	2049.5 – 2241.1
52	2232 – 2422	2261 – 2454	2266 – 2459	2223 – 2413	2241.3 – 2433.0	2241.4 – 2433.7	2241.7 – 2433.6	2241.1 – 2433.6
53	2423 – 2645	2455 – 2680	2460 – 2686	2414 – 2635	2433.0 – 2657.0	2433.7 – 2657.7	2433.6 – 2658.2	2433.6 – 2657.4
54	2646 – 2900	2681 – 2939	2687 – 2944	2636 – 2889	2657.0 – 2913.0	2657.7 – 2914.4	2658.2 – 2913.4	2657.4 – 2913.5
55	2901 – 3155	2940 – 3197	2945 – 3203	2890 – 3143	2913.0 – 3169.1	2914.4 – 3170.1	2913.4 – 3169.6	2913.5 – 3169.6
56	3156 – 3442	3198 – 3488	3204 – 3495	3144 – 3429	3169.1 – 3457.3	3170.1 – 3458.5	3169.6 – 3458.4	3169.6 – 3457.9
57	3443 – 3745	3489 – 3795	3496 – 3802	3430 – 3730	3457.3 – 3761.5	3458.5 – 3762.8	3458.4 – 3762.1	3457.9 – 3761.3
58	3746 – 4079	3796 – 4134	3803 – 4142	3731 – 4064	3761.5 – 4096.9	3762.8 – 4098.8	3762.1 – 4098.4	3761.3 – 4098.0
59	4080 – 4462	4135 – 4521	4143 – 4530	4065 – 4445	4096.9 – 4481.5	4098.8 – 4482.4	4098.4 – 4482.2	4098.0 – 4482.1
60	4463 – 4844	4522 – 4909	4531 – 4919	4446 – 4826	4481.5 – 4865.1	4482.4 – 4867.0	4482.2 – 4867.0	4482.1 – 4866.2
61	4845 – 5291	4910 – 5361	4920 – 5372	4827 – 5270	4865.1 – 5313.9	4867.0 – 5315.0	4867.0 – 5315.0	4866.2 – 5313.9
62	5292 – 5801	5362 – 5878	5373 – 5890	5271 – 5778	5313.9 – 5826.0	5315.0 – 5827.4	5315.0 – 5827.4	5313.9 – 5826.0
63	5802 – 6311	5879 – 6395	5891 – 6407	5779 – 6286	5826.0 – 6338.2	5827.4 – 6339.8	5827.4 – 6338.8	5826.0 – 6338.1
64	6312 – 7490	6396 – 7590	6408 – 7605	6287 – 7461	6338.2 – 7522.0	6339.8 – 7524.2	6338.8 – 7523.8	6338.1 – 7522.7
65	7491 – 8925	7591 – 9043	7606 – 9061	7462 – 8890	7522.0 – 8963.0	7524.2 – 8964.4	7523.8 – 8964.0	7522.7 – 8963.3
66	8926 – 10582	9044 – 10723	9062 – 10744	8891 – 10541	8963.0 – 10626.9	8964.4 – 10629.5	8964.0 – 10628.8	8963.3 – 10627.8
67	10583 – 12622	10724 – 12790	10745 – 12815	10542 – 12573	10626.9 – 12675.3	10629.5 – 12678.2	10628.8 – 12677.3	10627.8 – 12676.3
68	12623 – 14981	12791 – 15180	12816 – 15210	12574 – 14923	12675.3 – 15044.1	12678.2 – 15047.1	12677.3 – 15046.4	12676.3 – 15045.4
69	14982 – 17850	15181 – 18087	15211 – 18123	14924 – 17781	15044.1 – 17925.0	15047.1 – 17928.4	15046.4 – 17927.8	15045.4 – 17926.7
70	17851 – 21165	18088 – 21446	18124 – 21489	17782 – 21083	17925.0 – 21253.7	17928.4 – 21257.7	17927.8 – 21257.3	17926.7 – 21255.6
71	21166 – 25245	21447 – 25581	21490 – 25631	21084 – 25147	21253.7 – 25350.6	21257.7 – 25356.1	21257.3 – 25354.3	21255.6 – 25352.6
72	25246 – 29962	25582 – 30361	25632 – 30421	25148 – 29846	25350.6 – 30087.1	25356.1 – 30093.8	25354.3 – 30092.4	25352.6 – 30089.9
73	29963 – 35700	30362 – 36175	30422 – 36246	29847 – 35562	30087.1 – 35848.9	30093.8 – 35856.4	30092.4 – 35854.2	30089.9 – 35852.4
74	35701 – 42330	36176 – 42893	36247 – 42978	35563 – 42166	35848.9 – 42506.4	35856.4 – 42514.9	35854.2 – 42513.2	35852.4 – 42510.2
75	42331 – 50490	42894 – 51162	42979 – 51263	42167 – 50294	42506.4 – 50700.2	42514.9 – 50710.8	42513.2 – 50708.4	42510.2 – 50704.3
76	50491 – 124951	51163 – 126614	51264 – 126864	50295 – 124467	50700.2 – 125469.6	50710.8 – 125495.3	50708.4 – 125489.5	50704.3 – 125481.0

Table E.4: A-value ranges and DNL-corrected deposited energy ranges for the 77 DPI of the NO_EPT_foil/mag data products. The given ranges are specific for the HE2 detectors at a temperature configuration of -6.0°C.

	A-value range				Deposited energy range/ keV			
DPI	C1	C2	C3	C4	C1	C2	C3	C4
0	25 – 27	25 – 26	26 – 27	26 – 27	24.8 – 27.4	25.2 – 27.2	25.4 – 27.2	25.6 – 27.5
1	28 – 29	27 – 29	28 – 29	28 – 29	27.4 – 30.0	27.2 – 30.6	27.2 – 29.5	27.5 – 29.7
2	30 – 32	30 – 31	30 – 32	30 – 32	30.0 – 32.8	30.6 – 32.6	29.5 – 32.4	29.7 – 32.5
3	33 – 35	32 – 34	33 – 35	33 – 35	32.8 – 35.5	32.6 – 35.1	32.4 – 35.3	32.5 – 35.2
4	36 – 38	35 – 37	36 – 38	36 – 38	35.5 – 38.5	35.1 – 38.2	35.3 – 38.3	35.2 – 38.2
5	39 – 41	38 – 41	39 – 42	39 – 42	38.5 – 41.7	38.2 – 42.5	38.3 – 42.2	38.2 – 42.1
6	42 – 45	42 – 45	43 – 46	43 – 46	41.7 – 45.2	42.5 – 46.2	42.2 – 46.3	42.1 – 46.1
7	46 – 49	46 – 49	47 – 50	47 – 50	45.2 – 49.7	46.2 – 50.9	46.3 – 50.2	46.1 – 50.0
8	50 – 54	50 – 53	51 – 55	51 – 54	49.7 – 54.1	50.9 – 54.2	50.2 – 55.1	50.0 – 53.8
9	55 – 59	54 – 58	56 – 59	55 – 59	54.1 – 59.6	54.2 – 59.8	55.1 – 59.1	53.8 – 59.0
10	60 – 64	59 – 63	60 – 65	60 – 64	59.6 – 64.3	59.8 – 64.4	59.1 – 65.0	59.0 – 63.8
11	65 – 70	64 – 69	66 – 71	65 – 71	64.3 – 70.0	64.4 – 70.7	65.0 – 70.8	63.8 – 70.6
12	71 – 76	70 – 75	72 – 77	72 – 77	70.0 – 76.3	70.7 – 77.0	70.8 – 76.7	70.6 – 76.7
13	77 – 83	76 – 82	78 – 84	78 – 84	76.3 – 83.2	77.0 – 83.8	76.7 – 83.6	76.7 – 83.5
14	84 – 91	83 – 90	85 – 92	85 – 92	83.2 – 90.9	83.8 – 91.8	83.6 – 91.4	83.5 – 91.4
15	92 – 99	91 – 98	93 – 101	93 – 100	90.9 – 98.6	91.8 – 99.7	91.4 – 100.1	91.4 – 99.2
16	100 – 108	99 – 107	102 – 110	101 – 109	98.6 – 107.6	99.7 – 109.0	100.1 – 109.0	99.2 – 108.0
17	109 – 118	108 – 116	111 – 120	110 – 119	107.6 – 117.7	109.0 – 118.0	109.0 – 118.8	108.0 – 117.9
18	119 – 129	117 – 127	121 – 130	120 – 129	117.7 – 128.6	118.0 – 129.1	118.8 – 128.5	117.9 – 127.8
19	130 – 141	128 – 139	131 – 142	130 – 142	128.6 – 140.7	129.1 – 141.3	128.5 – 140.4	127.8 – 140.7
20	142 – 153	140 – 150	143 – 155	143 – 154	140.7 – 152.6	141.3 – 152.5	140.4 – 153.0	140.7 – 152.4
21	154 – 167	151 – 164	156 – 169	155 – 168	152.6 – 166.4	152.5 – 166.6	153.0 – 166.7	152.4 – 166.2
22	168 – 183	165 – 180	170 – 185	169 – 184	166.4 – 182.3	166.6 – 182.7	166.7 – 182.4	166.2 – 182.0
23	184 – 199	181 – 196	186 – 202	185 – 201	182.3 – 198.1	182.7 – 198.8	182.4 – 199.0	182.0 – 198.7
24	200 – 218	197 – 214	203 – 220	202 – 219	198.1 – 217.0	198.8 – 216.9	199.0 – 216.6	198.7 – 216.4
25	219 – 237	215 – 233	221 – 240	220 – 238	217.0 – 235.8	216.9 – 236.0	216.6 – 236.2	216.4 – 235.1
26	238 – 258	234 – 254	241 – 261	239 – 259	235.8 – 256.6	236.0 – 257.2	236.2 – 256.7	235.1 – 255.8
27	259 – 282	255 – 278	262 – 286	260 – 284	256.6 – 280.4	257.2 – 281.3	256.7 – 281.2	255.8 – 280.4
28	283 – 306	279 – 302	287 – 310	285 – 308	280.4 – 304.2	281.3 – 305.5	281.2 – 304.7	280.4 – 304.1
29	307 – 335	303 – 329	311 – 339	309 – 337	304.2 – 332.9	305.5 – 332.7	304.7 – 333.1	304.1 – 332.6
30	336 – 367	330 – 361	340 – 371	338 – 369	332.9 – 364.6	332.7 – 364.9	333.1 – 364.4	332.6 – 364.1
31	368 – 399	362 – 393	372 – 404	370 – 402	364.6 – 396.3	364.9 – 397.1	364.4 – 396.7	364.1 – 396.6
32	400 – 436	394 – 429	405 – 441	403 – 438	396.3 – 432.9	397.1 – 433.3	396.7 – 432.9	396.6 – 432.1
33	437 – 474	430 – 466	442 – 480	439 – 477	432.9 – 470.6	433.3 – 470.6	432.9 – 471.1	432.1 – 470.5
34	475 – 516	467 – 508	481 – 523	478 – 520	470.6 – 512.2	470.6 – 512.9	471.1 – 513.1	470.5 – 512.8
35	517 – 565	509 – 556	524 – 572	521 – 568	512.2 – 560.7	512.9 – 561.2	513.1 – 561.1	512.8 – 560.1
36	566 – 613	557 – 604	573 – 621	569 – 617	560.7 – 608.3	561.2 – 609.5	561.1 – 609.1	560.1 – 608.3
37	614 – 670	605 – 659	622 – 678	618 – 674	608.3 – 664.8	609.5 – 664.9	609.1 – 664.8	608.3 – 664.5
38	671 – 735	660 – 723	679 – 743	675 – 739	664.8 – 729.2	664.9 – 729.3	664.8 – 728.5	664.5 – 728.5
39	736 – 799	724 – 786	744 – 809	740 – 804	729.2 – 792.6	729.3 – 792.7	728.5 – 793.0	728.5 – 792.5
40	800 – 872	787 – 858	810 – 882	805 – 877	792.6 – 864.9	792.7 – 865.2	793.0 – 864.5	792.5 – 864.3
41	873 – 949	859 – 933	883 – 960	878 – 954	864.9 – 941.2	865.2 – 940.7	864.5 – 940.8	864.3 – 940.2
42	950 – 1034	934 – 1017	961 – 1046	955 – 1040	941.2 – 1025.4	940.7 – 1025.3	940.8 – 1025.0	940.2 – 1024.8
43	1035 – 1130	1018 – 1112	1047 – 1144	1041 – 1137	1025.4 – 1120.5	1025.3 – 1120.9	1025.0 – 1120.9	1024.8 – 1120.4
44	1131 – 1227	1113 – 1208	1145 – 1242	1138 – 1235	1120.5 – 1216.6	1120.9 – 1217.6	1120.9 – 1216.8	1120.4 – 1216.9
45	1228 – 1341	1209 – 1319	1243 – 1357	1236 – 1349	1216.6 – 1329.5	1217.6 – 1329.3	1216.8 – 1329.4	1216.9 – 1329.1
46	1342 – 1470	1320 – 1446	1358 – 1487	1350 – 1479	1329.5 – 1457.3	1329.3 – 1457.2	1329.4 – 1456.6	1329.1 – 1457.1
47	1471 – 1599	1447 – 1573	1488 – 1618	1480 – 1609	1457.3 – 1585.1	1457.2 – 1585.0	1456.6 – 1584.8	1457.1 – 1585.1
48	1600 – 1744	1574 – 1717	1619 – 1765	1610 – 1755	1585.1 – 1728.8	1585.0 – 1730.0	1584.8 – 1728.7	1585.1 – 1728.9
49	1745 – 1898	1718 – 1868	1766 – 1921	1756 – 1909	1728.8 – 1881.3	1730.0 – 1882.0	1728.7 – 1881.3	1728.9 – 1880.5
50	1899 – 2068	1869 – 2035	1922 – 2092	1910 – 2080	1881.3 – 2049.7	1882.0 – 2050.1	1881.3 – 2048.7	1880.5 – 2048.9
51	2069 – 2262	2036 – 2225	2093 – 2289	2081 – 2275	2049.7 – 2241.9	2050.1 – 2241.4	2048.7 – 2241.5	2048.9 – 2240.9
52	2263 – 2455	2226 – 2416	2290 – 2485	2276 – 2470	2241.9 – 2433.1	2241.4 – 2433.6	2241.5 – 2433.3	2240.9 – 2432.9
53	2456 – 2682	2417 – 2639	2486 – 2714	2471 – 2698	2433.1 – 2658.0	2433.6 – 2658.1	2433.3 – 2657.4	2432.9 – 2657.4
54	2683 – 2940	2640 – 2893	2715 – 2975	2699 – 2958	2658.0 – 2913.6	2658.1 – 2913.8	2657.4 – 2912.9	2657.4 – 2913.5
55	2941 – 3199	2894 – 3147	2976 – 3237	2959 – 3218	2913.6 – 3170.2	2913.8 – 3169.5	2912.9 – 3169.3	2913.5 – 3169.5
56	3200 – 3490	3148 – 3434	3238 – 3531	3219 – 3510	3170.2 – 3458.5	3169.5 – 3458.5	3169.3 – 3457.0	3169.5 – 3457.0
57	3491 – 3797	3435 – 3736	3532 – 3842	3511 – 3819	3458.5 – 3762.6	3458.5 – 3762.5	3457.0 – 3761.4	3457.0 – 3761.3
58	3798 – 4136	3737 – 4070	3843 – 4185	3820 – 4160	3762.6 – 4098.5	3762.5 – 4098.7	3761.4 – 4097.0	3761.3 – 4097.0
59	4137 – 4524	4071 – 4451	4186 – 4578	4161 – 4551	4098.5 – 4482.8	4098.7 – 4482.3	4097.0 – 4481.7	4097.0 – 4482.1
60	4525 – 4911	4452 – 4833	4579 – 4970	4552 – 4941	4482.8 – 4866.2	4482.3 – 4866.8	4481.7 – 4865.3	4482.1 – 4866.1
61	4912 – 5364	4834 – 5278	4971 – 5428	4942 – 5396	4866.2 – 5315.0	4866.8 – 5314.8	4865.3 – 5313.5	4866.1 – 5314.1
62	5365 – 5881	5279 – 5787	5429 – 5951	5397 – 5916	5315.0 – 5827.2	5314.8 – 5827.2	5313.5 – 5825.4	5314.1 – 5826.1
63	5882 – 6398	5788 – 6295	5952 – 6475	5917 – 6436	5827.2 – 6339.4	5827.2 – 6338.6	5825.4 – 6338.2	5826.1 – 6338.2
64	6399 – 7594	6296 – 7472	6476 – 7685	6437 – 7639	6339.4 – 7524.2	6338.6 – 7523.5	6338.2 – 7522.4	6338.2 – 7522.7
65	7595 – 9048	7473 – 8903	7686 – 9156	7640 – 9102	7524.2 – 8964.7	7523.5 – 8964.1	7522.4 – 8962.0	7522.7 – 8963.3
66	9049 – 10728	8904 – 10556	9157 – 10857	9103 – 10792	8964.7 – 10629.0	8964.1 – 10628.1	8962.0 – 10626.8	8963.3 – 10627.4
67	10729 – 12796	10557 – 12591	10858 – 12950	10793 – 12873	10629.0 – 12677.8	10628.1 – 12676.7	10626.8 – 12675.1	10627.4 – 12676.5
68	12797 – 15188	12592 – 14945	12951 – 15370	12874 – 15278	12677.8 – 15047.5	12676.7 – 15046.5	12675.1 – 15043.5	12676.5 – 15044.7
69	15189 – 18096	14946 – 17806	15371 – 18313	15279 – 18204	15047.5 – 17928.4	15046.5 – 17926.6	15043.5 – 17923.7	15044.7 – 17925.9
70	18097 – 21457	17807 – 21113	18314 – 21714	18205 – 21585	17928.4 – 21258.1	17926.6 – 21255.8	17923.7 – 21252.2	17925.9 – 21255.0
71	21458 – 25593	21114 – 25184	21715 – 25900	21586 – 25746	21258.1 – 25355.5	21255.8 – 25354.0	21252.2 – 25348.9	21255.0 – 25352.3
72	25594 – 30376	25185 – 29890	25901 – 30740	25747 – 30557	25355.5 – 30093.9	25354.0 – 30091.5	25348.9 – 30085.7	25352.3 – 30089.6
73	30377 – 36193	29891 – 35613	30741 – 36626	30558 – 36408	30093.9 – 35856.7	30091.5 – 35852.8	30085.7 – 35846.2	30089.6 – 35850.9
74	36194 – 42915	35614 – 42227	36627 – 43428	36409 – 43170	35856.7 – 42516.1	35852.8 – 42511.1	35846.2 – 42503.1	35850.9 – 42509.3
75	42916 – 51187	42228 – 50368	43429 – 51800	43171 – 51492	42516.1 – 50711.0	42511.1 – 50706.6	42503.1 – 50696.6	42509.3 – 50703.8
76	51188 – 126677	50369 – 124648	51801 – 128194	51493 – 127431	50711.0 – 125497.5	50706.6 – 125483.7	50696.6 – 125461.3	50703.8 – 125479.2

Table E.5: A-value ranges and DNL-corrected deposited energy ranges for the 77 DPI of the NO_EPT_foil/mag data products. The given ranges are specific for the HE2 detectors at a temperature configuration of -0.8°C.

	A-value range				Deposited energy range/ keV			
DPI	C1	C2	C3	C4	C1	C2	C3	C4
0	25 – 27	25 – 26	26 – 27	26 – 27	24.8 – 27.4	25.2 – 27.2	25.4 – 27.1	25.6 – 27.5
1	28 – 29	27 – 29	28 – 29	28 – 29	27.4 – 30.0	27.2 – 30.6	27.1 – 29.5	27.5 – 29.7
2	30 – 32	30 – 31	30 – 32	30 – 32	30.0 – 32.8	30.6 – 32.6	29.5 – 32.4	29.7 – 32.5
3	33 – 35	32 – 34	33 – 35	33 – 35	32.8 – 35.5	32.6 – 35.0	32.4 – 35.3	32.5 – 35.2
4	36 – 38	35 – 37	36 – 38	36 – 38	35.5 – 38.5	35.0 – 38.2	35.3 – 38.3	35.2 – 38.2
5	39 – 41	38 – 41	39 – 42	39 – 42	38.5 – 41.6	38.2 – 42.5	38.3 – 42.2	38.2 – 42.1
6	42 – 45	42 – 45	43 – 46	43 – 46	41.6 – 45.2	42.5 – 46.2	42.2 – 46.3	42.1 – 46.1
7	46 – 49	46 – 49	47 – 50	47 – 50	45.2 – 49.7	46.2 – 50.9	46.3 – 50.1	46.1 – 50.0
8	50 – 54	50 – 53	51 – 55	51 – 54	49.7 – 54.1	50.9 – 54.2	50.1 – 55.1	50.0 – 53.8
9	55 – 59	54 – 58	56 – 59	55 – 59	54.1 – 59.5	54.2 – 59.8	55.1 – 59.1	53.8 – 59.0
10	60 – 64	59 – 63	60 – 65	60 – 64	59.5 – 64.3	59.8 – 64.4	59.1 – 64.9	59.0 – 63.8
11	65 – 70	64 – 69	66 – 71	65 – 71	64.3 – 70.0	64.4 – 70.6	64.9 – 70.7	63.8 – 70.6
12	71 – 76	70 – 75	72 – 77	72 – 77	70.0 – 76.3	70.6 – 77.0	70.7 – 76.6	70.6 – 76.6
13	77 – 83	76 – 82	78 – 84	78 – 84	76.3 – 83.1	77.0 – 83.7	76.6 – 83.5	76.6 – 83.5
14	84 – 91	83 – 90	85 – 92	85 – 92	83.1 – 90.9	83.7 – 91.8	83.5 – 91.4	83.5 – 91.3
15	92 – 99	91 – 98	93 – 101	93 – 100	90.9 – 98.5	91.8 – 99.7	91.4 – 100.1	91.3 – 99.1
16	100 – 109	99 – 107	102 – 110	101 – 109	98.5 – 108.6	99.7 – 109.0	100.1 – 108.9	99.1 – 108.0
17	110 – 118	108 – 116	111 – 120	110 – 119	108.6 – 117.7	109.0 – 118.0	108.9 – 118.8	108.0 – 117.9
18	119 – 129	117 – 127	121 – 130	120 – 130	117.7 – 128.6	118.0 – 129.0	118.8 – 128.5	117.9 – 128.6
19	130 – 141	128 – 139	131 – 143	131 – 142	128.6 – 140.6	129.0 – 141.2	128.5 – 141.2	128.6 – 140.6
20	142 – 153	140 – 151	144 – 155	143 – 154	140.6 – 152.5	141.2 – 153.4	141.2 – 152.9	140.6 – 152.3
21	154 – 167	152 – 164	156 – 169	155 – 168	152.5 – 166.3	153.4 – 166.5	152.9 – 166.6	152.3 – 166.1
22	168 – 183	165 – 180	170 – 186	169 – 184	166.3 – 182.2	166.5 – 182.6	166.6 – 183.2	166.1 – 181.9
23	184 – 199	181 – 196	187 – 202	185 – 201	182.2 – 198.0	182.6 – 198.7	183.2 – 198.9	181.9 – 198.6
24	200 – 218	197 – 214	203 – 220	202 – 219	198.0 – 216.8	198.7 – 216.8	198.9 – 216.5	198.6 – 216.3
25	219 – 237	215 – 233	221 – 240	220 – 238	216.8 – 235.7	216.8 – 235.9	216.5 – 236.0	216.3 – 235.0
26	238 – 258	234 – 254	241 – 261	239 – 260	235.7 – 256.4	235.9 – 257.0	236.0 – 256.6	235.0 – 256.7
27	259 – 282	255 – 278	262 – 286	261 – 284	256.4 – 280.2	257.0 – 281.2	256.6 – 281.0	256.7 – 280.3
28	283 – 307	279 – 302	287 – 310	285 – 308	280.2 – 305.0	281.2 – 305.3	281.0 – 304.5	280.3 – 303.9
29	308 – 335	303 – 329	311 – 339	309 – 337	305.0 – 332.7	305.3 – 332.5	304.5 – 332.9	303.9 – 332.4
30	336 – 367	330 – 361	340 – 372	338 – 369	332.7 – 364.4	332.5 – 364.7	332.9 – 365.2	332.4 – 363.9
31	368 – 400	362 – 393	373 – 404	370 – 402	364.4 – 397.0	364.7 – 396.9	365.2 – 396.5	363.9 – 396.4
32	401 – 436	394 – 429	405 – 441	403 – 438	397.0 – 432.7	396.9 – 433.1	396.5 – 432.6	396.4 – 431.8
33	437 – 474	430 – 467	442 – 480	439 – 477	432.7 – 470.3	433.1 – 471.3	432.6 – 470.8	431.8 – 470.2
34	475 – 517	468 – 508	481 – 523	478 – 520	470.3 – 512.9	471.3 – 512.6	470.8 – 512.9	470.2 – 512.5
35	518 – 565	509 – 556	524 – 572	521 – 569	512.9 – 560.4	512.6 – 560.9	512.9 – 560.8	512.5 – 560.7
36	566 – 614	557 – 604	573 – 621	570 – 617	560.4 – 608.9	560.9 – 609.2	560.8 – 608.7	560.7 – 608.0
37	615 – 670	605 – 660	622 – 678	618 – 674	608.9 – 664.4	609.2 – 665.5	608.7 – 664.5	608.0 – 664.1
38	671 – 735	661 – 723	679 – 744	675 – 739	664.4 – 728.7	665.5 – 728.9	664.5 – 729.0	664.1 – 728.0
39	736 – 800	724 – 787	745 – 809	740 – 804	728.7 – 793.1	728.9 – 793.3	729.0 – 792.6	728.0 – 792.0
40	801 – 872	788 – 858	810 – 883	805 – 878	793.1 – 864.4	793.3 – 864.7	792.6 – 865.0	792.0 – 864.8
41	873 – 949	859 – 934	884 – 961	879 – 955	864.4 – 940.6	864.7 – 941.2	865.0 – 941.3	864.8 – 940.6
42	950 – 1034	935 – 1017	962 – 1046	956 – 1040	940.6 – 1024.8	941.2 – 1024.7	941.3 – 1024.4	940.6 – 1024.3
43	1035 – 1131	1018 – 1113	1047 – 1145	1041 – 1138	1024.8 – 1120.8	1024.7 – 1121.3	1024.4 – 1121.2	1024.3 – 1120.7
44	1132 – 1228	1114 – 1208	1146 – 1243	1139 – 1235	1120.8 – 1216.9	1121.3 – 1216.9	1121.2 – 1217.1	1120.7 – 1216.2
45	1229 – 1341	1209 – 1320	1244 – 1357	1236 – 1349	1216.9 – 1328.7	1216.9 – 1329.5	1217.1 – 1328.6	1216.2 – 1328.4
46	1342 – 1471	1321 – 1447	1358 – 1488	1350 – 1479	1328.7 – 1457.5	1329.5 – 1457.3	1328.6 – 1456.7	1328.4 – 1456.3
47	1472 – 1600	1448 – 1574	1489 – 1619	1480 – 1609	1457.5 – 1585.2	1457.3 – 1585.1	1456.7 – 1584.9	1456.3 – 1584.2
48	1601 – 1745	1575 – 1717	1620 – 1766	1610 – 1756	1585.2 – 1728.7	1585.1 – 1729.0	1584.9 – 1728.6	1584.2 – 1728.9
49	1746 – 1899	1718 – 1868	1767 – 1922	1757 – 1910	1728.7 – 1881.2	1729.0 – 1880.9	1728.6 – 1881.2	1728.9 – 1880.4
50	1900 – 2069	1869 – 2035	1923 – 2093	1911 – 2081	1881.2 – 2049.5	1880.9 – 2048.9	1881.2 – 2048.5	1880.4 – 2048.7
51	2070 – 2263	2036 – 2226	2094 – 2290	2082 – 2276	2049.5 – 2241.6	2048.9 – 2241.1	2048.5 – 2241.2	2048.7 – 2240.6
52	2264 – 2457	2227 – 2417	2291 – 2486	2277 – 2471	2241.6 – 2433.7	2241.1 – 2433.3	2241.2 – 2432.9	2240.6 – 2432.5
53	2458 – 2683	2418 – 2640	2487 – 2715	2472 – 2699	2433.7 – 2657.5	2433.3 – 2657.6	2432.9 – 2656.9	2432.5 – 2656.9
54	2684 – 2942	2641 – 2894	2716 – 2977	2700 – 2959	2657.5 – 2913.9	2657.6 – 2913.2	2656.9 – 2913.1	2656.9 – 2912.8
55	2943 – 3200	2895 – 3149	2978 – 3239	2960 – 3219	2913.9 – 3169.4	2913.2 – 3169.7	2913.1 – 3169.4	2912.8 – 3168.6
56	3201 – 3491	3150 – 3435	3240 – 3533	3220 – 3512	3169.4 – 3457.5	3169.7 – 3457.5	3169.4 – 3457.0	3168.6 – 3457.0
57	3492 – 3798	3436 – 3738	3534 – 3844	3513 – 3821	3457.5 – 3761.4	3457.5 – 3762.3	3457.0 – 3761.2	3457.0 – 3761.1
58	3799 – 4138	3739 – 4072	3845 – 4187	3822 – 4163	3761.4 – 4098.1	3762.3 – 4098.4	3761.2 – 4096.7	3761.1 – 4097.6
59	4139 – 4526	4073 – 4453	4188 – 4580	4164 – 4553	4098.1 – 4482.2	4098.4 – 4481.7	4096.7 – 4481.0	4097.6 – 4481.4
60	4527 – 4914	4454 – 4835	4581 – 4973	4554 – 4943	4482.2 – 4866.4	4481.7 – 4866.0	4481.0 – 4865.4	4481.4 – 4865.2
61	4915 – 5366	4836 – 5280	4974 – 5431	4944 – 5398	4866.4 – 5313.9	4866.0 – 5313.8	4865.4 – 5313.4	4865.2 – 5313.0
62	5367 – 5884	5281 – 5789	5432 – 5954	5399 – 5919	5313.9 – 5826.8	5313.8 – 5825.9	5313.4 – 5825.0	5313.0 – 5825.7
63	5885 – 6401	5790 – 6299	5955 – 6478	5920 – 6439	5826.8 – 6338.7	5825.9 – 6339.0	5825.0 – 6337.5	5825.7 – 6337.5
64	6402 – 7597	6300 – 7476	6479 – 7688	6440 – 7643	6338.7 – 7522.9	6339.0 – 7523.2	6337.5 – 7521.0	6337.5 – 7522.3
65	7598 – 9052	7477 – 8907	7689 – 9161	7644 – 9106	7522.9 – 8963.5	7523.2 – 8962.9	7521.0 – 8961.8	7522.3 – 8962.1
66	9053 – 10733	8908 – 10562	9162 – 10862	9107 – 10797	8963.5 – 10627.9	8962.9 – 10628.0	8961.8 – 10625.5	8962.1 – 10626.2
67	10734 – 12803	10563 – 12598	10863 – 12956	10798 – 12879	10627.9 – 12677.4	10628.0 – 12676.5	10625.5 – 12673.7	10626.2 – 12675.2
68	12804 – 15195	12599 – 14952	12957 – 15377	12880 – 15286	12677.4 – 15045.8	12676.5 – 15044.9	12673.7 – 15041.7	12675.2 – 15043.9
69	15196 – 18105	14953 – 17815	15378 – 18322	15287 – 18213	15045.8 – 17927.0	15044.9 – 17925.4	15041.7 – 17922.2	15043.9 – 17924.4
70	18106 – 21468	17816 – 21124	18323 – 21725	18214 – 21595	17927.0 – 21256.7	17925.4 – 21254.6	17922.2 – 21250.8	17924.4 – 21252.7
71	21469 – 25606	21125 – 25196	21726 – 25913	21596 – 25758	21256.7 – 25353.8	21254.6 – 25351.5	21250.8 – 25347.1	21252.7 – 25349.5
72	25607 – 30391	25197 – 29904	25914 – 30755	25759 – 30572	25353.8 – 30091.5	25351.5 – 30088.3	25347.1 – 30083.1	25349.5 – 30087.0
73	30392 – 36211	29905 – 35631	30756 – 36645	30573 – 36426	30091.5 – 35853.9	30088.3 – 35850.3	30083.1 – 35844.2	30087.0 – 35848.0
74	36212 – 42936	35632 – 42248	36646 – 43450	36427 – 43191	35853.9 – 42512.4	35850.3 – 42507.8	35844.2 – 42500.2	35848.0 – 42505.5
75	42937 – 51213	42249 – 50392	43451 – 51826	43192 – 51518	42512.4 – 50707.6	42507.8 – 50701.6	42500.2 – 50692.9	42505.5 – 50700.2
76	51214 – 126739	50393 – 124709	51827 – 128258	51519 – 127494	50707.6 – 125486.8	50701.6 – 125472.9	50692.9 – 125451.8	50700.2 – 125469.1

EPT LEVEL-2 CALIBRATION

After quantifying the detector-specific and temperature-depended deposited energy ranges of the 77 DPIs of the NO_EPT_mag/foil data products, corresponding response functions are calculated for each detector. From these detector-specific and temperature-depended response functions, new level-2 calibration factors (v03) are calculated for electrons in NO_EPT_foil, protons in NO_EPT_mag and helium in NO_EPT_mag. The three Tables on the following pages list these calibration factors. For details see Sect. D.

Table E.6: EPT level-2 calibration factors for electron in NO_EPT_foil. The given temperatures refer to onboard temperature configurations.

DPI	E_{low}/keV	E_{high}/keV	G_{Sun}/ mm^{2}sr -11.6°C	-6.0°C	G_{ASun}/ mm^{2}sr -11.6°C	-6.0°C	G_{North}/ mm^{2}sr -6.0°C	-0.8°C	G_{South}/ mm^{2}sr -6.0°C	-0.8°C
0	–	–	–	–	–	–	–	–	–	–
1	33.4	37.4	0.67	0.67	0.72	0.72	0.65	0.65	0.91	0.91
2	35.6	39.6	0.84	0.84	0.8	0.81	0.84	0.84	0.56	0.56
3	38.2	42.0	0.94	0.94	0.96	0.96	0.94	0.94	0.8	0.8
4	40.8	43.9	1.27	1.28	1.25	1.25	1.25	1.25	1.32	1.32
5	43.9	46.7	1.48	1.48	1.49	1.49	1.88	1.88	2.09	2.09
6	46.7	50.5	1.47	1.47	1.48	1.48	1.51	1.51	1.35	1.35
7	50.5	54.2	1.56	1.56	1.91	1.58	1.48	1.48	1.78	1.78
8	54.2	58.8	1.57	1.57	1.25	1.56	1.56	1.56	1.05	1.05
9	58.8	63.5	1.63	1.63	1.63	1.63	1.31	1.31	1.84	1.84
10	63.5	68.2	1.63	1.63	1.61	1.61	1.96	1.96	1.53	1.53
11	68.2	73.9	1.65	1.65	1.66	1.66	1.62	1.62	1.76	1.76
12	73.9	79.8	1.67	1.67	1.69	1.68	1.62	1.62	1.73	1.73
13	79.8	86.6	1.67	1.67	1.66	1.66	1.65	1.65	1.62	1.62
14	86.6	94.2	1.71	1.71	1.94	1.74	1.73	1.73	1.77	1.77
15	94.2	102.1	1.71	1.71	1.69	1.91	1.84	1.85	1.68	1.68
16	102.1	110.7	1.92	1.73	1.7	1.69	1.72	1.72	1.81	1.81
17	110.7	120.7	1.55	1.74	1.54	1.54	1.69	1.69	1.55	1.55
18	120.7	131.4	1.75	1.75	1.77	1.77	1.56	1.56	1.78	1.79
19	131.4	143.2	1.76	1.76	1.78	1.78	1.77	1.89	1.8	1.8
20	143.2	155.2	1.74	1.74	1.7	1.7	1.85	1.71	1.64	1.78
21	155.2	169.0	1.79	1.79	1.8	1.8	1.77	1.77	1.83	1.69
22	169.0	184.9	1.78	1.78	1.89	1.79	1.77	1.87	1.81	1.81
23	184.9	200.4	1.84	1.84	1.83	1.95	1.93	1.81	1.87	1.87
24	200.4	218.2	1.91	1.81	1.8	1.8	1.78	1.79	1.83	1.84
25	218.2	237.9	1.73	1.83	1.74	1.73	1.81	1.81	1.76	1.76
26	237.9	259.0	1.82	1.82	1.91	1.82	1.8	1.8	1.85	1.85
27	259.0	282.6	1.84	1.84	1.83	1.92	1.9	1.9	1.87	1.87
28	282.6	306.7	1.81	1.75	1.74	1.74	1.72	1.72	1.76	1.77
29	306.7	335.6	1.54	1.6	1.6	1.55	1.59	1.59	1.52	1.52
30	335.6	366.9	1.41	1.41	1.41	1.45	1.4	1.44	1.44	1.44
31	366.9	399.3	1.16	1.13	1.13	1.13	1.16	1.12	1.15	1.15
32	399.3	435.2	0.92	0.92	0.95	0.92	0.94	0.94	0.93	0.93
33	435.3	474.2	0.69	0.71	0.69	0.71	0.7	0.7	0.68	0.7
34	474.2	515.2	0.55	0.54	0.55	0.54	0.54	0.54	0.55	0.53
35	515.2	564.9	0.36	0.37	0.36	0.37	0.36	0.36	0.37	0.37
36	–	–	–	–	–	–	–	–	–	–
37	–	–	–	–	–	–	–	–	–	–
38	–	–	–	–	–	–	–	–	–	–
39	–	–	–	–	–	–	–	–	–	–
40	–	–	–	–	–	–	–	–	–	–
41	–	–	–	–	–	–	–	–	–	–
42	–	–	–	–	–	–	–	–	–	–
43	–	–	–	–	–	–	–	–	–	–
44	–	–	–	–	–	–	–	–	–	–
45	–	–	–	–	–	–	–	–	–	–
46	–	–	–	–	–	–	–	–	–	–
47	–	–	–	–	–	–	–	–	–	–
48	–	–	–	–	–	–	–	–	–	–
49	–	–	–	–	–	–	–	–	–	–
50	–	–	–	–	–	–	–	–	–	–
51	–	–	–	–	–	–	–	–	–	–
52	–	–	–	–	–	–	–	–	–	–
53	–	–	–	–	–	–	–	–	–	–
54	–	–	–	–	–	–	–	–	–	–
55	–	–	–	–	–	–	–	–	–	–
56	–	–	–	–	–	–	–	–	–	–
57	–	–	–	–	–	–	–	–	–	–
58	–	–	–	–	–	–	–	–	–	–
59	–	–	–	–	–	–	–	–	–	–
60	–	–	–	–	–	–	–	–	–	–
61	–	–	–	–	–	–	–	–	–	–
62	–	–	–	–	–	–	–	–	–	–
63	–	–	–	–	–	–	–	–	–	–
64	–	–	–	–	–	–	–	–	–	–
65	–	–	–	–	–	–	–	–	–	–
66	–	–	–	–	–	–	–	–	–	–
67	–	–	–	–	–	–	–	–	–	–
68	–	–	–	–	–	–	–	–	–	–
69	–	–	–	–	–	–	–	–	–	–
70	–	–	–	–	–	–	–	–	–	–
71	–	–	–	–	–	–	–	–	–	–
72	–	–	–	–	–	–	–	–	–	–
73	–	–	–	–	–	–	–	–	–	–
74	–	–	–	–	–	–	–	–	–	–
75	–	–	–	–	–	–	–	–	–	–
76	–	–	–	–	–	–	–	–	–	–

Table E.7: EPT level-2 calibration factors for protons in NO_EPT_mag. The given temperatures refer to onboard temperature configurations.

DPI	E_{low}/keV	E_{high}/keV	G_{Sun}/ mm^{2}sr		G_{ASun}/ mm^{2}sr		G_{North}/ mm^{2}sr		G_{South}/ mm^{2}sr	
			-11.6°C	-6.0°C	-11.6°C	-6.0°C	-6.0°C	-0.8°C	-6.0°C	-0.8°C
0	–	–	–	–	–	–	–	–	–	–
1	52.0	60.2	0.74	0.74	0.7	0.7	0.55	0.55	0.46	0.46
2	55.2	62.7	0.43	0.43	0.44	0.44	0.63	0.63	0.64	0.64
3	57.8	65.1	0.57	0.57	0.63	0.63	0.6	0.6	0.63	0.63
4	60.8	67.8	0.7	0.7	0.68	0.68	0.69	0.69	0.69	0.69
5	64.5	71.8	0.98	0.98	0.95	0.95	0.69	0.69	0.85	0.85
6	68.9	75.8	0.87	0.87	0.91	0.9	0.84	0.84	0.92	0.92
7	72.9	79.8	0.93	0.93	0.91	0.91	1.03	1.03	0.88	0.88
8	76.8	83.4	0.79	0.79	0.86	0.86	1.03	1.03	0.89	0.89
9	80.9	87.0	1.3	1.3	1.28	1.27	1.3	1.3	1.25	1.25
10	87.0	91.3	1.59	1.59	1.61	1.61	1.63	1.63	1.66	1.66
11	91.3	97.4	1.54	1.54	1.51	1.51	1.4	1.4	1.66	1.66
12	97.4	103.4	1.55	1.55	1.53	1.53	1.56	1.56	1.49	1.49
13	103.4	109.6	1.55	1.55	1.6	1.6	1.59	1.59	1.59	1.59
14	109.6	117.3	1.55	1.55	1.53	1.53	1.49	1.49	1.49	1.49
15	117.3	124.6	1.56	1.56	1.58	1.58	1.53	1.53	1.55	1.56
16	124.6	133.3	1.54	1.54	1.53	1.53	1.52	1.7	1.49	1.49
17	133.3	141.9	1.55	1.55	1.71	1.56	1.75	1.55	1.69	1.69
18	141.9	151.4	1.67	1.55	1.54	1.69	1.67	1.67	1.52	1.65
19	151.4	162.8	1.45	1.56	1.58	1.58	1.54	1.54	1.66	1.53
20	162.8	174.4	1.55	1.55	1.5	1.5	1.51	1.51	1.49	1.49
21	174.4	187.9	1.55	1.55	1.54	1.54	1.52	1.52	1.51	1.51
22	187.9	203.3	1.55	1.55	1.54	1.54	1.52	1.52	1.51	1.51
23	203.3	218.9	1.55	1.55	1.54	1.54	1.53	1.53	1.61	1.61
24	218.9	236.4	1.55	1.55	1.54	1.54	1.61	1.61	1.52	1.52
25	236.4	254.9	1.55	1.55	1.54	1.54	1.52	1.52	1.52	1.52
26	254.9	274.4	1.64	1.57	1.63	1.56	1.61	1.61	1.61	1.69
27	274.4	298.0	1.54	1.55	1.54	1.55	1.52	1.52	1.58	1.51
28	298.0	321.6	1.49	1.56	1.55	1.55	1.53	1.59	1.52	1.52
29	321.6	349.4	1.55	1.54	1.53	1.54	1.57	1.51	1.56	1.57
30	349.4	381.0	1.55	1.55	1.54	1.55	1.52	1.52	1.52	1.52
31	381.0	411.7	1.6	1.55	1.54	1.6	1.58	1.62	1.62	1.62
32	411.7	447.2	1.5	1.55	1.54	1.54	1.57	1.52	1.51	1.51
33	447.2	485.0	1.55	1.55	1.54	1.54	1.52	1.52	1.56	1.56
34	485.0	525.5	1.6	1.57	1.59	1.56	1.58	1.61	1.6	1.6
35	525.5	573.4	1.54	1.55	1.54	1.54	1.55	1.52	1.51	1.54
36	573.4	621.6	1.51	1.55	1.54	1.54	1.52	1.55	1.54	1.51
37	621.6	676.7	1.57	1.54	1.56	1.57	1.57	1.54	1.56	1.57
38	676.7	740.1	1.53	1.56	1.55	1.55	1.55	1.55	1.55	1.55
39	740.1	803.7	1.56	1.54	1.53	1.53	1.53	1.56	1.55	1.55
40	803.7	875.2	1.55	1.55	1.54	1.55	1.55	1.52	1.54	1.56
41	875.2	950.0	1.56	1.56	1.57	1.57	1.57	1.57	1.56	1.56
42	950.0	1034.2	1.53	1.53	1.54	1.52	1.54	1.54	1.55	1.53
43	1034.2	1129.4	1.56	1.56	1.55	1.55	1.53	1.55	1.54	1.55
44	1129.4	1225.8	1.54	1.54	1.53	1.54	1.54	1.54	1.55	1.53
45	1225.8	1337.6	1.55	1.55	1.55	1.54	1.56	1.55	1.55	1.55
46	1337.6	1464.1	1.57	1.55	1.56	1.56	1.55	1.56	1.55	1.55
47	1464.1	1593.4	1.53	1.54	1.54	1.53	1.53	1.53	1.54	1.54
48	1593.4	1737.2	1.55	1.55	1.54	1.56	1.55	1.55	1.55	1.56
49	1737.2	1886.7	1.57	1.57	1.57	1.56	1.57	1.57	1.56	1.56
50	1886.7	2053.7	1.56	1.56	1.55	1.55	1.56	1.56	1.56	1.56
51	2053.7	2247.9	1.52	1.52	1.53	1.53	1.53	1.52	1.53	1.52
52	2247.9	2437.5	1.56	1.56	1.55	1.56	1.55	1.56	1.56	1.56
53	2437.5	2660.2	1.55	1.55	1.55	1.55	1.55	1.55	1.55	1.55
54	2660.2	2920.9	1.52	1.51	1.51	1.51	1.51	1.52	1.51	1.51
55	2920.9	3172.5	1.57	1.57	1.57	1.57	1.57	1.56	1.57	1.57
56	3172.5	3460.9	1.54	1.54	1.54	1.54	1.54	1.54	1.54	1.54
57	3460.9	3762.0	1.56	1.55	1.55	1.56	1.55	1.55	1.56	1.56
58	3762.0	4099.3	1.53	1.53	1.53	1.52	1.53	1.53	1.53	1.53
59	4099.3	4482.1	1.54	1.54	1.55	1.55	1.54	1.54	1.55	1.54
60	4482.1	4870.1	1.51	1.51	1.51	1.51	1.51	1.51	1.51	1.51
61	4870.1	5314.7	1.54	1.54	1.54	1.54	1.54	1.54	1.54	1.54
62	5314.7	5832.2	1.53	1.53	1.53	1.53	1.53	1.53	1.53	1.53
63	5832.2	6131.6	1.56	1.55	1.54	1.55	1.54	1.54	1.55	1.55
64	–	–	–	–	–	–	–	–	–	–
65	–	–	–	–	–	–	–	–	–	–
66	–	–	–	–	–	–	–	–	–	–
67	–	–	–	–	–	–	–	–	–	–
68	–	–	–	–	–	–	–	–	–	–
69	–	–	–	–	–	–	–	–	–	–
70	–	–	–	–	–	–	–	–	–	–
71	–	–	–	–	–	–	–	–	–	–
72	–	–	–	–	–	–	–	–	–	–
73	–	–	–	–	–	–	–	–	–	–
74	–	–	–	–	–	–	–	–	–	–
75	–	–	–	–	–	–	–	–	–	–
76	–	–	–	–	–	–	–	–	–	–

Table E.8: EPT level-2 calibration factors for helium-4 in NO_EPT_mag. The given temperatures refer to onboard temperature configurations.

DPI	E_{low}/keV	E_{high}/keV	G_{Sun}/ mm^{2}sr		G_{ASun}/ mm^{2}sr		G_{North}/ mm^{2}sr		G_{South}/ mm^{2}sr	
			-11.6°C	-6.0°C	-11.6°C	-6.0°C	-6.0°C	-0.8°C	-6.0°C	-0.8°C
0	–	–	–	–	–	–	–	–	–	–
1	52.7	66.7	0.57	0.57	0.54	0.54	0.43	0.43	0.36	0.36
2	56.8	70.6	0.32	0.32	0.33	0.33	0.46	0.46	0.47	0.47
3	60.1	73.7	0.41	0.41	0.46	0.46	0.43	0.43	0.45	0.45
4	64.1	77.5	0.5	0.5	0.48	0.48	0.49	0.49	0.49	0.49
5	69.4	82.9	0.71	0.71	0.69	0.69	0.51	0.51	0.62	0.62
6	75.3	88.6	0.62	0.62	0.65	0.65	0.6	0.6	0.66	0.66
7	81.0	93.9	0.68	0.68	0.66	0.66	0.75	0.75	0.64	0.64
8	86.2	99.1	0.56	0.56	0.61	0.61	0.73	0.73	0.63	0.63
9	91.9	105.2	0.84	0.84	0.82	0.82	0.83	0.83	0.81	0.81
10	98.8	111.5	0.74	0.74	0.75	0.75	0.76	0.76	0.78	0.78
11	105.6	116.4	1.14	1.14	1.11	1.11	1.03	1.03	1.23	1.23
12	116.4	126.8	1.24	1.24	1.22	1.22	1.25	1.25	1.19	1.19
13	122.4	132.8	1.24	1.24	1.29	1.28	1.27	1.27	1.27	1.27
14	132.8	143.1	1.52	1.52	1.5	1.5	1.46	1.46	1.46	1.46
15	143.1	152.7	1.57	1.57	1.59	1.58	1.54	1.54	1.56	1.56
16	152.7	164.0	1.54	1.53	1.53	1.53	1.52	1.69	1.49	1.49
17	164.0	174.7	1.57	1.57	1.73	1.58	1.76	1.56	1.71	1.71
18	174.7	186.7	1.67	1.55	1.53	1.69	1.67	1.67	1.52	1.65
19	186.7	200.7	1.45	1.56	1.58	1.58	1.53	1.53	1.66	1.53
20	200.7	214.9	1.55	1.54	1.49	1.49	1.5	1.5	1.48	1.48
21	214.9	230.8	1.56	1.56	1.55	1.55	1.53	1.53	1.53	1.53
22	230.8	248.9	1.56	1.56	1.55	1.54	1.53	1.53	1.53	1.53
23	248.9	266.8	1.54	1.54	1.53	1.53	1.52	1.52	1.6	1.6
24	266.8	286.6	1.55	1.55	1.55	1.55	1.61	1.61	1.52	1.52
25	286.6	307.2	1.56	1.56	1.55	1.55	1.53	1.53	1.53	1.53
26	307.2	328.8	1.62	1.55	1.62	1.54	1.6	1.6	1.6	1.67
27	328.8	354.3	1.54	1.55	1.54	1.55	1.52	1.52	1.58	1.51
28	354.3	379.6	1.49	1.56	1.55	1.55	1.53	1.59	1.53	1.53
29	379.6	408.7	1.55	1.55	1.54	1.54	1.58	1.52	1.57	1.57
30	408.7	441.7	1.56	1.55	1.54	1.55	1.53	1.53	1.52	1.52
31	441.7	473.6	1.59	1.54	1.53	1.59	1.57	1.61	1.61	1.61
32	473.6	510.3	1.5	1.55	1.54	1.54	1.56	1.52	1.51	1.51
33	510.3	548.3	1.56	1.56	1.55	1.55	1.53	1.53	1.56	1.56
34	548.3	589.6	1.58	1.55	1.58	1.54	1.56	1.59	1.58	1.58
35	589.6	637.3	1.56	1.56	1.55	1.56	1.57	1.53	1.52	1.55
36	637.3	685.3	1.51	1.55	1.54	1.54	1.52	1.55	1.54	1.51
37	685.3	739.9	1.59	1.56	1.58	1.58	1.59	1.56	1.58	1.58
38	739.9	803.5	1.51	1.54	1.53	1.53	1.53	1.54	1.53	1.53
39	803.5	865.6	1.58	1.55	1.55	1.55	1.55	1.57	1.57	1.57
40	865.6	937.3	1.54	1.54	1.53	1.53	1.53	1.51	1.52	1.54
41	937.3	1011.5	1.55	1.55	1.57	1.57	1.57	1.57	1.56	1.56
42	1011.5	1092.9	1.56	1.56	1.57	1.55	1.57	1.57	1.58	1.56
43	1092.9	1188.8	1.53	1.53	1.53	1.53	1.51	1.52	1.51	1.53
44	1188.8	1283.1	1.56	1.56	1.55	1.57	1.57	1.57	1.57	1.56
45	1283.0	1391.2	1.58	1.58	1.59	1.57	1.59	1.58	1.58	1.58
46	1391.2	1517.0	1.56	1.55	1.55	1.55	1.54	1.56	1.55	1.55
47	1517.0	1645.4	1.52	1.52	1.52	1.52	1.52	1.52	1.52	1.52
48	1645.4	1784.9	1.58	1.58	1.57	1.59	1.58	1.57	1.58	1.59
49	1784.9	1937.9	1.53	1.53	1.53	1.52	1.53	1.53	1.52	1.52
50	1937.9	2101.6	1.57	1.57	1.56	1.56	1.57	1.57	1.57	1.57
51	2101.6	2290.4	1.55	1.55	1.56	1.56	1.55	1.55	1.55	1.55
52	2290.4	2484.9	1.52	1.52	1.51	1.52	1.51	1.52	1.52	1.52
53	2484.9	2706.9	1.55	1.55	1.55	1.55	1.55	1.55	1.55	1.55
54	2706.9	2959.1	1.57	1.56	1.56	1.56	1.56	1.57	1.56	1.56
55	2959.1	3214.6	1.54	1.54	1.54	1.54	1.54	1.53	1.54	1.54
56	3214.6	3497.5	1.56	1.56	1.56	1.56	1.56	1.56	1.56	1.56
57	3497.5	3799.1	1.55	1.55	1.55	1.55	1.55	1.55	1.55	1.55
58	3799.1	4137.5	1.53	1.53	1.53	1.52	1.53	1.53	1.53	1.53
59	4137.5	4516.5	1.56	1.56	1.57	1.56	1.56	1.56	1.57	1.56
60	4516.5	4901.5	1.54	1.54	1.54	1.54	1.54	1.54	1.54	1.54
61	4901.5	5348.7	1.54	1.54	1.54	1.55	1.55	1.54	1.54	1.54
62	5348.7	5855.9	1.56	1.56	1.56	1.56	1.56	1.56	1.56	1.56
63	5855.9	6372.3	1.53	1.53	1.53	1.53	1.53	1.53	1.53	1.53
64	6372.4	7543.8	1.56	1.56	1.56	1.56	1.56	1.56	1.56	1.56
65	7543.8	8989.3	1.54	1.54	1.54	1.54	1.54	1.54	1.54	1.54
66	8989.3	10639.1	1.55	1.55	1.55	1.55	1.55	1.55	1.55	1.55
67	10639.1	12687.0	1.53	1.53	1.53	1.53	1.53	1.53	1.53	1.53
68	12687.0	15048.0	1.54	1.54	1.53	1.54	1.54	1.53	1.53	1.54
69	15048.0	17926.7	1.53	1.53	1.53	1.53	1.53	1.53	1.53	1.53
70	17926.7	21259.3	1.53	1.53	1.53	1.53	1.53	1.53	1.53	1.53
71	21259.3	24506.8	1.52	1.52	1.52	1.52	1.52	1.52	1.52	1.52
72	–	–	–	–	–	–	–	–	–	–
73	–	–	–	–	–	–	–	–	–	–
74	–	–	–	–	–	–	–	–	–	–
75	–	–	–	–	–	–	–	–	–	–
76	–	–	–	–	–	–	–	–	–	–

F

EPT GCR BACKGROUND

Figures F.1 to F.4 show comparisons of the calculated GCR count rates and observed count rates in NO_EPT_foil and NO_EPT_mag data products of EPT for four different periods. The different lines show the calculated GCR count rates from protons (blue), helium (orange) and oxygen (green). The black line shows the sum of the calculated count rates from all three species. Dots show the actual measured count rates. The lower panels show the relative differences between the calculated sum of the GCR count rates and the actual measured count rates. For details, see Sect. 5.2.

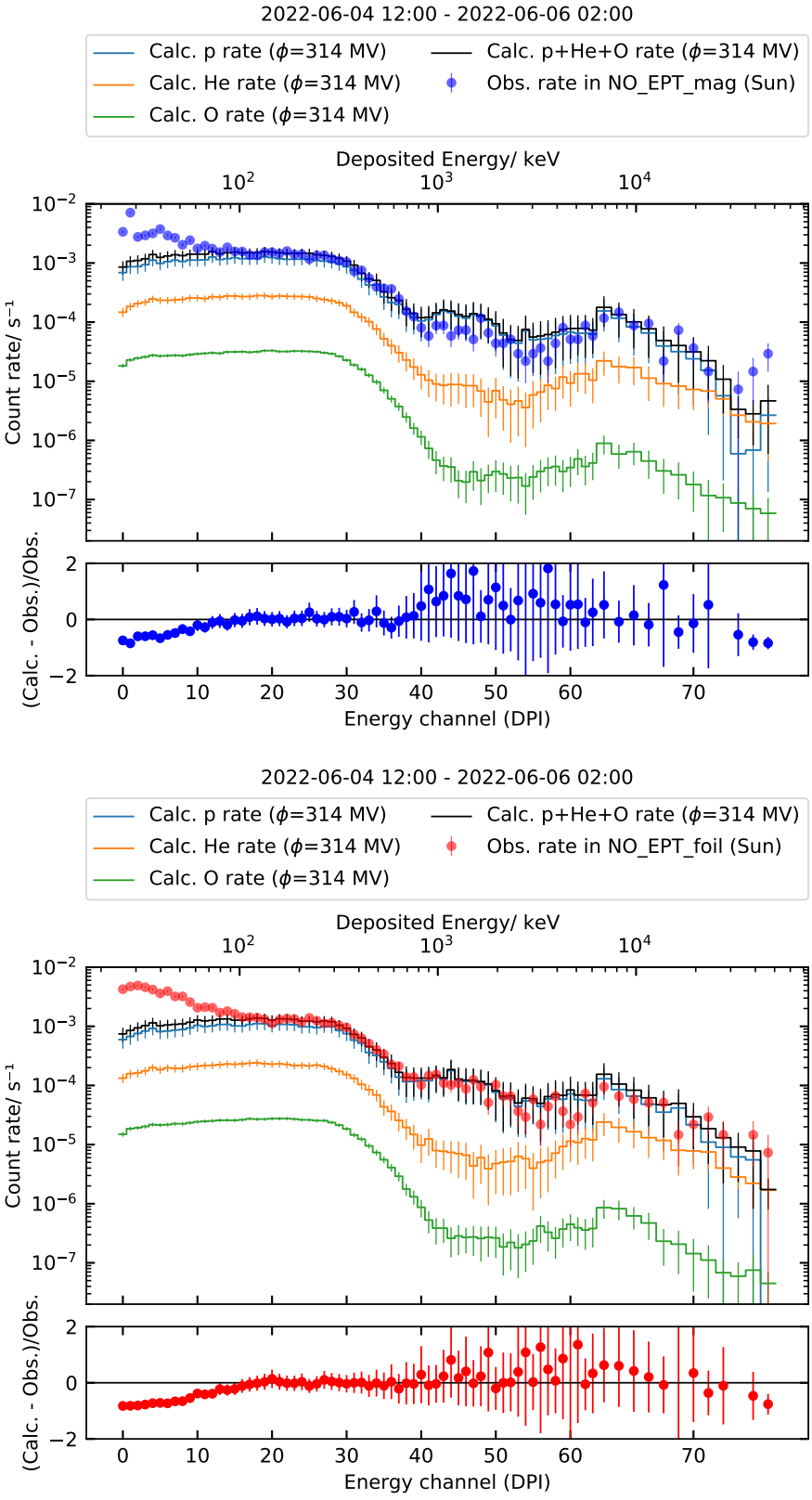

Figure F.1: GCR count rates in the EPT sunward looking magnet and foil detectors on 2022-06-04.

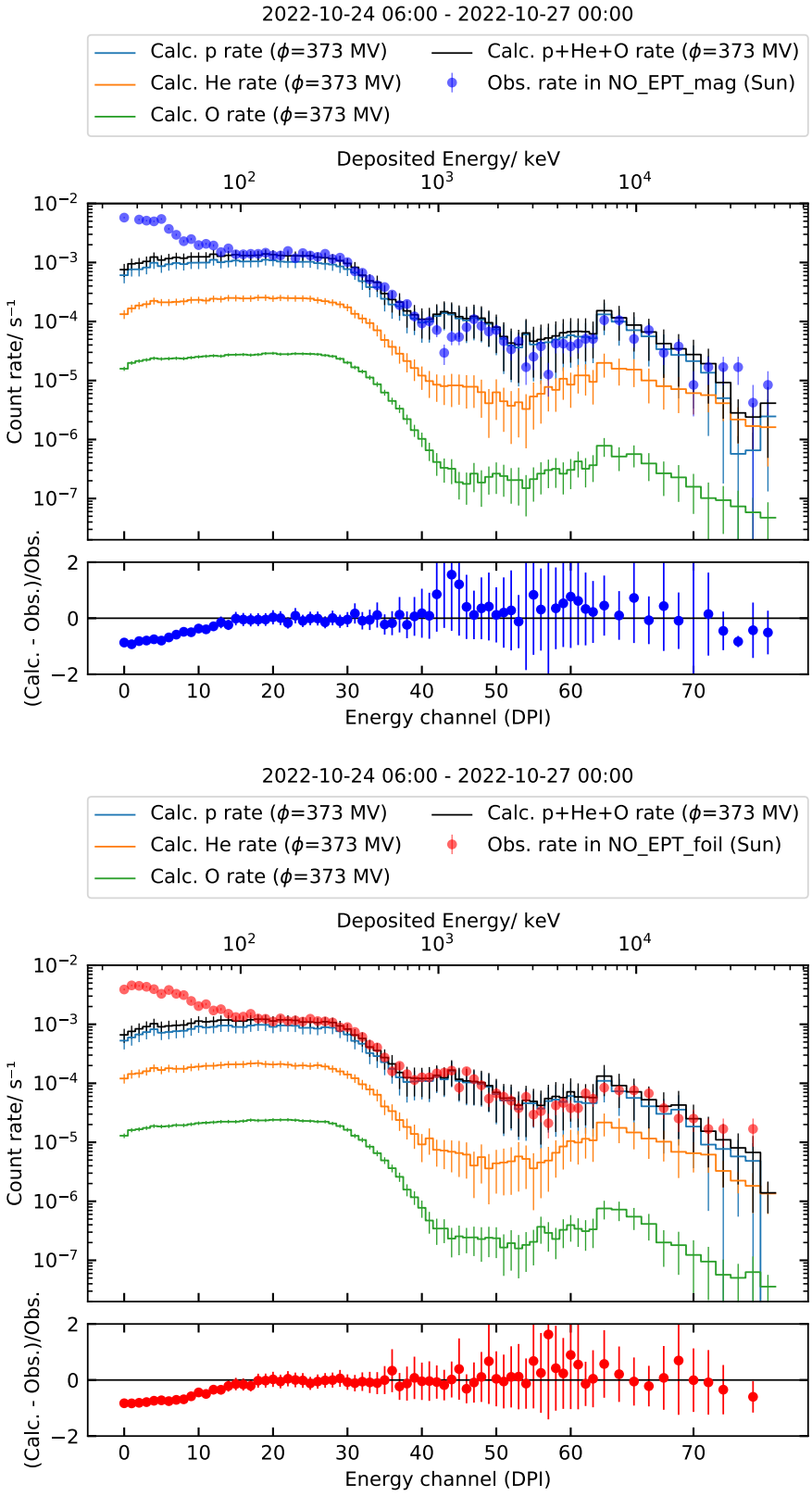

Figure F.2: GCR count rates in the EPT sunward looking magnet and foil detectors on 2022-10-24.

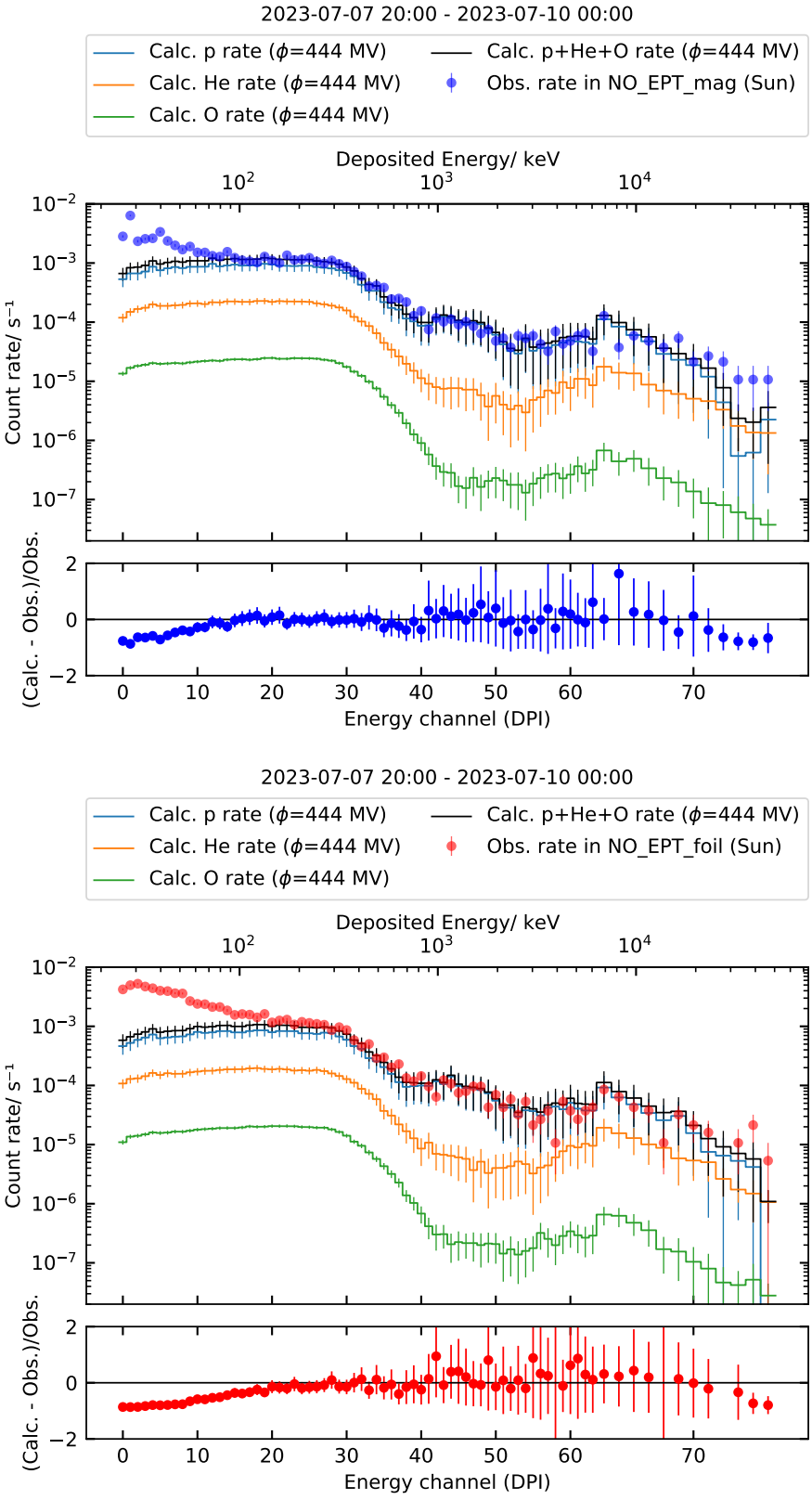

Figure F.3: GCR count rates in the EPT sunward looking magnet and foil detectors on 2023-07-07.

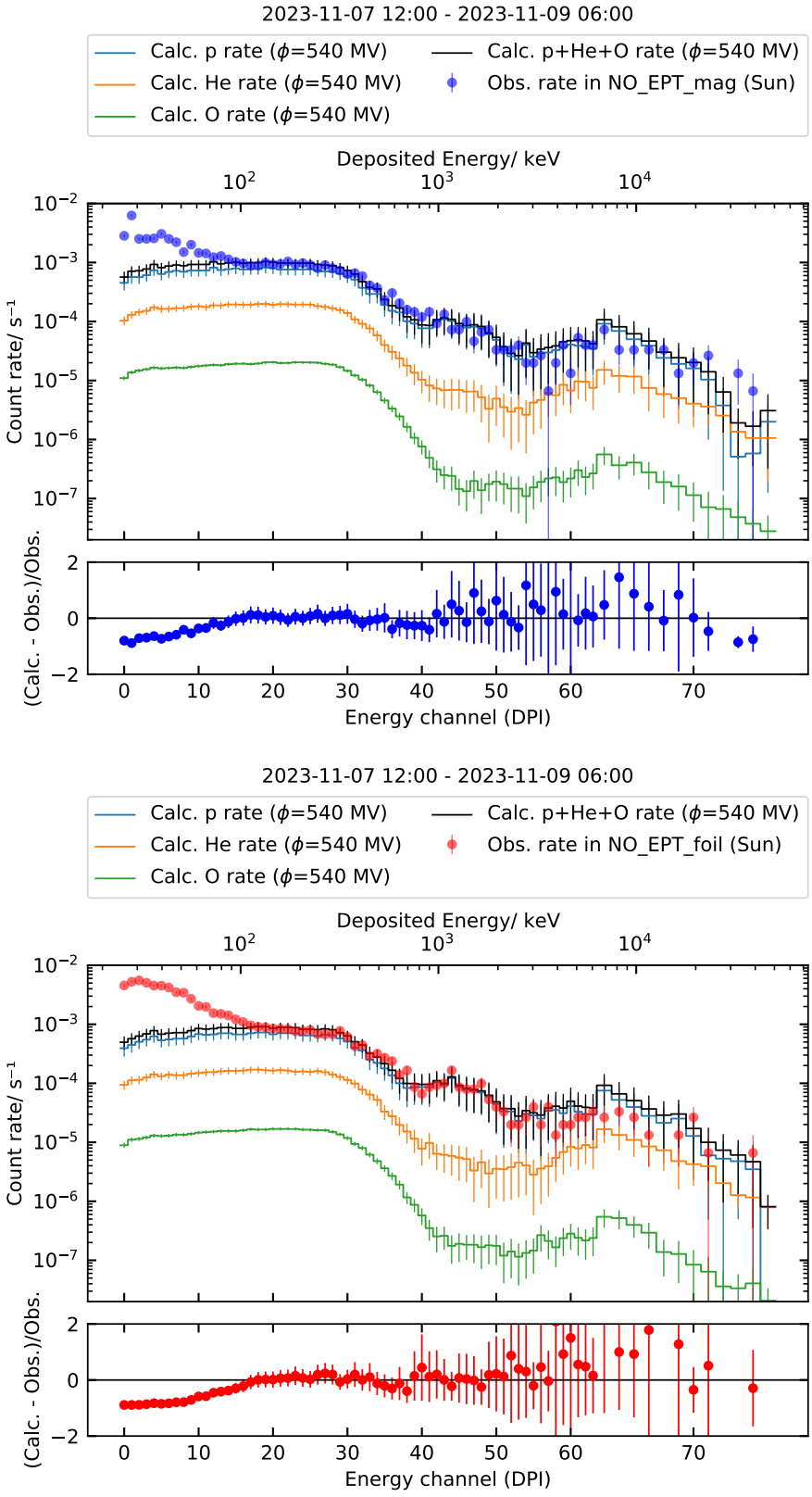

Figure F.4: GCR count rates in the EPT sunward looking magnet and foil detectors on 2023-11-07.

BIBLIOGRAPHY

Aellig, M. R., A. J. Lazarus, and J. T. Steinberg (July 2001). "The solar wind helium abundance: Variation with wind speed and the solar cycle." In: *grl* 28.14, pp. 2767–2770. DOI: 10.1029/2000GL012771.

Agueda, N. et al. (Nov. 2009). "Modeling solar near-relativistic electron events. Insights into solar injection and interplanetary transport conditions." In: *A&A* 507.2, pp. 981–993. DOI: 10.1051/0004-6361/200912224.

Aguilar, M. et al. (Feb. 2021). "The Alpha Magnetic Spectrometer (AMS) on the international space station: Part II - Results from the first seven years." In: *physrep* 894, pp. 1–116. DOI: 10.1016/j.physrep.2020.09.003.

Aharonian, F. A. et al. (Nov. 2004). "High-energy particle acceleration in the shell of a supernova remnant." In: *nat* 432.7013, pp. 75–77. DOI: 10.1038/nature02960.

Alfvén, H. (Jan. 1947). "Magneto hydrodynamic waves, and the heating of the solar corona." In: *mnras* 107, p. 211. DOI: 10.1093/mnras/107.2.211.

Antonucci, E., A. H. Gabriel, and B. R. Dennis (Dec. 1984). "The energetics of chromospheric evaporation in solar flares." In: *ApJ* 287, pp. 917–925. DOI: 10.1086/162749.

Apostolakis, J. et al. (Oct. 2009). "Geometry and physics of the Geant4 toolkit for high and medium energy applications." In: *Radiation Physics and Chemistry* 78.10, pp. 859–873. DOI: 10.1016/j.radphyschem.2009.04.026.

Aschwanden, M. J. (2005). *Physics of the Solar Corona. An Introduction with Problems and Solutions (2nd edition)*. Springer.

Barnes, C. W. and J. A. Simpson (Dec. 1976). "Evidence for interplanetary acceleration of nucleons in corotating interaction regions." In: *apjl* 210, pp. L91–L96. DOI: 10.1086/182311.

Berghmans, D. et al. (2021). "Extreme-UV quiet Sun brightenings observed by the Solar Orbiter/EUI." In: *A&A* 656, p. L4. DOI: 10.1051/0004-6361/202140380.

Bethe, H. A. (1939). "Energy Production in Stars." In: *Phys. Rev.* 55 (5), pp. 434–456. DOI: 10.1103/PhysRev.55.434.

Bieber, John W. et al. (2002). "Energetic Particle Observations during the 2000 July 14 Solar Event." In: *The Astrophysical Journal* 567.1, p. 622. DOI: 10.1086/338246.

Biermann, L. (Jan. 1951). "Kometenschweife und solare Korpuskularstrahlung." In: *zap* 29, p. 274.

Biesecker, D. A. et al. (Apr. 2002). "Solar Phenomena Associated with "EIT Waves"." In: *ApJ* 569.2, pp. 1009–1015. DOI: 10.1086/339402.

Binns, W. R. et al. (Sept. 2022). "The Isotopic Abundances of Galactic Cosmic Rays with Atomic Number $29 \leq Z \leq 38$." In: *ApJ* 936.1, 13. DOI: 10.3847/1538-4357/ac82e7.

Bogdan, T. J. et al. (Apr. 1988). "Distribution of Sunspot Umbral Areas: 1917–1982." In: *ApJ* 327, p. 451. DOI: 10.1086/166206.

Bougeret, J. L. et al. (Feb. 1995). "Waves: The Radio and Plasma Wave Investigation on the Wind Spacecraft." In: *ssr* 71.1-4, pp. 231–263. DOI: 10.1007/BF00751331.

Brüdern, M. et al. (July 2022). "A new method to determine solar energetic particle anisotropies and their associated uncertainties demonstrated for STEREO/SEPT." In: *A&A* 663, A89. DOI: 10.1051/0004-6361/202142761.

Brueckner, G. E. et al. (Dec. 1995). "The Large Angle Spectroscopic Coronagraph (LASCO)." In: *solphys* 162.1-2, pp. 357–402. DOI: 10.1007/BF00733434.

Buttighoffer, A. (July 1998). "Solar electron beams associated with radio type III." In: *A&A* 335, pp. 295–302.

Böhm, E., A. Kharytonov, and R. F. Wimmer-Schweingruber (2007). "Solar energetic particle spectra from the SOHO-EPHIN sensor by application of regularization methods." In: *A&A* 473.2, pp. 673–682. DOI: 10.1051/0004-6361:20077216.

Cane, H. V., R. E. McGuire, and T. T. von Rosenvinge (Feb. 1986). "Two Classes of Solar Energetic Particle Events Associated with Impulsive and Long-Duration Soft X-Ray Flares." In: *ApJ* 301, p. 448. DOI: 10.1086/163913.

Cane, H. V., D. V. Reames, and T. T. von Rosenvinge (Sept. 1988). "The role of interplanetary shocks in the longitude distribution of solar energetic particles." In: *jgr* 93.A9, pp. 9555–9567. DOI: 10.1029/JA093iA09p09555.

Carlsson, Mats, Bart De Pontieu, and Viggo H. Hansteen (Aug. 2019). "New View of the Solar Chromosphere." In: *araa* 57, pp. 189–226. DOI: 10.1146/annurev-astro-081817-052044.

Carrington, R. C. (Nov. 1858). "On the Distribution of the Solar Spots in Latitudes since the Beginning of the Year 1854, with a Map." In: *mnras* 19, pp. 1–3. DOI: 10.1093/mnras/19.1.1.

Carrington, R. C. (Nov. 1859). "Description of a Singular Appearance seen in the Sun on September 1, 1859." In: *mnras* 20, pp. 13–15. DOI: 10.1093/mnras/20.1.13.

Charbonneau, P. (Dec. 2020). "Dynamo models of the solar cycle." In: *Living Reviews in Solar Physics* 17. DOI: 10.1007/s41116-020-00025-6.

Cliver, E. W. et al. (Jan. 1995). "Extreme "Propagation" of Solar Energetic Particles." In: *International Cosmic Ray Conference*. Vol. 4. International Cosmic Ray Conference, p. 257.

Costanzo, D. et al. (2006). "The Geant4-Based Simulation Software of the ATLAS Detector." In: *2006 IEEE Nuclear Science Symposium Conference Record*. Vol. 1, pp. 5–11. DOI: 10.1109/NSSMIC.2006.356099.

Cummings, A. C. et al. (2016). "GALACTIC COSMIC RAYS IN THE LOCAL INTERSTELLAR MEDIUM: VOYAGER 1 OBSERVATIONS AND MODEL RESULTS." In: *The Astrophysical Journal* 831.1, p. 18. DOI: 10.3847/0004-637X/831/1/18.

Cummings, C. A. et al. (Jan. 1990). "Radial and Latitudinal Gradients of Anomalous Cosmic-Ray Oxygen and Helium from 1 to - 41 AU." In: *21st International Cosmic Ray Conference (ICRC21)*. Vol. 6. International Cosmic Ray Conference, p. 206.

Daibog, E. I. et al. (Jan. 2003). "Statistical properties of SEP event flux declines." In: *Advances in Space Research* 32.12, pp. 2655–2660. DOI: 10.1016/S0273-1177(03)00907-4.

Decker, R. B. et al. (Sept. 2005). "Voyager 1 in the Foreshock, Termination Shock, and Heliosheath." In: *Science* 309.5743, pp. 2020–2024. DOI: 10.1126/science.1117569.

Dennis, B. R., B. M. Uberall, and D. M. Zarro (1992). "The Neupert Effect - what can it Tell us about the Impulsive and Gradual Phases of Eruptive Flares." In: *IAU Colloq. 133: Eruptive Solar Flares*. Ed. by Zdenek Svestka, Bernard V. Jackson, and Marcos E. Machado. Vol. 399, p. 139. DOI: 10.1007/3-540-55246-4_90.

Desai, Mihir and Joe Giacalone (Dec. 2016). "Large gradual solar energetic particle events." In: *Living Reviews in Solar Physics* 13.1, 3. DOI: 10.1007/s41116-016-0002-5.

Ding, Z. et al. (Dec. 2022). "Modeling the 2020 November 29 solar energetic particle event using EUHFORIA and iPATH models." In: *A&A* 668, A71. DOI: 10.1051/0004-6361/202244732.

Dresing, N. et al. (Feb. 2020). "Statistical Results for Solar Energetic Electron Spectra Observed over 12 yr with STEREO/SEPT." In: *ApJ* 889.2, 143. DOI: 10.3847/1538-4357/ab64e5.

Dröge, W. (Jan. 2005). "Probing heliospheric diffusion coefficients with solar energetic particles." In: *Advances in Space Research* 35.4, pp. 532–542. DOI: 10.1016/j.asr.2004.12.007.

Dröge, W. et al. (Feb. 2010). "Anisotropic Three-Dimensional Focused Transport of Solar Energetic Particles in the Inner Heliosphere." In: *ApJ* 709.2, pp. 912–919. DOI: 10.1088/0004-637X/709/2/912.

Espinosa Lara, F. et al. (2024). In: *Solar Orbiter EPD-EPT level 3 data - Correcting for ion contamination in EPT level 3 electron data*.

Feldman, U., E. Landi, and N. A. Schwadron (July 2005). "On the sources of fast and slow solar wind." In: *Journal of Geophysical Research (Space Physics)* 110.A7, A07109. DOI: 10.1029/2004JA010918.

Forstner, J. L. Freiherr von (2020). "Multipoint observations of ICMEs in the inner heliosphere." PhD thesis. IEAP CAU Kiel.

Forveille, T. and Shore, S. (2020). "The Solar Orbiter mission." In: *A&A* 642, E1. DOI: 10.1051/0004-6361/202039499.

Gabriel, A. H. (May 1976). "A Magnetic Model of the Solar Transition Region." In: *Philosophical Transactions of the Royal Society of London Series A* 281.1304, pp. 339–352. DOI: 10.1098/rsta.1976.0031.

Gary, G. Allen (Oct. 2001). "Plasma Beta above a Solar Active Region: Rethinking the Paradigm." In: *solphys* 203.1, pp. 71–86. DOI: 10.1023/A:1012722021820.

Geant4 Collaboration (2024). *Geant4 Documentation*. URL: https://geant4.web.cern.ch/docs/.

Geant4 Docs (2023a). *Reference Physics Lists EM Liv*. https://geant4-userdoc.web.cern.ch/UsersGuides/PhysicsListGuide/html/electromagnetic/Liv.html. [Online; accessed 24-Aug-2023].

Geant4 Docs (2023b). *Reference Physics Lists QGSP_BERT*. https://geant4-userdoc.web.cern.ch/UsersGuides/PhysicsListGuide/html/reference_PL/QGSP_BERT.html. [Online; accessed 24-Aug-2023].

Gleeson, L. J. and W. I. Axford (Dec. 1968). "Solar Modulation of Galactic Cosmic Rays." In: *ApJ* 154, p. 1011. DOI: 10.1086/149822.

Gómez-Herrero, R. et al. (Jan. 2015). "Circumsolar Energetic Particle Distribution on 2011 November 3." In: *ApJ* 799.1, 55. DOI: 10.1088/0004-637X/799/1/55.

Gómez-Herrero, R. et al. (Dec. 2021). "First near-relativistic solar electron events observed by EPD onboard Solar Orbiter." In: *A&A* 656, L3. DOI: 10.1051/0004-6361/202039883.

Goossens, Marcel (2003). *An introduction to plasma astrophysics and magnetohydrodynamics*. Vol. 294. DOI: 10.1007/978-94-007-1076-4.

Gopalswamy, N., P. Mäkelä, and S. Yashiro (Jan. 2019). "A Catalog of Type II radio bursts observed by Wind/WAVES and their Statistical Properties." In: *Sun and Geosphere* 14, pp. 111–121. DOI: 10.31401/SunGeo.2019.02.03.

Gopalswamy, N. et al. (Apr. 2009). "The SOHO/LASCO CME Catalog." In: *Earth Moon and Planets* 104.1-4, pp. 295–313. DOI: 10.1007/s11038-008-9282-7.

Gosling, J. T. (Nov. 1993). "The solar flare myth." In: *jgr* 98.A11, pp. 18937–18950. DOI: 10.1029/93JA01896.

Gosling, J. T. et al. (Feb. 1981). "Interplanetary ions during an energetic storm particle event: The distribution function from solar wind thermal energies to 1.6 MeV." In: *jgr* 86.A2, pp. 547–554. DOI: 10.1029/JA086iA02p00547.

Grunau, J. (Apr. 19, 2013). *Internal document: SO-EPD-KIE-TN-0004-iss1 rev3 EPT-HET Detector descrition*.

Gurnett, D. A. et al. (Sept. 2013). "In Situ Observations of Interstellar Plasma with Voyager 1." In: *Science* 341.6153, pp. 1489–1492. DOI: 10.1126/science.1241681.

Hale, G. E. and S. B. Nicholson (Nov. 1925). "The Law of Sun-Spot Polarity." In: *ApJ* 62, p. 270. DOI: 10.1086/142933.

Hale, George E. et al. (Apr. 1919). "The Magnetic Polarity of Sun-Spots." In: *ApJ* 49, p. 153. DOI: 10.1086/142452.

Hamini, A. et al. (2021). "ORFEES – a radio spectrograph for the study of solar radio bursts and space weather applications." In: *J. Space Weather Space Clim.* 11, p. 57. DOI: 10.1051/swsc/2021039.

Hansen, P. C. (1992). "Analysis of Discrete Ill-Posed Problems by Means of the L-Curve." In: *SIAM Review* 34.4, pp. 561–580. DOI: 10.1137/1034115.

Hanser, F. A. and F. B. Sellers (Oct. 1996). "Design and calibration of the GOES-8 solar x-ray sensor: the XRS." In: *GOES-8 and Beyond*. Ed. by Edward R. Washwell. Vol. 2812. Society of Photo-Optical Instrumentation Engineers (SPIE) Conference Series, pp. 344–352. DOI: 10.1117/12.254082.

Hillas, A. M. (Jan. 1984). "The Origin of Ultra-High-Energy Cosmic Rays." In: *araa* 22, pp. 425–444. DOI: 10.1146/annurev.aa.22.090184.002233.

Horbury, T. S. et al. (Oct. 2020). "The Solar Orbiter magnetometer." In: *A&A* 642, A9. DOI: 10.1051/0004-6361/201937257.

Ivanchenko, V. et al. (July 2019). "Progress of Geant4 electromagnetic physics developments and applications." In: *European Physical Journal Web of Conferences*. Vol. 214. European Physical Journal Web of Conferences, 02046. DOI: 10.1051/epjconf/201921402046.

Jan, S et al. (2004). "GATE: a simulation toolkit for PET and SPECT." In: *Physics in Medicine & Biology* 49.19, p. 4543. DOI: 10.1088/0031-9155/49/19/007.

Jokipii, J. R. (Nov. 1966). "Cosmic-Ray Propagation. I. Charged Particles in a Random Magnetic Field." In: *ApJ* 146, p. 480. DOI: 10.1086/148912.

Jones, F. C. and D. C. Ellison (Dec. 1991). "The plasma physics of shock acceleration." In: *ssr* 58.1, pp. 259–346. DOI: 10.1007/BF01206003.

Kahler, S. W. (Oct. 2001). "The correlation between solar energetic particle peak intensities and speeds of coronal mass ejections: Effects of ambient particle intensities and energy spectra." In: *jgr* 106.A10, pp. 20947–20956. DOI: 10.1029/2000JA002231.

Kallenrode, M. B. (2004). *Space Physics : An Introduction to Plasmas and Particles in the Heliosphere and Magnetospheres*. DOI: 10.1007/978-3-662-09959-9.

Kallenrode, M. B. and E. W. Cliver (Aug. 2001). "Rogue SEP events: observational aspects." In: *International Cosmic Ray Conference*. Vol. 8. International Cosmic Ray Conference, p. 3314.

Kerdraon, A. and J. M. Delouis (1997). "The Nançay Radioheliograph." In: *Coronal Physics from Radio and Space Observations*. Ed. by Gerard Trottet. Vol. 483, p. 192. DOI: 10.1007/BFb0106458.

Khaksarighiri, S. et al. (2020). "Calculation of dose distribution in a realistic brain structure and the indication of space radiation influence on human brains." In: *Life Sciences in Space Research* 27, pp. 33–48. ISSN: 2214-5524. DOI: https://doi.org/10.1016/j.lssr.2020.07.003.

Kocharov, L. and J. Torsti (May 2002). "Hybrid Solar Energetic Particle Events Observed on Board Soho." In: *solphys* 207.1, pp. 149–157. DOI: 10.1023/A:1015540311183.

Kollhoff, A. et al. (2021). "The first widespread solar energetic particle event observed by Solar Orbiter on 2020 November 29." In: *A&A* 656, A20. DOI: 10.1051/0004-6361/202140937.

Kollhoff, A. et al. (2023). "Multi-spacecraft observations of near-relativistic electron events at different radial distances." In: *A&A* 675, A155. DOI: 10.1051/0004-6361/202345955.

Kouloumvakos, A. et al. (Apr. 2022). "The first widespread solar energetic particle event of solar cycle 25 on 2020 November 29. Shock wave properties and the wide distribution of solar energetic particles." In: *A&A* 660, A84. DOI: 10.1051/0004-6361/202142515.

Krimigis, S. M et al. (June 2011). "Zero outward flow velocity for plasma in a heliosheath transition layer." In: *nat* 474.7351, pp. 359–361. DOI: 10.1038/nature10115.

Krucker, Säm, P. H. Oakley, and R. P. Lin (Jan. 2009). "Spectra of Solar Impulsive Electron Events Observed Near Earth." In: *ApJ* 691.1, pp. 806–810. DOI: 10.1088/0004-637X/691/1/806.

Krucker, Säm et al. (Oct. 2020). "The Spectrometer/Telescope for Imaging X-rays (STIX)." In: *A&A* 642, A15. DOI: 10.1051/0004-6361/201937362.

Lario, D. et al. (Mar. 2008). "Influence of large-scale interplanetary structures on energetic particle propagation: September 2004 event at Ulysses and ACE." In: *Journal of Geophysical Research (Space Physics)* 113.A3, A03105. DOI: 10.1029/2007JA012721.

Lemen, J. R. et al. (Jan. 2012). "The Atmospheric Imaging Assembly (AIA) on the Solar Dynamics Observatory (SDO)." In: *solphys* 275.1-2, pp. 17–40. DOI: 10.1007/s11207-011-9776-8.

Lin, R. P. (May 1970). "The Emission and Propagation of 40 keV Solar Flare Electrons. I: The Relationship of 40 keV Electron to Energetic Proton and Relativistic Electron Emission by the Sun." In: *solphys* 12.2, pp. 266–303. DOI: 10.1007/BF00227122.

Lopez, R. E. (Oct. 1987). "Solar cycle invariance in solar wind proton temperature relationships." In: *jgr* 92.A10, pp. 11189–11194. DOI: 10.1029/JA092iA10p11189.

Lysenko, A. et al. (June 2019). "X-ray and gamma-ray emission of solar flares." In: *Physics-Uspekhi* 63. DOI: 10.3367/UFNe.2019.06.038757.

Maksimovic, M. et al. (Oct. 2020). "The Solar Orbiter Radio and Plasma Waves (RPW) instrument." In: *A&A* 642, A12. DOI: 10.1051/0004-6361/201936214.

Mason, G. M., J. E. Mazur, and J. R. Dwyer (1999). "3He Enhancements in Large Solar Energetic Particle Events." In: *The Astrophysical Journal* 525.2, p. L133. DOI: 10.1086/312349.

Masson, S. et al. (Feb. 2012). "Interchange Slip-Running Reconnection and Sweeping SEP Beams." In: *solphys* 276.1-2, pp. 199–217. DOI: 10.1007/s11207-011-9886-3.

Maunder, E. W. (June 1922a). "The sun and sun-spots, 1820-1920." In: *MNRAS* 82, pp. 534–543. DOI: 10.1093/mnras/82.9.534.

Maunder, E. Walter (Feb. 1922b). "The Prolonged Sunspot Minimum, 1645-1715." In: *Journal of the British Astronomical Association* 32, pp. 140–145.

McComas, D. J. et al. (Sept. 2008). "Weaker solar wind from the polar coronal holes and the whole Sun." In: *grl* 35.18, L18103. DOI: 10.1029/2008GL034896.

Meegan, C. et al. (Sept. 2009). "The Fermi Gamma-ray Burst Monitor." In: *ApJ* 702.1, pp. 791–804. DOI: 10.1088/0004-637X/702/1/791.

Meneguzzi, M., J. Audouze, and H. Reeves (Jan. 1971). "The production of the elements Li, Be, B by galactic cosmic rays in space and its relation with stellar observations." In: *A&A* 15, p. 337.

Mitalas, R. and K. R. Sills (Dec. 1992). "On the Photon Diffusion Time Scale for the Sun." In: *ApJ* 401, p. 759. DOI: 10.1086/172103.

Moraal, H. (2013). "Cosmic-Ray Modulation Equations." In: *Space Sci. Rev.* 176, pp. 299–319. DOI: 10.1007/s11214-011-9819-3.

Moreton, G. E. (Jan. 1960). "Hα Observations of Flare-Initiated Disturbances with Velocities ~1000 km/sec." In: *aj* 65, p. 494. DOI: 10.1086/108346.

Müller-Mellin, R. et al. (Apr. 2008). "The Solar Electron and Proton Telescope for the STEREO Mission." In: *ssr* 136.1-4, pp. 363–389. DOI: 10.1007/s11214-007-9204-4.

Müller, D. et al. (Oct. 2020). "The Solar Orbiter mission. Science overview." In: *A&A* 642, A1. DOI: 10.1051/0004-6361/202038467.

Munro, R. H. et al. (Feb. 1979). "The association of coronal mass ejection transients with other forms of solar activity." In: *solphys* 61.1, pp. 201–215. DOI: 10.1007/BF00155456.

Müller, D. et al. (Aug. 2012). "Solar Orbiter: Exploring the Sun–Heliosphere Connection." In: *Solar Physics* 285.1–2, 25–70. ISSN: 1573-093X. DOI: 10.1007/s11207-012-0085-7.

Neumaier, A. (1998). "Solving Ill-Conditioned and Singular Linear Systems: A Tutorial on Regularization." In: *SIAM Review* 40.3, pp. 636–666. DOI: 10.1137/S0036144597321909.

Neupert, W. M. (July 1968). "Comparison of Solar X-Ray Line Emission with Microwave Emission during Flares." In: *apjl* 153, p. L59. DOI: 10.1086/180220.

Neupert, W. M. (Sept. 1989). "Transient Coronal Extreme Ultraviolet Emission before and during the Impulsive Phase of a Solar Flare." In: *ApJ* 344, p. 504. DOI: 10.1086/167819.

Obridko, V. and Oleg Vaisberg (Mar. 2017). "On the history of the solar wind discovery." In: *Solar System Research* 51, pp. 165–169. DOI: 10.1134/S0038094617020058.

Owen, C. J. et al. (Oct. 2020). "The Solar Orbiter Solar Wind Analyser (SWA) suite." In: *A&A* 642, A16. DOI: 10.1051/0004-6361/201937259.

Parker, E. N. (Sept. 1955). "Hydromagnetic Dynamo Models." In: *ApJ* 122, p. 293. DOI: 10.1086/146087.

Parker, E. N. (Dec. 1957). "Sweet's Mechanism for Merging Magnetic Fields in Conducting Fluids." In: *jgr* 62.4, pp. 509–520. DOI: 10.1029/JZ062i004p00509.

Parker, E. N. (Nov. 1958). "Dynamics of the Interplanetary Gas and Magnetic Fields." In: *ApJ* 128, p. 664. DOI: 10.1086/146579.

Parker, E. N. (Jan. 1965). "The passage of energetic charged particles through interplanetary space." In: *planss* 13.1, pp. 9–49. DOI: 10.1016/0032-0633(65)90131-5.

Parsons, J. L. and L. W. Townsend (June 2000). "Interplanetary Crew Dose Rates for the August 1972 Solar Particle Event." In: *Radiation Research* 153.6, pp. 729–733. DOI: 10.1667/0033-7587(2000)153[0729:ICDRFT]2.0.CO;2.

Pehl, R. H. et al. (Feb. 1968). "Accurate determination of the ionization energy in semiconductor detectors." In: *Nuclear Instruments and Methods* 59.1, pp. 45–55. DOI: 10.1016/0029-554X(68)90342-X.

Pomoell, J. and S. Poedts (June 2018). "EUHFORIA: European heliospheric forecasting information asset." In: *Journal of Space Weather and Space Climate* 8, A35. DOI: 10.1051/swsc/2018020.

Posner, A., I. Richardson, and R. Strauss (Mar. 2024). *The SEP clock: A discussion of first proton arrival times in wide-spread solar energetic particle events*. DOI: 10.21203/rs.3.rs-4182789/v1.

Prise, A. J. et al. (May 2014). "An Investigation of the CME of 3 November 2011 and Its Associated Widespread Solar Energetic Particle Event." In: *Solar Physics* 289.5, pp. 1731–1744. DOI: 10.1007/s11207-013-0435-0.

Pulkkinen, A. et al. (2005). "Geomagnetic storm of 29–31 October 2003: Geomagnetically induced currents and their relation to problems in the Swedish high-voltage power transmission system." In: *Space Weather* 3.8. DOI: https://doi.org/10.1029/2004SW000123.

Rast, M. P. (Nov. 2003). "The Scales of Granulation, Mesogranulation, and Supergranulation." In: *ApJ* 597.2, pp. 1200–1210. DOI: 10.1086/381221.

Reames, D. V. (July 1988). "Bimodal Abundances in the Energetic Particles of Solar and Interplanetary Origin." In: *apjl* 330, p. L71. DOI: 10.1086/185207.

Reames, D. V. (Aug. 1990a). "Acceleration of Energetic Particles by Shock Waves from Large Solar Flares." In: *apjl* 358, p. L63. DOI: 10.1086/185780.

Reames, D. V. (June 1990b). "Energetic Particles from Impulsive Solar Flares." In: *apjs* 73, p. 235. DOI: 10.1086/191456.

Reames, D. V. (July 1995). "Solar energetic particles: A paradigm shift." In: *Reviews of Geophysics* 33.S1, pp. 585–589. DOI: 10.1029/95RG00188.

Reames, D. V. (Jan. 2013). "The Two Sources of Solar Energetic Particles." In: *Space Science Reviews* 175.1–4, 53–92. ISSN: 1572-9672. DOI: 10.1007/s11214-013-9958-9.

Reinhard, R. and G. Wibberenz (June 1974). "Propagation of Flare Protons in the Solar Atmosphere." In: *Solar Physics* 36.2, pp. 473–494. DOI: 10.1007/BF00151216.

Richardson, I. G., T. T. von Rosenvinge, and H. V. Cane (June 2015). "The Properties of Solar Energetic Particle Event-Associated Coronal Mass Ejections Reported in Different CME Catalogs." In: *solphys* 290.6, pp. 1741–1759. DOI: 10.1007/s11207-015-0701-4.

Richardson, I. G. et al. (Aug. 2014). "> 25 MeV Proton Events Observed by the High Energy Telescopes on the STEREO A and B Spacecraft and/or at Earth During the First ∼ Seven Years of the STEREO Mission." In: *solphys* 289.8, pp. 3059–3107. DOI: 10.1007/s11207-014-0524-8.

Rodríguez-García, L. et al. (Feb. 2023). "Solar energetic electron events measured by MESSENGER and Solar Orbiter. Peak intensity and energy spectrum radial dependences: Statistical analysis." In: *A&A* 670, A51. DOI: 10.1051/0004-6361/202244553.

Rodríguez-Pacheco, J. et al. (2020). "The Energetic Particle Detector - Energetic particle instrument suite for the Solar Orbiter mission." In: *A&A* 642, A7. DOI: 10.1051/0004-6361/201935287.

Ruffolo, D. (Apr. 1995). "Effect of Adiabatic Deceleration on the Focused Transport of Solar Cosmic Rays." In: *ApJ* 442, p. 861. DOI: 10.1086/175489.

SERPENTINE (2020).

SILSO World Data Center (2024). "The International Sunspot Number." In: *International Sunspot Number Monthly Bulletin and online catalogue*.

Schatten, K. H., J. M. Wilcox, and N. F. Ness (Mar. 1969). "A model of interplanetary and coronal magnetic fields." In: *solphys* 6.3, pp. 442–455. DOI: 10.1007/BF00146478.

Scholer, M. (1988). "Acceleration of Energetic Particles in Solar Flares." In: *Activity in Cool Star Envelopes*. Ed. by O. Havnes et al. Dordrecht: Springer Netherlands, pp. 195–210. ISBN: 978-94-009-2951-7.

Schwabe, Heinrich (Feb. 1844). "Sonnenbeobachtungen im Jahre 1843. Von Herrn Hofrath Schwabe in Dessau." In: *Astronomische Nachrichten* 21.15, p. 233. DOI: 10.1002/asna.18440211505.

Shibata, K. and T. Magara (Dec. 2011). "Solar Flares: Magnetohydrodynamic Processes." In: *Living Reviews in Solar Physics* 8.1, 6. DOI: 10.12942/lrsp-2011-6.

Simpson, J. A. (Jan. 1983). "Elemental and Isotopic Composition of the Galactic Cosmic Rays." In: *Annual Review of Nuclear and Particle Science* 33, pp. 323–382. DOI: 10.1146/annurev.ns.33.120183.001543.

Snyder, J.P. (1987). *Map Projections - A Working Manual*. Geological Survey Professional Paper 1395.

Solar Orbiter Archive (2025). www.cosmos.esa.int/web/soar/calibration-files#EPD. Accessed: 2025-01-10.

Spörer, G. (Jan. 1880). "Beobachtungen der Sonnenflecken von Januar 1874 bis December 1879." In: *Publikationen des Astrophysikalischen Observatoriums zu Potsdam* 2, pp. 1–81.

Stephens Jr., Daniel L., Lawrence W. Townsend, and Jennifer L. Hoff (May 2005). "Interplanetary crew dose estimates for worst case solar particle events based on historical data for the Carrington flare of 1859." In: *Acta Astronautica* 56.9-12, pp. 969–974. DOI: 10.1016/j.actaastro.2005.01.024.

Sullivan, J. D. (Jan. 1971). "Geometrical factor and directional response of single and multi-element particle telescopes." In: *Nuclear Instruments and Methods* 95, p. 5. DOI: 10.1016/0029-554X(71)90033-4.

Teegarden, B. J. et al. (Jan. 1974). "Interplanetary Mev electrons of Jovian origin." In: *jgr* 79.25, p. 3615. DOI: 10.1029/JA079i025p03615.

Temerin, M. and I. Roth (June 1992). "The Production of 3He and Heavy Ion Enrichments in 3He-rich Flares by Electromagnetic Hydrogen Cyclotron Waves." In: *apjl* 391, p. L105. DOI: 10.1086/186408.

Thejappa, G. et al. (2012). "Evidence for the oscillating two stream instability and spatial collapse of Langmuir waves in a solar type III radio burst." In: *The Astrophysical Journal Letters* 747.1, p. L1. DOI: 10.1088/2041-8205/747/1/L1.

Tikhonov, A.N. and V.I.A. Arsenin (1977). *Solutions of Ill-posed Problems*. Halsted Press book. Winston. ISBN: 9780470991244.

Toriumi, S. and H. Wang (May 2019). "Flare-productive active regions." In: *Living Reviews in Solar Physics* 16.1, 3. DOI: 10.1007/s41116-019-0019-7.

Uchida, Y. (May 1968). "Propagation of Hydromagnetic Disturbances in the Solar Corona and Moreton's Wave Phenomenon." In: *solphys* 4.1, pp. 30–44. DOI: 10.1007/BF00146996.

Usoskin, I. G. et al. (2005). "Heliospheric modulation of cosmic rays: Monthly reconstruction for 1951–2004." In: *Journal of Geophysical Research: Space Physics* 110.A12. DOI: https://doi.org/10.1029/2005JA011250.

Usoskin, Ilya G., Galina A. Bazilevskaya, and Gennady A. Kovaltsov (Feb. 2011). "Solar modulation parameter for cosmic rays since 1936 reconstructed from ground-based neutron monitors and ionization chambers." In: *Journal of Geophysical Research (Space Physics)* 116.A2, A02104. DOI: 10.1029/2010JA016105.

Vainio, R. et al. (Jan. 2007). "Modeling of Solar Energetic Particles in Interplanetary Space." In: *Space Weather : Research Towards Applications in Europe 2nd European Space Weather Week (ESWW2)*. Ed. by Jean Lilensten. Vol. 344. Astrophysics and Space Science Library, p. 27. DOI: 10.1007/1-4020-5446-7_4.

Wang, J. et al. (May 2020). "A Small-scale Filament Eruption Inducing a Moreton Wave, an EUV Wave, and a Coronal Mass Ejection." In: *ApJ* 894.1, 30. DOI: 10.3847/1538-4357/ab8565.

Webb, D. F. and R. A. Howard (Mar. 1994). "The solar cycle variation of coronal mass ejections and the solar wind mass flux." In: *jgr* 99.A3, pp. 4201–4220. DOI: 10.1029/93JA02742.

Wibberenz, G. and H. V. Cane (Oct. 2006). "Multi-Spacecraft Observations of Solar Flare Particles in the Inner Heliosphere." In: *ApJ* 650.2, pp. 1199–1207. DOI: 10.1086/506598.

Wiedenbeck, M. et al. (June 2007). "An Overview of the Origin of Galactic Cosmic Rays as Inferred from Observations of Heavy Ion Composition and Spectra." In: *Space Science Reviews* 130. DOI: 10.1007/s11214-007-9198-y.

Wraase, S. et al. (Aug. 2018). "The Solar Electron and Proton Telescope Aboard STEREO – Understanding Proton Spectra." In: *Solar Physics* 293.8. ISSN: 1573-093X. DOI: 10.1007/s11207-018-1321-6.

Yokoyama, T. and K. Shibata (Feb. 1998). "A Two-dimensional Magnetohydrodynamic Simulation of Chromospheric Evaporation in a Solar Flare Based on a Magnetic Reconnection Model." In: *apjl* 494.1, pp. L113–L116. DOI: 10.1086/311174.

Zank, G. P., W. K. M. Rice, and C. C. Wu (Nov. 2000). "Particle acceleration and coronal mass ejection driven shocks: A theoretical model." In: *jgr* 105.A11, pp. 25079–25096. DOI: 10.1029/1999JA000455.

Zhang, J. and K. P. Dere (2006). "A Statistical Study of Main and Residual Accelerations of Coronal Mass Ejections." In: *The Astrophysical Journal* 649.2, p. 1100. DOI: 10.1086/506903.

Zhang, M. and M. A. Lee (June 2013). "Stochastic Acceleration of Energetic Particles in the Heliosphere." In: *ssr* 176.1-4, pp. 133–146. DOI: 10.1007/s11214-011-9754-3.

Zhao, L.-L. et al. (2019). "ACR Proton Acceleration Associated with Reconnection Processes beyond the Heliospheric Termination Shock." In: *The Astrophysical Journal* 886.2, p. 144. DOI: 10.3847/1538-4357/ab4db4.

Zhao, X. Y. et al. (Dec. 2013). "A geometric factor calculation method based on the isotropic flux assumption." In: *Chinese Physics C* 37.12, 126201. DOI: 10.1088/1674-1137/37/12/126201.

Zurbuchen, T. H. and I. G. Richardson (Mar. 2006). "In-Situ Solar Wind and Magnetic Field Signatures of Interplanetary Coronal

Mass Ejections." In: *ssr* 123.1-3, pp. 31–43. DOI: 10.1007/s11214-006-9010-4.

van Ballegooijen, A. A. et al. (July 2011). "Heating of the Solar Chromosphere and Corona by Alfvén Wave Turbulence." In: *ApJ* 736.1, 3. DOI: 10.1088/0004-637X/736/1/3.

DANKSAGUNG

Für die Möglichkeit diese Arbeit zu erstellen und für den spannenden fachlichen Austausch möchte ich mich an dieser Stelle bei beiden Arbeitsgruppen der Extraterrestrischen Physik in Kiel herzlich bedanken. Besonderer Dank gilt Prof. Robert Wimmer-Schweingruber und Prof. Bernd Heber, die mir die Gelegenheit gegeben haben, in ihren Arbeitsgruppen mitzuwirken. Auch möchte ich mich bei dem gesamten EPD-Team bedanken, das ein so spannendes Projekt auf die Beine gestellt und mir immer mit Rat und Tat geholfen hat.
Ein ganz lieber Dank gilt auch Anne, Stefan und Patrick für das Korrekturlesen und die vielen hilfreichen Kommentare.
Ich werde die spannende Zeit als Promotionsstudent, das gemeinsame Arbeiten, die Pausen in der Mensa und die verlässliche Kaffeeversorgung für immer in guter Erinnerung behalten.

EIDESSTATTLICHE VERSICHERUNG

Ich versichere an Eides statt, dass die vorliegende Abhandlung – abgesehen von der Beratung durch meinen Betreuer und der angegebenen Literatur – nach Inhalt und Form meine eigene Arbeit ist und dass die Arbeit unter Einhaltung der Regeln guter wissenschaftlicher Praxis der Deutschen Forschungsgemeinschaft entstanden ist. Ich versichere weiter, dass die Arbeit weder ganz oder zum Teil schon einer anderen Stelle im Rahmen eines Prüfungsverfahrens vorgelegen hat. Teile dieser Arbeit wurden bereits in Fachzeitschriften veröffentlicht und sind als solche gekennzeichnet. Die Quellennachweise der jeweiligen Veröffentlichungen befinden sich in den zugehörigen Literaturverzeichnissen. Ich versichere zudem, dass mir kein akademischer Grad entzogen wurde.

Kiel, 4. März 2025

Alexander L. Kollhoff